Rheological Behavior of Colloidal Suspensions: the Effects of Hydrodynamic Interactions

Thesis by

David R. Foss

In Partial Fulfillment of the Requirements

for the Degree of

Doctor of Philosophy

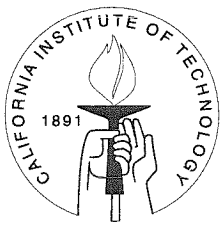

California Institute of Technology

Pasadena, California

1999

(Submitted May 11, 1999)

Acknowledgements

Over the past four and a half years, many people have given me the support which has allowed me to obtain my degree. First, I would like to thank my advisor John Brady. His door was always open for frequent discussions from which I learned a great deal. His guidance and constructive criticism have helped me grow as a researcher. His long leash, patience and understanding are greatly appreciated.

Many members of the group made the days staring at the monitors pass by more quickly than maybe they should have. Gene, Douglas, Yvette, Mike, Saud, Sundar, Ganesh, Phil, Johan and Kengo, thank you for many thoughtful discussions — and many entertaining ones, too. In particular, I would like to thank Mike Vicic for showing me the ropes when I first joined the group. Also, I would like to thank Suresh Guptha for all his indespensible help on all problems involving hardware, programming, file restoration and LaTeX.

Outside the group, I had many friends on campus to keep me occupied. During classes, Pete and Alex made homework and studying fun and something to look forward to. Jason and Tim were two of the best roommates a guy could ever have. Great fun was had hiking and moviegoing with Jeremy, Doris, Guru, Sumit, Mon, Vidya, Fay and Steve. Jeremy and Doris deserve additional mention as they were kind enough to lend me their car these last few months. I always looked forward to going to the pool and the gym with Pedro, Anne & Anette. Many long discussions with Margie prove that she is much more than just a great secretary, but a great friend. I would also especially like to thank Lori Giver and Nikki Takarabe for the great amount of fun, laughter and support they gave me when I needed it the most.

Escaping from the academic environment was necessary from time to time and there is no greater escape than hanging out with the 'Claremont buddies' in Claremont and elsewhere. Paul, Roomie, Mak, Mang, Adam, No Wai, Henry, Eliza, and Linus, your fun-loving lunacy certainly gave me lots of weekends to look forward to.

Last, but certainly not least, I would like to thank my family for all the love and support they've given me over the past few years. All the fun, stories, understanding, gifts, care packages, visits, email, phone calls, and more, certainly made me feel at home even when I was not there. Ann Marie, Emily, Mary Ellen, Mom, and Dad... Thank you.

Abstract

The rheological behavior of hard-sphere colloidal suspensions in simple shear flow is examined theoretically and by dynamic simulation. The Stokesian Dynamics and Brownian Dynamics simulation techniques are used to study suspensions with and without many-body hydrodynamic interactions, respectively. Suspensions near equilibrium, where Brownian motion dominates, and at high shear rates, where hydrodynamic forces dominate, are examined. Steady-state simulations are performed using both simulation algorithms. The Brownian Dynamics system is found to be shear-thinning at low shear rates and undergoes a phase transition at high shear rates to a phase of hexagonally-packed strings aligned in the flow direction. Inclusion of hydrodynamic interactions eliminates the phase transition at high shear rates. Instead, the suspension is found to shear thicken due to a boundary layer of high particle probability that forms near contact where convection balances Brownian diffusion. This increases the role of strong hydrodynamic lubrication forces. Shear thinning and thickening data from many different volume fractions are collapsed using scaling theories. A previous steady-state theoretical analysis of the boundary layer at high shear rates (Brady & Morris 1997) is extended to include unsteady flow conditions. Theoretical results are found to be in agreement with start-up and flow-cessation simulations. A relation between start-up flow at low shear rates and the relaxation of equilibrium fluctuations is made. Equilibrium fluctuations are characterized using the shear-stress autocorrelation function and Green-Kubo formulae. Behavior of this function at short times is related to the behavior in an oscillatory shear flow at high frequencies that is also well-described by a boundary layer where unsteady convection balances Brownian diffusion. A new method for determining the components of the long-time self-diffusion tensor is proposed. Self-diffusion is found to be a decreasing function of volume fraction near equilibrium and an increasing function of volume fraction at high shear rates. Data is in agreement with previous theory and experi-

ment. Due to the buildup of particle probability along the compressional axis relative to the extensional axis in simple shear flow, there is a nonzero off-diagonal component to the long-time self-diffusion tensor which is proportional to the shear rate. This component is positive near equilibrium and negative at high shear rates.

Contents

List of Figures

List of Tables

Chapter 1

Introduction

This thesis concerns the behavior of colloidal dispersions at equilibrium and in simple shear flow. A colloidal dispersion consists of particles in a suspending fluid such that the particles are large enough to enable treatment of the solvent as a continuum, but small enough to be affected by Brownian motion due to thermal fluctuations in the solvent. Because of the small size of the particles, solvent-mediated low-Reynolds-number hydrodynamic forces are present. Other colloidal forces of nonhydrodynamic origin may also be present, such as gravitational, electrostatic, or repulsive and/or attractive interparticle forces. In this work, we are concerned with dispersions of monodisperse hard spheres suspended in a Newtonian solvent.

Although the body of this thesis is divided into four independent and self-contained chapters, there is a common theme prevalent throughout: the effect of hydrodynamic interactions on the rheology, diffusion, and microstructure of colloidal suspensions. Hydrodynamic interactions consist of both many-body far-field interactions and strong close-ranged pairwise-additive lubrication forces.

To study the behavior of these dispersions, we use two different simulation techniques. The first technique is Brownian Dynamics which employs a simple and efficient algorithm to study colloidal dispersions under shear in the absence of hydrodynamic interactions. The second technique is Stokesian Dynamics which is computationally intensive but includes full hydrodynamic interactions. Comparing and contrasting results from each simulation technique provides insight into the mechanisms involved in the behavior of colloidal dispersions.

In chapter 2, we examine the rheological behavior of hard-sphere dispersions in the absence of hydrodynamic interactions at steady state using the Brownian Dynamics technique. At low shear rates, the suspensions are found to be well-dispersed and disordered. As the shear rate is increased, the system undergoes a transition into an ordered phase. Self-diffusivities are found to be increasing functions of shear rate with the exception of a precitious decrease at the onset of the ordered phase. The viscosity is found to be a decreasing function of shear rate — the suspension shear thins — and the effects of density on this behavior are examined with the aid of recent scaling theories. The behavior of the first and second normal stress differences are

examined. The first normal stress difference is positive while the second normal stress difference is negative. The magnitudes of each normal stress difference are found to be zero at very low shear rates, rise to a maximum as the shear rate increases and then decrease again. The osmotic pressure is also examined and is proportional to the thermal energy of the system near equilibrium and to the imposed shear rate at high shear rates.

The steady-state rheology of hard-sphere dispersions is also studied for the case where hydrodynamic interactions are included in chapter 3. The Stokesian Dynamics simulation technique is used limiting the size of the systems studied due to high computational cost. The suspensions are found to be well-dispersed and disordered at all shear rates — no ordered phase is found — in contrast to previously reported results. Short-time self-diffusivities are found to be decreasing functions of shear rate. Long-time self-diffusivities are found to be increasing functions of shear rate, scaling as the single particle Stokes-Einstein diffusivity near equilibrium and proportional to the shear rate at high shear rates. The separate hydrodynamic and Brownian contributions to the suspension stress are determined. The behavior of the suspension stress is dominated by the Brownian contribution at low shear rates and by the hydrodynamic contribution at high shear rates. The suspension shear thins at low shear rates due to the decay of the Brownian contribution, while the hydrodynamic contribution remains constant. At high shear rates, the viscosity increases with shear rate — the suspension shear thickens — as a thin boundary layer near particle contact of high particle probability forms increasing the role of strong hydrodynamic lubrication forces. Simulation is found to be in good agreement with experiment. Recent two particle scaling theories are employed to collapse the data. The normal stress differences are also studied with quality data being limited to intermediate and high shear rates. At low shear rates, the first normal stress difference is positive while the second is negative. As the shear rate is increased the first normal stress difference changes sign and both normal stress differences are negative at high shear rates.

The transient behavior of the stress and microstructure is examined in chapter 4 using both Brownian Dynamics and Stokesian Dynamics simulation techniques. Equi-

librium fluctuations are characterized by the shear-stress autocorrelation function, which can be related to linear viscoelastic behavior by well-established Green-Kubo theories. Without hydrodynamic interactions, the shear-stress autocorrelation function is found to diverge at short times as $t^{-1/2}$ indicating that the elastic modulus diverges at high frequency in a small amplitude oscillatory shear flow. Inclusion of hydrodynamic interactions produces different behavior. The shear-stress autocorrelation function approaches a constant at short times indicating that the elastic modulus approaches a finite limit at high frequencies. The high-frequency modulus is compared to experiment. Transient behavior of the stress in nonequilibrium situations is also analyzed. A previous steady-state theory for suspensions at high shear rate is extended to start-up and flow-cessation situations. Start-up and flow-cessation simulations are performed showing good agreement with the theoretic analysis. The microstructure is also analyzed during start-up and flow-cessation providing further evidence of the relaxation mechanisms proposed.

The behavior of the long-time self-diffusion tensor as a function of both density and shear rate is examined in detail in chapter 5. A new method is employed to obtain quality data for long-time self-diffusivities by averaging data from many short simulations. Systems with and without hydrodynamic interactions are examined. When hydrodynamic interactions are included, rotational self-diffusion is studied and all the diffusivities can be divided into their hydrodynamic and Brownian contributions. Diffusivities are found to be decreasing functions of volume fraction near equilibrium scaling as the single particle Stokes-Einstein diffusivity. At high shear rates, the diffusivity is proportional to the shear rate and is found to be an increasing function of volume fraction. Both translational and rotational self-diffusion tensors are found to have one nonzero off-diagonal component in simple shear flow due to a buildup of particles in the compressional zone. This component is proportional to the shear rate for all shear rates. The translational off-diagonal component is positive near equilibrium and negative at high shear rates and the rotational off-diagonal self-diffusivity is negative near equilibrium and positive at high shear rates.

Chapter 2

Brownian Dynamics simulation of hard-sphere colloidal dispersions

2.1 Introduction

This paper addresses the structure, diffusion and rheology of colloidal dispersions of hard spheres in the absence of hydrodynamic interactions. Colloidal dispersions consist of small particles suspended in a Newtonian solvent. The particles are large enough so that the suspending fluid can be treated as a continuum, yet small enough that the particles are affected by Brownian motion, which arises from thermal fluctuations in the surrounding fluid. Thus, the behavior of the particles in the dispersion is governed by the many-body Langevin equation.

A method for simulating Brownian particles was first presented by Ermak & McCammon (1978) and Fixman (1978) in the same issue of the *Journal of Chemical Physics*. Elimination of hydrodynamic interactions between particles simplifies matter greatly and there has been extensive work utilizing Brownian Dynamics in this case to simulate particles with many different interparticle potentials (Heyes 1988, Xue & Grest 1990, Rastogi *et al.* 1996). Hard-sphere dispersions have proven difficult to simulate, however, due to the singular and discontinuous nature of the hard-sphere interparticle potential.

Cichocki & Hinsen (1992) first simulated hard-spheres at equilibrium in order to measure the long-time self-diffusivity. In that work, interparticle collisions are resolved by rejecting random Brownian steps that result in particle overlap. Later, Heyes & Melrose (1993) and Schaertl & Sillescu (1994) independently developed the same method for simulation of hard spheres for measuring shear thinning and self-diffusion, respectively. This method is used in this work and is described in the following section. Here, we deviate from their method of calculation of the suspension stress and provide a more detailed analysis of the rheology, including data on the microstructure, self-diffusivities, shear viscosity, normal stress differences and osmotic pressure.

Since the inception of this work, a new method for hard-sphere Brownian Dynamics simulation has been proposed which implements the hard-sphere potential by treating the overlap of particles as elastic collisions (Strating 1999) — essentially a

Molecular Dynamics simulation is performed within each individual time step of the Brownian Dynamics simulation. While one can question if this is appropriate for Brownian particles, it does eliminate all residual particle overlaps which are present in other models. Strating presented results on the shear thinning of the viscosity, but no results of normal stress differences, osmotic pressure, or long-time self-diffusion were presented.

In the following section, we detail the Brownian Dynamics algorithm used in this work and describe a new method for determining the pairwise interparticle forces responsible for the hard-sphere-like behavior that facilitates calculation of 'instantaneous' values of all components of the particle contribution to the bulk stress tensor. In section 2.3 we discuss the results of these simulations. The structure is disordered at low shear rates and as the shear rate is increased, the suspension undergoes a gradual phase transition first to sliding-layers stacked in the velocity-gradient direction and eventually to hexagonally packed strings aligned in the flow direction. Self-diffusion is found to be an increasing function with shear rate with the exception of a precipitous decrease where the ordered phase forms. The viscosity is found to decrease with shear rate — or shear thin — and comparisons are made with two particle scaling theories based on various proposed characteristic relaxation time scales. With consideration a finite high-shear limiting viscosity that would be present in the absence of an ordered phase, we find that a characteristic relaxation time scale based on the equilibrium long-time self-diffusivity collapse the viscosity data for all volume fractions quite well. We finish with some concluding remarks and suggestions for future studies in section 2.4.

2.2 Simulation method

Brownian Dynamics can be described as a simplification of Stokesian Dynamics (Bossis & Brady 1987, 1989; Brady & Bossis 1988, Foss & Brady 1999b (ch. 3)) where the hydrodynamic interactions between the particles are neglected. For N rigid particles suspended in an incompressible Newtonian fluid of viscosity η and density ρ,

the particle motion is described by the coupled N-body Langevin equation:

$$\mathbf{m}\cdot\frac{d\boldsymbol{U}}{dt} = \boldsymbol{F}^H + \boldsymbol{F}^B + \boldsymbol{F}^P, \tag{2.1}$$

where $\mathbf{m}$ is the generalized mass/moment of inertia tensor, $\boldsymbol{U}$ is the particle translational/rotational velocity vector, and the force/torque vectors $\boldsymbol{F}$ represent: (i) the hydrodynamic forces $\boldsymbol{F}^H$ exerted on the particles due to their motion relative to the fluid, (ii) the deterministic non-hydrodynamic forces $\boldsymbol{F}^P$, which may be either interparticle or external, and (iii) the stochastic forces $\boldsymbol{F}^B$ that give rise to Brownian motion.

Since hydrodynamic interactions are neglected, $\boldsymbol{F}^H$ consists of only Stokes drag:

$$\boldsymbol{F}^H = -6\pi\eta a(\boldsymbol{U} - \langle \boldsymbol{U} \rangle),$$

where $\langle \boldsymbol{U} \rangle$ is the imposed flow evaluated at the particle center. For linear shear flow, $\langle \boldsymbol{U} \rangle = \dot{\boldsymbol{\Gamma}}\cdot\boldsymbol{x}$, where $\dot{\boldsymbol{\Gamma}}$ is the velocity gradient tensor of the bulk flow. The deterministic, non-hydrodynamic force $\boldsymbol{F}^P$ is arbitrary and may be any form of interparticle or external force. The stochastic or Brownian force $\boldsymbol{F}^B$ arises from the thermal fluctuations in the fluid and is characterized by

$$\overline{\boldsymbol{F}^B} = 0 \quad \text{and} \quad \overline{\boldsymbol{F}^B(0)\boldsymbol{F}^B(t)} = 2kT(6\pi\eta a)\boldsymbol{I}\delta(t). \tag{2.2}$$

In (2.2) the overbars denote an ensemble average over the thermal fluctuations in the fluid, k is Boltzmann's constant, T is the absolute temperature, $6\pi\eta a\boldsymbol{I}$ is the hydrodynamic resistance tensor ($\boldsymbol{R}_{FU}$) in the absence of hydrodynamic interactions, $\boldsymbol{I}$ is the unit isotropic tensor and $\delta(t)$ is the delta function. The amplitude of the correlation between the Brownian forces at time 0 and at time t results from the fluctuation-dissipation theorem for the N-body system.

The deterministic nonhydrodynamic force $\boldsymbol{F}^P$ can be of any form (interparticle or external); in this work it will be of hard-sphere form as discussed below.

The particle evolution equation is obtained by integrating (2.1) over a time step

Δt that is large compared to τ_p the inertial relaxation time ($\tau_p = m/6\pi\eta a$), but small compared with the time over which the configuration changes. A second integration in time produces the evolution equation for the particle positions with an error of $o(\Delta t)$:

$$\Delta \boldsymbol{x} = Pe\langle \boldsymbol{U} \rangle \Delta + \boldsymbol{F}^P \Delta t + \boldsymbol{X}(\Delta t),$$

$$\overline{\boldsymbol{X}} = 0 \quad \text{and} \quad \overline{\boldsymbol{X}(\Delta t)\boldsymbol{X}(\Delta t)} = 2\boldsymbol{I}\Delta t. \tag{2.3}$$

Here, $\Delta \boldsymbol{x}$ is the change in particle position during the time step, Δt, and $\boldsymbol{X}(\Delta t)$ is a random displacement due to Brownian motion that has zero mean and covariance given by the short-time self-diffusion tensor, which in the absence of hydrodynamic interactions is simply $2D\boldsymbol{I}$, where $D = kT/6\pi\eta a$ is the diffusion coefficient of a single isolated particle. Without hydrodynamic interactions, each particle rotates freely with a diffusivity identically equal to the dilute limit Stokes-Einstein rotational diffusivity, $D^r = kT/8\pi\eta a^3$, and rotational motion is completely decoupled from translational motion; with hydrodynamics rotational and translational motion are coupled. The interparticle or external forces have been converted to velocities for the purpose of calculating the particle trajectories by multiplication of the hydrodynamic mobility, which for Brownian Dynamics is simply $(6\pi\eta a)^{-1}\boldsymbol{I}$.

In (2.3), $\boldsymbol{x}$ has been nondimensionalized by the characteristic particle size a; the time by the diffusive time scale a^2/D; the imposed velocity $\langle \boldsymbol{U} \rangle$ by $\dot{\gamma}a$, where $\dot{\gamma} = |\dot{\boldsymbol{\Gamma}}|$ is the magnitude of the shear rate; the shear forces by $6\pi\eta\dot{\gamma}a^2$; and the interparticle forces by kT/a. The Péclet number, $Pe = \dot{\gamma}a^2/D = 6\pi\eta\dot{\gamma}a^3/kT$, measures the relative importance of shear and Brownian forces, and $\dot{\gamma}^* = 6\pi\eta\dot{\gamma}a^2/|\boldsymbol{F}^P|$ is a nondimensional shear rate giving the relative importance of shear and interparticle or externally imposed forces.

In this work, we are interested in a monodisperse suspension of hard spheres. In the case where full hydrodynamic interactions are included, lubrication forces are sufficient to prevent the particles from overlapping, and the hard-sphere force at contact, $\boldsymbol{F}^P = \frac{1}{2}kT\hat{\boldsymbol{r}}\delta(r - 2a)$, has no dynamic consequence and none needs to be imposed in simulation (Foss & Brady 1999b (ch. 3)). Here, however, the lubrication

forces are absent and a force of hard-sphere type must be introduced. One option is to choose a pairwise steep, but 'soft', repulsive interparticle repulsive force: $\boldsymbol{F}^P \sim \hat{\boldsymbol{r}} r^{-n}$, where n is a parameter that determines the softness of the potential. The larger the n, the closer the potential approximates the hard-sphere potential. These potentials can be difficult to apply in practice as the time step must be set smaller as the potential gets steeper in order to resolve the full dynamics of each particle-particle collision. If the time step is too large, the interparticle separation could jump to a distance where the magnitude of the force is extremely large generating an aphysically large displacement in the following time step which often results in particle overlap. Much more important, however, with a soft repulsive force, the effective hard-sphere radius is a function of shear rate or Pe, as the interparticle separation where shear forces balance a soft potential varies with Pe. A changing effective radius results in a changing effective volume fraction, which is very inconvenient when trying to isolate the shear-rate and volume-fraction dependences of various rheological quantities.

To overcome this limitation, we have employed a 'potential-free' algorithm developed by Heyes & Melrose (1993) (see also Schaertl & Sillescu (1994) for an application to diffusion) in which the Brownian and affine displacements are made first, and then the simulation checks for particle overlaps, and displaces the overlapping particles along their lines of centers according to

$$\Delta \boldsymbol{x}^{HS} = \frac{1}{2}\hat{\boldsymbol{r}}(\Delta r - 2a)H(2a - \Delta r), \tag{2.4}$$

where $\Delta \boldsymbol{x}^{HS}$ is the hard-sphere displacement, Δr is the interparticle separation after the affine and Brownian displacements. The Heaviside step function is included to ensure that the displacement is only applied to overlapped particles, and the coefficient $\frac{1}{2}$ is chosen to return the particles back to contact. This algorithm cannot resolve all the overlaps, as displacements are applied in a pairwise fashion. Thus, for the 'potential-free algorithm', the particle evolution equation is:

$$\Delta \boldsymbol{x} = Pe\langle \boldsymbol{U} \rangle + \Delta \boldsymbol{x}^{HS} + \boldsymbol{X}(\Delta t),$$

$$\overline{\boldsymbol{X}} = 0 \quad \text{and} \quad \overline{\boldsymbol{X}(\Delta t)\boldsymbol{X}(\Delta t)} = 2\boldsymbol{I}\Delta t. \tag{2.5}$$

At this point, Heyes & Melrose (1993) determine the stress by calculating the pair-distribution function, $g(\boldsymbol{r})$, at contact and scaling the interparticle stress tensor with the $\hat{\boldsymbol{r}}\hat{\boldsymbol{r}}$ tensor so that an isotropic distribution returns the known theoretical value for the equilibrium hard-sphere osmotic pressure, $nkT(1 + 4\phi g(2a))$. Here, we deviate from their method directly calculating pairwise interparticle forces that would have result in the hard-sphere displacements during the course of a time step. This is done by examining the original evolution equation (2.3) and equating the contribution due to the interparticle force with the hard-sphere displacements; in dimensional form we have:

$$\boldsymbol{F}^P = 6\pi\eta a \frac{\Delta \boldsymbol{x}^{HS}}{\Delta t}, \tag{2.6}$$

which is simply the average Stokes drag on the particle during the course the hard-sphere displacement. Once the interparticle forces from each collision are known, they can be used to calculate the stress without explicitly determining the pair-distribution function at contact $g(2a)$. The bulk stress is defined as the average stress over the volume V containing the N particles and is given, in the absence of hydrodynamic interactions, by

$$\langle \boldsymbol{\Sigma} \rangle = -\langle p \rangle \boldsymbol{I} + 2\eta(1 + \frac{5}{2}\phi)\langle \boldsymbol{E} \rangle - nkT\boldsymbol{I} - n\langle \boldsymbol{x}\boldsymbol{F}^P \rangle. \tag{2.7}$$

Here, $\langle p \rangle$ is the fluid pressure which is arbitrary for an incompressible fluid, $-nkT\boldsymbol{I}$ is the isotropic stress associated with the thermal energy of the Brownian particles, and $\boldsymbol{F}^P$ is determined by equation (2.6). The hydrodynamic contribution to the stress reduces to the single-particle Newtonian Einstein correction, $\frac{5}{2}\phi$, and the so-called direct Brownian contribution to the stress is zero without hydrodynamic interactions. All of the rheologically interesting behavior is contained in the $\langle \boldsymbol{x}\boldsymbol{F}^P \rangle$ contribution; this is the sole contribution reported in this work.

We are also interested in the diffusive motion of the particles, and several 'particle diffusivities' can be defined. The short-time self-diffusivity, $\boldsymbol{D}_0^s$, measures the average

instantaneous particle mobility which, in the absence of hydrodynamics, is simply DI and appears in the particle evolution equation as the variance of the random Brownian step. The long-time self-diffusivity, $\boldsymbol{D}^s_\infty$, measures the ability of a particle to wander far from its starting point and is calculated from simulation as one-half the time rate of mean-square particle displacement:

$$\boldsymbol{D}^s_\infty = \lim_{t\to\infty} \frac{1}{2}\frac{d}{dt}\langle(\boldsymbol{x} - \boldsymbol{x}^a)^2\rangle. \tag{2.8}$$

Here, the affine contribution, $\Delta\boldsymbol{x}^a = \langle\boldsymbol{U}\rangle\Delta t$, to the particle displacements from the imposed simple shear flow is subtracted off at each instant in time when calculating the mean-square displacements. When a particle diffuses in the velocity-gradient direction, its corresponding affine velocity also changes which causes a strong convectively-enhanced contribution to mean-square displacements that grows as t^3 for $\langle x(t)x(t)\rangle$ and t^2 for $\langle x(t)y(t)\rangle$. Subtraction of the affine contribution removes all of the strong convectively-enhanced contributions to the diffusion allowing us to probe the underlying diffusive behavior in which all of the different mean-square displacements grow linearly at long times.

Due to the simplicity of this algorithm, the simulations can be performed efficiently at a computational cost of $O(N)$. For this reason, large numbers of particles — up to 1331 in our case — can be studied in the same amount of time required for conventional Stokesian Dynamics algorithms to analyze a much smaller systems. This greatly reduces the amount of noise present in the system and results in quantitatively more accurate rheological data.

2.3 Results

A large number of simulations have been performed over a range of volume fraction, $0.30 \leq \phi \leq 0.55$, and Péclet number, $0 \leq Pe \leq 10^4$, in order to examine the Pe-dependence of the rheological properties and the effects of the volume fraction on this dependence in hopes of deducing the relevant diffusivity involved in determining

the time scale for the suspension. For $Pe \leq 1$ time was non-dimensionalized by a^2/D as in (2.3), while for $Pe \geq 1$ time was non-dimensionalized with the inverse shear rate $1/\dot{\gamma}$. All runs for all Péclet numbers were started from a random hard-sphere configuration generated by allowing systems to equilibrate at $Pe = 0$ for volume fractions below the hard sphere phase boundary $\phi = 0.494$ or by a 'density quenching' technique (Rintoul & Torquato 1996, Clarke & Wiley 1987) for higher volumer fractions. The averages reported are over all particles and over time. The duration of the simulations was $100\dot{\gamma}t$ for $Pe \geq 1$ and $300 - 1000tD/a^2$ for $Pe < 1$. Systems were allowed to reach a steady-state — no residual transient due a phase transition were included — before averaging was begun. The runs were divided up into statistically independent subintervals in order to determine the statistical variation in properties. The three axes (x, y, z) of the cubic unit cell represent the velocity, velocity-gradient, and vorticity directions, respectively.

2.3.1 Structure

The suspension microstructure plays an important role in determining the other rheological properties and therefore will be discussed first. Figure 2.1 shows a projection of the pair distribution function $g(\boldsymbol{r})$ onto the flow–velocity-gradient plane for $\phi = 0.45$, $N = 1331$ at various Pe. At low Pe, the structure is nearly isotropic as denoted by the lack of angular variation in the first and second nearest-neighbor rings. As the Péclet number is increased, there is a buildup in particles in the compressional zone and a depletion of particles in the extensional zones, as first predicted by Batchelor (1977) and as evident by the oval pattern at $Pe = 1$. At higher Péclet numbers, one sees horizontal lines which are indicative of a string-ordered phase that is widely known to exist for systems where the effects of hydrodynamic lubrication interactions are not present (Bossis & Brady 1984, Erpenbeck 1984, Heyes 1986, Xue & Grest 1990, Rastogi *et al.* 1996, Foss & Brady 1999b (ch. 3)).

The order is shown more clearly in figure 2.2 where $g(\boldsymbol{r})$ has been projected onto the vorticity–velocity-gradient plane. The formation of order appears to be

gradual, occurring over a decade of Pe. At $Pe = 10$ and 30, layers of particle probability which are stacked in the gradient- or y-direction become noticeable. By $Pe = 100$, the pattern of peaks in $g(\boldsymbol{r})$ indicative of the hexagonally-packed string phase becomes apparent, though the order is fairly short-ranged. The peaks are seen to first occur where the layers of probability in the y-direction intersect with the first and second nearest-neighbor rings. At the largest shear rate, $Pe = 1000$, a longer-ranged, but multiple hexagonal pattern is apparent. Figures 2.3-2.6 show snapshots of the vorticity–velocity-gradient plane of the entire simulation cell. The transition from a disordered microstructure to a layered structure to the hexagonal string phase is clearly shown. At $Pe = 1000$, there is dramatic ordering of all the particles in the cell. The hexagonal-string lattice is imperfect, with varying orientation in different regions of the unit cell. This variation of orientation of the hexagonally-packed strings is what causes the multiple-hexagonal pattern in the projections of $g(\boldsymbol{r})$ seen in figure 2.2.

2.3.2 Diffusion

As noted in the previous section, the short-time self-diffusivity is simply the average instantaneous particle mobility, which, in the absence of hydrodynamic interactions, is simply $D\boldsymbol{I}$ and does not vary with ϕ or Pe. The long-time self-diffusivities are defined by (2.8) and are calculated from mean-square displacement data monitored during the simulation runs. Due the the large number of particles in the system, the mean-square displacements are calculated internally in each run instead of being reconstructed from stored particle locations.

At this point, we would like to note that long steady-state runs are not the best way to obtain good mean-square displacement data. We have obtained data that we feel is more accurate and internally consistent from large numbers of short start-up flow simulations (Foss & Brady 1999a (ch. 5)) that probe only the disordered microstructure, which in some flow regimes is not stable (*e.g.*, figure 2.6). Since this work deals with steady-state simulations run for long intervals, we will only present the diffusion data obtained from these types of runs, including those in which an

ordered phase forms.

Typical mean-square displacement curves are shown in figure 2.7. Diffusivities are calculated from these curves by discarding the first 20 time units of each curve and fitting a line through the remaining portion of the curve. This is also done for independent subsegments of the curve to measure the uncertainty in the diffusivity calculation.

The diagonal components of the long-time self-diffusivity tensor plotted as a function of Pe for $\phi = 0.45$ are shown in figure 2.8. At low Pe, all the diffusivities are roughly equal and much less than the isolated particle value. As Pe is increased, the diffusivities increase and start to show anisotropy as $D^s_{\infty,zz}$ is generally smaller than $D^s_{\infty,xx}$ and $D^s_{\infty,yy}$. At higher Pe, there is first a small decrease in $D^s_{\infty,yy}$ at $Pe \approx 30$ where the sliding layer phase is formed. The layers are stacked in the gradient- or y-direction inhibiting particle motion from layer to layer. This is followed by a precipitous drop in both $D^s_{\infty,yy}$ and $D^s_{\infty,zz}$ at $Pe \approx 100$ owing to the formation of the strings that line up in the x-direction and pack in the zy-plane. Note that $D^s_{\infty,xx}$ does not show the same decrease, which is indicative of imperfections in the string structure and that particles are indeed moving, however rarely, from string to string. String-to-string diffusion involves diffusion in the $y-$ and $z-$directions and is measured by $D^s_{\infty,yy}$, and $D^s_{\infty,zz}$, which have decreased by an order of magnitude but are still non-zero.

If we say that there is there is no movement from string to string, then in order for a particle to diffuse in the x-direction, it must push all the particles in that string forward. In a periodic suspension, this is analagous to the diffusion of multiple particles around a ring as illustrated in figure 2.9. The diffusivity in this case is known to be D/N_p, where N_p is the number of particles in the ring, or periodic string (Rallison 1988). For $N = 1331$, $N_p \approx 11$, which would imply that $D^s_{\infty,xx}$ should be approximately $0.1D$. The data in figure 2.8 does not show this; $D^s_{\infty,xx}$ is much larger and grows linearly with Pe indicating that particles must be diffusing laterally from string to string. In fact, after the formation of the strings, all diffusivities grow linearly with Pe indicating that the relevant scale for diffusion in this regime is $\dot{\gamma}a^2$,

not $kT/\eta a$. This is the same scaling found for high-Pe shear-induced diffusion in disordered systems (Eckstein *et al.* 1977, Leighton & Acrivos 1987, Breedveld *et al.* 1998, Foss & Brady 1999a (ch. 5), 1999b (ch. 3)). The $\dot{\gamma}a^2$ scaling for the diffusivity arises from a new source of 'noise' in the system caused by multiple particle-particle collisions. The diffusivity can be thought of as a velocity fluctuation times a particle displacement. The velocity fluctuation is caused by the relative motion between particles arrested by the hard-sphere force at contact in shear flow and is thus $O(\dot{\gamma}a)$ whereas the particle displacement is $O(a)$ allowing the incident particles to avoid particle overlap.

2.3.3 Rheology

When examining the suspension stress, all of the interesting nonNewtonian rheological behavior is due to the contribution from the hard-sphere-like interparticle force $\langle \boldsymbol{x}\boldsymbol{F}^P \rangle$. All results reported below are due solely to this contribution.

Viscosity

The suspension viscosity relative to that of the solvent is defined for simple shear flow from the xy-components of the bulk stress and rate of strain:

$$\eta_r \equiv \frac{\Sigma_{xy}}{2\eta E_{xy}}.$$

First, we analyze the fluctuations in the stress and microstructure at equilibrium to determine the zero-shear viscosity by the following dimensional Green-Kubo formula (Nägele & Bergenholtz 1998):

$$\eta_0 = \eta'_\infty + \frac{V}{kT}\int_0^\infty \langle \sigma_{xy}(t)\sigma_{xy}(0)\rangle dt. \tag{2.9}$$

Here, the high-frequency dynamic viscosity, η'_∞, represents the viscous contribution to the stress at equilibrium and is given by $\eta(1+\frac{5}{2}\phi)$ in the absence of hydrodynamic interactions. The instantaneous stress — here, the stress due to the interparticle force

— is denoted by $\sigma_{xy}(t)$. Although the time-average of $\sigma_{xy}(t)$ is zero, it fluctuates about its average value along with the microstructure due to Brownian motion. The shear stress autocorrelation function $\langle \sigma_{xy}(t)\sigma_{xy}(0)\rangle$ analyzes the nature of the relaxation of these fluctuations. Here, we use the subscript xy for ease of notation, but since there are no preferred directions at equilibrium, we can also autocorrelate the xz- and yz-components of the stress tensor and average the three functions to reduce statistical noise. A more thorough analysis of the time-dependent behavior of the shear stress autocorrelation function is contained in a related work (Foss & Brady 1999c (ch. 4)). Here, we are interested in the determination of the low shear viscosity. Simulations are performed at equilibrium ($Pe = 0$) using a time step of $\Delta t = 2.5 \times 10^{-4} a^2/D$ for at least 400 000 steps for calculation of the shear-stress autocorrelation function. Results for the zero-shear viscosity as a function of volume fraction are shown in table 2.1 and figure 2.10.

Figure 2.11 shows results for the suspension viscosity as a function of Pe for various N over a range of volume fraction between $0.30 \leq \phi \leq 0.55$. The curves show shear thinning behavior that is characteristic of Brownian suspensions. For $\phi = 0.40$, multiple N are used and show no N-dependence, providing confidence that the results can be extrapolated to infinite N. Note that there is a discontinuous drop in the viscosity for $Pe \approx 100$ that is coincident with the transition to an ordered phase.

Now we turn our attention to collapsing the viscosity data for all ϕ with the aid of scaling arguments based on two-particle theories and volume-fraction dependent time scales. Shear thinning behavior in the absence of hydrodynamic interactions occurs when the deformed microstructure that gives rise to large viscosities at very low Pe is unable to keep up with the flow as the shear rate is increased — the same reasons that it occurs when hydrodynamic interactions are included (Foss & Brady 1999b (ch. 3)). Shear thinning is a result of a decrease in the Brownian viscosity when hydrodynamic interactions are included. Here, the sole contribution to the stress of rheological interest is that due to the interparticle force. The stress due to a hard-sphere interparticle force is analagous to the direct contribution due to Brownian

motion when hydrodynamics interactions are included and stress can be written as an integral of the pair-distribution function at contact,

$$n\langle \boldsymbol{x}\boldsymbol{F}^P\rangle = -n^2kTa\int_{r=2a}\hat{\boldsymbol{r}}\hat{\boldsymbol{r}}g(\boldsymbol{r})dS, \tag{2.10}$$

where $\hat{\boldsymbol{r}} = \boldsymbol{r}/r$. The low-shear viscosity can be extracted from (2.10) by using the first perturbation due to flow to the equilibrium structure, $f(\boldsymbol{r})$, defined by $g(\boldsymbol{r}) = g^0(\boldsymbol{r})[1 + f(\boldsymbol{r})]$, where $g^0(\boldsymbol{r})$ is the equilibrium pair-distribution function. The equilibrium stress is simply the isotropic osmotic pressure, $-\Pi^0\boldsymbol{I}$. The first contribution to the viscosity is due to the $O(Pe)$ correction to the microstructure and results in a constant low-Pe Newtonian plateau with viscosity equal to the zero-shear viscosity, η_0; thus we can write

$$f(\boldsymbol{r}) = \hat{P}e\hat{f}(\boldsymbol{r}),$$

where $\hat{f}(\boldsymbol{r})$ is independent of the flow strength and $\hat{P}e = Pe/\hat{D}(\phi)$. Here, $\hat{D}(\phi)$ is the characteristic diffusivity nondimensionalized by the Stokes-Einstein diffusivity, D. Substituting the expression for $f(\boldsymbol{r})$ into the contact integral in (2.10) gives the following expression for the deviatoric part of the interparticle stress:

$$n\langle \boldsymbol{x}\boldsymbol{F}^P\rangle + \Pi^0\boldsymbol{I} = -\frac{27}{2\pi}\eta\dot{\gamma}\phi^2\,\frac{g^0(2;\phi)}{\hat{D}(\phi)}\int\hat{\boldsymbol{r}}\hat{\boldsymbol{r}}\hat{f}(2;\theta,\varphi)d\Omega. \tag{2.11}$$

Here, θ and φ are the two angular variables in spherical coordinates and $d\Omega$ represents the solid angle. In (2.11), the equilibrium contact value of the radial distribution function can be approximated very well by the Carnahan-Starling equation of state:

$$g^0(2;\phi) = \frac{1-0.5\phi}{(1-\phi)^3}, \quad \phi \le 0.50.$$

For higher volume fractions, Rintoul & Torquato (1996) have determined $g^0(2;\phi)$ for metastable disordered hard spheres by molecular dynamics simulation (Rintoul & Torquato 1996) and their results match the Carnahan-Starling equation of state at

its boundary of validity, $\phi = 0.50$. We have one volume fraction, $\phi = 0.55$, from this high-density regime for which we use $g^0(2) = 8.22$.

The characteristic diffusivity is determined by the appropriate relaxation time for rheological response: $a^2/\hat{D}(\phi)D$. With this scaled Péclet number, all of the Pe-dependence of the microstructure at all volume fractions is included in $\hat{Pe}$. In the dilute limit, all particle diffusivities are equal to the diffusivity of an isolated particle, D. Thus, $\hat{D} = 1$ and (2.11) reduces to the interparticle (or Brownian) stress as previously calculated by two-particle theories (Batchelor 1977, Brady & Vicic 1995, Lionberger 1998, Vicic 1999).

The precise nature of the characteristic diffusivity, $\hat{D}(\phi)$, is not known, and several quantities have been suggested. Brady (1993b) suggests using the equilibrium short-time self-diffusivity, $\hat{D}(\phi) = D_0^s(\phi)/D$, as this incorporates the effects of hydrodynamic interactions. Here, in the absence of hydrodynamic interactions, the short-time self-diffusivity is equal to that of an isolated particle, D. Thus, $\hat{D} = 1$ and $\hat{Pe} = Pe$. A plot of the viscosity using this scaling is shown in figure 2.12. This collapse is reasonably successful at lower volume fractions, but fails for $\phi > 0.40$.

Another possible choice for the characteristic diffusivity, $\hat{D}(\phi)$, is the equilibrium long-time self-diffusivity, $D_\infty^s(\phi)/D$, as it incorporates multiple-particle effects even in the absence of hydrodynamic interactions. A plot of the viscosity data using this scaling is shown in figure 2.13. This collapse appears to be more successful in that it correctly determines the shape of the shear thinning curves, but the data for each volume fraction are far from being coincident.

Other values for the characteristic diffusivity have been proposed, such as the collective diffusivity at the peak of the structure factor, $D^c(\boldsymbol{k}_{max})$ (Verberg *et al.* 1997, Pusey *et al.* 1997). Scaling of the data with this diffusivity is not currently possible because we have not calculated it from simulation. A further discussion of rheological scaling theories and the results of using them on systems containing full hydrodynamic interactions is included in a related work (Foss & Brady 1999b (ch. 3)).

Thus far when collapsing the viscosity data, we have used the total interparticle contribution to the stress without subtracting off any limiting value at high Pe that

may be present. This is not neccesary when hydrodynamic interactions are included as the Brownian stress — responsible for shear thinning in that case — vanishes like Pe^{-1}. Also, no subtraction appeared necessary in this work, as the order formation at high Pe results in very small values of the interparticle force contribution to the viscosity. This negligibly small high-shear viscosity is not in agreement with two-particle theoretical results where hard-spheres in the absence of hydrodynamic interactions approach a finite high-Pe plateau that is equal one-half the low-shear viscosity (Brady & Morris 1997, Vicic 1999). Of course, an ordered phase is not present in a two-particle theory and the predictions of such a theory are only valid in a disordered microstructure.

Despite the ordering that does occur in our steady-state Brownian Dynamics simulations, there are reasons for studying the behavior in the absence of order. First, a large portion of the shear thinning behavior occurs at low Pe where the string-ordered phase is not present. The dynamic microstructure present at low Pe occurs on time scales that do not appear related to the ordered structure that is present at high Pe. Disordered shear thinning and the formation of the ordered phase are independent physical processes. Another reason for studying the disordered regime is for comparing results with and without hydrodynamic interactions. Shear thinning occurs in both cases, but the system with hydrodynamic interactions included — simulated by Stokesian Dynamics — shows no string-ordered phase (Foss & Brady 1999b (ch. 3)).

The disordered high-Pe behavior in the absence of hydrodynamic interactions is evident in our related work (Foss & Brady 1999c (ch. 4)). Short start-up flow simulations from equilibrium configurations show that the transient behavior of the shear stress reaches a metastable plateau after approximately one strain. By contrast, the formation of the ordered string phase occurs in approximately twenty strains at $\phi = 0.45$. A comparison of the shear-rate dependent viscosity data obtained from short start-up flow and long steady-state simulations for $\phi = 0.45$ and $N = 1331$ is shown in figure 2.14. The two sets of data are indistinguishable at low Pe as there is no steady-state order present in that regime. At high Pe, one can see the effects of the

ordered phase. The steady-state data drops to near zero as the order forms while the values obtained from the start-up flow simulations show that the viscosity approaches a finite nonzero limit at high Pe. The high-shear limit, η_∞, is approximately 25% of the zero-shear limit in contrast to the 50% previously predicted in a dilute-limit two-particle theory (Brady & Morris 1997). This quantitative change can be explained by multiparticle interactions and the effects of volume fraction which are not present in a two particle system. The important result here is that a significant high-shear limit to the hard-sphere force contribution to the viscosity does exist in the absence of order. High-Pe limits to the viscosity as a function of volume fraction are shown in figure 2.15. As one would expect, the values are between the low-shear viscosities and the single-particle Einstein values — where the interparticle force contribution is zero.

Now that the disordered high-shear limits to the viscosity have been defined and etermined, they can be subtracted off from the steady-state values in order to obtain a collapse of the shear thinning data that would exist if the suspensions always remained disordered. It is to these disordered suspensions that the scaling ideas in eq. (2.11) apply. Figure 2.16 shows the uncollapsed viscosity data as a function of Pe for various volume fractions. (Note the negative values obtained at high Pe represent a suppression of the viscosity below the metastable disordered values due to the string-ordered microstructure and can be ignored when examining the shear-thinning behavior.) Figures 2.17 and 2.18 show collapses of the viscosity data using the equilibrium short- and long-time self-diffusivities as the characteristic diffusivities, respectively. As before, the use of the short-time self-diffusivity works reasonably well for the lower volume fractions and fails for $\phi > 0.45$. Use of the long-time self-diffusivity is quite successful. Again, the shape of the curve is correctly predicted, but the shift in the curves observed in figure 2.13 is removed when the η_∞ is subtracted off before performing the collapse. From these simulation results it appears that $D^s_\infty(\phi)$ is the proper time scale for characterizing the shear thinning behavior in Brownian suspensions.

Normal stress differences

The first and second normal stress differences are defined by

$$N_1 = \langle \Sigma_{xx} \rangle - \langle \Sigma_{yy} \rangle, \tag{2.12a}$$

$$N_2 = \langle \Sigma_{yy} \rangle - \langle \Sigma_{zz} \rangle. \tag{2.12b}$$

The normal stress differences are plotted as a function of Pe for $N = 1331$ and $\phi = 0.45$ in figures 2.19 and 2.20. The large system sizes here aid in producing better data, especially at low Pe, than has been obtained for smaller systems involving hydrodynamic interactions (Foss & Brady 1999b (ch. 3)). Flow-reversal symmetry arguments require that the normal stresses, when nondimensionalized by $\eta\dot{\gamma}$, vanish when $Pe \to 0$, which is evident in the figures. Here, N_1 increases with Pe achieves a maximum at $Pe \approx 1$ and then decays back towards zero. Similar behavior is seen in N_2, but with the opposite sign. At around $Pe \approx 100$ there is a discontinuous positive jump in both N_1 and N_2 corresponding to the onset of the ordered phase. The jump in N_1 is related to a decrease in the amount of collisions in the flow direction relative to the gradient direction in the ordered phase. Gradient-direction collisions remain quite common as particles are kept in their strings by collisions with particles in neighboring strings while flow-direction collisions decrease as this involves collisions between particles within the same string. Unlike systems which include hydrodynamic interactions (Foss & Brady 1999b (ch. 3)), N_1 does not change sign.

Like the viscosity, the normal stress differences can also be determined from the full interparticle stress tensor given by (2.11). Thus, collapses of data for different volume fractions can be examined to aid in the determination of $\hat{D}$. For these collapses we use only data obtained from simulations containing 1331 particles. Normal stress differences are quite difficult to measure at low Pe and smaller systems exhibit uncertainties too large to extract the underlying physical behavior.

The use of the short-time self-diffusivity as the characteristic diffusivity ($\hat{D} = 1$) to collapse the normal stress difference data is show in figures 2.21 and 2.22. All curves vanish as $Pe \to 0$ increase in magnitude to a maximum and then decrease

again. The scaling theory is not designed to collapse values of the stress at high Pe due to the order present. The normal stress difference data is also collapsed using the equilibrium long-time self-diffusivity as the characteristic diffusivity for rheological response in figures 2.23 and 2.24. There are only three sets of data, so caution must be used in drawing any firm conclusions, but using $\hat{D}(\phi) = D^s_\infty(\phi)/D$ does appear to better locate the maximums of each normal stress difference curve.

Osmotic pressure

The osmotic pressure is given by

$$\Pi = -\frac{1}{3}(\langle \Sigma_{xx} \rangle + \langle \Sigma_{yy} \rangle + \langle \Sigma_{zz} \rangle).$$

When nondimensionalized by nkT, the particle contribution to the osmotic pressure at equilibrium is equal to $4\phi g(2;\phi)$ (Brady 1993a) and arises from the $\langle \boldsymbol{x}\boldsymbol{F}^P \rangle$ term in equation (2.7). Figure 2.25 shows the equilibrium osmotic pressure as a function of ϕ showing that the simulation algorithm in this work underestimates the osmotic pressure relative to the Carnahan-Starling values by five to ten percent which can be accounted for by the small amount of 'softness' in the interparticle force caused by unresolved particle overlaps.

The Pe-dependence of the osmotic pressure is shown in figure 2.26 for $\phi = 0.45$ and $N = 1331$. The osmotic pressure remains roughly constant for low Pe and then grows linearly with Pe at high Pe indicative of an $\eta\dot{\gamma}$ scaling at high shear rates. Like all the other stresses, one can note a discontinuity in the data at $Pe \approx 100$ where the disorder-order transistion occurs. Also on figure 2.26 is the osmotic pressure following subtraction of its equilibrium value in order to determine the effect of the flow on the pressure at low shear rates. Recent theoretical work (Brady & Vicic 1995) predicts that this quantity scales like $nkTPe^2$ at low shear rates — the same behavior as the normal stress differences. This is in agreement with our data.

2.4 Concluding remarks

The behavior of hard-sphere suspensions is analyzed in the absence of hydrodynamic interactions using a Brownian Dynamics simulation technique, which involved manual displacement of overlapped particle pairs along their lines of centers. The algorithm is similar to that used previously by Heyes & Melrose (1993) and Schaertl and Sillescu (1994). Here, we extended their work to calculate the values of the interparticle forces associated with each particle-particle interaction and from these forces determined the shear and normal stresses.

Simulations are performed in simple shear flow with the strength of the flow determined by the Péclet number, Pe, which measures the relative size of the Brownian and shear forces. Brownian motion dominates at low Pe as large viscosities are present and shear thinning behavior is exhibited as the deformation of the microstructure cannot keep up with the flow. Collapses of the viscosity data for all ϕ are performed using scaling theories based on volume-fraction dependent characteristic time scales, $a^2/\hat{D}(\phi)$. Use of the short-time self-diffusivity for $\hat{D}(\phi)$, although adequate at lower volume fractions, fails for $\phi > 0.40$. The equilibrium long-time self-diffusivity for $\hat{D}(\phi)$ corrected produces the shape, but not the location of the viscosity curve. A correct collapse is obtained by subtracting off a high-shear limiting viscosity that would be present if the suspension did not order as the further decrease in the viscosity due to the formation of the ordered phase is not related to shear thinning.

The normal stress differences are found to vanish in the zero-shear-rate limit and each grow in magnitude with Pe — N_1 is positive while N_2 is negative — displaying a maximum/minimum near $Pe = 1$. The signs persist through the ordered phase due to a large amount of particles contacting in the gradient directions as the particles are kept in the strings by collisions with neighboring strings and a small amount of collisions in the flow direction as collisions between neighboring particles in a string become rare. The osmotic pressure is small and scales as nkT. The long-time self-diffusivities are small and scale with the Stokes-Einstein diffusivity, D. Both the osmotic pressure and the long-time self-diffusivities increase as Pe increases.

At $Pe \approx 100$, the suspension undergoes a disorder-order transition to a hexagonally-packed string-ordered phase. Accompanying this phase transition is a discontinuous drop in the values of the viscosity, osmotic pressure, and long-time diffusivity. At very large Pe, the interparticle force contribution to the viscosity is approximately zero due to the strong ordering of the particles. The osmotic pressure scales as $\eta\dot{\gamma}$. The long-time self-diffusivities scale as $\dot{\gamma}a^2$ indicating string-to-string diffusion is occurring.

The Brownian Dynamics algorithm used in this work is quite simple which enables the study of very large systems which are often necessary in order to obtain meaningful rheological data. The method can easily be modified to study a number of different problems such as bidisperse suspensions and weakly flocculating dispersions in simple shear or planar extensional flow.

Acknowledgments

The authors would like to thank S. Torquato for providing some equilibrium metastable disordered configurations from above the freezing transition. Partial support for this work was provided by grants from NSF and NASA.

References

Batchelor, G.K. 1977 The effect of Brownian motion on the bulk stress in a suspension of spherical particles. *J. Fluid Mech.* **83**, 97.

Bossis, G. & Brady, J.F. 1984 Dynamic simulation of sheared suspensions. I. General method. *J. Chem. Phys.* **80**, 5141.

Bossis, G. & Brady, J.F. 1987 Self-diffusion of Brownian particles in concentrated suspensions under shear. *J. Chem. Phys.* **87**, 5437.

Bossis, G. & Brady, J.F. 1989 The rheology of Brownian suspensions. *J. Chem. Phys.* **91**, 1866.

Brady, J.F. 1993a Brownian motion, hydrodynamics, and the osmotic pressure. *J. Chem. Phys.* **98**, 3335.

Brady, J.F. 1993b The rheological behavior of concentrated colloidal dispersions. *J. Chem. Phys.* **99**, 567.

Brady, J.F. & Bossis, G. 1988 Stokesian dynamics. *Ann. Rev. Fluid Mech.* **20**, 111.

Brady, J.F. & Morris, J.F. 1997 Microstructure of strongly sheared suspensions and its impact on rheology and diffusion. *J. Fluid Mech.* **348**, 103.

Brady, J.F. & Vicic, M. 1995 Normal stresses in colloidal dispersions. *J. Rheol.* **39**, 545.

Cichocki, B. & Hinsen, K. 1992 Dynamic computer simulation of concentrated hard sphere suspensions. *Physica A* **187**, 145.

Clarke, A.S. & Wiley, J.D. 1987 Numerical simulation of the dense random packing of a binary mixture of hard spheres: Amorphous metals. *Phys. Rev. B* **35**, 7350.

Erpenbeck, J.J. 1984 Shear viscosity of the hard-sphere fluid via nonequilibrium molecular dynamics. *Phys. Rev. Lett.* **52**, 1333.

Fixman, M. 1978 Simulation of polymer dynamics. I. General theory. *J. Chem. Phys.* **69**, 1527.

Foss, D.R. & Brady, J.F. 1999a Self-diffusion in sheared suspensions by dynamic simulation. *J. Fluid Mech.* (submitted).

Foss, D.R. & Brady, J.F. 1999b Structure, diffusion, and rheology of Brownian suspensions by Stokesian Dynamics simulation. *J. Fluid Mech.* (submitted).

Foss, D.R. & Brady, J.F. 1999c Stress relaxation in colloidal dispersions. J. Rheol. (to be submitted).

Heyes, D.M. 1986 Shear thinning and thickening of the Lennard-Jones liquid. *J. Chem. Soc., Faraday Trans. 2* **82**, 1365.

Heyes, D.M. 1988 Shear thinning of dense suspensions modeled by Brownian dynamics. *Phys. Lett.* **132**, 399.

Heyes, D.M. & Melrose, J.R. 1993 Brownian dynamics simulations of model hard-sphere suspensions. *J. Non-Newtonian Fluid Mech.* **46**, 1.

Lionberger, R.A. 1998 Shear thinning of colloidal dispersions. *J. Rheol.* **42**, 843.

Morris, J.F. & Brady, J.F. 1996 Self-diffusion in sheared suspensions. *J. Fluid Mech.* **312**, 223.

Poon, W.C.K., Meeker, S.P., Pusey, P.N., & Segrè, P.N. 1996 Viscosity and structural relaxation in concentrated hard-sphere colloids. *J. Non-Newtonian Fluid Mech.* **67**, 179.

Pusey, P.N., Segrè, P.N., Behrend, O.P., Meeker, S.P., & Poon, W.C.K. 1997 Dynamics of concentrated colloidal suspensions *Physica A* **235**, 1.

Rallison, J.M. 1988 Brownian diffusion in concentrated suspensions of interacting particles. *J. Fluid Mech.* **186**, 471.

Rastogi, S.R. 1995 *Nonequilibrium Brownian Dynamics of Colloidal Suspensions* Ph.D. Thesis, University of Delaware.

Rastogi, S.R., Wagner, N.J., & Lustig, S.R. 1996 Rheology, self-diffusion, and microstructure of charged colloids under simple shear by massively parallel nonequilibrium Brownian dynamics. *J. Chem. Phys.* **104**, 9234.

Rintoul, M.D. & Torquato, S. 1996 Computer Simulations of dense hard-sphere systems. *J. Chem. Phys.* **105**, 9258.

Schaertl, W. & Sillescu H. 1994 Brownian Dynamics Simulations of Colloidal Hard Spheres. Effects of Sample Dimensionality on Self-Diffusion. *J. Stat. Phys.* **74**, 687.

Strating, P. 1999 Brownian dynamics simulation of a hard-sphere suspension. *Phys. Rev. E* **59**, 2175.

Verberg, R., de Schepper, I.M., & Cohen, E.G.D. 1997 Viscosity of colloidal suspensions *Phys. Rev. E* **55**, 3143.

Vicic M. 1999 *Rheology and Microstructure of Complex Fluids: Dispersions, Emulsions and Polymer Solutions.* Ph.D. Thesis, California Institute of Technology.

Xue, W. & Grest, G.S. 1990 Shear-induced alignment of colloidal particles in the presence of shear flow, *Phys. Rev. Lett.* **64**, 419.

ϕ	N	$t_{final}D_0/a^2$	η_0^P
0.20	1331	1500	0.131
0.30	1331	500	0.414
0.35	1331	500	0.808
0.40	1331	100	1.25
0.45	1331	100	3.05
0.50	1331	1000	6.91
0.52	2000	300	12.7
0.525	1331	100	14.0
0.55	1331	1000	34.5

Table 2.1: Data for zero-shear viscoity, η_0^P, as a function of ϕ from Brownian Dynamics, $N = 1331, 2000$. The interparticle contribution, η_0^P, is calculated from a Green-Kubo formula involving time-integration of the shear-stress autocorrelation function, Eq. (2.9). The hydrodynamic contribution is the high frequency dynamic viscosity, η'_∞, and is equal to $\eta(1 + \frac{5}{2}\phi)$ in the absence of hydrodynamic interactions.

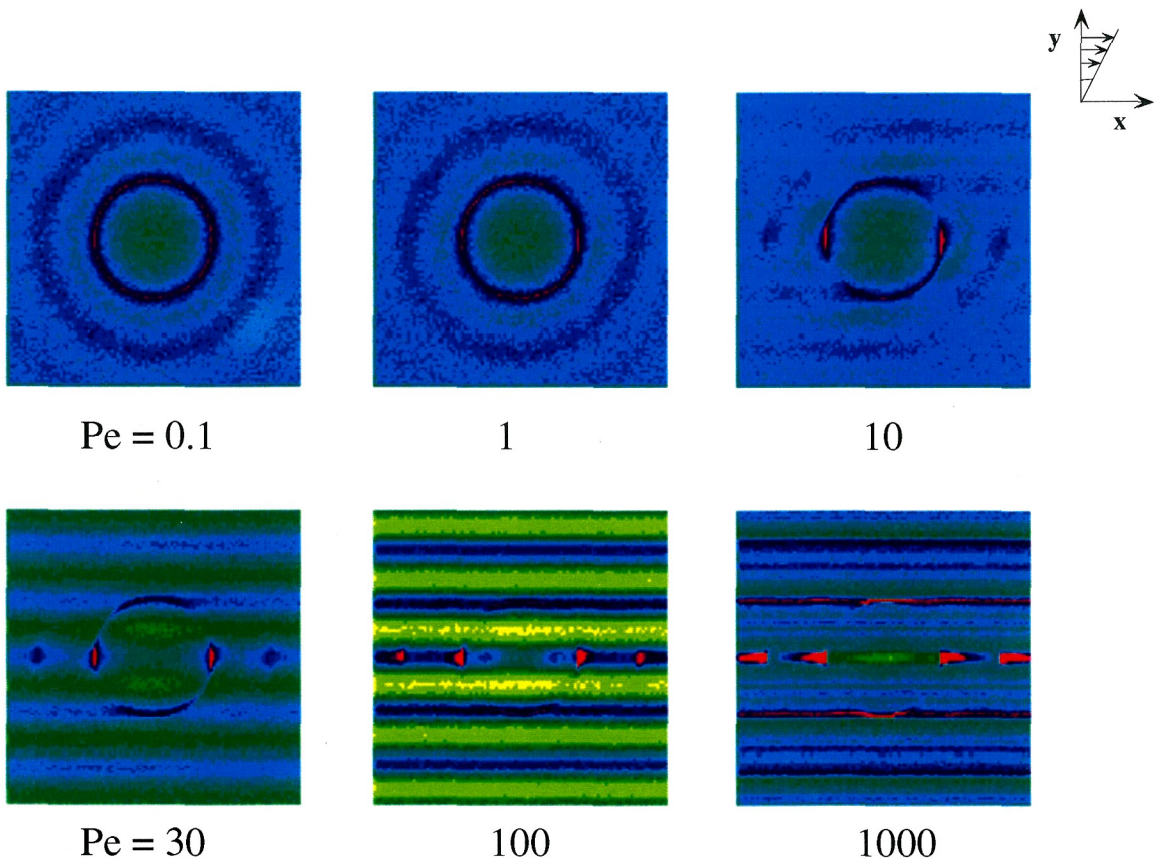

Figure 2.1: The pair-distribution function projected into the velocity–velocity-gradient plane for $N = 1331$ and $\phi = 0.45$.

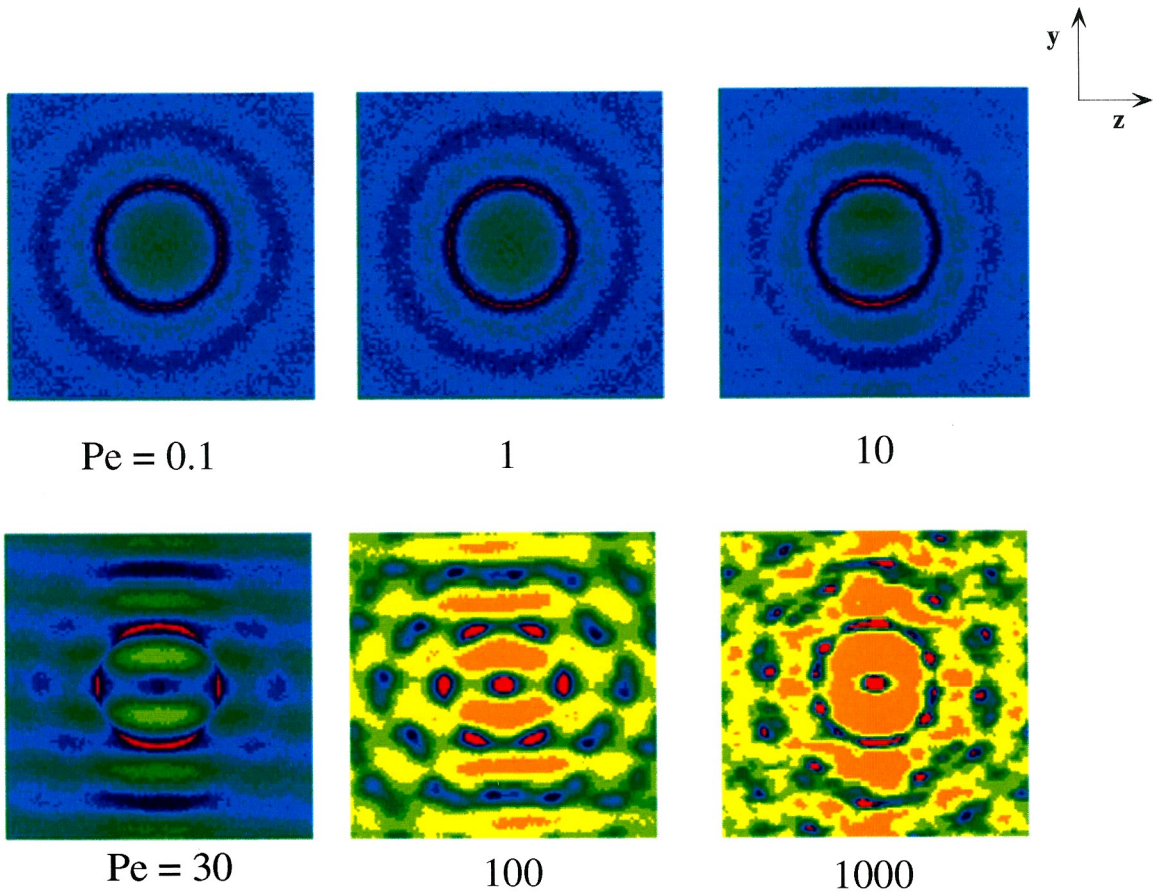

Figure 2.2: The pair-distribution function projected into the vorticity–velocity-gradient plane for $N = 1331$ and $\phi = 0.45$.

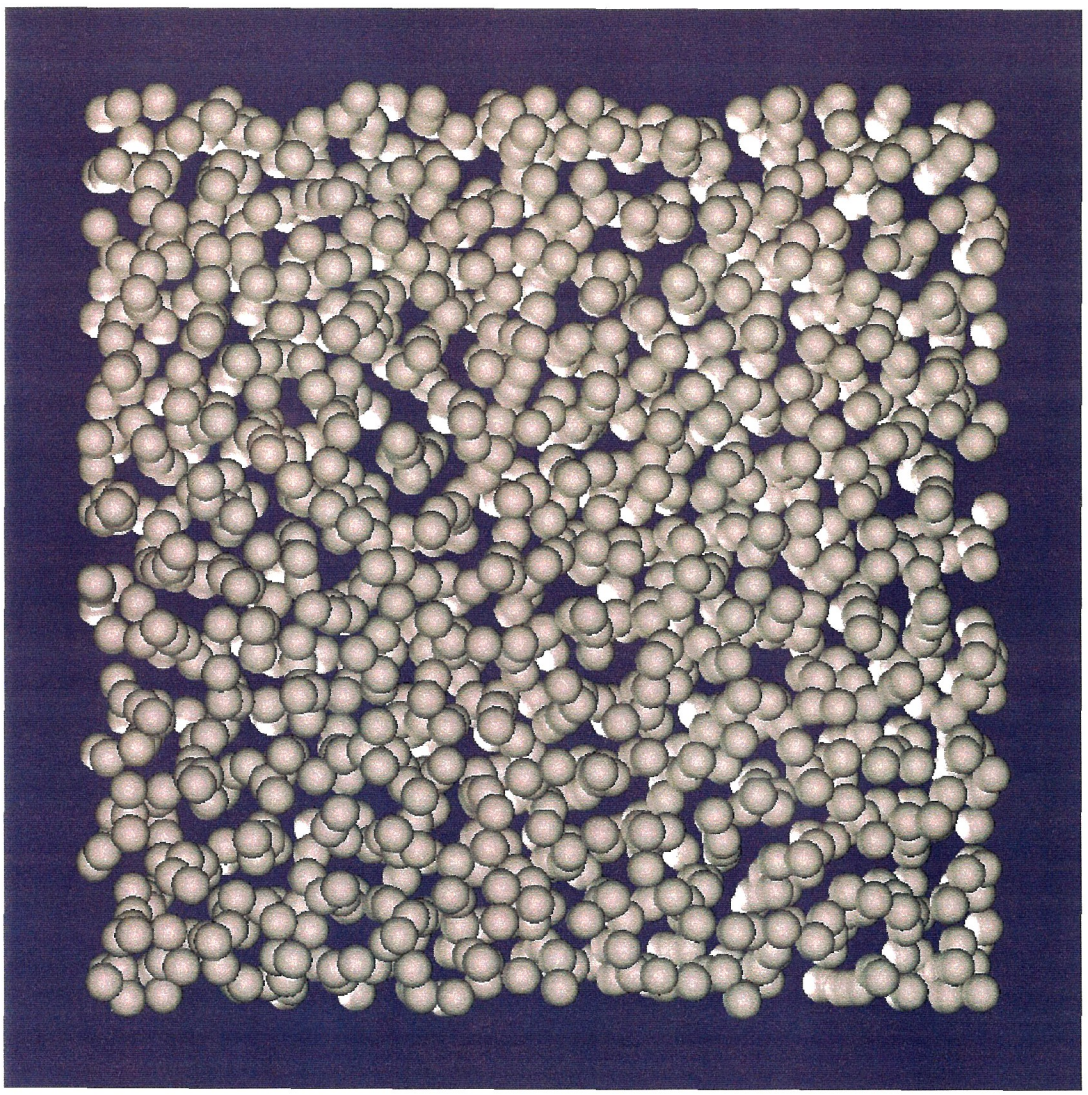

Figure 2.3: A snapshot of the unit cell as viewed from the vorticity–velocity-gradient plane for $N = 1331$, $\phi = 0.45$, and $Pe = 10$. Little order is seen as the projections in figures 2.1 and 2.2 confirm. The particles in the figure are shown with a radius of $\frac{1}{2}a$ to afford visualization.

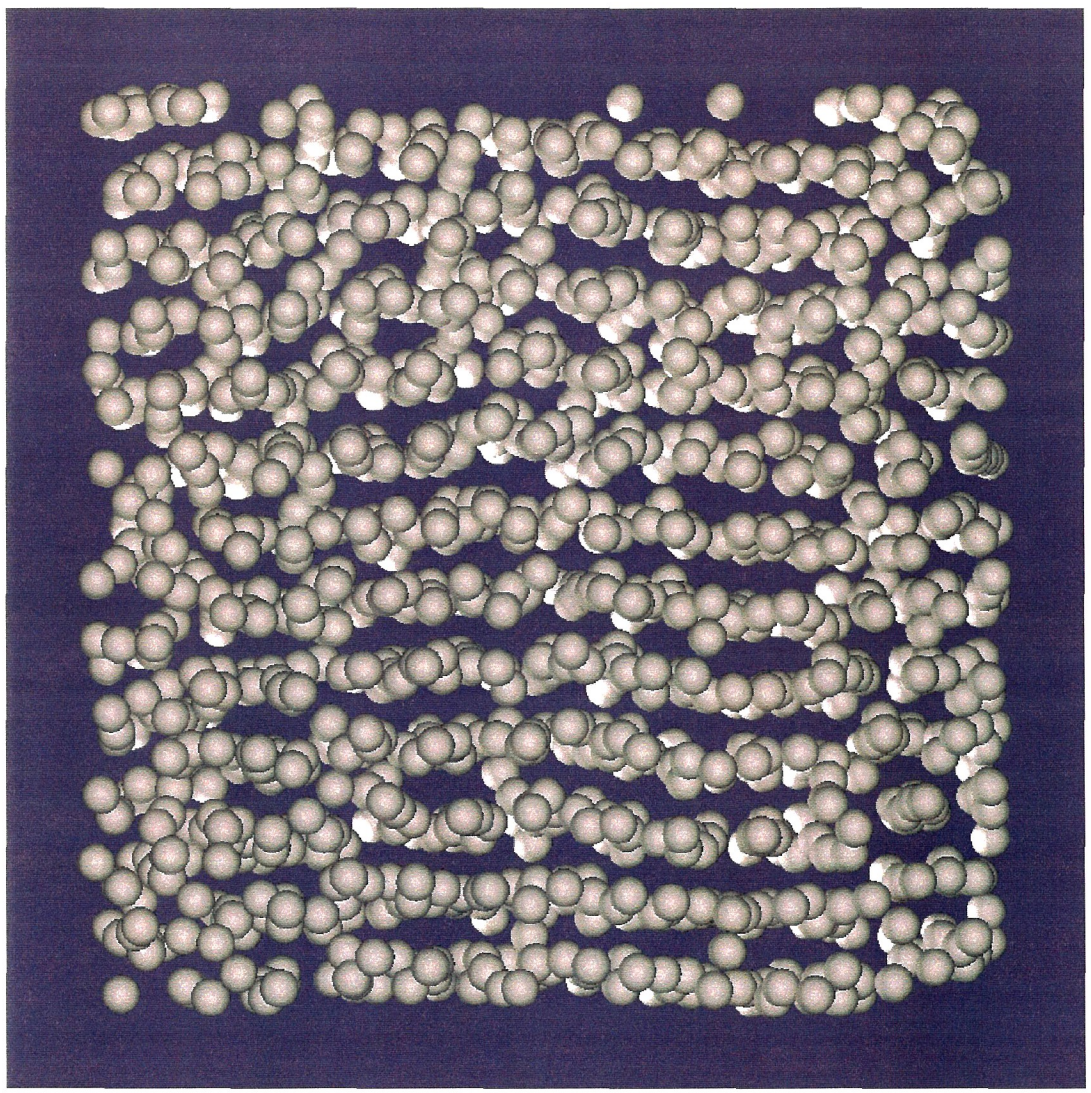

Figure 2.4: A snapshot of the unit cell as viewed from the vorticity–velocity-gradient plane for $N = 1331$, $\phi = 0.45$, and $Pe = 30$. Sliding layers of particles are evident as seen in figure 2.2. The particles in the figure are shown with a radius of $\frac{1}{2}a$ to afford visualization.

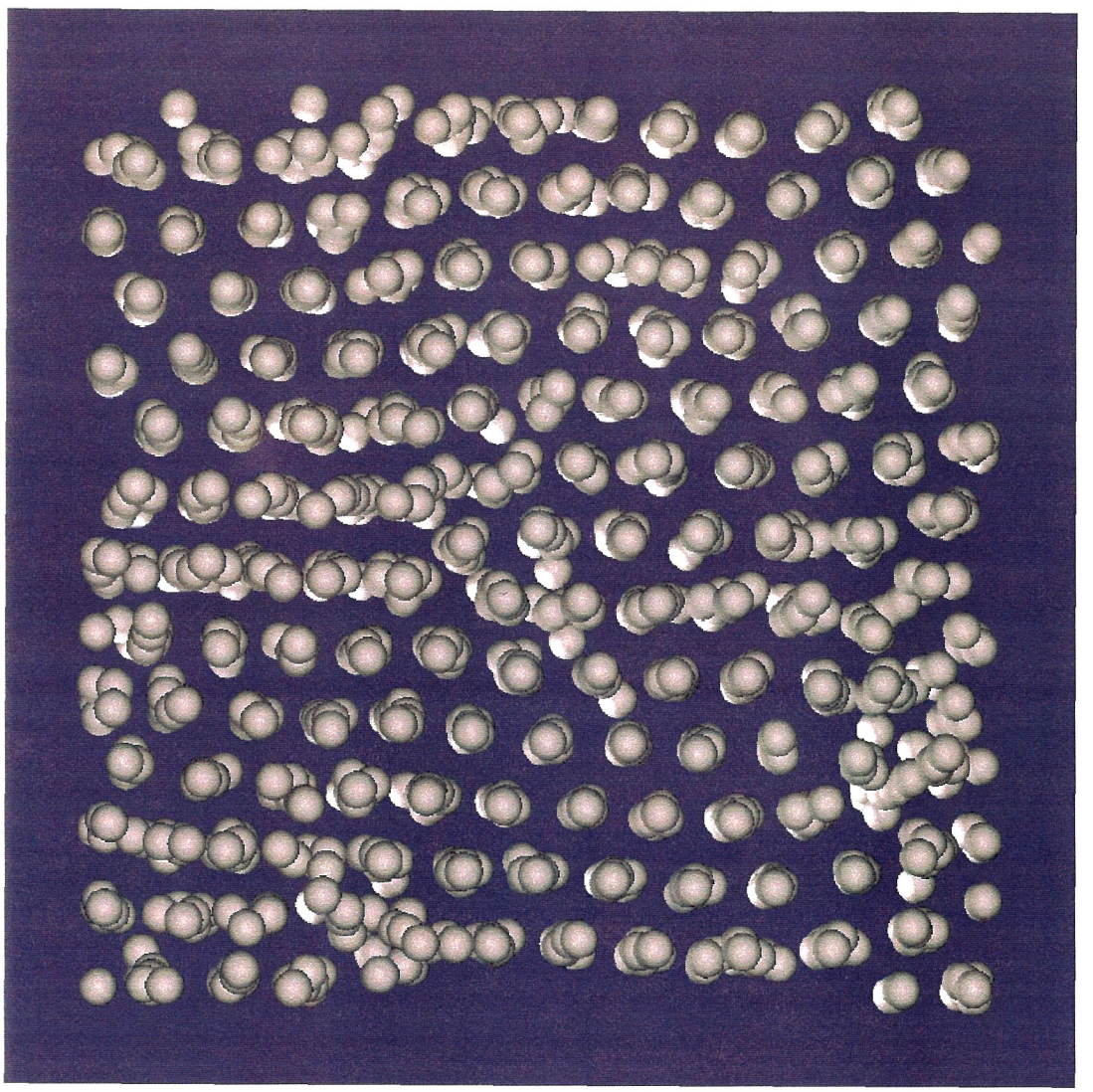

Figure 2.5: A snapshot of the unit cell as viewed from the vorticity–velocity-gradient plane for $N = 1331$, $\phi = 0.45$, and $Pe = 100$. Further ordering of the suspension into hexagonally-packed strings within the sliding layers is evident. The particles in the figure are shown with a radius of $\frac{1}{2}a$ to afford visualization.

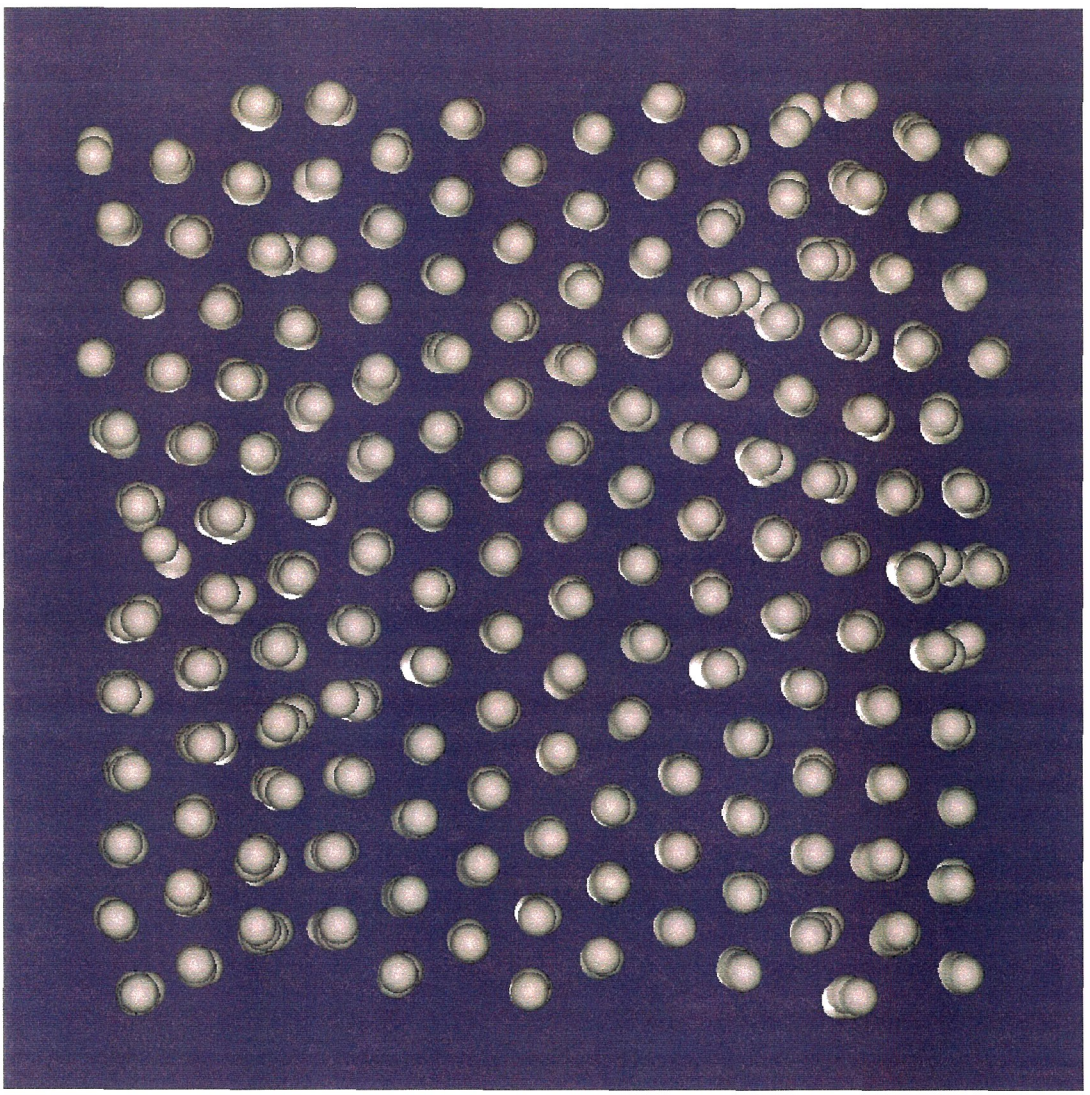

Figure 2.6: A snapshot of the unit cell as viewed from the vorticity–velocity-gradient plane for $N = 1331$, $\phi = 0.45$, and $Pe = 1000$. The entire unit cell has ordered into strings which are packed hexagonally with varying orientation in different regions of the cell. The particles in the figure are shown with a radius of $\frac{1}{2}a$ to afford visualization.

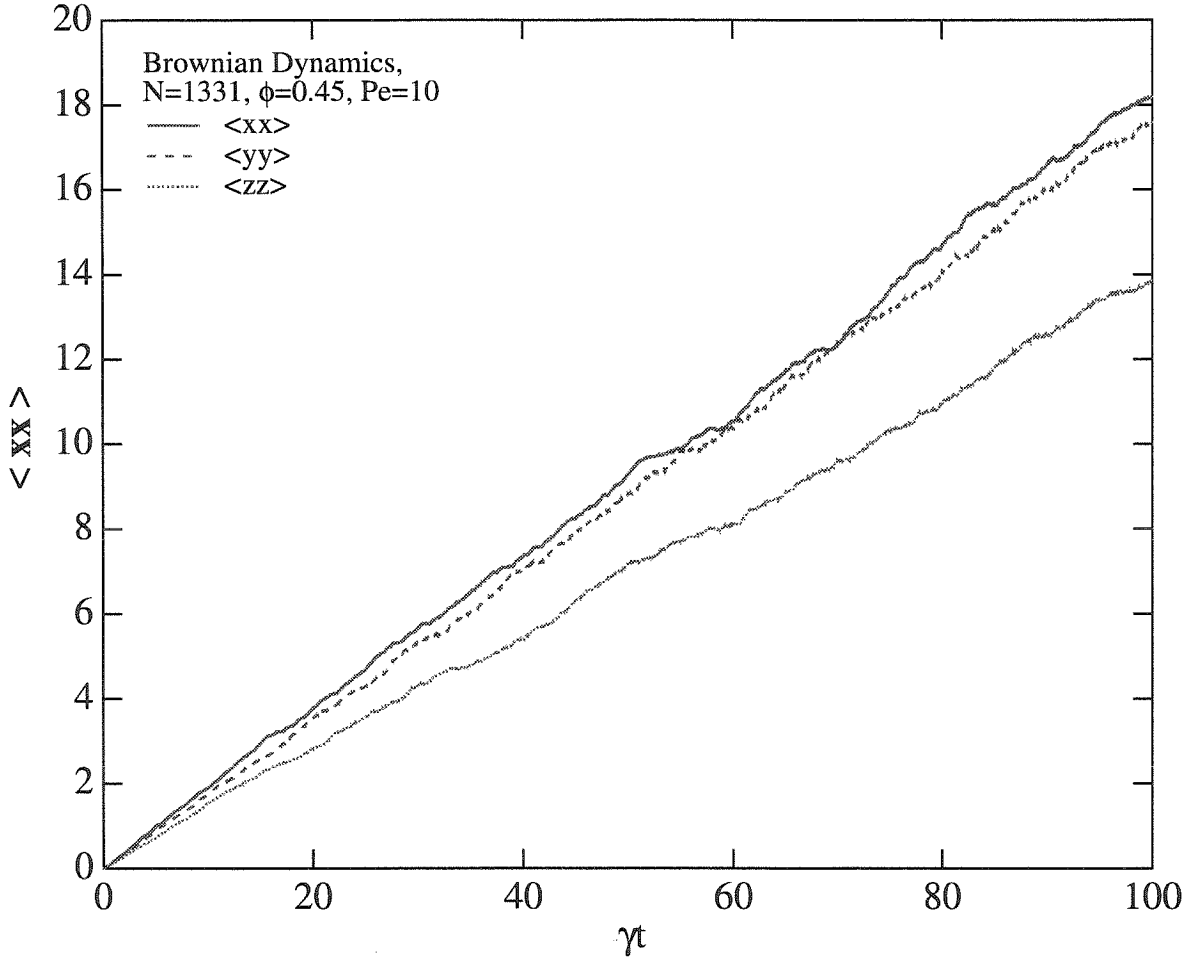

Figure 2.7: Typical mean-square-displacement curves generated from the simulation which are used in calculating the long-time self-diffusivities. Data shown here is for $N = 1331$, $\phi = 0.45$ and $Pe = 10$.

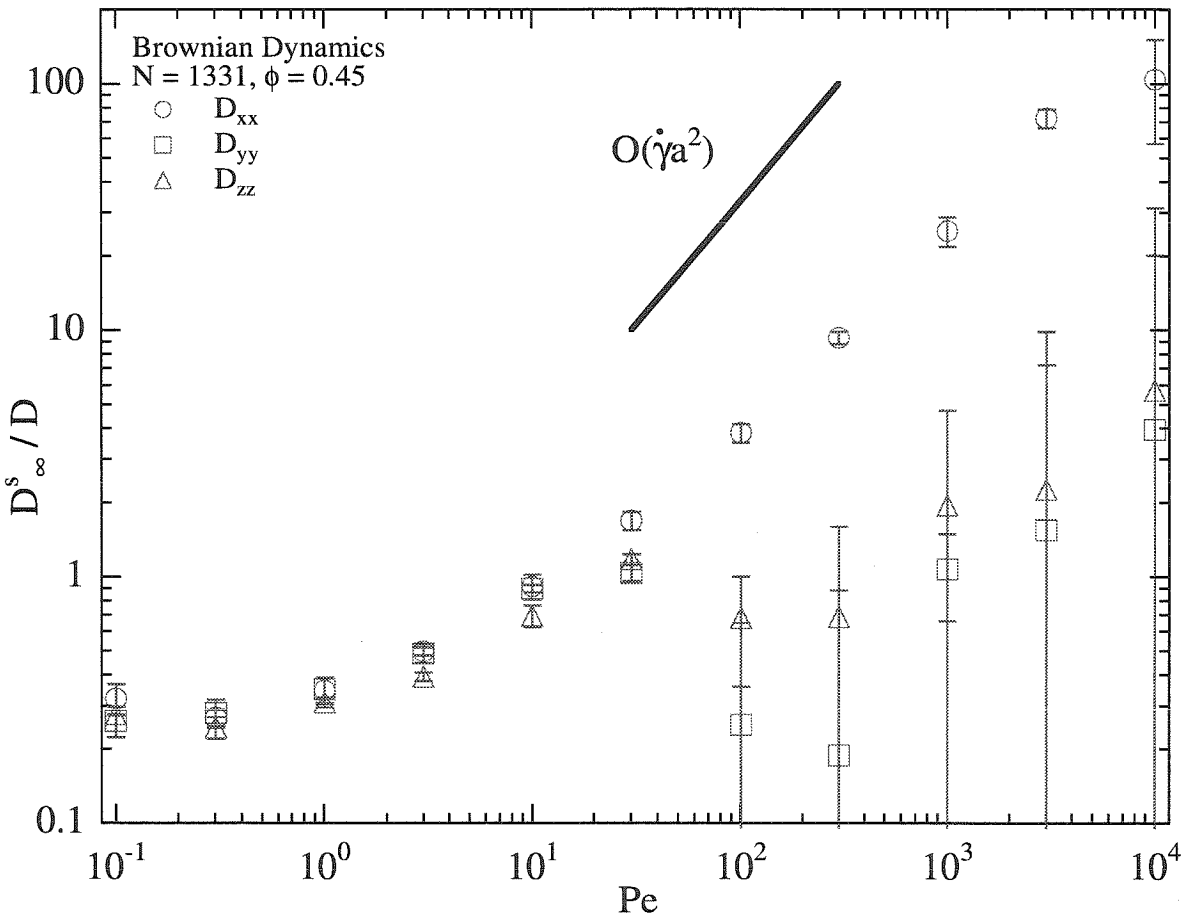

Figure 2.8: Long-time self-diffusivities for $N = 1331$ and $\phi = 0.45$.

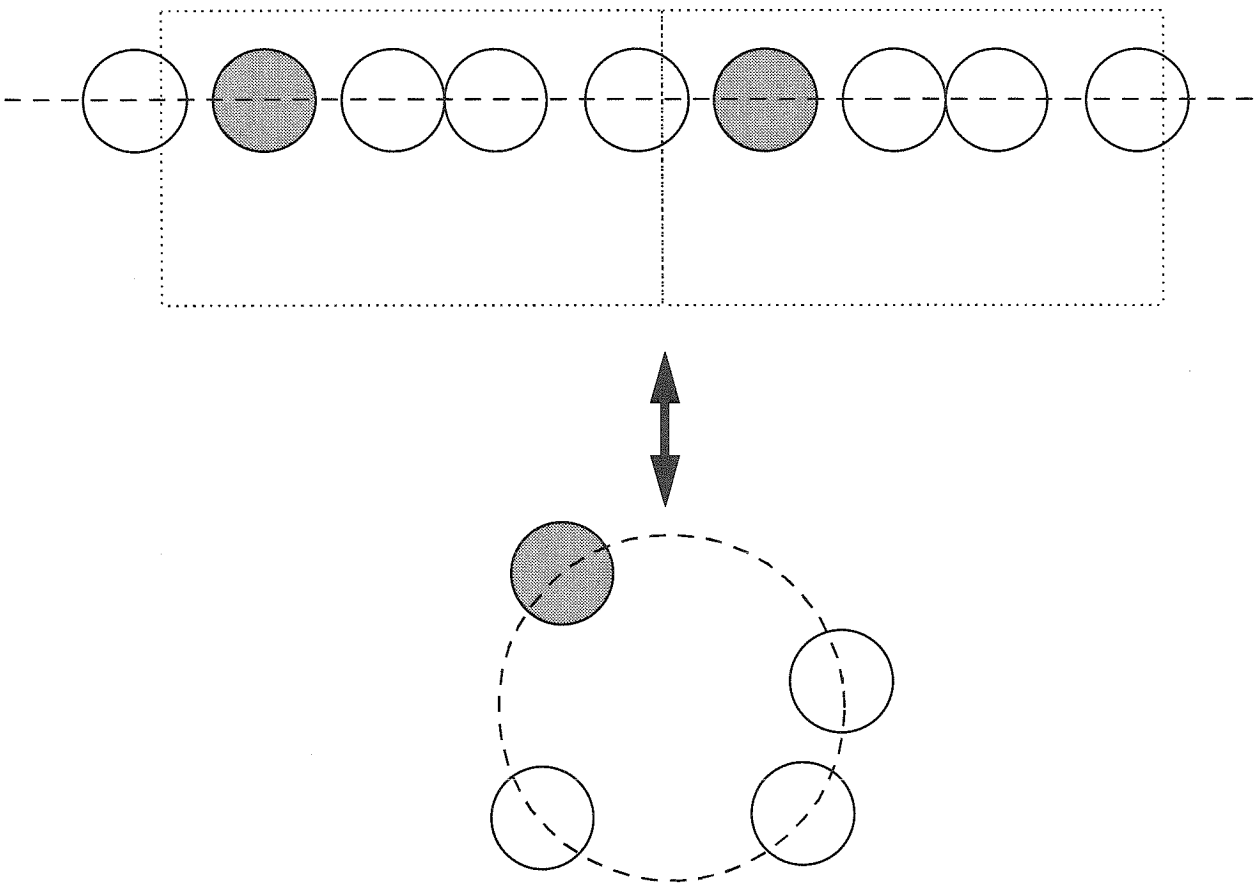

Figure 2.9: Diffusion of particles aligned in strings in a periodic cell is analogous to particle diffusion around a ring. In order for one particle to diffuse long distances in a given direction, all of the particles in the ring (or string) must also move in that same direction, resulting in a diffusivity of D/N_p, where N_p is the number of particles in the ring (or string) and D is the diffusivity of an isolated particle (Rallison 1988).

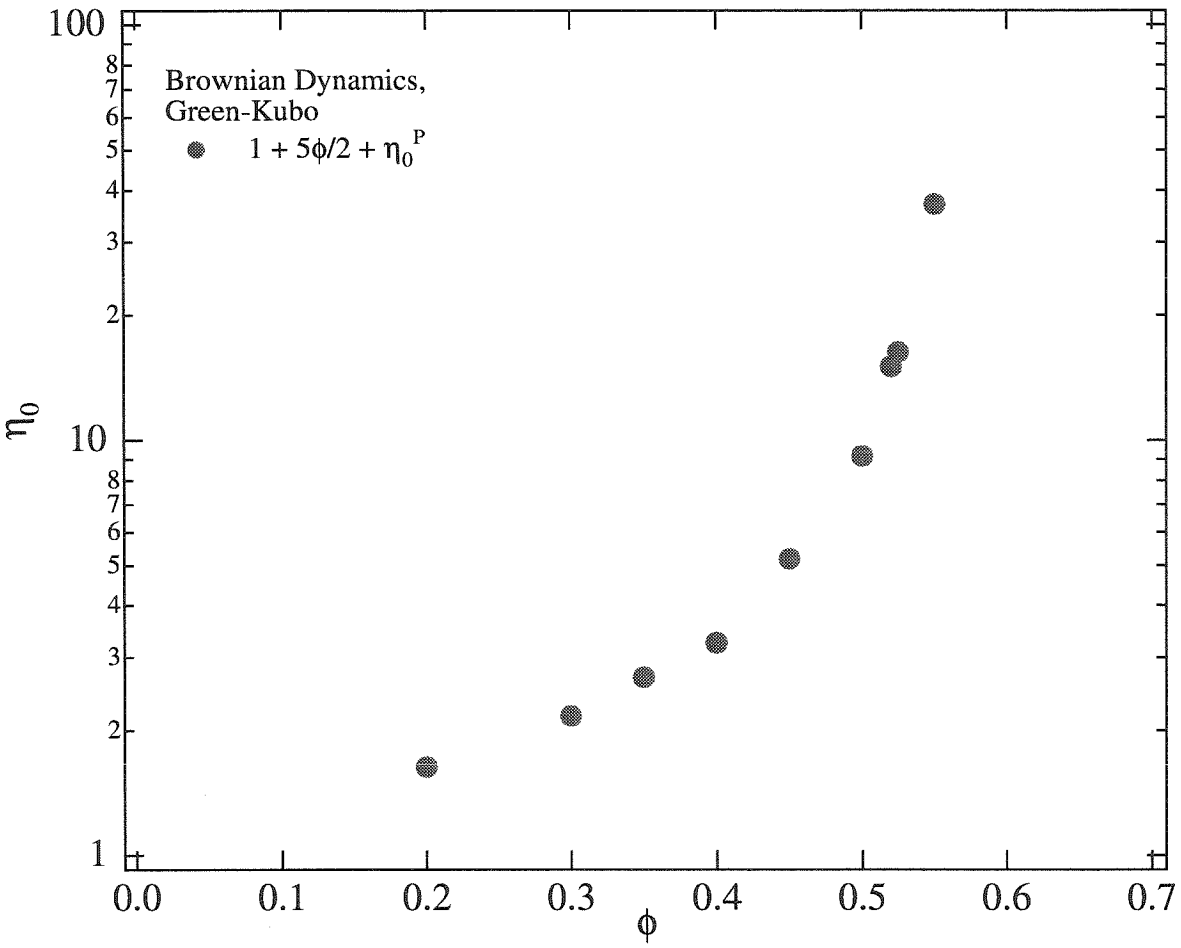

Figure 2.10: Zero shear relative viscosity, η_0, as a function of volume fraction ϕ from Brownian Dynamics simulation. Values are determined from an equilibrium Green-Kubo analysis.

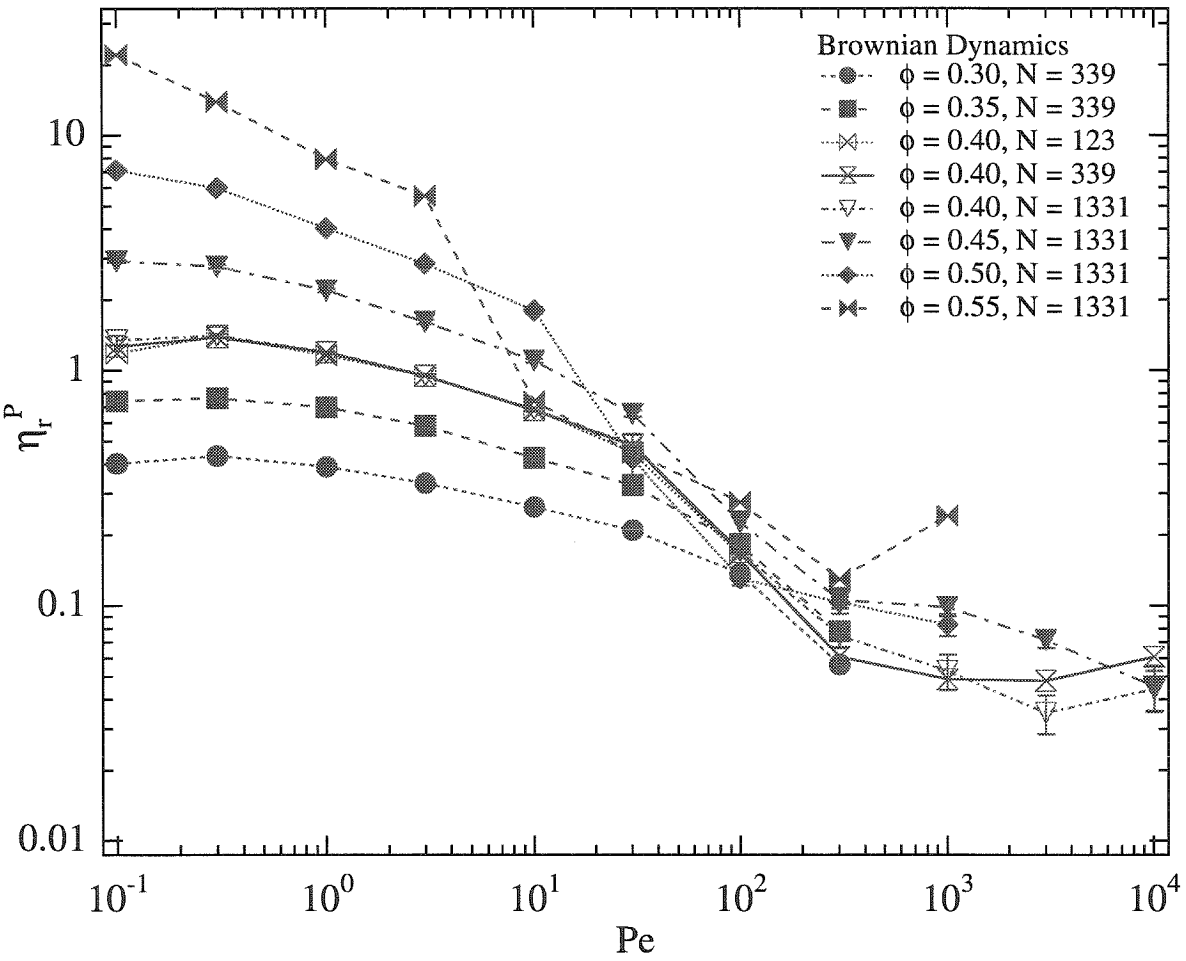

Figure 2.11: Interparticle contribution to the relative viscosity as a function of Pe for various N and ϕ.

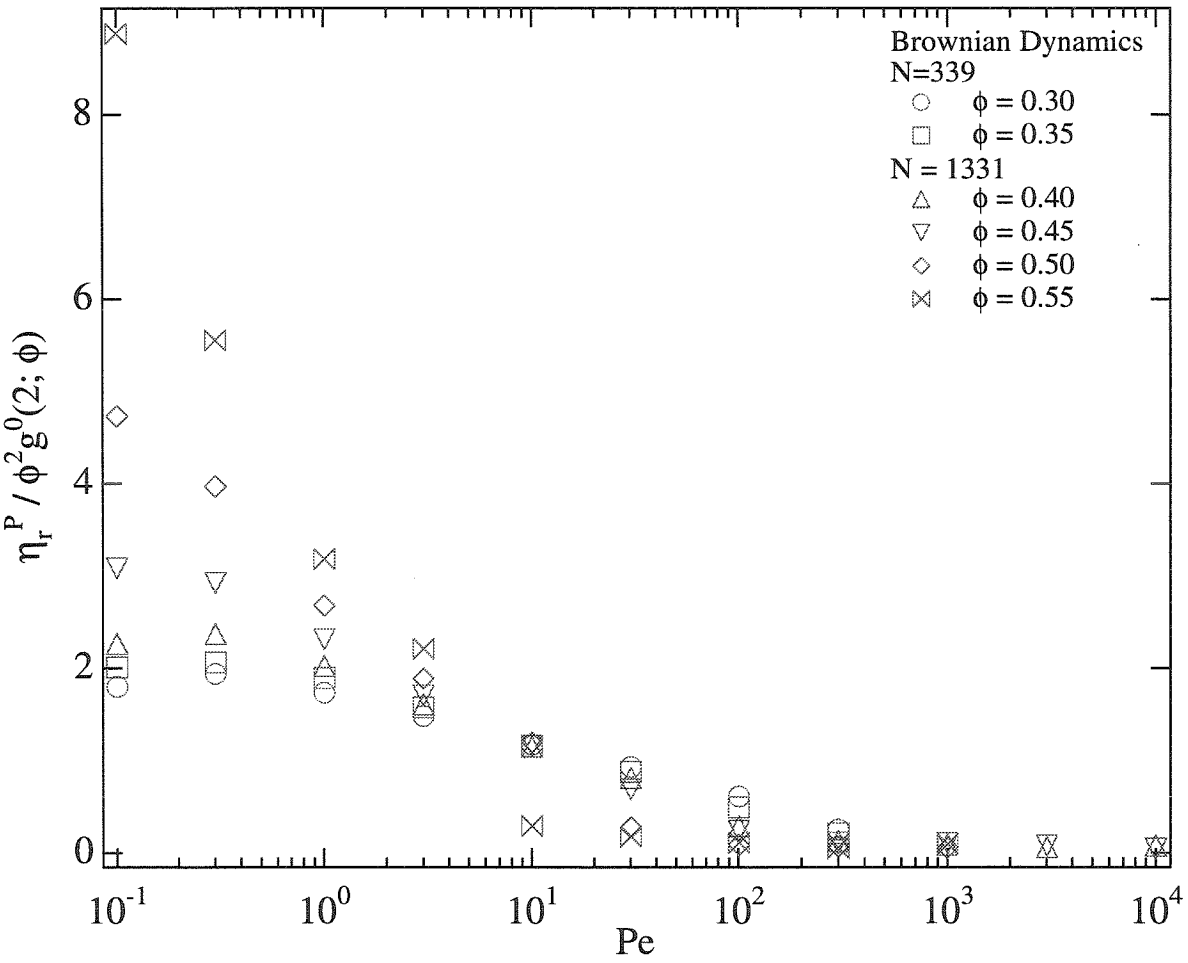

Figure 2.12: The interparticle force contribution to the viscosity, η^P, scaled by $\phi^2 g^0(2)$ and plotted as a function of Pe for volume fractions $0.30 \leq \phi \leq 0.55$. Here, the characteristic diffusivity, $\hat{D}$, is simply equal to its dilute-limit Stokes Einstein value $D = kT/6\pi\eta a$.

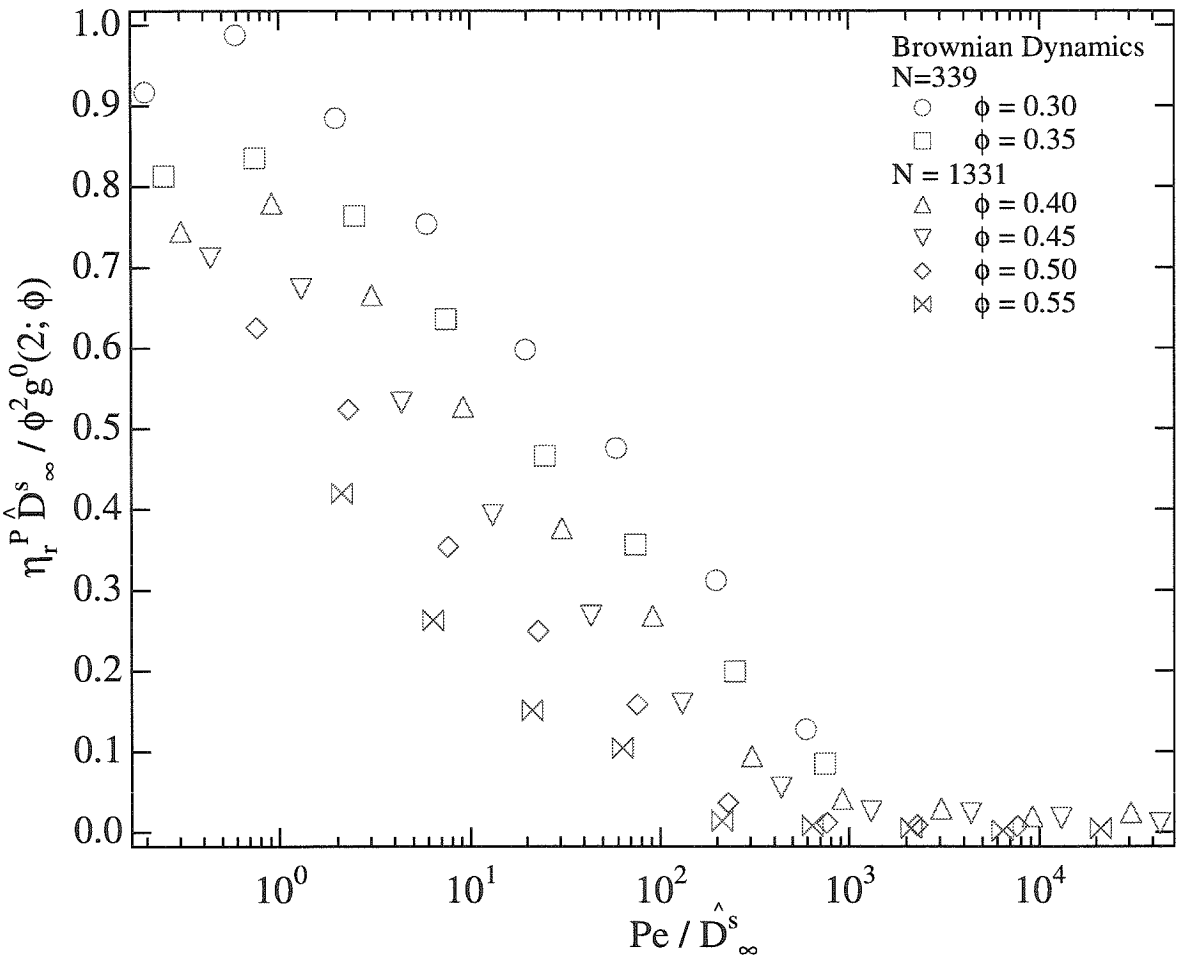

Figure 2.13: The interparticle force contribution to the viscosity, η^P, scaled by $\phi^2 g^0(2)/\hat{D}^s_\infty$ and plotted as a function of rescaled Péclet number $Pe/\hat{D}^s_\infty$ for volume fractions $0.30 \leq \phi \leq 0.55$. Here, $\hat{D}^s_\infty$ is the equilibrium long-time self-diffusivity scaled by the Stokes Einstein value $D = kT/6\pi\eta a$.

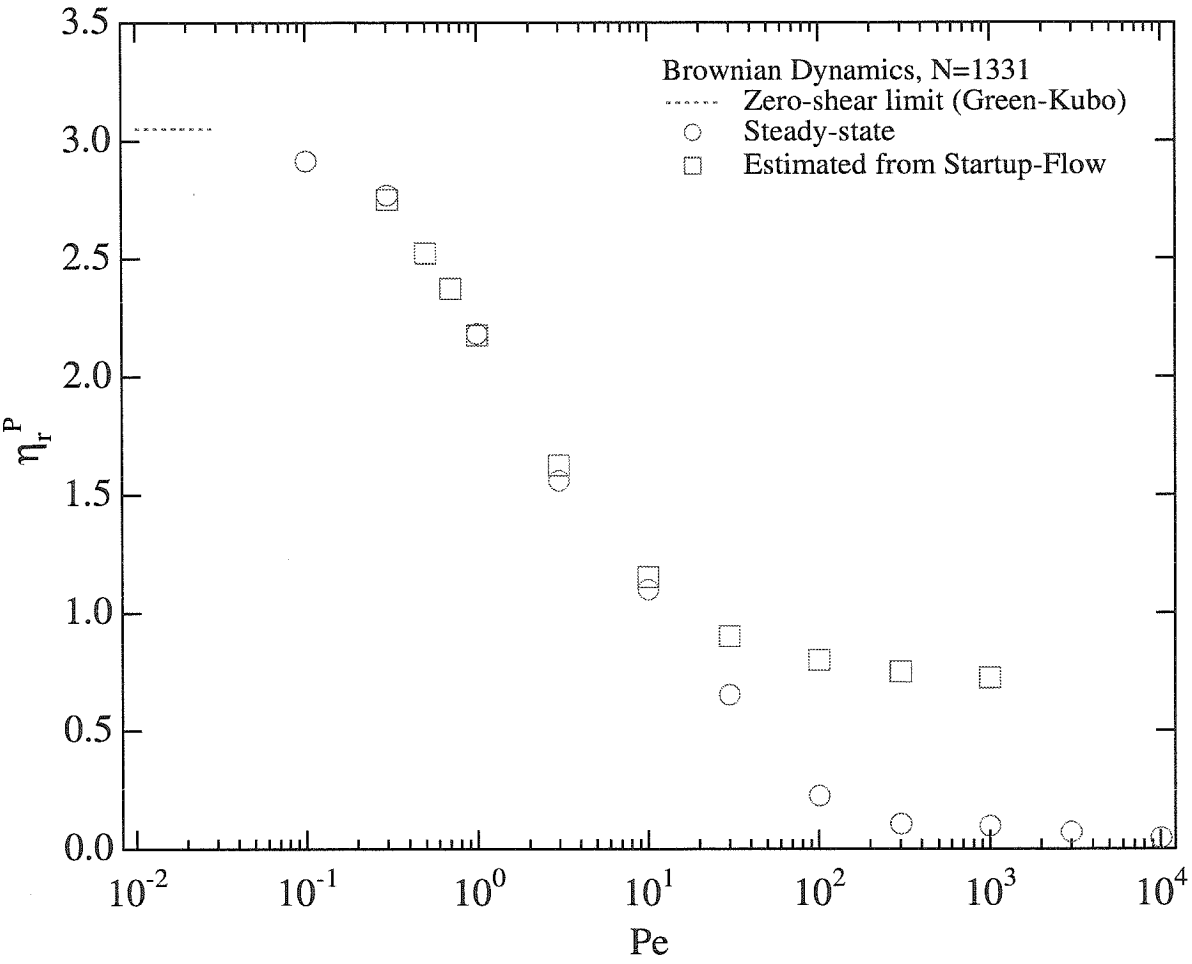

Figure 2.14: The interparticle force contribution to the relative viscosity as a function of Péclet number for $N = 1331$ and $\phi = 0.45$. Data are shown from both the steady state simulations of this work and the start-up flow simulations from equilibrium configurations of a related work (Foss & Brady 1999c).

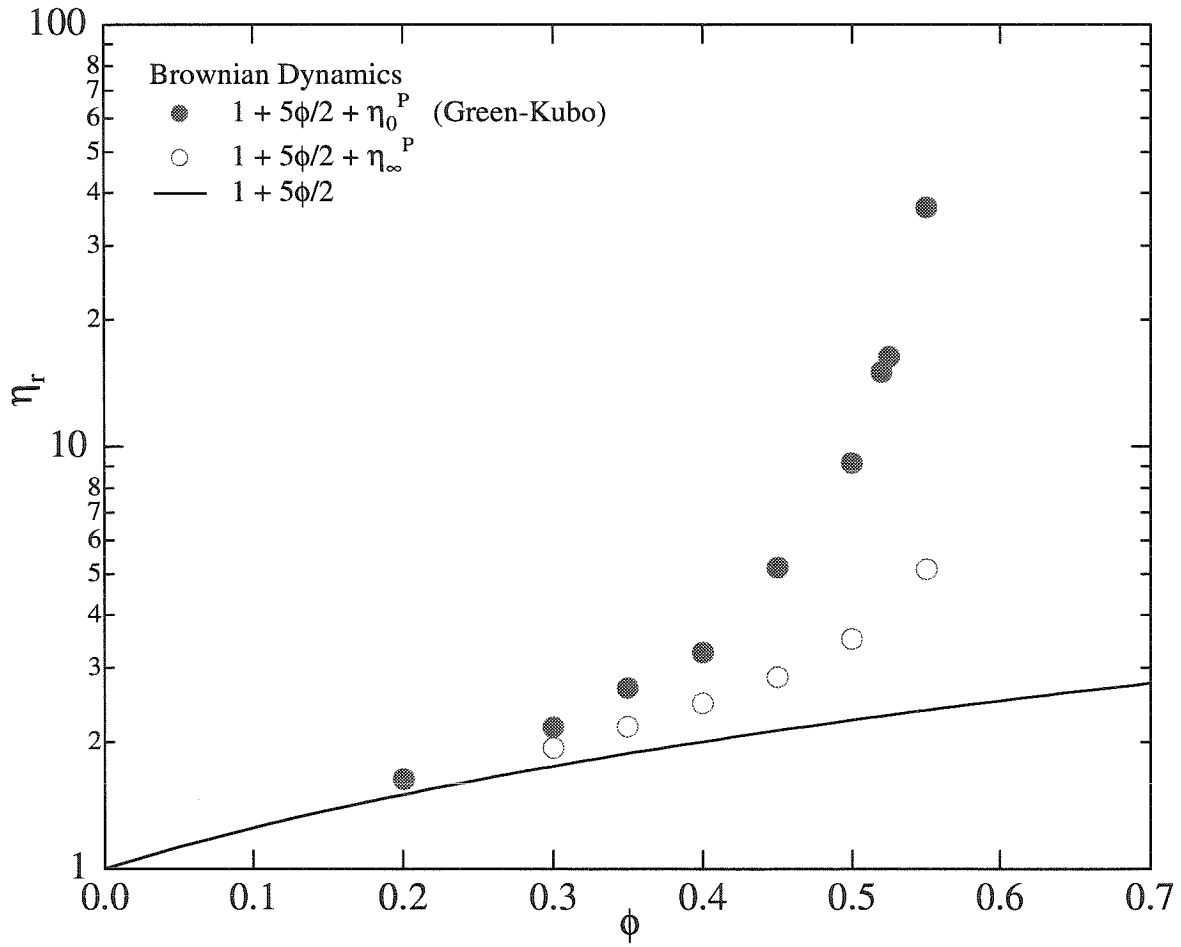

Figure 2.15: The zero-shear viscosity, η_0, disordered high-shear limiting viscosity, η_∞, and the single-particle hydrodynamic Einstein viscosity $1 + \frac{5}{2}\phi$ as functions of ϕ for $N = 1331$. Here, η_∞ values are determined from an average of 91 start-up flow simulations from equilibrium configurations (Foss & Brady 1999c) at $Pe = 1000$.

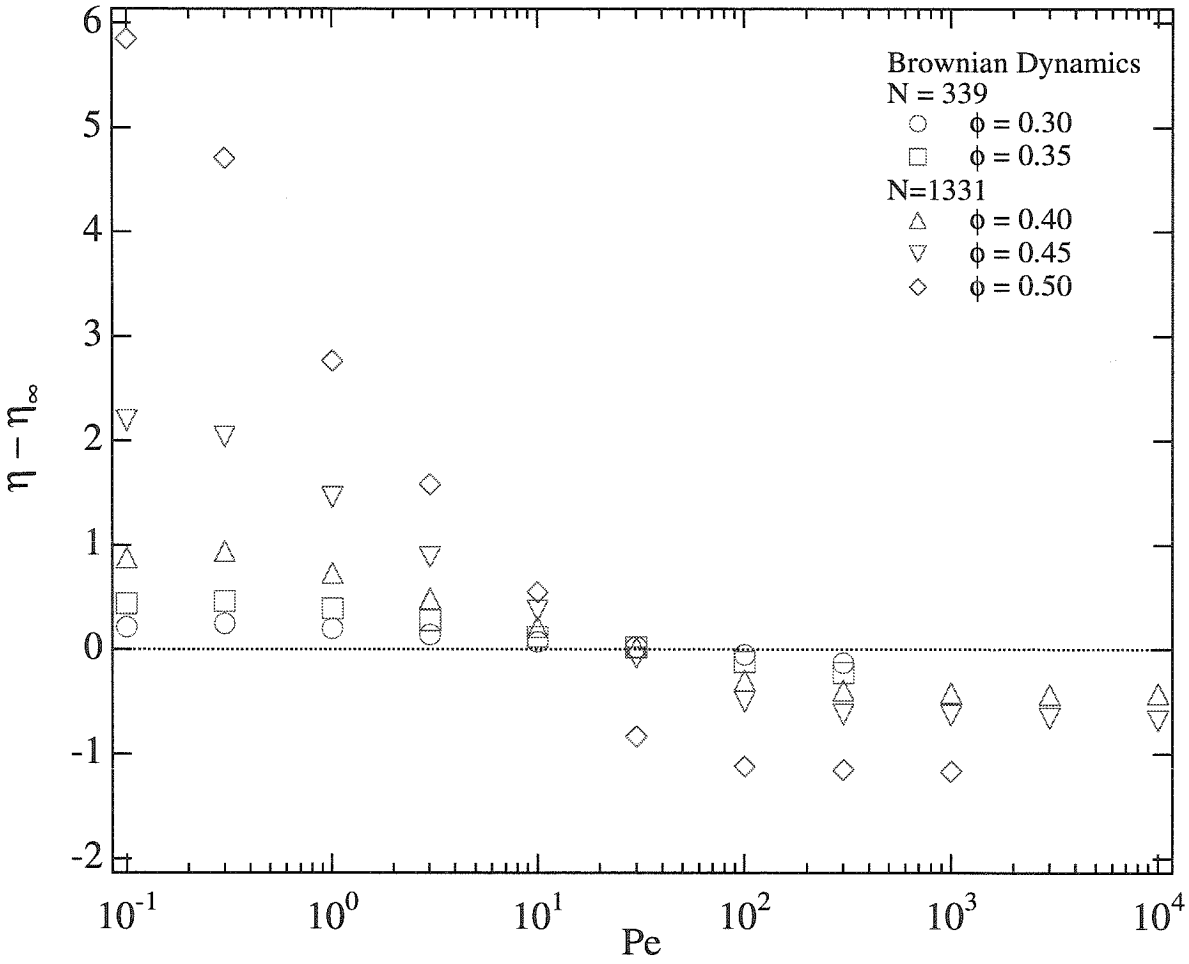

Figure 2.16: The interparticle contribution to the relative viscosity following subtraction of its limiting high-shear disordered values as a function of Pe for various volume fractions.

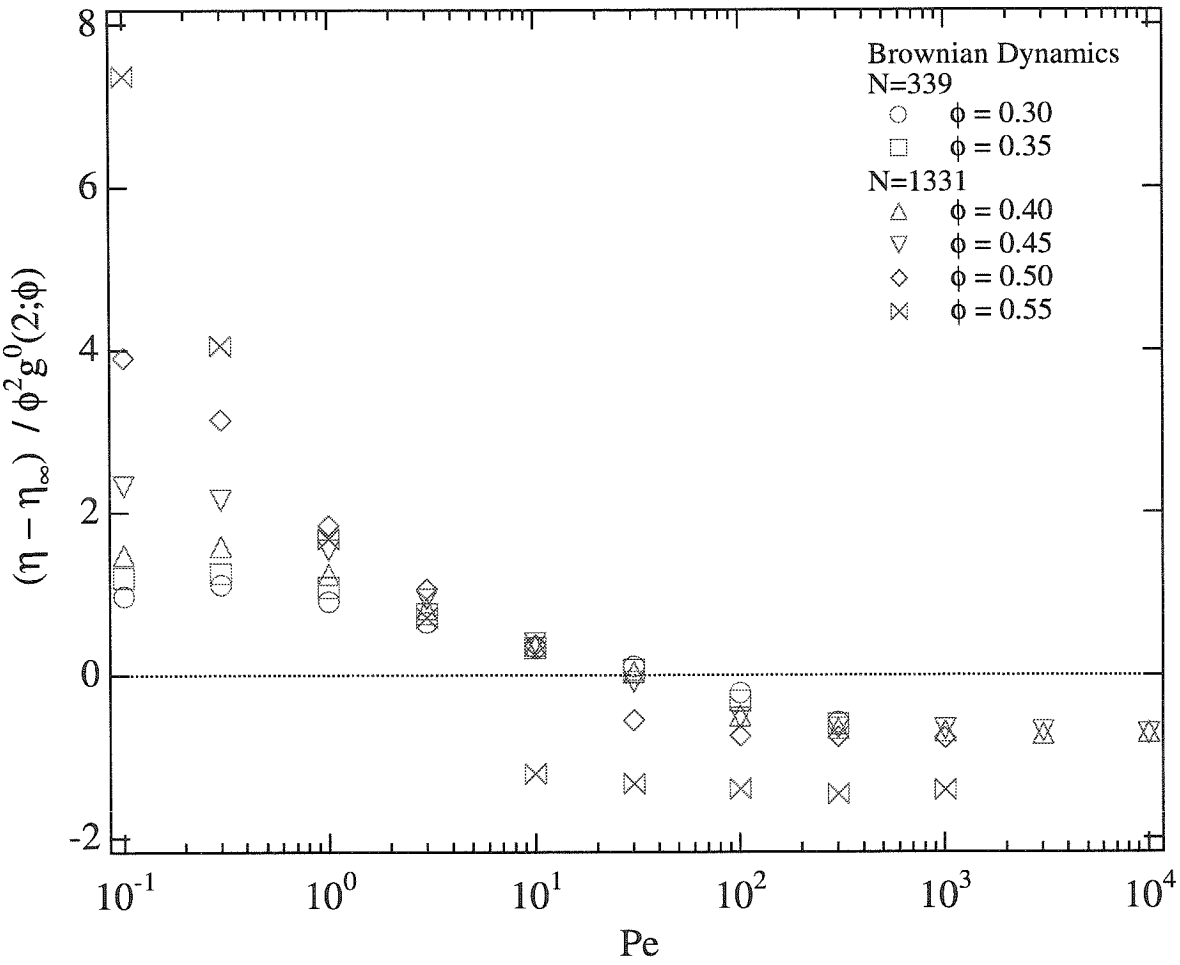

Figure 2.17: The interparticle force contribution to the viscosity following subtraction of its limiting high shear disordered value, $\eta_r^P - \eta_\infty^P$, scaled by $\phi^2 g^0(2)$ and plotted as a function of Pe for volume fractions $0.30 \leq \phi \leq 0.55$. Here, the characteristic diffusivity, $\hat{D}$, is the short-time self-diffusivity which is simply equal to its dilute-limit Stokes Einstein value $D = kT/6\pi\eta a$.

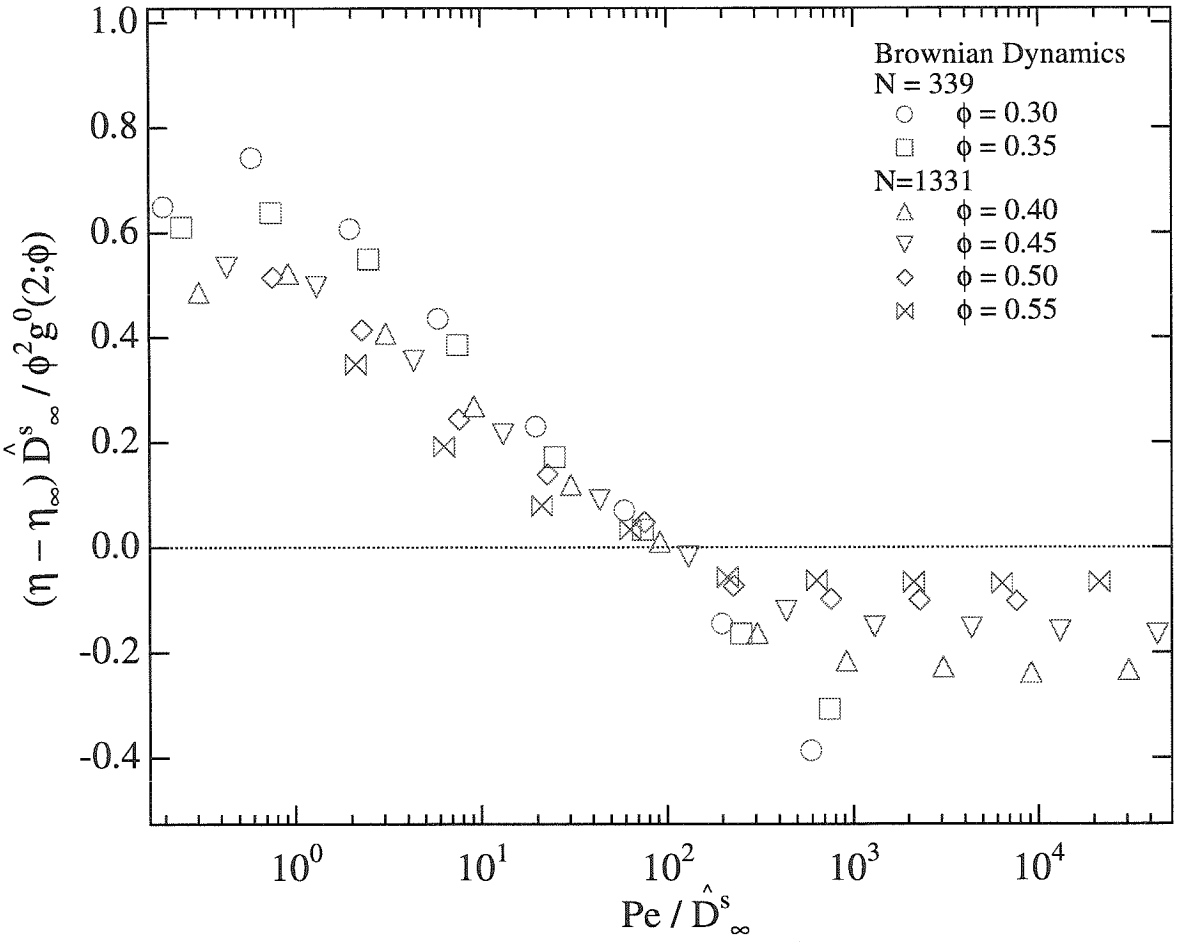

Figure 2.18: The interparticle force contribution to the viscosity following subtraction of its limiting high shear disordered value, $\eta^P - \eta^P_\infty$, scaled by $\phi^2 g^0(2)/\hat{D}^s_\infty$ and plotted as a function of $Pe/\hat{D}^s_\infty$ for volume fractions $0.30 \leq \phi \leq 0.55$. Here, $\hat{D}^s_\infty$ is the equilibrium long-time self-diffusivity scaled by the Stokes Einstein value $D = kT/6\pi\eta a$.

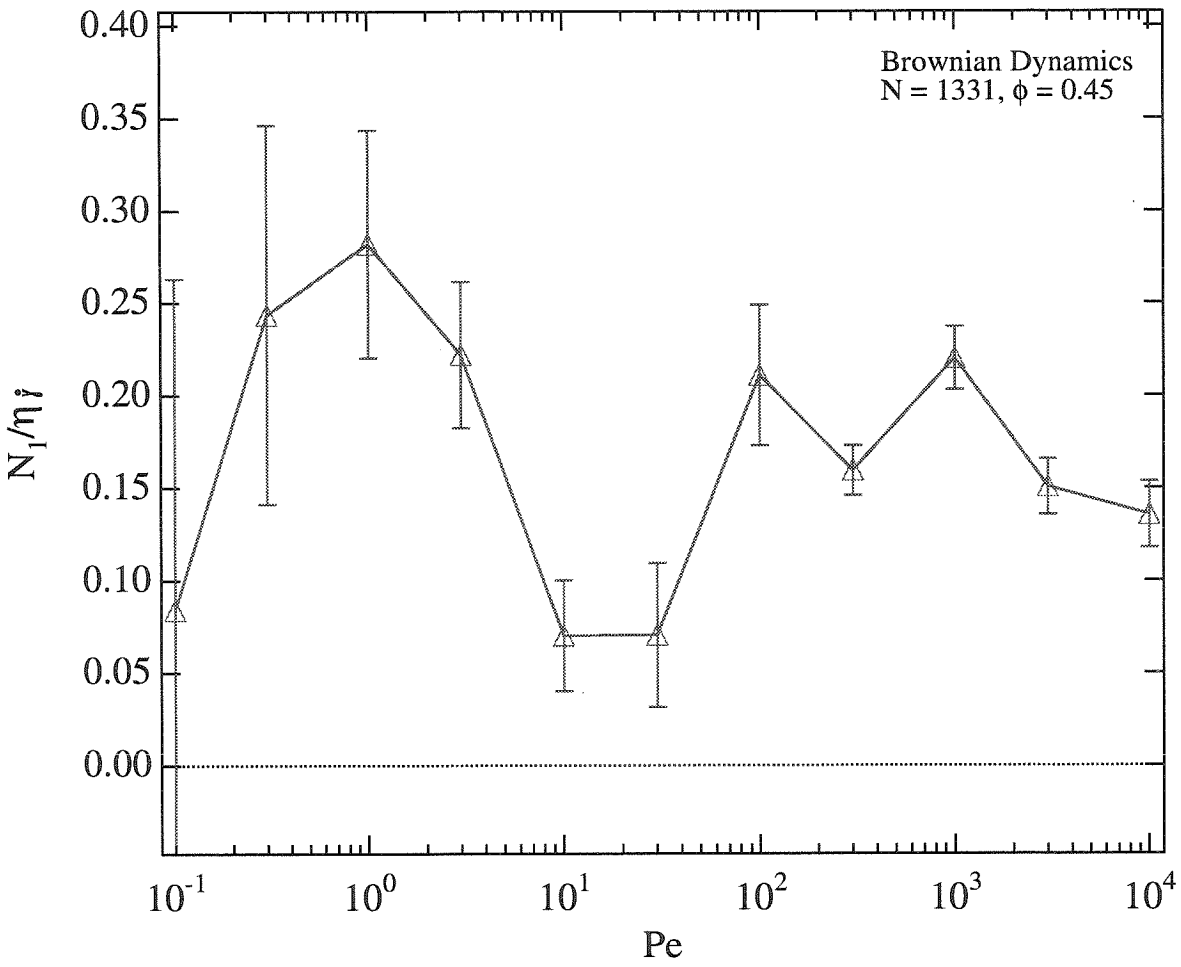

Figure 2.19: The first normal stress difference, nondimensionalized by $\eta\dot{\gamma}$, as a function of Péclet number for $N = 1331$ and $\phi = 0.45$.

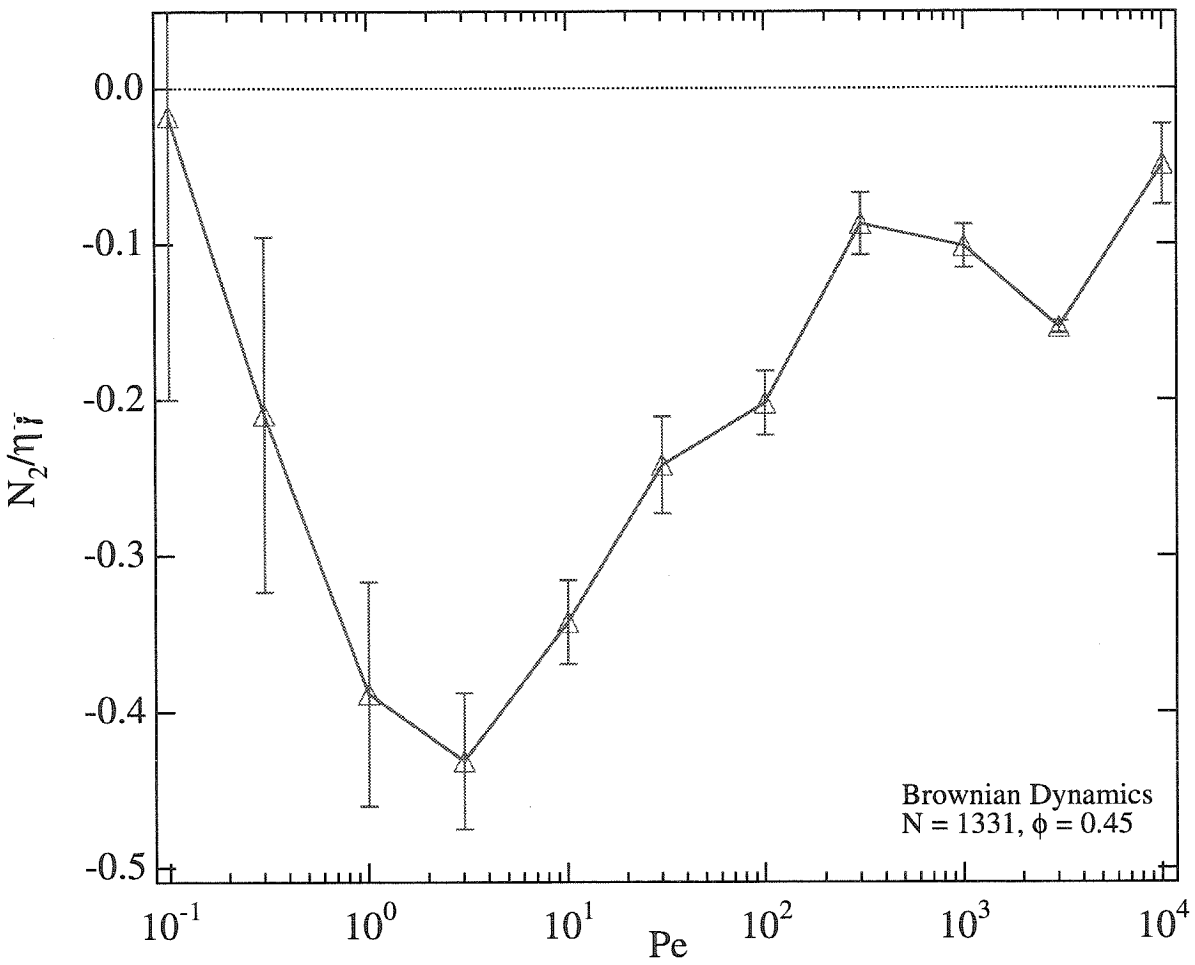

Figure 2.20: The first normal stress difference, nondimensionalized by $\eta\dot{\gamma}$, as a function of Péclet number for $N = 1331$ and $\phi = 0.45$.

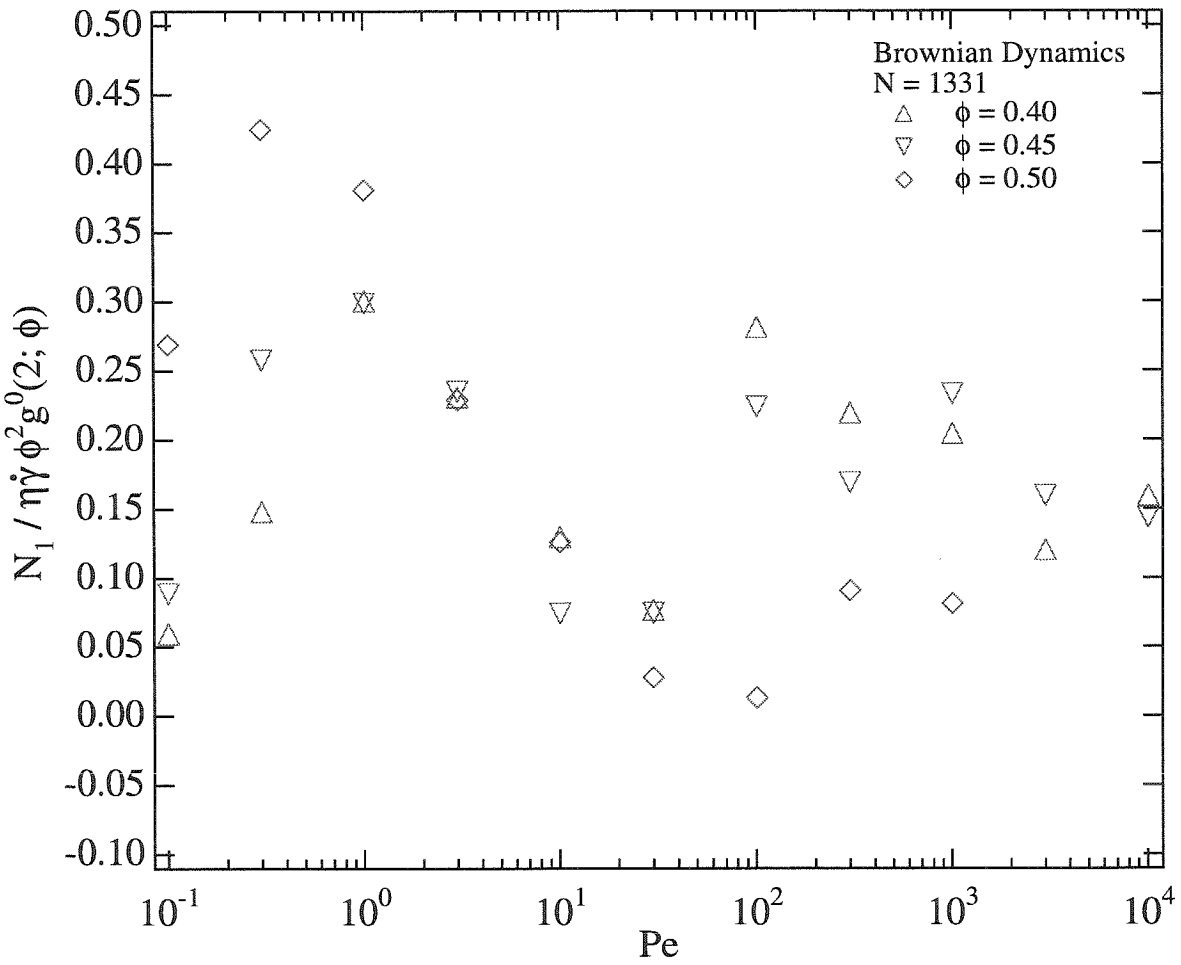

Figure 2.21: The first normal stress difference, N_1, scaled by $\phi^2 g^0(2)\eta\dot{\gamma}$ and plotted as a function of Pe for various volume fractions. Here, the characteristic diffusivity, $\hat{D}$, is simply equal to its dilute-limit Stokes Einstein value $D = kT/6\pi\eta a$.

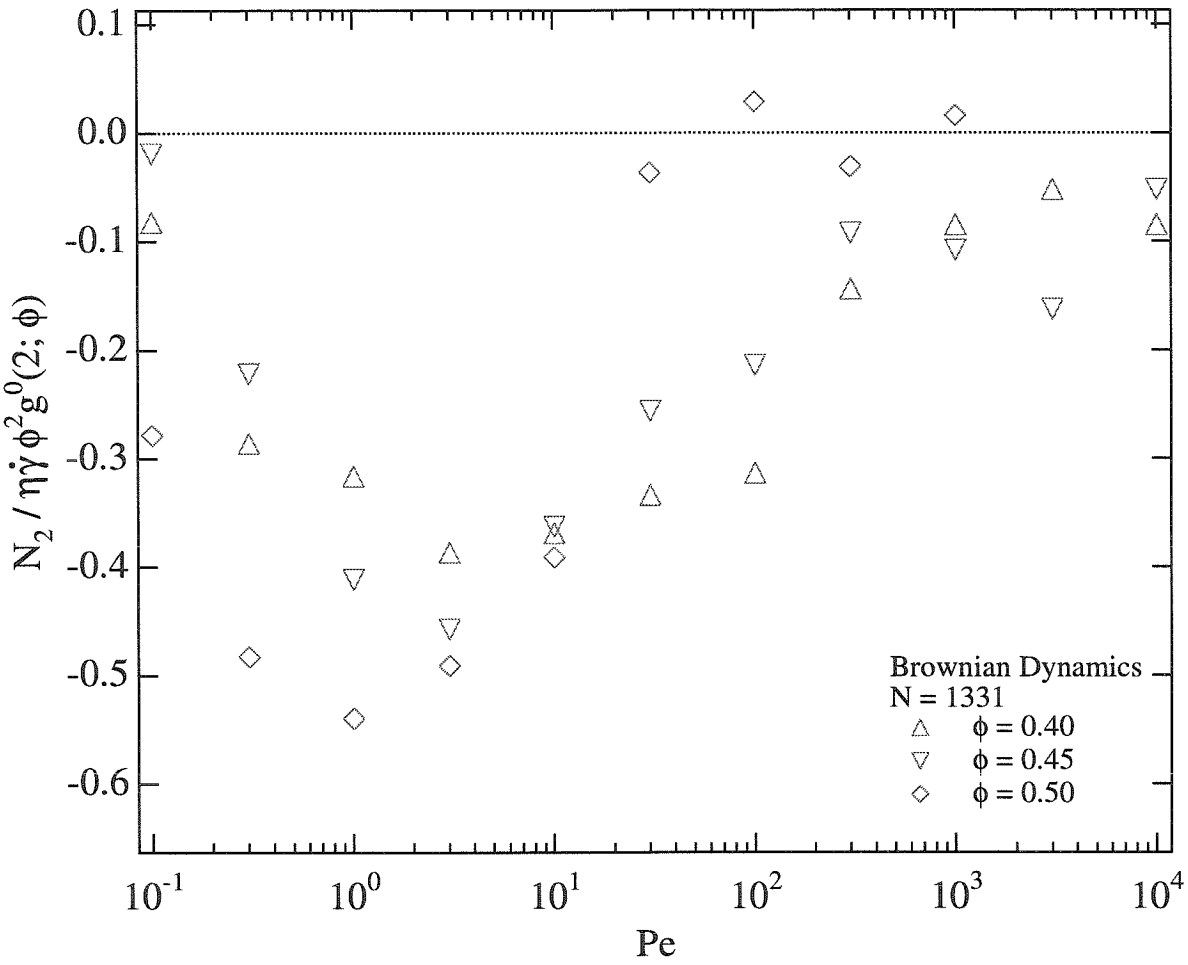

Figure 2.22: The second normal stress difference, N_2, scaled by $\phi^2 g^0(2)\eta\dot{\gamma}$ and plotted as a function of Pe for various volume fractions. Here, the characteristic diffusivity, $\hat{D}$, is simply equal to its dilute-limit Stokes Einstein value $D = kT/6\pi\eta a$.

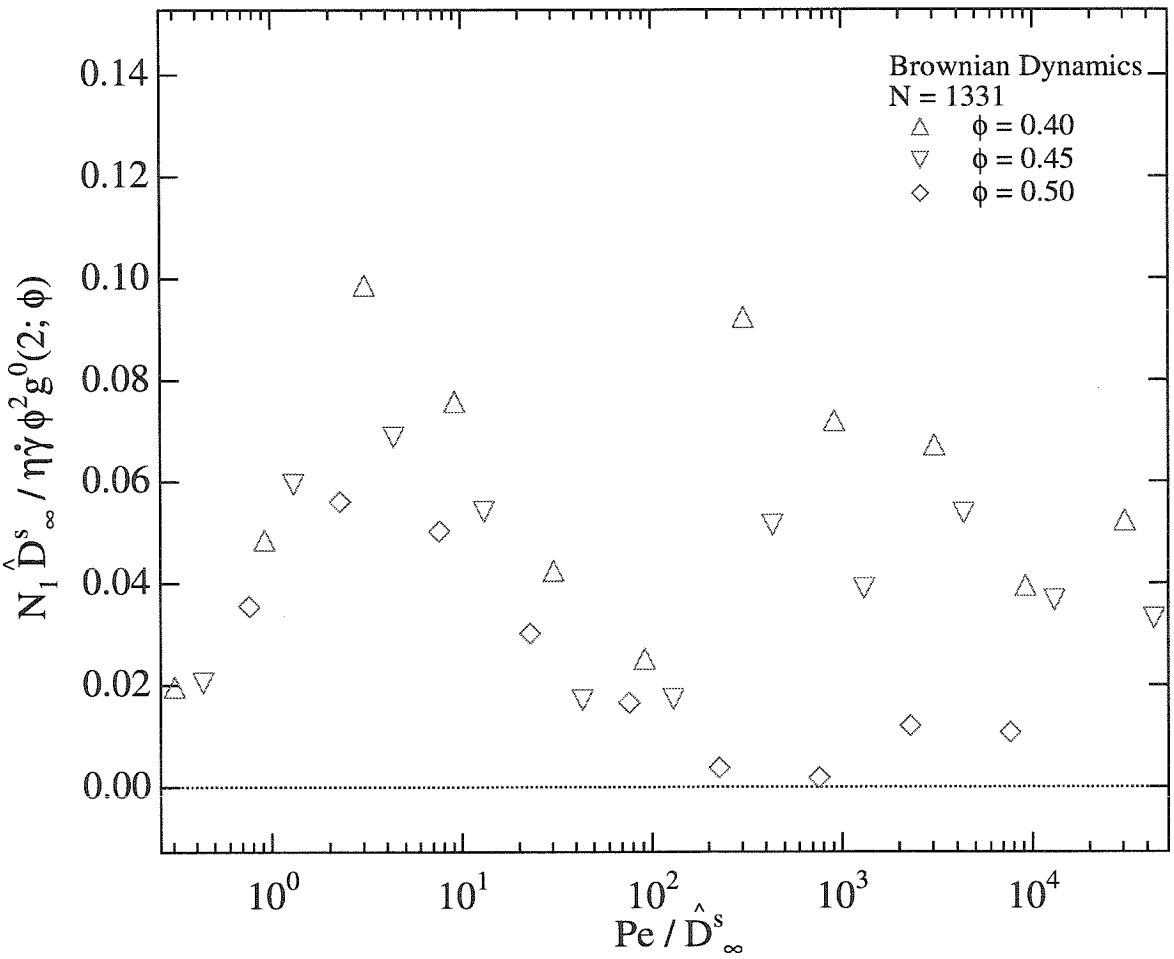

Figure 2.23: The first normal stress difference, N_1, scaled by $\phi^2 g^0(2)\eta\dot{\gamma}/\hat{D}^s_\infty$ and plotted as a function of rescaled Péclet number $Pe/\hat{D}^s_\infty$ for various volume fractions. Here, $\hat{D}^s_\infty$ is the equilibrium long-time self-diffusivity scaled by the Stokes Einstein value $D = kT/6\pi\eta a$.

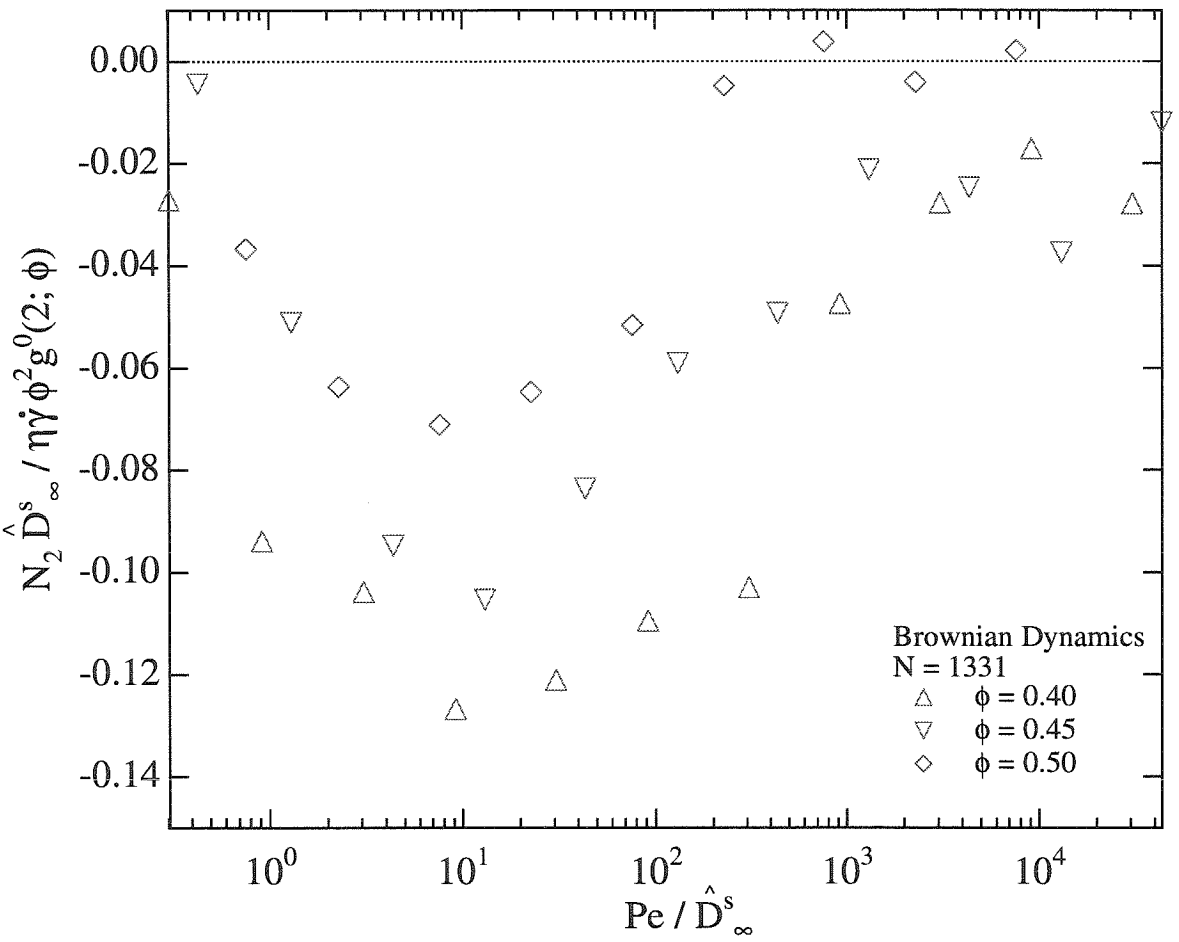

Figure 2.24: The second normal stress difference, N_2, scaled by $\phi^2 g^0(2)\eta\dot{\gamma}/\hat{D}^s_\infty$ and plotted as a function of rescaled Péclet number $Pe/\hat{D}^s_\infty$ for various volume fractions. Here, $\hat{D}^s_\infty$ is the equilibrium long-time self-diffusivity scaled by the Stokes Einstein value $D = kT/6\pi\eta a$.

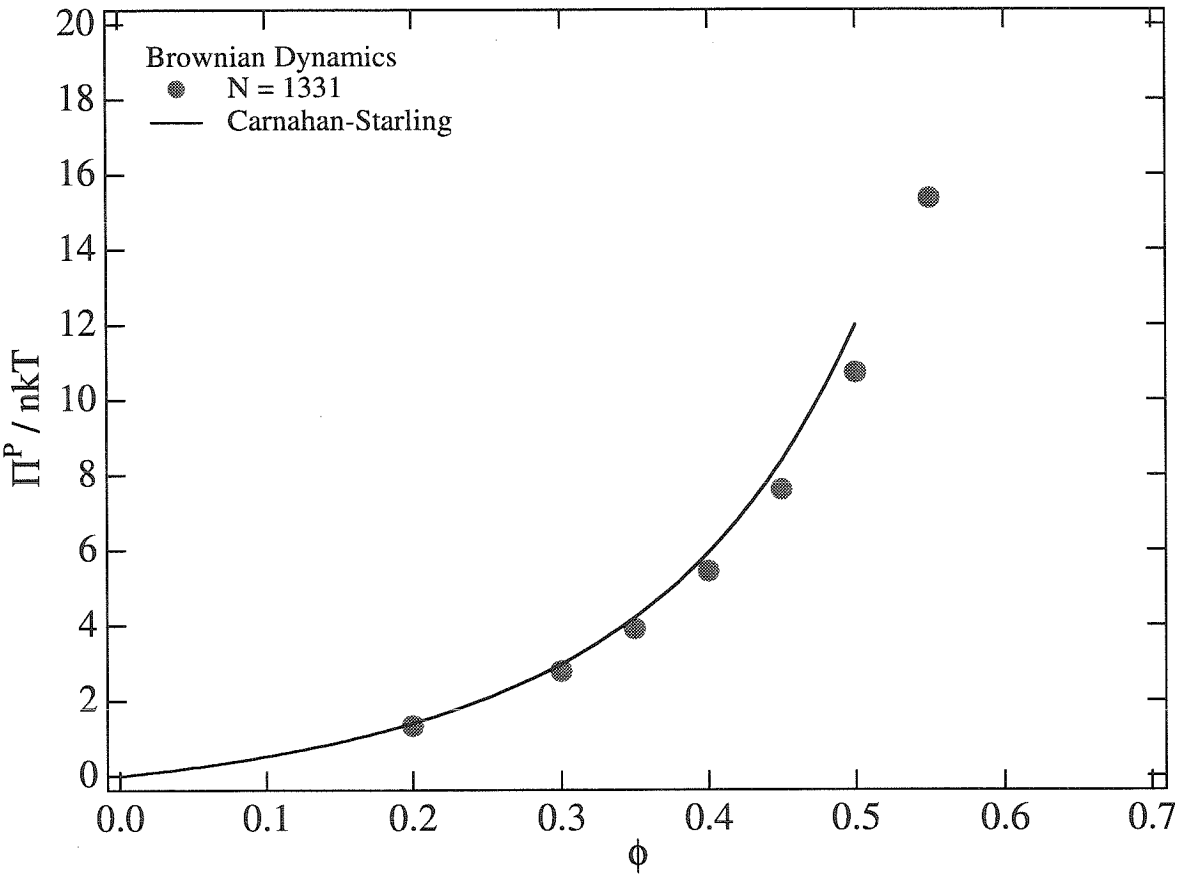

Figure 2.25: The equilibrium osmotic pressure, Π^0, nondimensionalized by nkT, as a function of volume fraction, ϕ.

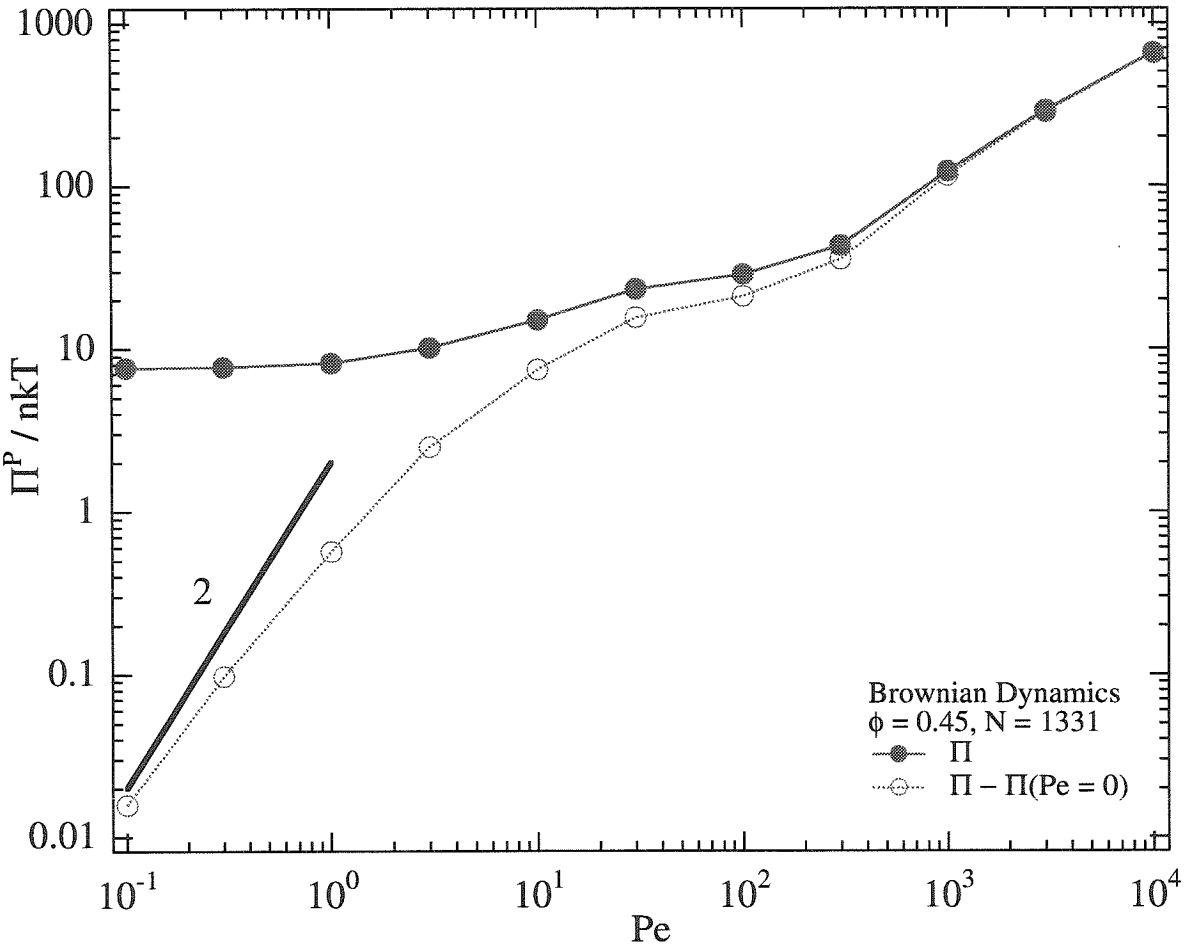

Figure 2.26: The interparticle force contribution to the osmotic pressure, Π, nondimensionalized by nkT as a function of Pe for $N = 1331$ and $\phi = 0.45$. Also on the plot is the same data with the equilibrium value of the osmotic pressure subtracted off in order to show the initial growth of the pressure with Pe from its equilibrium value.

$\phi = 0.30$				
Pe	N	Δt	$NSTEPS$	η_r^F
0.1	339	5×10^{-4}	2 000 000	0.4015 ± 0.0735
0.3	339	2.5×10^{-4}	1 200 000	0.4335 ± 0.0595
1	339	2.5×10^{-4}	400 000	0.3905 ± 0.0195
3	339	2.5×10^{-4}	400 000	0.3345 ± 0.0185
10	339	2.5×10^{-4}	400 000	0.2620 ± 0.0040
30	339	2.5×10^{-4}	400 000	0.2080 ± 0.0100
100	339	2.5×10^{-4}	400 000	0.1370 ± 0.0075
300	339	2.5×10^{-4}	400 000	0.0565 ± 0.0065

Table 2.2: Relative viscosity data as a function of Pe from Brownian Dynamics at $\phi = 0.30$.

$\phi = 0.30$			
Pe	N	$N_1^F/\eta\dot{\gamma}$	$N_2^F/\eta\dot{\gamma}$
0.1	339	0.0335 ± 0.1595	-0.0795 ± 0.2075
0.3	339	0.0005 ± 0.0415	-0.0295 ± 0.0480
1	339	0.0615 ± 0.0690	-0.0945 ± 0.0375
3	339	0.0775 ± 0.0260	-0.0885 ± 0.0105
10	339	0.0485 ± 0.0225	-0.0963 ± 0.0135
30	339	0.0305 ± 0.0210	-0.0905 ± 0.0080
100	339	0.0495 ± 0.0130	-0.0945 ± 0.0085
300	339	0.0725 ± 0.0055	-0.0655 ± 0.0060

Table 2.3: Normal stress difference data as a function of Pe from Brownian Dynamics at $\phi = 0.30$.

$\phi = 0.35$				
Pe	N	Δt	$NSTEPS$	η_r^F
0.1	339	5×10^{-4}	2 000 000	0.7440 ± 0.0865
0.3	339	2.5×10^{-4}	1 200 000	0.7415 ± 0.0490
1	339	2.5×10^{-4}	400 000	0.6975 ± 0.0250
3	339	2.5×10^{-4}	400 000	0.5830 ± 0.0070
10	339	2.5×10^{-4}	400 000	0.4220 ± 0.0065
30	339	2.5×10^{-4}	400 000	0.3255 ± 0.0105
100	339	2.5×10^{-4}	400 000	0.1810 ± 0.0125
300	339	2.5×10^{-4}	400 000	0.0775 ± 0.0060

Table 2.4: Relative viscosity data as a function of Pe from Brownian Dynamics at $\phi = 0.35$.

$\phi = 0.35$			
Pe	N	$N_1^F/\eta\dot{\gamma}$	$N_2^F/\eta\dot{\gamma}$
0.1	339	0.0335 ± 0.1595	-0.0795 ± 0.0415
0.3	339	0.1075 ± 0.0655	-0.1695 ± 0.0510
1	339	0.1070 ± 0.0495	-0.0885 ± 0.0260
3	339	0.0730 ± 0.0305	-0.1380 ± 0.0230
10	339	0.0515 ± 0.0070	-0.1400 ± 0.0145
30	339	0.0145 ± 0.0170	-0.1070 ± 0.0110
100	339	0.0980 ± 0.0180	-0.1265 ± 0.0085
300	339	0.1045 ± 0.0065	-0.0770 ± 0.0050

Table 2.5: Normal stress difference data as a function of Pe from Brownian Dynamics at $\phi = 0.35$.

$\phi = 0.40$				
Pe	N	Δt	$NSTEPS$	η_r^F
0.1	339	5×10^{-4}	2 000 000	1.1895 ± 0.1570
0.3	339	2.5×10^{-4}	1 200 000	1.3745 ± 0.0555
1	339	2.5×10^{-4}	400 000	1.2020 ± 0.0215
3	339	2.5×10^{-4}	400 000	0.9360 ± 0.0175
10	339	2.5×10^{-4}	400 000	0.6765 ± 0.0195
30	339	2.5×10^{-4}	400 000	0.4780 ± 0.0265
100	339	2.5×10^{-4}	400 000	0.1670 ± 0.0230
300	339	2.5×10^{-4}	400 000	0.0605 ± 0.0045

Table 2.6: Relative viscosity data as a function of Pe from Brownian Dynamics at $\phi = 0.40$.

$\phi = 0.40$			
Pe	N	$N_1^F/\eta\dot{\gamma}$	$N_2^F/\eta\dot{\gamma}$
0.1	339	-0.1280 ± 0.2915	-0.0755 ± 0.4105
0.3	339	0.1585 ± 0.0470	-0.1285 ± 0.1170
1	339	0.2485 ± 0.0820	-0.1910 ± 0.0380
3	339	0.0680 ± 0.0520	-0.1815 ± 0.0460
10	339	0.0860 ± 0.0315	-0.2215 ± 0.0335
30	339	0.0185 ± 0.0225	-0.1915 ± 0.0345
100	339	0.1205 ± 0.0120	-0.1135 ± 0.0155
300	339	0.1290 ± 0.0170	-0.0820 ± 0.0185

Table 2.7: Normal stress difference data as a function of Pe from Brownian Dynamics at $\phi = 0.40$.

$\phi = 0.40$				
Pe	N	Δt	$NSTEPS$	η_r^F
0.1	1331	5×10^{-4}	2 000 000	1.3200 ± 0.0620
0.3	1331	2.5×10^{-4}	1 000 000	1.4015 ± 0.0235
1	1331	2.5×10^{-4}	400 000	1.2030 ± 0.0085
3	1331	2.5×10^{-4}	400 000	0.9510 ± 0.0090
10	1331	2.5×10^{-4}	400 000	0.6770 ± 0.0150
30	1331	2.5×10^{-4}	400 000	0.4840 ± 0.0090
100	1331	2.5×10^{-4}	400 000	0.1695 ± 0.0105
300	1331	2.5×10^{-4}	400 000	0.0745 ± 0.0085
1000	1331	2.5×10^{-4}	400 000	0.0525 ± 0.0090
3000	1331	2.5×10^{-4}	400 000	0.0350 ± 0.0065
10000	1331	2.5×10^{-4}	400 000	0.0440 ± 0.0085

Table 2.8: Relative viscosity data as a function of Pe from Brownian Dynamics at $\phi = 0.40$.

$\phi = 0.40$			
Pe	N	$N_1^F/\eta\dot{\gamma}$	$N_2^F/\eta\dot{\gamma}$
0.1	1331	0.0350 ± 0.0335	-0.0490 ± 0.1070
0.3	1331	0.0875 ± 0.0795	-0.1695 ± 0.0510
1	1331	0.1780 ± 0.0280	-0.2110 ± 0.0480
3	1331	0.1365 ± 0.0300	-0.2285 ± 0.0495
10	1331	0.0765 ± 0.0140	-0.2185 ± 0.0250
30	1331	0.0455 ± 0.0175	-0.1975 ± 0.0080
100	1331	0.1665 ± 0.0055	-0.1860 ± 0.0145
300	1331	0.1300 ± 0.0130	-0.0855 ± 0.0155
1000	1331	0.1210 ± 0.0100	-0.0500 ± 0.0130
3000	1331	0.0710 ± 0.0105	-0.0310 ± 0.0160
10000	1331	0.0945 ± 0.0120	-0.0505 ± 0.0125

Table 2.9: Normal stress difference data as a function of Pe from Brownian Dynamics at $\phi = 0.40$.

$\phi = 0.40$					
Pe	N	Δt	$NSTEPS$	Π/nkT	$\Pi/\eta\dot{\gamma}$
0.0	1331	2.5×10^{-4}	400 000	5.4421 ± 0.0091	
0.1	1331	5×10^{-4}	2 000 000	5.2585	94.653
0.3	1331	2.5×10^{-4}	1 000 000	5.4889 ± 0.0092	32.933 ± 0.0550
1	1331	2.5×10^{-4}	400 000	5.7112 ± 0.0187	10.280 ± 0.0335
3	1331	2.5×10^{-4}	400 000	6.7958	4.0775
10	1331	2.5×10^{-4}	400 000	9.8840	1.7791
30	1331	2.5×10^{-4}	400 000	16.592	0.9955
100	1331	2.5×10^{-4}	400 000	21.144	0.3806
300	1331	2.5×10^{-4}	400 000	31.341	0.1887
1000	1331	2.5×10^{-4}	400 000	72.977	0.1314
3000	1331	2.5×10^{-4}	400 000	159.54	0.0957
10000	1331	2.5×10^{-4}	400 000	612.26	0.1102

Table 2.10: Osmotic pressure data as a function of Pe from Brownian Dynamics at $\phi = 0.40$.

$\phi = 0.40$				
Pe	N	D_{xx}	D_{yy}	D_{zz}
0.0	1331	$.3364 \pm .01635$	$.3577 \pm .04977$	$.2973 \pm .04913$
0.1	1331	$.3851 \pm .02745$	$.3350 \pm .02625$	$.3353 \pm .02062$
0.3	1331	$.3398 \pm .03409$	$.3346 \pm .02026$	$.3519 \pm .03408$
1	1331	$.4167 \pm .03141$	$.3879 \pm .04077$	$.3143 \pm .03143$
3	1331	$.5421 \pm .05003$	$.5624 \pm .08206$	$.4556 \pm .05852$
10	1331	$.8921 \pm .07279$	$.9244 \pm .04438$	$.7199 \pm .07141$
30	1331	$1.699 \pm .1754$	$1.593 \pm .07620$	$1.243 \pm .1497$
100	1331	$3.184 \pm .3979$	$.4033 \pm .3581$	$.8796 \pm .4192$
300	1331	5.004 ± 1.000	$.1298 \pm .6455$	$.6591 \pm .9285$
1000	1331	15.31 ± 2.564	$.3317 \pm 1.937$	$.8538 \pm 2.432$
3000	1331	42.72 ± 11.67	$.9689 \pm 5.859$	2.845 ± 7.878
10000	1331	156.3 ± 16.07	2.347 ± 4.738	24.36 ± 16.89

Table 2.11: Long-time self-diffusivities, nondimensionalized by the Stokes-Einstein diffusivity, D_0, as a function of Pe from Brownian Dynamics at $\phi = 0.40$.

$\phi = 0.45$				
Pe	N	Δt	$NSTEPS$	η_r^F
0.1	1331	2.5×10^{-4}	4 000 000	2.9150 ± 0.0370
0.3	1331	2.5×10^{-4}	1 200 000	2.7680 ± 0.0525
1	1331	2.5×10^{-4}	400 000	2.1835 ± 0.0360
3	1331	2.5×10^{-4}	400 000	1.6060 ± 0.0330
10	1331	2.5×10^{-4}	400 000	1.0970 ± 0.0205
30	1331	2.5×10^{-4}	400 000	0.6525 ± 0.0195
100	1331	2.5×10^{-4}	400 000	0.2255 ± 0.0250
300	1331	2.5×10^{-4}	400 000	0.1050 ± 0.0130
1000	1331	2.5×10^{-4}	400 000	0.0975 ± 0.0080
3000	1331	2.5×10^{-4}	400 000	0.0715 ± 0.0055
10000	1331	2.5×10^{-4}	400 000	0.0455 ± 0.0100

Table 2.12: Relative viscosity data as a function of Pe from Brownian Dynamics at $\phi = 0.45$.

$\phi = 0.45$			
Pe	N	$N_1^F/\eta\dot{\gamma}$	$N_2^F/\eta\dot{\gamma}$
0.1	1331	0.0840 ± 0.1790	-0.0180 ± 0.1820
0.3	1331	0.2435 ± 0.1025	-0.2095 ± 0.1140
1	1331	0.2820 ± 0.0615	-0.3885 ± 0.0720
3	1331	0.2220 ± 0.0395	-0.4315 ± 0.0435
10	1331	0.0700 ± 0.0300	-0.3425 ± 0.0270
30	1331	0.0705 ± 0.0390	-0.2420 ± 0.0310
100	1331	0.2110 ± 0.0380	-0.2020 ± 0.0205
300	1331	0.1595 ± 0.0135	-0.0870 ± 0.0200
1000	1331	0.2200 ± 0.0170	-0.1015 ± 0.0140
3000	1331	0.1505 ± 0.0150	-0.1535 ± 0.0040
10000	1331	0.1355 ± 0.0180	-0.0490 ± 0.0260

Table 2.13: Normal stress difference data as a function of Pe from Brownian Dynamics at $\phi = 0.45$.

$\phi = 0.45$					
Pe	N	Δt	$NSTEPS$	Π/nkT	$\Pi/\eta\dot{\gamma}$
0.0	1331	2.5×10^{-4}	400 000	7.6131 ± 0.0076	
0.1	1331	2.5×10^{-4}	4 000 000	7.6266 ± 0.0050	154.44 ± 0.1013
0.3	1331	2.5×10^{-4}	1 200 000	7.7092 ± 0.0081	52.037 ± 0.0547
1	1331	2.5×10^{-4}	400 000	8.1728 ± 0.0245	16.550 ± 0.0496
3	1331	2.5×10^{-4}	400 000	10.093 ± 0.0718	6.8128 ± 0.0485
10	1331	2.5×10^{-4}	400 000	15.053 ± 0.1487	3.0482 ± 0.0301
30	1331	2.5×10^{-4}	400 000	23.057 ± 0.4336	1.5563 ± 0.0293
100	1331	2.5×10^{-4}	400 000	28.523 ± 2.3585	0.5776 ± 0.0478
300	1331	2.5×10^{-4}	400 000	42.759 ± 3.8247	0.2886 ± 0.0258
1000	1331	2.5×10^{-4}	400 000	122.21 ± 7.5935	0.2475 ± 0.0154
3000	1331	2.5×10^{-4}	400 000	289.17 ± 15.710	0.1952 ± 0.0106
10000	1331	2.5×10^{-4}	400 000	656.70 ± 77.503	0.1330 ± 0.0157

Table 2.14: Osmotic pressure data as a function of Pe from Brownian Dynamics at $\phi = 0.45$.

$\phi = 0.45$				
Pe	N	D_{xx}	D_{yy}	D_{zz}
0.0	1331	$.2331 \pm .02330$	$.2392 \pm .02274$	$.2350 \pm .02454$
0.1	1331	$.3183 \pm .04684$	$.2585 \pm .03605$	$.2753 \pm .03190$
0.3	1331	$.2663 \pm .01938$	$.2791 \pm .03591$	$.2439 \pm .02504$
1	1331	$.3452 \pm .04065$	$.3483 \pm .04085$	$.3086 \pm .01442$
3	1331	$.4961 \pm .01735$	$.4866 \pm .04327$	$.3904 \pm .01610$
10	1331	$.9089 \pm .1051$	$.8908 \pm .03322$	$.3921 \pm .06981$
30	1331	$1.680 \pm .1466$	$1.032 \pm .07532$	$1.175 \pm .05548$
100	1331	$3.815 \pm .3318$	$.2540 \pm .3962$	$.6771 \pm .3209$
300	1331	$9.327 \pm .5325$	$.1883 \pm .6930$	$.6835 \pm .9032$
1000	1331	25.22 ± 3.446	$1.071 \pm .4105$	1.942 ± 2.765
3000	1331	72.46 ± 6.268	1.546 ± 5.680	2.255 ± 7.620
10000	1331	103.7 ± 46.66	3.935 ± 16.14	5.672 ± 25.45

Table 2.15: Long-time self-diffusivities, nondimensionalized by the Stokes-Einstein diffusivity, D_0, as a function of Pe from Brownian Dynamics at $\phi = 0.45$.

$\phi = 0.50$				
Pe	N	Δt	$NSTEPS$	η_r^F
0.1	1331	2.5×10^{-4}	4 000 000	7.1010 ± 0.1190
0.3	1331	2.5×10^{-4}	1 200 000	5.9550 ± 0.1125
1	1331	2.5×10^{-4}	400 000	4.0245 ± 0.0290
3	1331	2.5×10^{-4}	400 000	2.8230 ± 0.0300
10	1331	2.5×10^{-4}	400 000	1.7990 ± 0.0310
30	1331	2.5×10^{-4}	400 000	0.4185 ± 0.0115
100	1331	2.5×10^{-4}	400 000	0.1300 ± 0.0090
300	1331	2.5×10^{-4}	400 000	0.1030 ± 0.0060
1000	1331	2.5×10^{-4}	400 000	0.0825 ± 0.0085

Table 2.16: Relative viscosity data as a function of Pe from Brownian Dynamics at $\phi = 0.50$.

$\phi = 0.50$			
Pe	N	$N_1^F/\eta\dot{\gamma}$	$N_2^F/\eta\dot{\gamma}$
0.1	1331	0.4035 ± 0.3220	-0.4175 ± 0.0825
0.3	1331	0.6370 ± 0.1695	-0.7235 ± 0.1245
1	1331	0.5830 ± 0.0980	-0.8345 ± 0.1415
3	1331	0.3445 ± 0.1175	-0.7445 ± 0.0775
10	1331	0.1890 ± 0.0310	-0.5870 ± 0.0095
30	1331	0.0415 ± 0.0535	-0.0545 ± 0.0890
100	1331	0.0195 ± 0.0085	0.0430 ± 0.0195
300	1331	0.1365 ± 0.0260	-0.0470 ± 0.0220
1000	1331	0.1220 ± 0.0110	0.0245 ± 0.0250

Table 2.17: Normal stress difference data as a function of Pe from Brownian Dynamics at $\phi = 0.50$.

$\phi = 0.50$					
Pe	N	Δt	$NSTEPS$	Π/nkT	$\Pi/\eta\dot{\gamma}$
0.0	1331	2.5×10^{-4}	400 000	10.723 ± 0.0358	
0.03	1331	2.5×10^{-4}	400 000	10.726 ± 0.0345	804.45 ± 2.5875
0.1	1331	2.5×10^{-4}	4 000 000	10.780 ± 0.0070	242.55 ± 0.1575
0.3	1331	2.5×10^{-4}	1 200 000	11.077 ± 0.0107	83.078 ± 0.0803
1	1331	2.5×10^{-4}	400 000	12.147 ± 0.0210	27.331 ± 0.0473
3	1331	2.5×10^{-4}	400 000	15.837 ± 0.0659	11.878 ± 0.0494
10	1331	2.5×10^{-4}	400 000	24.151 ± 0.3862	5.4340 ± 0.0869
30	1331	2.5×10^{-4}	400 000	21.200 ± 3.3560	1.5900 ± 0.2517
100	1331	2.5×10^{-4}	400 000	25.532 ± 1.3924	0.5745 ± 0.0313
300	1331	2.5×10^{-4}	400 000	49.537 ± 1.9817	0.3715 ± 0.0149
1000	1331	2.5×10^{-4}	400 000	132.11 ± 8.6106	0.2972 ± 0.0194

Table 2.18: Osmotic pressure data as a function of Pe from Brownian Dynamics at $\phi = 0.50$.

$\phi = 0.50$				
Pe	N	D_{xx}	D_{yy}	D_{zz}
0.0	1331	$.1283 \pm .01321$	$.1297 \pm .01146$	$.1273 \pm .01411$
0.03	1331	$.1313 \pm .02255$	$.1475 \pm .02279$	$.1235 \pm .01262$
0.1	1331	$.2021 \pm .03306$	$.1778 \pm .02945$	$.1364 \pm .02412$
0.3	1331	$.1955 \pm .02212$	$.2085 \pm .01545$	$.1470 \pm .02459$
1	1331	$.2975 \pm .02210$	$.2893 \pm .02676$	$.2464 \pm .03166$
3	1331	$.4539 \pm .03789$	$.4927 \pm .05482$	$.3617 \pm .04079$
10	1331	$.9029 \pm .09924$	$.8412 \pm .07044$	$.7422 \pm .03608$
30	1331	$1.311 \pm .3018$	$.3052 \pm .3046$	$.3872 \pm .2467$
100	1331	$2.580 \pm .3074$	$.0187 \pm .1753$	$.0712 \pm .2859$
300	1331	$7.395 \pm .7426$	$.1042 \pm 1.048$	$.3371 \pm 1.414$
1000	1331	24.51 ± 0.472	$.4715 \pm 1.335$	1.022 ± 1.644

Table 2.19: Long-time self-diffusivities, nondimensionalized by the Stokes-Einstein diffusivity, D_0, as a function of Pe from Brownian Dynamics at $\phi = 0.50$.

$\phi = 0.55$				
Pe	N	Δt	$NSTEPS$	η_r^F
0.1	1331	2.5×10^{-4}	4 000 000	22.069 ± 0.2580
0.3	1331	2.5×10^{-4}	1 200 000	13.821 ± 0.3555
1	1331	2.5×10^{-4}	400 000	7.9095 ± 0.3560
3	1331	2.5×10^{-4}	400 000	5.5090 ± 0.0630
10	1331	2.5×10^{-4}	400 000	0.7365 ± 0.0890
30	1331	2.5×10^{-4}	400 000	0.4465 ± 0.0205
100	1331	2.5×10^{-4}	400 000	0.2743 ± 0.0030
300	1331	2.5×10^{-4}	400 000	0.1297 ± 0.0050
1000	1331	2.5×10^{-4}	400 000	0.2407 ± 0.0216

Table 2.20: Relative viscosity data as a function of Pe from Brownian Dynamics at $\phi = 0.55$.

$\phi = 0.55$			
Pe	N	$N_1^F/\eta\dot{\gamma}$	$N_2^F/\eta\dot{\gamma}$
0.1	1331	1.5360 ± 0.6695	-2.3945 ± 0.4820
0.3	1331	1.3610 ± 0.2315	-2.1575 ± 0.2110
1	1331	1.0315 ± 0.1410	-1.9300 ± 0.1910
3	1331	0.6920 ± 0.1360	-1.5750 ± 0.0940
10	1331	0.3880 ± 0.2765	-0.5865 ± 0.1965
30	1331	0.4865 ± 0.0765	-0.0785 ± 0.0775
100	1331	-0.1137 ± 0.0312	-0.0712 ± 0.0476
300	1331	-0.1971 ± 0.0169	0.1712 ± 0.0121
1000	1331	0.2142 ± 0.0423	0.0173 ± 0.0090

Table 2.21: Normal stress difference data as a function of Pe from Brownian Dynamics at $\phi = 0.55$.

$\phi = 0.55$					
Pe	N	Δt	$NSTEPS$	Π/nkT	$\Pi/\eta\dot{\gamma}$
0.01	1331	2.5×10^{-4}	400 000	15.388 ± 0.0590	3808.5 ± 723.24
0.03	1331	2.5×10^{-4}	400 000	15.524 ± 0.0784	1280.7 ± 6.4680
0.1	1331	2.5×10^{-4}	4 000 000	15.973 ± 0.0180	395.33 ± 0.4455
0.3	1331	2.5×10^{-4}	1 200 000	17.014 ± 0.0242	140.37 ± 0.1997
1	1331	2.5×10^{-4}	400 000	19.612 ± 0.0466	48.540 ± 0.1153
3	1331	2.5×10^{-4}	400 000	28.076 ± 0.1225	23.163 ± 0.1011
10	1331	2.5×10^{-4}	400 000	18.246 ± 1.3438	4.5159 ± 0.3326
30	1331	2.5×10^{-4}	400 000	26.600 ± 1.2073	2.1945 ± 0.0996
100	1331	2.5×10^{-4}	400 000	52.880 ± 0.4735	1.3088 ± 0.0117
300	1331	2.5×10^{-4}	400 000	86.880 ± 2.3673	0.7160 ± 0.0195
1000	1331	2.5×10^{-4}	400 000	353.68 ± 23.381	0.8754 ± 0.0579

Table 2.22: Osmotic pressure data as a function of Pe from Brownian Dynamics at $\phi = 0.55$.

$\phi = 0.55$				
Pe	N	D_{xx}	D_{yy}	D_{zz}
0.01	1331	$.0489 \pm .00699$	$.0469 \pm .00784$	$.0462 \pm .00414$
0.03	1331	$.0529 \pm .01077$	$.0451 \pm .00907$	$.0441 \pm .00587$
0.1	1331	$.1239 \pm .02307$	$.1109 \pm .02387$	$.0676 \pm .00438$
0.3	1331	$.1357 \pm .01211$	$.1396 \pm .02323$	$.1202 \pm .01356$
1	1331	$.2577 \pm .01624$	$.2553 \pm .02680$	$.1996 \pm .02605$
3	1331	$.4552 \pm .03382$	$.4246 \pm .04841$	$.3991 \pm .03713$
10	1331	$.5859 \pm .17841$	$.1459 \pm .25064$	$.1832 \pm .26849$
30	1331	$1.019 \pm .16500$	$.0781 \pm .03605$	$.0847 \pm .05853$
100	1331	$4.904 \pm .80276$	$-.0080 \pm .13896$	$.0811 \pm .19684$
300	1331	$3.352 \pm .79880$	$.0672 \pm .47447$	$.0310 \pm .05853$
1000	1331	59.51 ± 9.4779	$.2748 \pm 1.3769$	$.2643 \pm 1.6523$

Table 2.23: Long-time self-diffusivities, nondimensionalized by the Stokes-Einstein diffusivity, D_0, as a function of Pe from Brownian Dynamics at $\phi = 0.55$.

Chapter 3

Structure, diffusion and rheology of Brownian suspensions by Stokesian Dynamics simulation

3.1 Introduction

Suspensions of small particles dispersed in a fluid occur in a wide variety of natural and industrial settings, such as slurries, paints, pastes, dyes, polymers, proteins, many foodstuffs, and ceramic sols. In these microstructured fluids the suspended particles interact through hydrodynamic, interparticle, and Brownian (or thermal) forces. The balance between thermal and interparticle forces determines the equilibrium behavior. Under the action of an external driving force such as shear, hydrodynamic forces come into play and compete with thermal and interparticle forces to set the structure and determine properties. The understanding of colloidal dispersions has increased dramatically in the last decade as a result of three parallel developments: (1) experiments on well-characterized model hard-sphere systems (de Kruif *et al.* 1985, van der Werff & de Kruif 1989, van der Werff *et al.* 1989, Ackerson 1990, etc.), (2) scaling theories for the behavior at high solids concentration (Brady 1993b, Brady & Morris 1997), and (3) Stokesian Dynamics simulations (Bossis & Brady 1984, 1987, 1989; Brady & Bossis 1985, 1988; Phung & Brady 1992, Phung 1993, Phung *et al.* 1996, Ball & Melrose 1995, Dratler & Schowalter 1996). Stokesian Dynamics, a general molecular-dynamics-like method for simulating suspensions at low particle Reynolds number, accurately calculates the many-body interactions necessary to capture the hydrodynamic forces transmitted through the fluid.

In this work we report on simulation studies of rheology, diffusion, and structure of concentrated monodisperse suspensions of hard spheres. In a hard-sphere suspension particles interact through hydrodynamic and Brownian forces only, and the system is described by the minimal number of parameters — the volume fraction ϕ and the Péclet number, Pe. The Péclet number is the ratio of hydrodynamic shear to thermal forces, or alternatively the ratio of Brownian and flow time scales and is given by $Pe = \dot{\gamma}a^2/D$, where $\dot{\gamma}$ is the magnitude of the shear rate, and $D = kT/6\pi\eta a$ is the Stokes-Einstein diffusivity of an isolated spherical particle of radius a and thermal energy kT in a fluid of viscosity η.

As the Péclet number is varied, the simulations reveal two characteristic regimes

of suspension behavior. At low Péclet number ($Pe \leq 10$) the equilibrium structure is distorted by the flow and the suspension viscosity shear thins. The shear thinning is shown to be caused by the decrease of the direct Brownian contribution to the stress as the deformation of the structure cannot keep up with the flow. The hydrodynamic contribution to the stress remains constant and equal to the high-frequency dynamic viscosity, η'_∞, throughout the shear thinning process. The zero-shear rate viscosity is determined both as the limiting value of the steady shear viscosity as the shear rate vanishes and from the decay of the shear stress autocorrelation at equilibrium (Nägele & Bergenholtz 1998). The simulation viscosities show no variation with the size of, or the number of particles in, a unit cell ($27 \leq N \leq 123$) and compare well with experiment (van der Werff & de Kruif 1989). Normal stress differences have proven difficult to measure accurately at low Péclet number but are determined by the direct Brownian contribution to the stress. The first normal stress difference is positive and the second negative. Unlike polymer systems, however, both normal stress differences are of comparable magnitude.

At high Péclet number the shearing forces overcome Brownian motion and push particles into close contact where the short-range hydrodynamic lubrication forces are important. The suspension exhibits shear thickening due to the increase in the hydrodynamic contribution to the stress caused by the formation of clusters that are bound by lubrication forces as first shown by Bossis & Brady (1989). The first normal stress difference changes sign, and both normal stress differences are negative and appear to approach an $O(\eta\dot{\gamma})$ high Pe asymptote. The long-time self-diffusivity also grows dramatically with Pe and reaches a purely hydrodynamic $O(\dot{\gamma}a^2)$ limit at high Pe. The appearance of diffusive motion and normal stress differences in the deterministic pure hydrodynamic limit is surprising. Recent theoretical work by Brady & Morris (1997) has shown, however, that the high-Pe limit is singular, and the residual effect of weak Brownian motion introduces irreversibility, which may result in finite normal stress differences and diffusive motion.

An unfortunate error in the simulation code used in our previous work (Phung & Brady 1992, Phung 1993, Phung *et al.* 1996) has been discovered and corrected

for this paper (see §3.2 for details of this error). The main effect of this correction is the absence of a flow-induced string-ordered phase at intermediate Péclet numbers and high concentrations that was observed in the earlier work. The low-Péclet shear thinning regime ($Pe \leq 1$) is not affected. The high-Péclet shear-thickening behavior is changed (slightly) quantitatively, but not qualitatively.

In the next section we outline the Stokesian Dynamics simulation method. In section 3.3 we present and discuss the simulation results for rheology, diffusion, and structure in concentrated colloidal dispersions of Brownian hard spheres at volume fractions in the range of $0.316 \leq \phi \leq 0.49$. Conclusions are given in section 3.4.

3.2 Simulation method

A detailed derivation of the simulation method can be found elsewhere (Durlofsky *et al.* 1987; Bossis & Brady 1987; Brady & Bossis 1988; Brady *et al.* 1988; Bossis & Brady 1989, Phung, *et al.* 1996); here, we shall proceed quickly. For N rigid particles suspended in an incompressible Newtonian fluid of viscosity η and density ρ, the fluid motion is governed by the Navier-Stokes equations, while the particle motion is described by the coupled N-body Langevin equation:

$$\boldsymbol{m} \cdot \frac{d\boldsymbol{U}}{dt} = \boldsymbol{F}^H + \boldsymbol{F}^P + \boldsymbol{F}^B. \tag{3.1}$$

In (3.1) $\boldsymbol{m}$ is the generalized mass/moment of inertia tensor, $\boldsymbol{U}$ is the particle translational/rotational velocity vector of dimension $6N$, and the $6N$ force/torque vectors $\boldsymbol{F}$ represent: (1) the hydrodynamic forces $\boldsymbol{F}^H$ exerted on the particles due to their motion relative to the fluid, (2) the deterministic non-hydrodynamic forces $\boldsymbol{F}^P$, which may be either interparticle or external, and (3) the stochastic forces $\boldsymbol{F}^B$ that give rise to Brownian motion.

When the motion is such that the particle Reynolds number is small; *i.e.*, $Re = \rho a^2 \dot{\gamma}/\eta \ll 1$ for the shear flows considered here, the hydrodynamic force/torque

exerted on the particles in a suspension undergoing a bulk linear flow is

$$\boldsymbol{F}^H = -\boldsymbol{R}_{FU}\cdot(\boldsymbol{U} - \langle \boldsymbol{U} \rangle) + \boldsymbol{R}_{FE}:\langle \boldsymbol{E} \rangle. \tag{3.2}$$

In (3.2), $\langle \boldsymbol{U} \rangle = \langle \dot{\boldsymbol{\Gamma}} \rangle \cdot \boldsymbol{x}$ is the imposed bulk flow evaluated at the particle centers, $\langle \dot{\boldsymbol{\Gamma}} \rangle = \langle \boldsymbol{E} \rangle + \langle \boldsymbol{\Omega} \rangle$, and $\langle \boldsymbol{E} \rangle$ and $\langle \boldsymbol{\Omega} \rangle$ are the bulk rate of strain and vorticity tensors, respectively, and are constant in space but may be arbitrary functions of time. The configuration-dependent resistance tensors $\boldsymbol{R}_{FU}(\boldsymbol{x})$ and $\boldsymbol{R}_{FE}(\boldsymbol{x})$ give the hydrodynamic force/torque on the particles due to their motion relative to the fluid and due to an imposed flow, respectively. The vector $\boldsymbol{x}$ represents the generalized configuration vector specifying the location and orientation of all N particles.

The deterministic, non-hydrodynamic force $\boldsymbol{F}^P$ is arbitrary and may be any form of interparticle or external force. In this work we shall consider hard spheres under the action of hydrodynamic and Brownian forces only so that $\boldsymbol{F}^P = 0$. The stochastic or Brownian force $\boldsymbol{F}^B$ arises from the thermal fluctuations in the fluid and is characterized by

$$\overline{\boldsymbol{F}^B} = 0 \quad \text{and} \quad \overline{\boldsymbol{F}^B(0)\boldsymbol{F}^B(t)} = 2kT\boldsymbol{R}_{FU}\delta(t). \tag{3.3}$$

In (3.3) the over bar denotes an average over the rapid fluctuations of the solvent molecules, k is Boltzmann's constant, T is the absolute temperature, and $\delta(t)$ is the delta function. The amplitude of the correlation between the Brownian forces at time 0 and at time t results from the fluctuation-dissipation theorem.

The evolution equation for the particles is obtained by integrating (3.1) over a time step Δt that is large compared with τ_p, the inertial relaxation time ($\tau_p = m/6\pi\eta a$), but small compared with the time over which the configuration changes. A second integration in time produces the evolution equation for the particle positions (both translational and orientational) with error of $o(\Delta t)$:

$$\Delta \boldsymbol{x} = Pe\{\langle \boldsymbol{U} \rangle + \boldsymbol{R}_{FU}^{-1}\cdot[\boldsymbol{R}_{FE}:\langle \hat{\boldsymbol{E}} \rangle + \dot{\gamma}^{*-1}\boldsymbol{F}^P]\}\Delta t + \nabla\cdot\boldsymbol{R}_{FU}^{-1}\Delta t + \boldsymbol{X}(\Delta t),$$

$$\overline{\boldsymbol{X}} = 0 \quad \text{and} \quad \overline{\boldsymbol{X}(\Delta t)\boldsymbol{X}(\Delta t)} = 2\boldsymbol{R}_{FU}^{-1}\Delta t. \tag{3.4}$$

Here, $\Delta\boldsymbol{x}$ is the change in particle position during the time step Δt, and $\boldsymbol{X}(\Delta t)$ is a random displacement due to Brownian motion that has zero mean and covariance given by the inverse of the resistance tensor. In (3.4) $\boldsymbol{x}$ has been nondimensionalized by the characteristic particle size a; the time by the diffusive time scale a^2/D, where $D = kT/6\pi\eta a$ is the diffusion coefficient of a single isolated particle; the rate of strain tensor $\langle\hat{\boldsymbol{E}}\rangle$ by $\dot{\gamma}$, where $\dot{\gamma} = |\langle\dot{\boldsymbol{\Gamma}}\rangle|$ is the magnitude of the shear rate; the shear forces by $6\pi\eta a^2\dot{\gamma}$; and the interparticle forces by their magnitude $|\boldsymbol{F}^P|$. The Péclet number, $Pe = \dot{\gamma}a^2/D = 6\pi\eta a^3\dot{\gamma}/kT$, measures the relative importance of shear and Brownian forces, and $\dot{\gamma}^* = 6\pi\eta a^2\dot{\gamma}/|\boldsymbol{F}^P|$ is a nondimensional shear rate giving the relative importance of shear and interparticle or externally imposed forces. For simulations where $Pe > 1$ it is convenient to non-dimensionalize the time step Δt with the inverse shear rate $1/\dot{\gamma}$. This is done by replacing Δt in (3.4) by $\Delta t/Pe$ producing an alternate form of the evolution equation:

$$\Delta\boldsymbol{x} = \{\langle\boldsymbol{U}\rangle + \boldsymbol{R}_{FU}^{-1}\cdot[\boldsymbol{R}_{FE}:\langle\hat{\boldsymbol{E}}\rangle + \dot{\gamma}^{*-1}\boldsymbol{F}^P]\}\Delta t + \frac{1}{Pe}\nabla\cdot\boldsymbol{R}_{FU}^{-1}\Delta t + \frac{1}{Pe^{1/2}}\boldsymbol{X}(\Delta t),$$

$$\overline{\boldsymbol{X}} = 0 \quad \text{and} \quad \overline{\boldsymbol{X}(\Delta t)\boldsymbol{X}(\Delta t)} = 2\boldsymbol{R}_{FU}^{-1}\Delta t. \tag{3.5}$$

The high-Péclet form of the evolution equation was incorrect in the Stokesian Dynamics code that was used for recently published results (Phung & Brady 1992, Phung 1993 and Phung *et al.* 1996). The random displacement term, $\boldsymbol{X}(\Delta t)$, had a $1/Pe$ coefficient which is too small for $Pe > 1$ affecting the results of those simulations. If we had simple diffusive motion in which the mobility was independent of the configuration, then one could simply rescale the shear rate by $Pe^{1/2}$ to convert the incorrect $(1/Pe)$ results to the correct behavior $(1/Pe^{1/2})$. However, the configuration-dependent mobility gives rise to the deterministic displacement $\nabla\cdot\boldsymbol{R}_{FU}^{-1}\Delta t$, which acts like a repulsive force between particles, and this rescaling produces too large of a repulsive force ($1/Pe^{1/2}$ instead of $1/Pe$). It is well known that suspensions with nonhydrodynamic repulsive forces order into string phases if the forces are strong

enough and the volume fraction is high enough (Bossis & Brady 1984, Rastogi 1995). Thus, the error in the earlier simulations acted to enhance this 'repulsive' force and produce ordering where there should be none as we show in this work. Note, this only affects the behavior for $Pe > 1$; the correct scaling for $Pe < 1$ is used in Phung *et al.* (1996).

The macroscopic properties are found from appropriate definitions and averages over particles and over time in a dynamic simulation. Here we shall be primarily interested in diffusion and rheology. Several 'particle diffusivities' may be defined. The short-time self-diffusivity $\boldsymbol{D}_0^s$, which measures the average instantaneous mobility of a particle, is given by an average over all configurations: $\boldsymbol{D}_0^s = \langle \boldsymbol{D}_{ii} \rangle$, where the subscript ii (no sum on i) indicates that only the diagonal or self terms are included in the sum, and the angle brackets denote an average over all configurations and all identical particles. The N-particle diffusion tensor $\boldsymbol{D}$ is given by the Stokes-Einstein relation:

$$\boldsymbol{D} \equiv kT\boldsymbol{R}_{FU}^{-1}. \tag{3.6}$$

The long-time self-diffusivity $\boldsymbol{D}_\infty^s$, which measures the ability of a particle to wander far from its starting point, is defined as the limit as time approaches infinity of one half of the time rate of change of the mean-square position of a particle:

$$\boldsymbol{D}_\infty^s = \lim_{t\to\infty} \frac{1}{2}\frac{d}{dt}\langle(\boldsymbol{x} - \langle \boldsymbol{x} \rangle)^2\rangle. \tag{3.7}$$

For rheology, the bulk stress $\langle \boldsymbol{\Sigma} \rangle$ is needed. This is defined as an average over the volume V containing the N particles and is given by

$$\langle \boldsymbol{\Sigma} \rangle = -\langle p \rangle \boldsymbol{I} + 2\eta \langle \boldsymbol{E} \rangle + \langle \boldsymbol{\Sigma}_p \rangle, \tag{3.8}$$

where $\langle p \rangle$ is a constant setting the level of the pressure in the incompressible medium, and $2\eta\langle \boldsymbol{E} \rangle$ is the deviatoric stress contribution from the fluid. The particle contribu-

tion to the stress $\langle \boldsymbol{\Sigma}_p \rangle$ is given by

$$\langle \boldsymbol{\Sigma}_p \rangle = -nkT\boldsymbol{I} + n\{\langle \boldsymbol{S}^H \rangle + \langle \boldsymbol{S}^P \rangle + \langle \boldsymbol{S}^B \rangle\}. \tag{3.9}$$

Here, $-nkT\boldsymbol{I}$ is the isotropic stress associated with the thermal energy of the Brownian particles, $\boldsymbol{I}$ is the isotropic tensor, and n is the number density of particles. There are three contributions to the bulk stress; (a) a mechanical or contract stress transmitted by the fluid due to the shear flow, $\langle \boldsymbol{S}^H \rangle$; (b) a stress due to the interparticle forces, $\langle \boldsymbol{S}^P \rangle$; and (c) a direct contribution from Brownian $\langle \boldsymbol{S}^B \rangle$; they are given by

$$\langle \boldsymbol{S}^H \rangle = -\langle \boldsymbol{R}_{SU} \cdot \boldsymbol{R}_{FU}^{-1} \cdot \boldsymbol{R}_{FE} - \boldsymbol{R}_{SE} \rangle : \langle \boldsymbol{E} \rangle, \tag{3.10a}$$

$$\langle \boldsymbol{S}^P \rangle = -\langle (\boldsymbol{R}_{SU} \cdot \boldsymbol{R}_{FU}^{-1} + \boldsymbol{x}\boldsymbol{I}) \cdot \boldsymbol{F}^P \rangle, \tag{3.10b}$$

$$\langle \boldsymbol{S}^B \rangle = -kT \langle \nabla \cdot (\boldsymbol{R}_{SU} \cdot \boldsymbol{R}_{FU}^{-1}) \rangle. \tag{3.10c}$$

The configuration-dependent resistance tensors $\boldsymbol{R}_{SU}(\boldsymbol{x})$ and $\boldsymbol{R}_{SE}(\boldsymbol{x})$ are similar to $\boldsymbol{R}_{FU}$ and $\boldsymbol{R}_{FE}$ and relate the particle 'stresslet' $\boldsymbol{S}$ to the particle velocities and to the imposed rate of strain, respectively. The stresslet is the symmetric first moment of the force distribution integrated over the particle surface.

The hydrodynamic resistance tensors $\boldsymbol{R}_{FU}$, $\boldsymbol{R}_{FE}$, etc., that appear in the evolution equation and macroscopic stress are computed in the same manner as discussed in Phung *et al.* (1996) and are not repeated here. Suffice it to say that the method accurately accounts for the near-field lubrication effects and the dominant many-body interactions. Periodic boundary conditions are used and all divergent and conditionally convergent hydrodynamic interactions are accelerated with the Ewald summation technique. As currently implemented, calculation of the hydrodynamic interactions requires $O(N^3)$ operations and thus limits the simulations to small systems ($27 \leq N \leq 123$). The same time integration scheme used by Phung *et al.* (1996) is employed here.

The simulation results are for a monodisperse suspension of Brownian hard spheres. For particles interacting as hard spheres the interparticle force is identically zero,

$\boldsymbol{F}^P \equiv 0$. The no-slip hydrodynamic boundary condition at particle surfaces guarantees that the particles behave as hard spheres (Brady 1993a). This can be appreciated by noting that an interparticle force of hard-sphere type at contact $r = 2a$ between two particles, $\boldsymbol{F}^P = \frac{1}{2}kT\hat{\boldsymbol{r}}\delta(r-2a)$, has no dynamical consequence. Since the relative mobility of two particles vanishes at contact as $r - 2a$ due to the lubrication interactions, the relative velocity caused by a hard-sphere force is proportional to $(r-2a)\delta(r-2a)$ and vanishes. Simulations with $\boldsymbol{F}^P \equiv 0$ at $Pe \equiv 0$ were shown by Phung *et al.* (1996) to produce precisely the expected hard-sphere behavior. Similarly, the stress contribution from hard-sphere forces at contact is zero ($\boldsymbol{S}^P \equiv 0$).

3.3 Results

A large number of simulations were performed for a range in volume fraction of $0.316 \leq \phi \leq 0.49$, Péclet numbers ranging from 0 to 10^4 and the number of particles N in the unit cell ranging from 27 to 123. Many of the long runs were divided into statistically independent subintervals in order to determine the statistical variation in the properties. All runs for all Péclet numbers were started using hard-sphere equilibrium configurations obtained from a Monte Carlo procedure. For each run, the first 10 000 to 20 000 time steps were ignored when computing average properties. The properties reported are averages over all particles and over time. All simulations are for simple shear flow with the flow, velocity-gradient, and vorticity directions along the three axes (x, y, z) of the cubic unit cell. The presentation below is divided into three parts: rheology, diffusion and structure.

3.3.1 Rheology

Shear viscosity

In steady simple shear flow the viscosity of a suspension is related to the (x, y) components of the bulk stress and rate of strain in the following manner:

$$\eta_r \equiv \frac{\Sigma_{xy}}{2\eta E_{xy}}.$$

The individual Brownian ($\boldsymbol{S}^B$) and hydrodynamic ($\boldsymbol{S}^H$) contributions to the relative viscosity are denoted as η_r^B and η_r^H, respectively; hence

$$\eta_r = 1 + \eta_r^B + \eta_r^H, \tag{3.11}$$

where the 1 is the solvent contribution.

First, we can analyze the fluctuations in stress at equilibrium and extract the zero-shear limiting viscosity from the following dimensional Green-Kubo formula (Nägele & Bergenholtz 1998):

$$\eta_0 = \eta'_\infty + \frac{V}{kT}\int_0^\infty \langle \sigma_{xy}(t)\sigma_{xy}(0)\rangle dt. \tag{3.12}$$

Here, η'_∞ is the high-frequency dynamic viscosity, which represents the viscous contribution to the stress at equilibrum, and is easily calculated from simulation. The instantaneous Brownian shear stress is given by $\sigma_{xy}(t)$. Although its average over long times is zero, the Brownian stress fluctuates along with the microstructure due to Brownian motion. The shear stress autocorrelation function $\langle \sigma_{xy}(t)\sigma_{xy}(0)\rangle$ analyzes the nature of the relaxation of these fluctuations. Here, we use the subscript xy for simplicity, but since there are no preferred directions at equilibrium, we can also autocorrelate the xz- and yz-components of the Brownian stress tensor and average the three functions to reduce statistical noise. Simulations were run at $Pe = 0$ using a time step of $\Delta t = 5 \times 10^{-4}$ for 400000 steps to calculate the shear-stress autocorrelation function. A discussion of the time-dependent behavior of the auto-

correlation function is presented elsewhere (Foss & Brady 1999b (ch. 4)). Here we are only interested in the zero-shear viscosity η_0.

The zero-shear rate viscosity from the Green-Kubo formula is shown in table 3.1 and compared with data from steady-shear simulation and experiment as a function of volume fraction, ϕ, in figure 3.1. The values calculated in this work from Green-Kubo analysis are virtually indistinguishable from the previously reported viscosities of Phung (1993) determined from steady-state averages at the lowest shear rate ($Pe = 0.01$). This gives us confidence that the simulations were indeed performed at low enough Pe to measure the limiting zero-shear viscosity. General agreement is found between the values obtained from Stokesian Dynamics and the experimental data.

We now turn our focus to the shear-rate dependence of the suspension stress. A representative viscosity versus Péclet number curve (figure 3.2) for a volume fraction of 0.45 and $N = 27$ shows the individual contributions to the viscosity as a function of the Péclet number. The Brownian viscosity shear thins, becoming insignificant compared to the hydrodynamic viscosity for $Pe > 10$. The hydrodynamic viscosity remains roughly constant and equal to the high-frequency dynamic viscosity, η'_∞, throughout the shear thinning process and then increases for $Pe > 10$. Thus, the total viscosity goes through two regions of behavior, a shear thinning region at low Pe and a shear thickening region at high Pe. The constancy of the hydrodynamic viscosity and the shear thinning of the Brownian viscosity has been observed in the stress jump experiments of Mackay and Kaffashi (1995) and the optical measurements of Bender and Wagner (1996). The uncertainty in the viscosities is shown in table 3.2.

Shear thinning can be explained in the following manner: the Brownian stress arises from the flow-induced deformation of the equilibrium structure — particles diffuse against the flow towards their unstressed configuration and the resultant stress is directly proportional to the deformation. This deformation is known to be linear in the Péclet number for very small Péclet numbers. Since the viscosity of a suspension is simply the stress non-dimensionalized by $\eta\dot{\gamma}$, the viscosity scales as the 'deformation'$/Pe$, hence $\eta_r^B \sim O(1)$ as $Pe \to 0$. In order for the Brownian viscosity to remain constant as Pe is increased, the flow-induced deformation must continue to

increase linearly with Pe. However, the Péclet number is also the ratio of the relaxation time due to diffusion a^2/D to the time scale of the flow $1/\dot{\gamma}$, and as the Péclet number increases the particle motion cannot keep up with the flow and the structural deformation saturates. Hence the Brownian viscosity decreases as $Pe \to \infty$. Recent theoretical work (Brady & Morris 1997) predicts the Brownian viscosity to decay as $1/Pe$, which is in fair agreement with the results of the simulations (cf. table 3.2).

The hydrodynamic stress arises because the particles are rigid and do not deform as fluid elements. For the volume fractions studied here, $0.316 \leq \phi \leq 0.49$, the hydrodynamic viscosity varies little between a random and a regular array and is roughly the same for any 'well-dispersed' structure. Although the structure evolves quite significantly at low Péclet numbers (cf. figure 3.20), the suspension remains 'well-dispersed' and the hydrodynamic viscosity is constant. In simple shear flow particles are pushed together along the compressive axis of the flow, while the action of Brownian motion is to keep particles apart and well dispersed. (In fact it is the $\nabla \cdot \boldsymbol{R}_{FU}^{-1}$ term in (3.4)–(3.5) that acts as a repulsive radial force and balances the hydrodynamic squeezing force along the compressive axis (Bossis & Brady 1989).) At high Péclet numbers hydrodynamic forces dominate everywhere except in a thin $O(Pe^{-1})$ boundary layer adjacent to particle surfaces where there is a balance of hydrodynamic and Brownian forces (Brady & Morris 1997). Once the Péclet number exceeds $O(10)$ hydrodynamic forces are capable of pushing two particles close enough together for the strong lubrication forces to come into play; lubrication forces are singular near contact as $1/(r-2a)$, with this singularity being felt when $r - 2a \leq 10^{-2}a$. As the Péclet number is increased, particles are progressively 'stuck' together by the strong lubrication forces and form noncompact aggregates or clusters. As shown in earlier work on monolayers (Bossis & Brady 1989), the cluster size grows as the Péclet number increases. Associated with a growing cluster size is an increase in the contact value of the pair-distribution function reported in table 3.4. The increased contact value is also evident in the sharpening of the first nearest neighbor peak in figure 3.20.

Although the stress is purely hydrodynamic at large Péclet number, this does not

mean that Brownian motion does not play a role. The limit $Pe \to \infty$ is singular and the residual effect of Brownian motion at particle contact limits the ultimate size of the clusters. The relative tangential motion of two particles is resisted by a weak logarithmic dependence on particle separation and the small amount of Brownian motion provides a means for two near touching particles to move relative to one another and break the connectivity of the cluster dramatically affecting the viscosity (Bossis, Meunier & Brady 1991). Previously reported results (Phung *et al.* 1996) in the pure hydrodynamic limit ($Pe^{-1} \equiv 0$) have not been affected by the nondimensionalization error as they include no Brownian motion. These simulations in the pure hydrodynamic limit failed to reach a steady state. A typical run in this regime would proceed in time with the viscosity slowly increasing until suddenly a large cell-spanning cluster would form jamming particles together, sending the viscosity to enormous values, and halting the integration. Reducing the time step allowed only a very small additional advance in time. Increasing the size of the unit cell delayed the onset of the catastrophic shear thickening but did not eliminate it.

The problems with ($Pe^{-1} \equiv 0$) simulations have also been discussed by Ball & Melrose (1995), Melrose & Ball (1995), and Dratler & Schowalter (1996). In fact, a high-Péclet-number asymptote for the viscosity was not obtained for any of the volume fractions studied here. The size of the time step, Δt, for the largest Péclet (10^4) runs for each volume fraction are 2.5×10^{-4} compared to 5×10^{-4} for most of the other runs. This is because $Pe = 10^4$ runs with $\Delta t = 5 \times 10^{-4}$ displayed the same problems with growing clusters, diverging viscosities and halted integration as the aforementioned ($Pe^{-1} \equiv 0$) runs. The most likely explanation for this is that the larger time step is unable to properly resolve the Pe^{-1} boundary layer as the Péclet number gets large. One can see that as $Pe \to \infty$, the time step necessary to capture the proper physics of the boundary layer would have to scale as Pe^{-1}, which becomes an unreasonable constraint numerically and is consistent with the pathological behavior of simulations run in the pure hydrodynamic limit ($Pe^{-1} \equiv 0$). Previous simulations with the erroneous high-Pe evolution equation were able to run at Péclet numbers as high as 10^6 (Phung, *et al.* 1996, Phung 1993). The random steps

in those simulations were too small compared to the deterministic $\nabla \cdot \boldsymbol{R}_{FU}^{-1}$ term. The relative 'enhancement' of the $\nabla \cdot \boldsymbol{R}_{FU}^{-1}$ term in those simulations caused the particles to act as if there were an *additional* radially repulsive force acting between them. The ability of those runs to achieve a steady state at higher Péclet numbers is consistent with the increased robustness of $Pe^{-1} \equiv 0$ simulations with repulsive interparticle forces (Brady & Bossis 1985, Dratler & Schowalter 1996, Yurkovetsky 1998).

This sensitivity to small scale surface interactions and the singular nature of the $Pe \to \infty$ limit have important implications for the interpretation of experimental viscosity measurements at high concentrations and shear rates because seemingly small factors can dramatically influence the results. It may also explain why measurements of viscosity at high concentrations in the pure hydrodynamic limit show a large amount of scatter (an order of magnitude) from one researcher to the next, although the reproducibility for an individual researcher was good (Thomas 1965). It also suggests that if short-range surface effects can be controlled and the Péclet number is made large enough, the clusters should grow to the size of the experimental apparatus and the measured viscosity should depend on the size of the measuring cell.

In figure 3.3 we compare the simulation viscosities with the experiments of van der Werff & de Kruif (1989) on monodisperse spherical silica particles that have been shown to behave to a very good approximation as hard spheres. The simulation and experimental viscosities are in good quantitative agreement considering the strong dependence of the viscosity on volume fraction at high volume fraction and the uncertainty in precisely determining the experimental volume fraction. The experiments do not show shear thickening as their Péclet numbers were too low. Additional experiments by the same group up to $Pe = 1200$ did not display shear thickening. It may be that shear thickening occurs at a slightly higher Péclet number in these systems, possibly due to the fact that the silica particles are coated with short hydrocarbon chains and therefore are weakly repulsive when brought into near contact. However, shear thickening due solely to the growth of clusters as first predicted in the monolayer simulations has been observed experimentally (D'Haene, Mewis & Fuller 1993, Bender & Wagner 1995, 1996).

Figure 3.4 shows the total relative viscosity plotted as a function of Péclet number for all volume fractions studied. More detailed figures showing the separate hydrodynamic and Brownian contributions for each volume fraction can be found in the tables and figures at the end of this chapter; the trends are identical to those shown in figure 3.2 for $\phi = 0.45$. The uncertainty in the viscosities are comparable to those shown in table 3.2 for $\phi = 0.45$. To examine the shear thinning and thickening behavior and to compare with existing theories, it is important to separate out the contribution to the viscosity resulting from the hydrodynamic interactions that are present in the equilibrium configuration — the high-frequency dynamic viscosity $\eta'_\infty/\eta = 1 + \eta^H_r(Pe = 0)$. The remaining viscosity, $\Delta\eta/\eta = \eta_r - \eta'_\infty/\eta$, arises from particle interactions (hydrodynamic and Brownian) in the nonequilibrium structure induced by the flow. Theories have been advanced to predict $\Delta\eta$ as a function of concentration and shear rate which we now discuss.

Let us first examine the shear thickening regime $Pe \geq O(10)$. Brady & Morris (1997) showed that the limit of large Péclet number is singular with an $O(Pe^{-1})$ thin boundary layer at particle-particle contact in which Brownian and hydrodynamic forces balance. Brady & Morris also showed that the hydrodynamic contribution to the stress from this boundary layer, which is the dominant contribution at high Pe, scales as $S^H_{b.l.} \sim \dot{\gamma}\eta'_\infty(\phi)\phi^2 g^\infty(2;\phi)$, where $g^\infty(2;\phi)$ is the pair-distribution function just outside the boundary layer *at* the high Péclet number (∞) and the concentration of interest, and $\eta'_\infty(\phi)$ is the (dimensional) high frequency dynamic viscosity. A simple physical explanation for this scaling is the following.

The stress from the boundary layer is a two-body effect and near contact the hydrodynamic stress can be estimated from the moment of the hydrodynamic shear force

$$\boldsymbol{S}^H_{b.l.} \sim -n^2 \int_{b.l.} \boldsymbol{r}\boldsymbol{F}^{shear} g(\boldsymbol{r}) d\boldsymbol{r}. \tag{3.13}$$

The hydrodynamic shear force scales as $\boldsymbol{F}^{shear} \sim -3\pi\eta'_\infty(\phi)a^2\dot{\gamma} \times \hat{\boldsymbol{r}}(\hat{\boldsymbol{r}}\cdot\hat{\boldsymbol{E}}\cdot\hat{\boldsymbol{r}})$, where $\hat{\boldsymbol{r}}$ is the unit vector along the line of centers of the two particles, and the angle brackets on $\hat{\boldsymbol{E}}$ denoting a suspension average have been dropped. In a concentrated

suspension the shear force is enhanced over that for two particles alone in the fluid in essence because it acts through the suspension, while the resistance to this squeezing force is through the solvent as only solvent can be in the gap between two near touching particles. Stokesian Dynamics simulations at high Pe (Brady & Bossis 1985, Bossis, Brady & Mathis 1988) bear this out and show that the relative velocity of two particles near contact is enhanced in a concentrated suspension and an estimate for the ϕ-dependence of that enhancement is $\eta'_\infty(\phi)$.

Although the boundary-layer thickness is small, $O(Pe^{-1})$, and therefore one might expect that the contribution in (3.13) would be small, along the compressive axes of the flow, $\hat{\boldsymbol{r}}\cdot\hat{\boldsymbol{E}}\cdot\hat{\boldsymbol{r}} < 0$ (cf. figure 3.20), the pair-distribution function within the boundary layer is large, $O(Pe)$. Brady & Morris (1997) show that along the compressive axes $g_{b.l.}(\boldsymbol{r}) \sim Pe\, g^\infty(2;\phi)\bar{g}(\theta,\varphi)$, where $g^\infty(2;\phi)$ is the value of the pair-distribution function just outside the boundary layer, and $\bar{g}(\theta,\varphi)$ is the $O(1)$ angular variation within the boundary layer. Thus, the integral (3.13) for the stress from the boundary layer is

$$\boldsymbol{S}^H_{b.l.} \sim \eta'_\infty(\phi)\dot{\gamma}\phi^2 g^\infty(2;\phi) \int_{\hat{\boldsymbol{r}}\cdot\hat{\boldsymbol{E}}\cdot\hat{\boldsymbol{r}}<0} \hat{\boldsymbol{r}}\hat{\boldsymbol{r}}(\hat{\boldsymbol{r}}\cdot\hat{\boldsymbol{E}}\cdot\hat{\boldsymbol{r}})\bar{g}(\theta,\varphi)d\Omega, \tag{3.14}$$

where $d\Omega$ represents the solid angle and the limits of angular integration are restricted to regimes where $g(\boldsymbol{r}) \sim O(Pe)$, *i.e.*, the compressive axes. For a simple radial-balance approximation, Brady & Morris show that $\bar{g}(\theta,\varphi) = -\hat{\boldsymbol{r}}\cdot\hat{\boldsymbol{E}}\cdot\hat{\boldsymbol{r}}$. The expression for the boundary-layer stress (3.14) is only approximate due to the approximations that have been made for the shear forces, etc. Further, there are other contributions to the hydrodynamic stress from particle interactions outside the boundary layer and along the extensional axes, but we expect these to be no larger and therefore (3.14) to give a reasonable estimate of the hydrodynamic stress over and above the high-frequency dynamic viscosity (which is associated with the disordered structure outside the boundary layer).

In addition to an estimate of the hydrodynamic stress, the analysis of Brady & Morris (1997) also shows that the Péclet number needs to be rescaled in the shear-thickening regime. Since the Péclet number is the ratio of shear forces to Brownian

forces, the rescaled Péclet number is simply $\bar{Pe} = 6\pi\eta'_\infty(\phi)a^3\dot{\gamma}/kT = Pe\,\eta'_\infty(\phi)/\eta$. From figure 3.4 one sees that the higher the concentration, the earlier shear thickening begins, in agreement with this rescaling.

The last item needed is the contact value of the pair-distribution function outside the boundary layer $g^\infty(2;\phi)$. On this the theory of Brady & Morris (1997) is silent. We could use simulation results, but then that would not result in a predictive theory. Instead, we have chosen to use the *equilibrium* pair distribution for hard spheres, $g^0(2;\phi)$, which is a known function of ϕ, for example from the Carnahan-Starling equation of state:

$$g^0(2;\phi) = \frac{1-\frac{1}{2}\phi}{(1-\phi)^3}, \quad \phi < 0.50.$$

This is, of course, not correct, but it should give a reasonable estimate over the range of ϕ investigated here. Near close packing, this would not necessarily be a good estimate as $g^0(2)$ diverges at random close packing $\phi_{rc} \approx 0.63$ (not with the Carnahan-Starling equation, however), while $g^\infty(2)$ may diverge in a different manner and at different maximum concentration.

These arguments suggest that a plot of

$$\frac{\Delta\eta}{\eta'_\infty(\phi)}\frac{1}{\phi^2 g^0(2;\phi)} = \frac{\eta(\phi;\bar{Pe}) - \eta'_\infty(\phi)}{\eta'_\infty(\phi)\phi^2 g^0(2;\phi)}$$

versus $\bar{Pe} = Pe\ \eta'_\infty(\phi)/\eta$ should collapse the shear thickening behavior to a single universal curve for all ϕ. Figure 3.5 shows the data for all shear rates in figure 3.4 replotted according to this scaling estimate. The shear thickening data collapse quite well, showing that $\bar{Pe}$ is the appropriate scale for the shear rate and that the boundary layer scaling with the equilibrium pair-distribution function $g^0(2;\phi)$ collapse the magnitude well.

Figure 3.5 also shows that the viscosity does not approach an assymptote as $Pe \to \infty$. This is shown more clearly in figure 3.6 where only the scaled hydrodynamic viscosity (over and above the high frequency dynamic viscosity) is plotted versus the scaled Péclet number. This behavior confirms the results of Ball & Melrose (1995) and Dratler & Schowalter (1996) that in the pure hydrodynamic limit

($Pe \to \infty$ for hard spheres) a steady shear viscosity does not exist because hydrodynamic clusters form whose size diverges as $Pe \to \infty$. The growth with $\bar{Pe}$ in figure 3.6 is very weak, approximately as $\ln \bar{Pe}$, although caution must be exercised in drawing firm conclusions because the system sizes are small and the periodicity would likely affect the detailed behavior. One would expect, for example, that there would be a critical volume fraction below which infinite clusters would not form and an asymptotic viscosity would exist.

In figure 3.5 we plotted the data for all shear rates according to the high-shear-rate scaling behavior and, while the spread in the shear thinning data is reduced, this scaling does not appear to completely collapse the shear thinning data. At low shear rates it is the Brownian contribution to the stress that is responsible for shear thinning. To obtain an estimate for the shear thinning behavior, we start by rewriting the Brownian contribution to the stress in the equilivalent form

$$n\langle \boldsymbol{S}^B \rangle = -n^2 kTa \int_{r=2a} \hat{\boldsymbol{r}}\hat{\boldsymbol{r}} g(\boldsymbol{r}) dS + nkT\langle \boldsymbol{R}_{SU} \cdot \boldsymbol{R}_{FU}^{-1} \cdot \nabla \ln P_N \rangle, \qquad (3.15)$$

which can be obtained from (3.10c) by introducing the probability density for the N-particle configuration $P_N(\boldsymbol{x}, t)$ and integrating by parts (Brady 1993a). This form for $\langle \boldsymbol{S}^B \rangle$ is particularly convenient in that is separates out the contribution for particles in contact (the first integral), which is of exactly the same form as in atomic or molecular hard spheres, from the remainder which is due to hydrodynamic interactions ($\boldsymbol{R}_{SU}$) among particles.

Here, we focus on the contact integral which has been shown to give a good estimate of the Brownian stress at high densities (Brady 1993b). The low-shear viscosity can be extracted from this integral by using the first perturbation due to flow to the equilibrium structure, $f(\boldsymbol{r})$, defined by $g(\boldsymbol{r}) = g^0(\boldsymbol{r})[1 + f(\boldsymbol{r})]$. The equilibrium stress is just the isotropic osmotic pressure, $-\Pi^0 \boldsymbol{I}$. The first contribution to the viscosity is due to the $O(Pe)$ correction to the microstructure and results in a constant low-Pe Newtonian plateau with viscosity equal to the zero-shear viscosity,

η_0; thus we can write

$$f(\boldsymbol{r}) = \hat{Pe}\hat{f}(\boldsymbol{r}),$$

where $\hat{f}(\boldsymbol{r})$ is independent of the flow strength and $\hat{Pe} = Pe/\hat{D}(\phi)$, where $\hat{D}(\phi)$ is the characteristic diffusivity nondimensionalized by the Stokes-Einstein diffusivity, D. Substituting the expression for $f(\boldsymbol{r})$ into the contact integral in (3.15) gives the following expression for the deviatoric part of the Brownian stress:

$$n\langle \boldsymbol{S}^B \rangle + \Pi^0 \boldsymbol{I} = -\frac{27}{2\pi}\eta\dot{\gamma}\phi^2 \frac{g^0(2;\phi)}{\hat{D}(\phi)} \int \hat{\boldsymbol{r}}\hat{\boldsymbol{r}}\hat{f}(2;\theta,\varphi)d\Omega. \tag{3.16}$$

The characteristic diffusivity is determined by the appropriate relaxation time for rheological response: $a^2/\hat{D}(\phi)D$. With this scaled Péclet number, all of the Pe-dependence of the microstructure at all volume fractions is included in $\hat{Pe}$. In the dilute limit, all particle diffusivities are equal to the diffusivity of an isolated particle, D. Thus, $\hat{D} = 1$ and (3.16) reduces to the the Brownian stress as previously calculated by various two-particle theories (Batchelor 1977, Brady & Vicic 1995, Lionberger 1998, Vicic 1999).

The precise nature of $\hat{D}(\phi)$ is still an open question. Many quantities have been suggested. Brady (1993b) suggests using the equilibrium short-time self-diffusivity, $\hat{D}(\phi) = D_0^s(\phi)/D \approx \eta/\eta'_\infty(\phi)$, as this incorporates the primary effect of the hydrodynamic interactions. The shear thinning collapse from this scaling is the same as the one used above to collapse the shear thickening data in figure 3.5. As noted before, this scaling is effective in reducing the spread in the data, but a sufficient collapse is not obtained. One can see this more clearly when the same scaling is used for only the Brownian contribution to the stress in figure 3.7. Nevertheless, use of the short-time self-diffusivity is successful in removing all of the hydrodynamics, and thus data from suspensions with and without hydrodynamic interactions should be indistinguishable with this scaling (Foss & Brady 1999c (ch. 2)).

Apparently, simply scaling out the hydrodynamics is not sufficient, and there appears to be another contribution to $\hat{D}(\phi)$ from the relaxation of the dynamic microstructure. A simple choice would be to use the equilibrium long-time self-

diffusivity, $\hat{D}(\phi) = D^s_\infty(\phi)/D$. A collapse of the viscosity data using this scaling is shown in figure 3.8. We have used the values of $\hat{D}^s_\infty(\phi)$ obtained from these simulations (cf. §3.3.2). This choice of $\hat{D}(\phi)$ arguably collapses the data somewhat better than figure 3.5, especially at the higher volume fractions. Note that the collapse of the shear thickening data is much worse than before as the arguments presented here concern only the Brownian stress. A plot of the collapse of only the Brownian contribrition to the viscosity is shown in figure 3.9.

Another diffusivity often suggested as a good candidate for $\hat{D}(\phi)$ is the wavelength-dependent collective diffusivity evaluated at the peak of the structure factor, $D^c(k_{max})/D$ (Verberg *et al.* 1997, Pusey *et al.* 1997), as this represents relaxation of the dominant 'cage' structure and is also the slowest rate of structural decay present. No plots of this possible collapse are shown as we have not calculated $D^c(k_{max})/D$ in our simulation.

There may be no simple relationship between $\hat{D}(\phi)$ and a previously known diffusivity. The aforementioned relationship between $\hat{D}(\phi)$ and $D^s_0(\phi)/D$ was first suggested by the experimental data of van der Werff *et al.* (1989). Although, in general, this collapse of our data is unsuccessful, it does appear valid for the lower volume fractions ($\phi \leq 0.40$). Data from experiments by Shikata & Pearson (1994) show that the relationship between $\hat{D}(\phi)$ and $D^s_0(\phi)/D_0$ holds up to $\phi = 0.50$ before it breaks down. They suggest that at higher volume fractions, other relaxation processes, perhaps associated with a glass transition, become increasingly important at high densities. Pusey *et al.* (1997) also note a particularly strong slowing down of the structural relaxation for $\phi > 0.40$.

Normal stress differences

The first and second normal stress differences are defined by

$$N_1 = \langle \Sigma_{xx} \rangle - \langle \Sigma_{yy} \rangle, \tag{3.17a}$$

$$N_2 = \langle \Sigma_{yy} \rangle - \langle \Sigma_{zz} \rangle, \tag{3.17b}$$

and the individual Brownian and hydrodynamic contributions for $\phi = 0.45$ are shown in figures 3.10 and 3.11. Uncertainties for the normal stress differences are given in table 3.3. Tables and figures for the other volume fractions are available at the end of the chapter. Note that the hydrodynamic contributions are negative for all Pe while the Brownian contribution is positive for N_1 and negative for N_2.

Flow-reversal symmetry requires that both normal stress differences vanish as $Pe \to 0$. At low Péclet numbers, the normal stress differences are dominated by the Brownian contributions resulting in a positive N_1 and a negative N_2 (Brady & Vicic 1995). The quality of the data at low Pe in figures 3.10 and 3.11 is quite poor and one cannot discern a trend towards zero for small Pe. It appears that the Brownian noise at low Péclet numbers that makes low-shear viscosities difficult to measure both in simulation and by experiment may be even worse for measuring normal stress differences. The normal stress differences show much greater fluctuation from one time step to the next requiring very long runs and perhaps large systems to obtain meaningful averages. The signs of each of the normal stress differences, however, are discernable and correct.

The sign of the Brownian contribution to each normal stress difference can be ascertained by examining the microstructure and how it affects the integrand, $-\hat{\boldsymbol{r}}\hat{\boldsymbol{r}}g(\boldsymbol{r})$, of the contact integral for the Brownian stress in (3.15). Figure 3.12 shows two projections of the radial distribution function, $g(\boldsymbol{r})$ into the xy-plane. The projections are divided into eight sections, each labelled with a plus or a minus. The signs correspond to the effect that a particle in that region would have on the normal stress differences given that the stress tensor is proportional to $-\hat{\boldsymbol{r}}\hat{\boldsymbol{r}}g(\boldsymbol{r})$. For determining the sign of the second normal stress difference, the microstructure is assumed to be axisymmetric outside the plane of shear as is seen below to be the case (cf. figure 3.21). The projections in figure 3.12 show that in addition to the buildup of particle probability in the compressional zone, some of the this probability has been convected downstream into the neighboring extensional zone creating an asymmetry about the compressional axis. From the relative magnitudes of the probabilities in the eight labelled sections of each projection, one can see that N_1^B is positive and

N_2^B is negative due to the deficit of particle pairs along the extensional axis where Brownian motion pushes particles apart and hydrodynamic shear forces pull them apart. Physically, N_1^B is positive because Brownian motion acts like a repulsive force between two particles and pushes them apart along the compressive and extensional axes, which would then push apart the plates of a rheometer.

As the Péclet number increases from zero, the deformation, and thus the Brownian contribution to the normal stress differences, also increases. A maximum is reached near $Pe \approx 1$ as the deformation cannot keep up with the flow and the Brownian contributions decay at high Péclet numbers like $1/Pe$ (Brady & Morris 1997) while the hydrodynamic contributions take over.

The signs of the hydrodynamic normal stress differences can also be explained by examining the suspension microstructure. At high Péclet number, the hydrodynamic stress is dominated by the boundary layer and the normal stress differences can be determined from (3.14) and thus the relevant tensor to examine is $\hat{\boldsymbol{r}}\hat{\boldsymbol{r}}(\hat{\boldsymbol{r}}\cdot\hat{\boldsymbol{E}}\cdot\hat{\boldsymbol{r}})g(\boldsymbol{r})$. Projections of the pair-distribution function into the shear plane, similar to those used to explain the signs of the Brownian contribution, are shown in figure 3.13. Again, the projections are divided into eight sections, but this time with signs corresponding to the contribution to the normal stress differences given by the stress tensor that is proportional to $\hat{\boldsymbol{r}}\hat{\boldsymbol{r}}(\hat{\boldsymbol{r}}\cdot\hat{\boldsymbol{E}}\cdot\hat{\boldsymbol{r}})$. Examining the relative magnitudes of the probabilities in the eight labelled secitoned shows that both N_1^H and N_2^H are negative. As is the case at low Péclet numbers, the contribution from the first and second quadrant spanning the compressional axes essentially cancel, leaving the dominant contribution from the third quadrant above the extensional axes. Here, the hydrodynamic stress is negative because the flow must pull apart the closely spaced particles stuck together by the lubrication forces. This pulling apart would in turn pull together the plates of a rheometer and hence give a negative first normal stress difference. The hydrodynamic contribution to the normal stress differences is much smaller than the Brownian at low Pe and increases in magnitude as the Péclet number is increased, resulting in a sign change of N_1 for Pe near 10.

In the pure hydrodynamic limit ($Pe^{-1} \equiv 0$) the normal stress differences are ex-

pected to vanish because of symmetry requirements. However, the singular boundary-layer behavior as $Pe \to \infty$ results in an asymmetric pair-distribution function at contact, clearly seen in figure 3.20 for $Pe = 10^3$, and normal stress differences that approach an $O(\eta\dot{\gamma})$ assymptote at very high Péclet numbers. Brady & Morris (1997) show that for perfect hard spheres without interparticle forces, the asymmetry vanishes as $Pe^{-0.22}$ as $Pe \to \infty$. Again, hard spheres in the limit of pure hydrodymamics are singular. If a repulsive force is added, no matter how short-ranged, the asymmetry will not vanish as $Pe \to \infty$ resulting in finite normal stress differences. As discussed earlier, it is numerically difficult to resolve the boundary layer at very high Péclet numbers and this difficulty may result in the particles behaving as if there was an interparticle force present and explain why the normal stress differences obtained from simulation do not vanish at high Péclet numbers. Experimentally, perfect hard spheres are difficult to achieve, and one should expect finite normal stress differences. Unfortunately, no experimental data is available for normal stress differences on model hard-sphere suspensions (or non-hard-sphere suspensions for that matter).

At high Péclet numbers the theory of Brady & Morris (1997) used to collapse the shear thickening viscosity can also be used to collapse the first and second normal stress differences. Figures 3.14 and 3.15 show N_1 and N_2 scaled with $\eta'_\infty(\phi)\dot{\gamma}\phi^2 g^0(2;\phi)$ as a function of the scaled Péclet number $\bar{Pe} = Pe\ \eta'_\infty(\phi)/\eta$. The data for all concentration collapse reasonably well onto a single curve. The scaling theory with $\hat{D}(\phi)$ could also be used to scale the normal stress differences at low Péclet nubmer, but the quality of the simulation data is too poor to draw any conclusions from the comparison.

The particle contribution to the stress defined in (3.9) is not traceless and the hydrodynamic functions necessary to compute the trace — the shear-rate dependent osmotic pressure — were determined in Jeffrey, Morris & Brady (1993) and have been used in recent non-Brownian simulations (Yurkovetsky 1998). The extension to Brownian simulations has not yet been made and remains a goal for future work.

3.3.2 Diffusion

In figures 3.16 and 3.17 we show the average translational and rotational mobilities of a particle, D_0^s and D_0^r, respectively, as a function of Pe. At $Pe \equiv 0$ these instantaneous mobilities (multiplied by kT) correspond to the short-time self-diffusion coefficients. The mobilities have been normalized by the infinite dilution self-diffusion coefficients $kT/6\pi\eta a$ and $kT/8\pi\eta a^3$, respectively, and are averages of the separate xx-, yy- and zz-components. The individual rotational mobilities are all identical to within the statistical uncertainty, while the yy- and zz-components of the translation mobility are identical and the xx-component is perhaps 10% larger. The local mobility is to a very good approximation isotropic despite the structure formed during flow. The most important feature to note is that the mobilities remain roughly constant until the suspension starts to shear thicken, after which they decrease monotonically with increasing Pe. This decrease is a manifestation of the closely touching particle clusters that form hindering the local motion of a particle.

The long-time mean-square displacement of a Brownian particle is convectively enhanced by the flow. For a simple shear flow the mean-square displacement is expected to grow in time according to (Elrick 1962, Morris & Brady 1996)

$$\langle x^2(t)\rangle = 2D_{xx}t + 2D_{yy}t[1 + \tfrac{1}{3}(Pe\ t)^2], \tag{3.18a}$$

$$\langle y^2(t)\rangle = 2D_{yy}t, \tag{3.18b}$$

$$\langle z^2(t)\rangle = 2D_{zz}t, \tag{3.18c}$$

$$\langle x(t)y(t)\rangle = 2D_{xy}t + D_{yy}t(Pe\ t), \tag{3.18d}$$

as $t \to \infty$. Because the x-displacement is dominated by the convective dispersion growing as t^3, it not possible to determine the D_{xx} and D_{xy} coefficients by simply monitoring the displacements. An alternate method that removes the convectively-enhanced dispersion and leaves the underlying diffusive motion is to subtract off the contributions to the particle motion in (3.4)–(3.5) due to the affine flow, $\Delta\boldsymbol{x}^a = \langle\boldsymbol{U}\rangle\Delta t$, when calculating the mean-square displacements, which leads to the following

temporal behavior

$$\langle (\boldsymbol{x} - \boldsymbol{x}^a)(\boldsymbol{x} - \boldsymbol{x}^a) \rangle = 2\boldsymbol{D}^s_\infty t, \tag{3.19}$$

as $t \to \infty$. All elements of the long-time self-diffusivity tensor, $\boldsymbol{D}^s_\infty$, can be calculated directly using this method. Apart from the xy-component, the other off-diagonal components of $\boldsymbol{D}^s_\infty$ were examined and found to be negligible. This method has been particularly useful in calculating the diffusivities in planar extensional flow (Sami 1996) where the affine flow has components in both the x- and y- directions which lead to exponential rather than algebraic growth of the convectively enhanced terms.

We present results from steady-shear simulations of this work by examining the particle mean-square displacements for the small system at long times. Analysis done here at quite long times (between 10 and 20 dimensionless time units) would seem to be appropriate due to the infinite time limit in the definition of the long-time diffusivity (3.7), however, the mean-square displacements are time-correlation functions that relate particle positions from one time to another. Such correlation functions are quite difficult to accurately measure at long times due to the growth of statistical noise with time. In a related work (Foss & Brady 1999a (ch. 5)) we use a different method that focuses on the behavior of the mean-square displacements during many short simulations, but still long enough to have attained the long-time assymptote which we believe produces more accurate and consistent data. We include the long-time analysis in this work despite the increased noise in the data because it is at *long* times and serves as a good comparison with our other work. The statistical error on the long-time self-diffusivities is about 30%. For a more detailed discussion of the long-time self-diffusivity in flow, see Foss & Brady (1999a) (ch. 5).

The Péclet-number dependence for $\phi = 0.45$ of the $xx-$, $yy-$, $zz-$components of $\boldsymbol{D}^s_\infty$ normalized by the diffusion coefficient of an isolated particle is shown in figure 3.18. Data for the other volume fractions can be found in tables and figures at the end of this chapter. As $Pe \to 0$ the diffusivities approach the long-time self-diffusivities of equilibrium dispersions and agree well with the experimental measurements of van Megen *et al.* (1986); a comparison of these data with experiment can be

found in Brady (1994). The action of the flow is to enhance the self-diffusivity, with the leading correction scaling as $Pe^{3/2}$ (Morris & Brady 1996). As the Péclet number increases, the self-diffusivities continue to increase without the 'dip' at intermediate Péclet numbers that was present in the previous work (Phung *et al* 1996). The 'dip' was evidence of the formation of an ordered phase in this region of Péclet number causing the diffusivities to plunge. The monotonically increasing behavior of the diffusivites is an indication that no ordered phase is present in the current simulations (cf. figure 3.20). As $Pe \to \infty$, the results show that the normalized self-diffusivities grow approximately linearly with Pe, or in dimensional terms $D_{yy} \sim \dot{\gamma} a^2$, corresponding to hydrodynamic diffusion. The simulation results for the shear-induced or hydrodynamic diffusivities show quite a bit of scatter, but are in reasonable agreement (within a factor of 2; see Foss & Brady 1999a) (ch. 5) with the experiments of Eckstein *et al.* (1977), Leighton & Acrivos (1987) and Phan & Leighton (1993). Again, the singular effect of Brownian motion is important in leading to diffusive behavior as $Pe \to \infty$. A pure hydrodynamic system is completely deterministic and, although the evolution equations for particle positions are highly nonlinear and give rise to deterministic chaos, the small amount of Brownian motion (or surface roughness or interparticle forces) provides the necessary irreversibility for the chaos to set in. We were not able to determine long-time self-diffusivities from the simulations with $N > 27$ as the runs were not long enough to reach the asymptotic temporal behavior; thus, we do not know the effect of the size of the simulation cell on the diffusivities. The values obtained here are in agreement with the monolayer results of Bossis & Brady (1987) when allowance is made for converting area fraction to volume fraction.

The enhancement of the long-time self-diffusivity by flow is indicative of a completely new mechanism for creating diffusive motion in sheared suspensions. Direct particle-particle 'collisions' induced by the shearing motion are responsible for the random walk. The action of this new mechanism is seen in figure 3.19 where the long-time self-diffusivities in the zz-direction at $Pe = 0.01$ and $Pe = 1000$ are shown as a function of the volume fraction. At low Péclet numbers the long-time diffusivity decreases with increasing concentration, while at high Péclet number it increases with

increasing ϕ. At low Pe particle interactions hinder the motion of a tagged particle, while at high Pe they help. At intermediate Péclet numbers one should therefore find the long-time diffusivities to be independent of ϕ. Unfortunately, experimental data are only available at zero and infinite Pe.

3.3.3 Structure

An analysis of the microstructure shows that no ordered phase is present for the full range of Pe and volume fractions studied $0.316 \leq \phi \leq 0.49$. Figure 3.20 shows the projection of the pair-distribution function into the plane of shear for $\phi = 0.45$. Near equilibrium, the flow provides a weak perturbation to the equilibrium behavior. The hint of an eight-fold symmetry seen in figures 3.20 and 3.21 at small Pe is due to the small size of the simulation cell. This structure is completely absent for larger systems as seen in figure 3.22. As the Péclet number increases, the first nearest-neighbor peak at contact becomes intensified along the compressive axes of the flow and becomes less intense along the extensional axes. Physically, particles are being convected together along the compressive axis (the upstream side), come into near contact, rotate together as a doublet, and then depart on the downstream side where Brownian motion and the shearing flow act together to separate the particles. The intensification and sharpening of the nearest-neighbor peak as the Péclet number increases is further qualitative evidence of the $O(Pe^{-1})$ boundary layer discussed by Brady & Morris (1997).

It is important to note that in contrast to the earlier work (Phung & Brady 1992, Phung 1993, Phung *et al* 1996), no ordered structure is obtained using the correct high-Pe evolution equation (3.5). Figure 3.21 shows the projection of the pair-distribution function in the velocity-gradient–vorticity plane and no hexagonal pattern typical of flow-induced string-ordering is evident. Analysis of larger systems ($N = 123$) has also failed to show any order (see figure 3.22). The ordering in the earlier work can be directly attributed to the $\nabla \cdot \boldsymbol{R}_{FU}^{-1}$ term in the evolution equation which acts like a radially repulsive Brownian force (Bossis & Brady 1987).

In the earlier work, this term is 'enhanced' by a factor of $Pe^{1/2}$ in comparison to the other Brownian displacement term providing an additional repulsion between particles. This repulsion prevents the the particles from getting close enough for the singular hydrodynamic lubrication forces to come into play. These close-ranged forces cause particles to form temporary doublets that rotate in shear flow and disrupt any order that may form. A simulation performed with a pairwise-additive short-range repulsive DLVO-type interparticle force also removes the lubrication forces and enables the suspension to order (see figure 3.23). The form for the DLVO-type force is for two constant-charge spheres immersed in an ionic solvent (Russel *et al.* 1989), which is the same form used in previous Stokesian Dynamics simulations (Bossis & Brady 1984, Yurkovetsky 1998), and is given by

$$\boldsymbol{F}^P = -|\boldsymbol{F}^P| \frac{e^{-\tau h}}{1 - e^{-\tau h}} \hat{\boldsymbol{r}},$$

where, $\hat{\boldsymbol{r}}$ is the unit vector along the line of centers of a pair of particles, $h = (r - 2a)/a$ is nondimensional particle separation, and $\tau = \kappa a$ is the nondimensional inverse Debye length (κ^{-1} is the Debye length). For this particular run, we use $|\boldsymbol{F}^P| = 200kT/a$, and $\tau = 100$.

Flow-induced ordering is commonly seen experimentally in electrostatically-stabilized dispersions (Ackerson 1990, Laun *et al.* 1992, Chen *et al.* 1994) which utilize DLVO-type repulsive forces between the particles to prevent flocculation. Evidently, these repulsive forces are sufficiently long-ranged and strong enough to exclude the lubrication forces and allow the string-ordered phase to form in certain ranges of shear rate. Our first paper on Stokesian Dynamics (Bossis & Brady 1984) showed order for a suspension of non-Brownian particles interacting through hydrodynamic and repulsive colloidal forces. Non-equilibrium molecular dynamics simulations have also exhibited string formation (Erpenbeck 1984, Hess 1985, Heyes 1986), as have Brownian Dynamics simulations (Heyes 1988; Xue & Grest 1990, Rastogi 1995, Foss & Brady 1999c (ch. 2)) where all hydrodynamic interactions are neglected, *i.e.*, setting $\boldsymbol{R}_{FU} = \boldsymbol{I}$, and $\boldsymbol{R}_{FE} = \boldsymbol{R}_{SU} = \boldsymbol{R}_{SE} = 0$ in (3.2)–(3.10c). What the above examples

all have in common is the absence of short-ranged lubrication forces that tend to disrupt any order that may form. Interestingly, sterically stabilized colloidal dispersions in which short polymer chains are grafted onto particle surfaces have not been observed to string order. Evidently, the steric layers do not prevent the lubrication interactions.

There has been no evidence of any effect of system size for the simulations performed for $\phi < 0.49$. At $\phi = 0.49$ and $Pe = 100$, some order was found for $N = 27$, while a simulation with $N = 63$ shows no order (see figure 3.24); no noticeable change is the viscosities was observed however. These finite-size effects become increasingly important as the volume fraction is increased. $N = 27$ simulations for $\phi > 0.49$ have shown a strong tendency to order over the full range of Péclet numbers despite the lack of order in the limited number of runs we have been able to perform for larger systems where $N = 123$ and, unlike the case above, the effect of the order on the viscosities was quite significant. Clearly, larger runs must be used to examine the rheological behavior for these very dense suspensions.

The absence of string ordering for non-repulsive systems makes a strong argument about the connection between shear thinning/thickening and flow-induced ordering. It has often been stated that shear thinning is caused by the formation of an ordered phase causing the suspension to flow more easily. Similarly, the onset of shear thickening has often been connected with the melting of this order. Since no order has been observed here, there is no necessary relationship between flow-induced order and shear thinning/thickening.

3.4 Conclusions

In this paper we have investigated the nonequilibrium behavior of concentrated colloidal dispersions of hard spheres in simple shear flow by Stokesian Dynamics simulation. The suspension is governed by the competition between Brownian and hydrodynamic forces as measured by the Péclet number. At low Péclet number the perturbation to the equilibrium structure is small, but the suspension shear thins

dramatically. This shear thinning results from the decrease of the direct Brownian contribution to the stress as the structural deformation cannot keep up with the shear flow. The hydrodynamic contribution to the viscosity remains constant and equal to the high frequency dynamic viscosity throughout the shear thinning process.

At high Péclet numbers ($Pe > 10$), the effects of Brownian motion give way to hydrodynamic forces which result in a thin boundary layer of high particle probability near contact whose thickness scales as $O(Pe^{-1})$ where hydrodynamic and Brownian forces balance (as shown by Brady & Morris 1997). More particle pairs near contact increase the effects of lubrication forces causing the viscosity to increase. As the Péclet number is increased, the boundary layer becomes thinner and the probability density in the boundary layer increases, further enhancing the effects of lubrication, and the suspension shear thickens.

In the infinite-Péclet-number limit a suspension of perfect hard spheres appears to be singular in that a small amount of Brownian motion or interparticle forces has a dramatic effect on structure and properties. The thin $O(Pe^{-1})$ boundary layer leads to an asymmetry in the pair-distribution function and a loss of flow reversal symmetry. This asymmetry produces $O(\eta\dot{\gamma})$ hydrodynamic normal stress differences and $O(\dot{\gamma}a^2)$ shear-induced particle diffusivities in the infinite Pe limit.

No flow-induced ordering was observed over the range of volume fractions studied here ($0.316 \leq \phi \leq 0.49$) due to actions of close-ranged lubrication forces. Systems with repulsive forces are known to exhibit this type of ordering due to the exclusion of hydrodynamic lubrication. Otherwise, analogous behavior in terms of shear thinning and thickening formartion has been seen in colloidal dispersions with repulsive forces. Indeed, one can often scale the behavior of repulsive systems by using an equivalent volume fraction that incorporates the short-range repulsion into an effective particle radius (Ackerson 1990, Brady 1993b). Long-range repulsive forces are somewhat different in that hydrodynamic interactions are minimized or absent, which results in a different scaling for the dependence of the viscosity on concentration (Brady 1993b), but the shear thinning and ordering phenomena are still present.

Although the results we have presented here are for small systems sizes, the vis-

cosities appear to agree quantitatively with experiment. There are no measurements of normal stresses or diffusivities, however. The results give confidence that Stokesian Dynamics can be used to quantitatively study the behavior of colloidal dispersions over a wide range of conditions.

The highest volume fraction studied in this work is $\phi = 0.49$. It is well known that monodisperse hard-spheres undergo an equilibrium phase transition at $\phi \approx 0.494$ to a crystalline structure. Suspensions above this transition exhibit shear-induced melting upon inception of a simple shear flow. It is possible that hard-sphere suspensions at these large densities may also exhibit a string-ordered microstructure at high shear rates. Simulations of such dense suspensions require larger system sizes than are currently practical using conventional Stokesian Dynamics. As simulation algorithms improve and hardware computational speed increases, we look forward to studying the behavior of very dense colloidal dispersions.

Acknowledgments

This work would not have been possible without the assistance of Thanh N. Phung who wrote the Stokesian Dynamics codes. The work was supported in part by grants CTS-9020646, CTS-9420415, and INT-9415673 from the National Science Foundation.

References

Ackerson, B.J. 1990 Shear induced order and shear processing of model hard sphere suspensions *J. Rheol.* **34**, 553.

Ball, R.C. & Melrose, J.R. 1995 Lubrication breakdown in hydrodynamic simulations of concentrated colloids. *Adv. Colloid Interface Sci.* **59** 19.

Batchelor, G.K. 1977 The effect of Brownian motion on the bulk stress in a suspension of spherical particles. *J. Fluid Mech.* **83**, 97.

Bender, J.W. & Wagner, N.J. 1995 Optical measurement of the contribution of col-

loidal forces to the rheology of concentrated suspensions *J. Colloid Interface Sci.* **172**, 171.

Bender, J.W. & Wagner, N.J. 1996 Reversible shear thickening in monodisperse and bidisperse colloidal dispersions *J. Rheol.* **40**, 899.

Bossis, G. & Brady, J.F. 1984 Dynamic simulation of sheared suspensions. I. General method. *J. Chem. Phys.* **80**, 5141.

Bossis, G. & Brady, J.F. 1987 Self-diffusion of Brownian particles in concentrated suspensions under shear. *J. Chem. Phys.* **87**, 5437.

Bossis, G. & Brady, J.F. 1989 The rheology of Brownian suspensions. *J. Chem. Phys.* **91**, 1866.

Bossis, G. Brady, J.F. & Mathis, C. 1988 Shear-induced structure in colloidal suspensions I: Numerical simulation *J. Colloid Interface Sci.***126**, 1.

Bossis, G., Meunier, A. & Brady, J.F. 1991 Hydrodynamic stress of fractal aggregates of spheres. *J. Chem. Phys.* **94**, 5064.

Brady, J.F. & Bossis, G. 1985 The rheology of concentrated suspensions of spheres in simple shear flow by numerical simulation. *J. Fluid Mech.* **155**, 105.

Brady, J.F. & Bossis, G. 1988 Stokesian dynamics. *Ann. Rev. Fluid Mech.* **20**, 111.

Brady, J.F. 1993a Brownian motion, hydrodynamics, and the osmotic pressure. *J. Chem. Phys.* **98**, 3335.

Brady, J.F. 1993b The rheological behavior of concentrated colloidal dispersions. *J. Chem. Phys.* **99**, 567.

Brady, J.F. 1994 The long-time self-diffusivity in concentrated colloidal dispersions. *J. Fluid Mech.* **272**, 109.

Brady, J.F., Lester, J., Phillips, R. & Bossis, G. 1988 Dynamic simulation of hydrodynamically interacting suspensions. *J. Fluid Mech.* **195**, 257.

Brady, J.F. & Morris, J.F. 1997 Microstructure of strongly-sheared suspensions and its impact on rheology and diffusion. *J. Fluid Mech.* **348**, 103.

Brady, J.F. & Vicic, M. 1995 Normal stresses in colloidal dispersions. *J. Rheol.* **39**, 545.

Chen, L.B., Ackerson, B.J. & Zukoski, C.F. 1994 Rheological consequences of microstructural transitions in colloidal crystals. *J. Rheol.* **38**, 193.

D'Haene, P., Mewis, J. & Fuller, G.G. 1993 Scattering dichroism measurements of flow-induced structure of a shear thickening suspension. *J.Colloid Interface Sci.* **156**, 350.

Dratler, D.I. & Schowalter, W.R. 1996 Dynamic Simulation of suspensions of non-Brownian hard spheres. *J. Fluid Mech.* **325**, 53.

Durlofsky, L.J., Brady, J.F. & Bossis, G. 1995 Dynamic simulation of hydrodynamically interacting particles. *J. Fluid. Mech.* **180**, 21.

Eckstein, E.C., Bailey, D.G. & Shapiro, A.H. 1977 Self-diffusion in shear flow of a suspensions. *J. Fluid Mech.* **79**, 191.

Elrick, D.E. 1962 Source functions for diffusion in uniform shear flow. *Aust. J. Phys.* **15**, 283.

Erpenbeck, J.J. 1984 Shear viscosity of the hard-sphere fluid via nonequilibrium molecular dynamics. *Phys. Rev. Lett.* **52**, 1333.

Foss, D.R. & Brady, J.F. 1999a Self-diffusion in sheared suspensions by dynamic simulation. *J. Fluid Mech.* (submitted).

Foss, D.R. & Brady, J.F. 1999b Stress relaxation in colloidal dispersions. *J. Rheol.* (submitted).

Foss, D.R. & Brady, J.F. 1999c Brownian Dynamics simulation of hard-sphere colloidal dispersions. (unpublished).

Hess, S. 1985 Shear-induced melting and reentrant positional ordering in a system of spherical particles. *Int. J. Thermophys.* **6**, 657.

Heyes, D.M. 1986 Some physical consequences of large shear rates on simple fluids. *J. Chem. Phys.* **85**, 997.

Heyes, D.M. 1988 Shear thinning of dense suspensions modeled by Brownian dynamics. *Phys. Lett.* **132**, 399.

Jeffrey, D.J., Morris, J.F. & Brady, J.F. 1993 The pressure moments for two rigid spheres in low-Reynolds-number flow. *Phys. Fluids A* **5**, 2317.

Kruif, C.G. de, van Iersel, E.M.F., Vrij, A. & Russel, W.B. 1985 Hard sphere colloidal dispersion: viscosity as a function of shear rate and volume fraction. *J. Chem. Phys.* **83**, 4717.

Laun, H.M., Bung, R., Hess, S., Loose, W., Hess, O., Hahn, K., Hädicke, E., Hingmann, R., Schmidt, F. & Linder, P. 1992 Rheological and small angle neutron scattering investigation of shear-induced particle structures of concentrated polymer dispersions submitted to plane Poiseuille and Couette flow. *J. Rheol.* **36**, 743.

Leighton, D. & Acrivos, A. 1987 Measurement of self-diffusion in concentrated suspensions of spheres. *J. Fluid Mech.* **177**, 109.

Lionberger, R.A. 1998 Shear thinning of colloidal dispersions. *J. Rheol.* **42**, 843.

Mackay, M.E. & Kaffashi, B. 1995 Stress jumps of colloidal suspensions, measurements of the elastic-like and viscous-like stress components. *J. Colloid Interface Sci.* **174**, 117.

Megen, W. van, Underwood, S.M. & Snook, I. 1986 Tracer diffusion in concentrated colloidal dispersions. *J. Chem. Phys.* **85**, 4065.

Melrose, J.R. & Ball, R.C. 1995 The pathological behavior of sheared hard spheres with hydrodynamic interactions. *Europhys. Letters* **32** 535.

Morris, J.F. & Brady, J.F. 1996 Self diffusion in sheared suspensions. *J. Fluid Mech.* **312**, 223.

Nägele, G. & Bergenholtz, J. 1998 Linear viscoelasticity of colloidal mixtures. *J. Chem. Phys.* **108**, 9893.

Phan, S. E. & Leighton, D. L. 1993 Measurement of the shear-induced tracer diffusivity in concentrated suspensions. *J. Fluid Mech.* (submitted).

Phung, T.N. 1993 *Behavior of Concentrated Colloidal Suspensions by Stokesian Dynamics Simulation.* Ph.D. Thesis, California Institute of Technology.

Phung, T.N. & Brady, J.F. 1992 Microstructured fluids: structure, diffusion and rheology of colloidal dispersions. In *Slow Dynamics in Condensed Matter* (ed. Kawasaki, Tokuyama and Kawakatsu). AIP Conference Proc. 256, *Am. Inst. of Phys.* New York. 391.

Phung, T.N., Brady, J.F. & Bossis, G. 1996 Stokesian Dynamics simulations of Brownian suspensions. *J. Fluid Mech.* **313**, 181.

Pusey, P.N., Segrè, P.N., Behrend, O.P., Meeker, S.P. & Poon, W.C.K. 1997 Dynamics of concentrated colloidal suspensions *Physica A* **235**, 1.

Rastogi, S.R. 1995 *Nonequilibrium Brownian Dynamics of Colloidal Suspensions.* Ph.D. Thesis, University of Delaware.

Russel, W.B., Saville, D.A. & Schowalter, W.R. 1989 *Colloidal Dispersions* Cambridge University Press.

Sami, S. 1996 *Stokesian Dynamics simulations of Brownian suspensions in extensional flow.* M.S. Thesis, California Institute of Technology.

Segrè, P.H., Meeker, S.P., Pusey, P.N. & Poon, W.C.K. 1995 Viscosity and structural relaxation in suspensions of hard-sphere colloids. *Phys. Rev. Lett.* **75**, 958.

Thomas, D.G. 1965 Transport characteristics of suspensions. VIII. A note on the viscosity of Newtonian suspensions of uniform spherical particles. *J. Colloid Interface Sci.* **20**, 267.

Verberg, R., de Schepper, I.M. & Cohen, E.G.D. 1997 Viscosity of colloidal suspensions *Phys. Rev. E* **55**, 3143.

Vicic M. 1999 *Rheology and Microstructure of Complex Fluids: Dispersions, Emulsions and Polymer Solutions.* Ph.D. Thesis, California Institute of Technology.

Werff, J.C. van der & de Kruif, C.G. 1989 Hard-sphere colloidal dispersions: the scaling of rheological properties with particle size, volume fraction, and shear rate. *J. Rheol.* **33**, 421.

Werff, J.C. van der, de Kruif, C.G., Blom, C. and Mellema , J. 1989 Linear viscoelastic behavior of dense hard-sphere dispersions. *Phys. Rev. A* **39**, 67.

Xue, W. & Grest, G.S. 1990 Shear-induced alignment of colloidal particles in the presence of a shear flow. *Phys. Rev. Lett.* **64**, 419.

Yurkovetsky, Y. 1998 *I. Statistical Mechanics of Bubbly Liquids. II. Behavior of Sheared Suspensions of Non-Brownian Particles.* Ph.D. Thesis, California Institute of Technology.

ϕ	η_0^B	η'_∞	η_0
0.20	0.14	1.81	1.95
0.316	0.68	2.87	3.55
0.37	2.0	3.66	5.7
0.40	2.8	4.28	7.1
0.419	4.8	4.78	9.6
0.45	9.5	5.61	15.1
0.47	18.8	6.19	24.0
0.49	24.2	7.05	31.3

Table 3.1: Data for zero-shear viscoity, η_0, and its different contributions as a function of ϕ from Stokesian Dynamics, $N = 27$. The Brownian contribution, η_0^B, is calculation from a Green-Kubo formula involving time-integration of the shear-stress autocorrelation function, Eq. (3.12). The hydrodynamic contribution is the high frequency dynamic viscosity, η'_∞, and is determined by calculating $1+\eta^H$ in the $Pe \to 0$ limit. All viscosities are nondimensionalized by the solvent viscosity, η.

Pe	N	Δt	$NSTEPS$	η_r^H	η_r^B
0.01*	27	5×10^{-4}	1 000 000	4.61 ± 0.01	9.0 ± 9.1
0.10	27	5×10^{-4}	1 000 000	4.54 ± 0.05	7.00 ± 1.11
0.30	27	5×10^{-4}	200 000	4.60 ± 0.16	5.79 ± 0.69
1.00	27	5×10^{-4}	200 000	4.78 ± 0.13	3.70 ± 0.27
3.00	27	5×10^{-4}	200 000	4.91 ± 0.29	2.00 ± 0.27
5.00	27	5×10^{-4}	200 000	5.07 ± 0.27	1.46 ± 0.21
7.00	27	5×10^{-4}	200 000	5.28 ± 0.18	1.23 ± 0.07
10.00	27	5×10^{-4}	200 000	5.59 ± 0.47	1.07 ± 0.21
20.00	27	5×10^{-4}	200 000	6.30 ± 0.30	0.76 ± 0.09
10^2	27	5×10^{-4}	200 000	7.56 ± 0.41	0.22 ± 0.03
2×10^2	27	5×10^{-4}	200 000	8.02 ± 0.28	0.12 ± 0.01
10^3	27	5×10^{-4}	200 000	9.25 ± 0.59	0.029 ± 0.004
10^4	27	2.5×10^{-4}	400 000	11.64 ± 1.11	0.004 ± 0.001
0.01*	63	5×10^{-4}	80 000	4.42 ± 0.01	10.2 ± 8.2
0.43*	63	10^{-3}	40 000	4.78 ± 0.02	6.48 ± 0.13
10.0	63	5×10^{-4}	200 000	5.77 ± 0.21	1.10 ± 0.10
10^3	63	5×10^{-4}	200 000	8.87 ± 0.18	0.026 ± 0.001
0.43*	123	5×10^{-4}	80 000	4.65	5.454
10.0	123	10^{-3}	60 000	5.696	1.094
10^3	123	10^{-3}	50 000	8.954	0.028

Table 3.2: Simulations data with $\phi = 0.45$. Column (1) is the Peclet number and column (2) is the number of particles. Columns (3) and (4) are the time step and the total number of time steps. Columns (5) and (6) give the Brownian and hydrodynamic contributions to the shear viscosity (normalized by the solvent viscosity). Initial particle configurations of all the runs are random. The error estimates were determined by dividing a simulation run up into statistically independent subintervals (5 - 10) and comparing the averages for each interval (see Phung 1993). *Data obtained from Phung (1993).

Pe	N	Δt	$NSTEPS$	$N_1/\eta\dot{\gamma}$	$N_2/\eta\dot{\gamma}$
0.01*	27	5×10^{-4}	1 000 000	20.7 ± 14.9	-10.43 ± 5.10
0.10	27	5×10^{-4}	1 000 000	4.13 ± 3.08	-3.07 ± 2.94
0.30	27	5×10^{-4}	200 000	5.01 ± 2.72	-3.41 ± 2.59
1.00	27	5×10^{-4}	200 000	0.95 ± 0.57	-2.12 ± 1.11
3.00	27	5×10^{-4}	200 000	-0.45 ± 0.17	-1.21 ± 0.77
5.00	27	5×10^{-4}	200 000	-0.65 ± 0.57	-1.13 ± 0.33
7.00	27	5×10^{-4}	200 000	-0.53 ± 0.12	-1.32 ± 0.14
10.00	27	5×10^{-4}	200 000	-0.25 ± 0.76	-1.39 ± 0.47
20.00	27	5×10^{-4}	200 000	-1.20 ± 0.67	-1.43 ± 0.34
10^2	27	5×10^{-4}	200 000	-1.37 ± 0.38	-1.62 ± 0.56
2×10^2	27	5×10^{-4}	200 000	-1.09 ± 0.41	-1.87 ± 0.36
10^3	27	5×10^{-4}	200 000	-1.81 ± 0.79	-1.61 ± 0.38
10^4	27	2.5×10^{-4}	400 000	-1.12 ± 1.27	-2.44 ± 0.51
0.01*	63	5×10^{-4}	80 000		
0.43*	63	10^{-3}	40 000	0.86 ± 0.10	-1.34 ± 0.11
10.0	63	5×10^{-4}	200 000	-0.42 ± 0.26	-1.30 ± 0.31
10^3	63	5×10^{-4}	200 000	-1.66 ± 0.42	-1.63 ± 0.27
0.43*	123	5×10^{-4}	80 000	1.043	-1.313
10.0	123	10^{-3}	60 000	-0.340	-1.146
10^3	123	10^{-3}	50 000	-0.340	-1.683

Table 3.3: Simulations data with $\phi = 0.45$. Column (1) is the Peclet number and column (2) is the number of particles. Columns (3) and (4) are the time step and the total number of time steps. Columns (5) and (6) give the first and second normal stress differences. Initial particle configurations of all the runs are random. The error estimates were determined by dividing a simulation run up into statistically independent subintervals (5 - 10) and comparing the averages for each interval (see Phung 1993). *Data obtained from Phung (1993).

Pe	N	$\langle g(2)\rangle_\Omega$	D_0^s	D_0^r	D_{xx}	D_{yy}	D_{zz}
0.00*	27		0.210	0.604		0.059	0.055
0.01*	27	4.20	0.172	0.553		0.068	0.058
0.10	27	4.47	0.177	0.554		0.069	0.096
0.30	27	4.82	0.174	0.549		0.115	0.083
1.00	27	5.80	0.168	0.534		0.146	0.151
3.00	27	7.73	0.159	0.514		0.311	0.257
5.00	27	9.22	0.154	0.503		0.636	0.425
7.00	27	10.9	0.149	0.492		0.846	0.405
10.00	27	13.6	0.140	0.473		0.688	0.452
20.00	27	20.8	0.129	0.446		1.247	0.885
10^2	27	39.0	0.105	0.383		2.349	5.457
2×10^2	27	43.1	0.099	0.364		6.788	3.374
10^3	27	49.9	0.088	0.321		47.27	22.58
10^4	27	59.2	0.069	0.256		644.5	230.6
0.01*	63	4.51	0.204	0.558			
0.43*	63	4.46	0.184	0.541			
0.43*	123	4.94	0.204	0.551			
10.00	123	14.1	0.163	0.471			
10^3	123	50.3	0.101	0.317			

Table 3.4: Same runs as in Table 1 but showing the angularly-averaged pair-distribution function at contact and the self-diffusivities normalized by the isolated particle Brownian diffusivities. The error on the short-time self-diffusivities is ± 1 in the last digit, and for the long-time self-diffusivities, the error is about 30%. *Data obtained from Phung (1993).

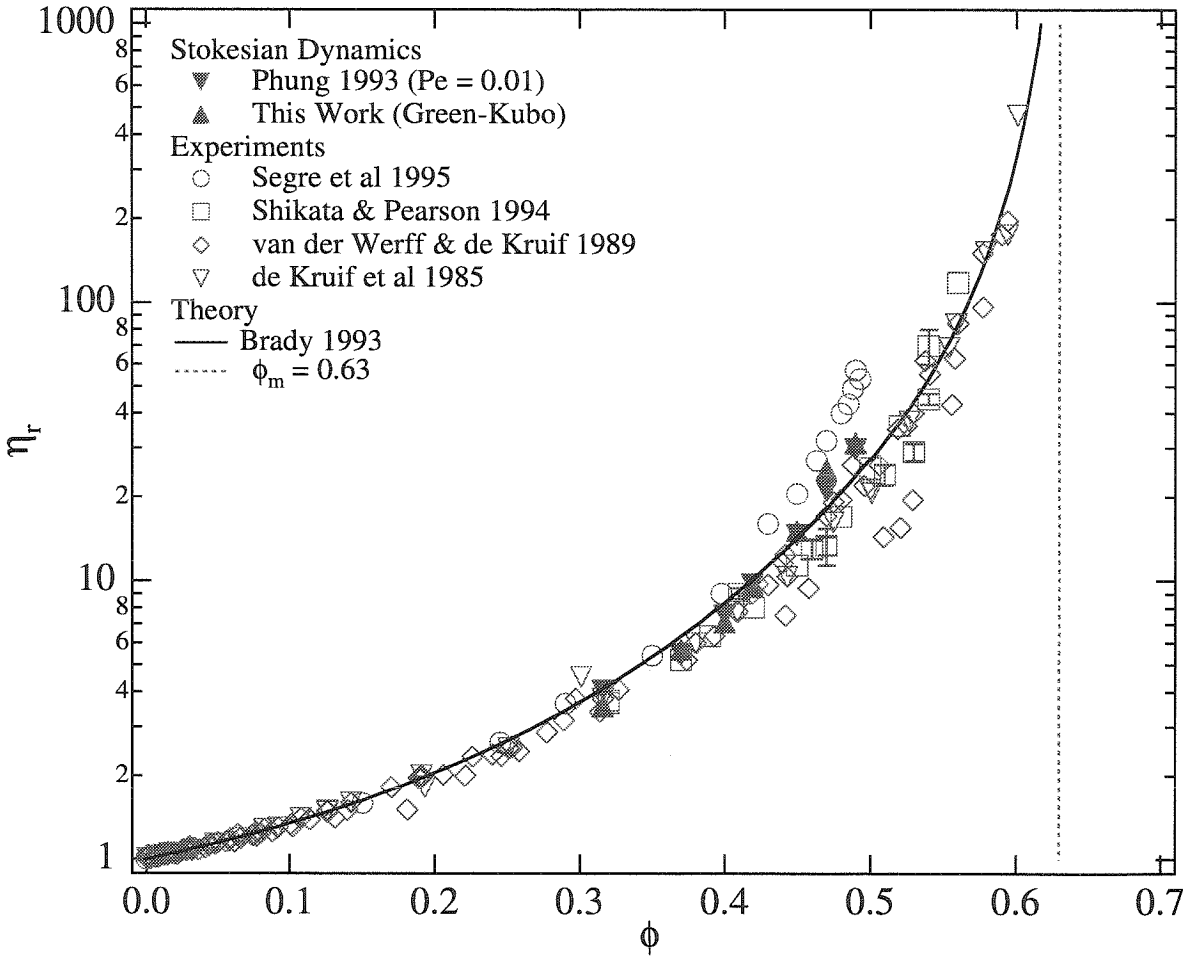

Figure 3.1: Zero shear limiting relative viscosity, η_0, as a function of volume fraction ϕ from both simulation and experiment. Simulation results include both previously measured values from runs at $Pe = 0.01$ (Phung 1993) and values determined in this work from an equilibrium Green-Kubo analysis.

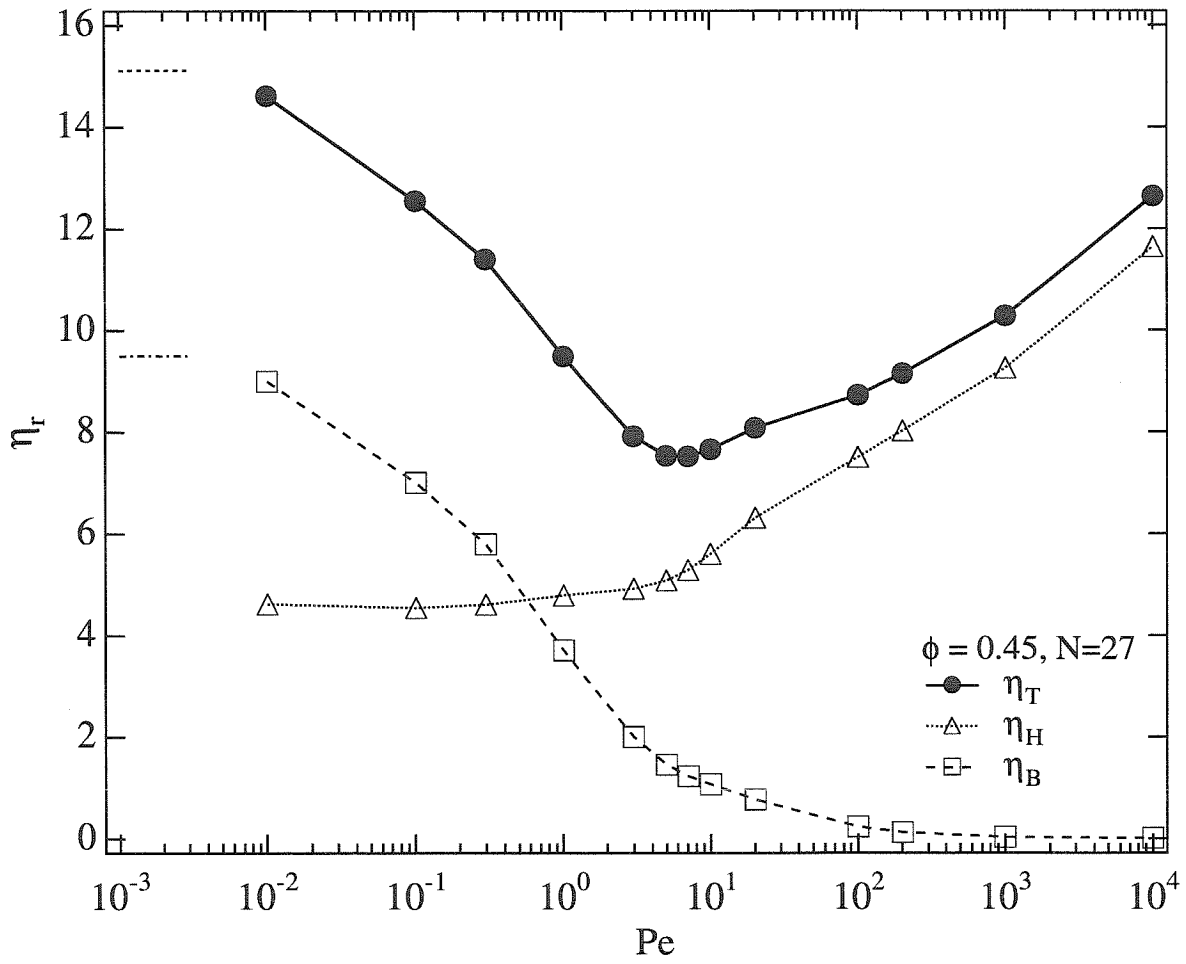

Figure 3.2: Peclet number dependence of the different contributions to the relative viscosity of hard-sphere suspensions at $\phi = 0.45$ determined by Stokesian Dynamics. The horizontal lines on the far left represent the $Pe \to 0$ limits independently determined by an equilibrium Green-Kubo analysis.

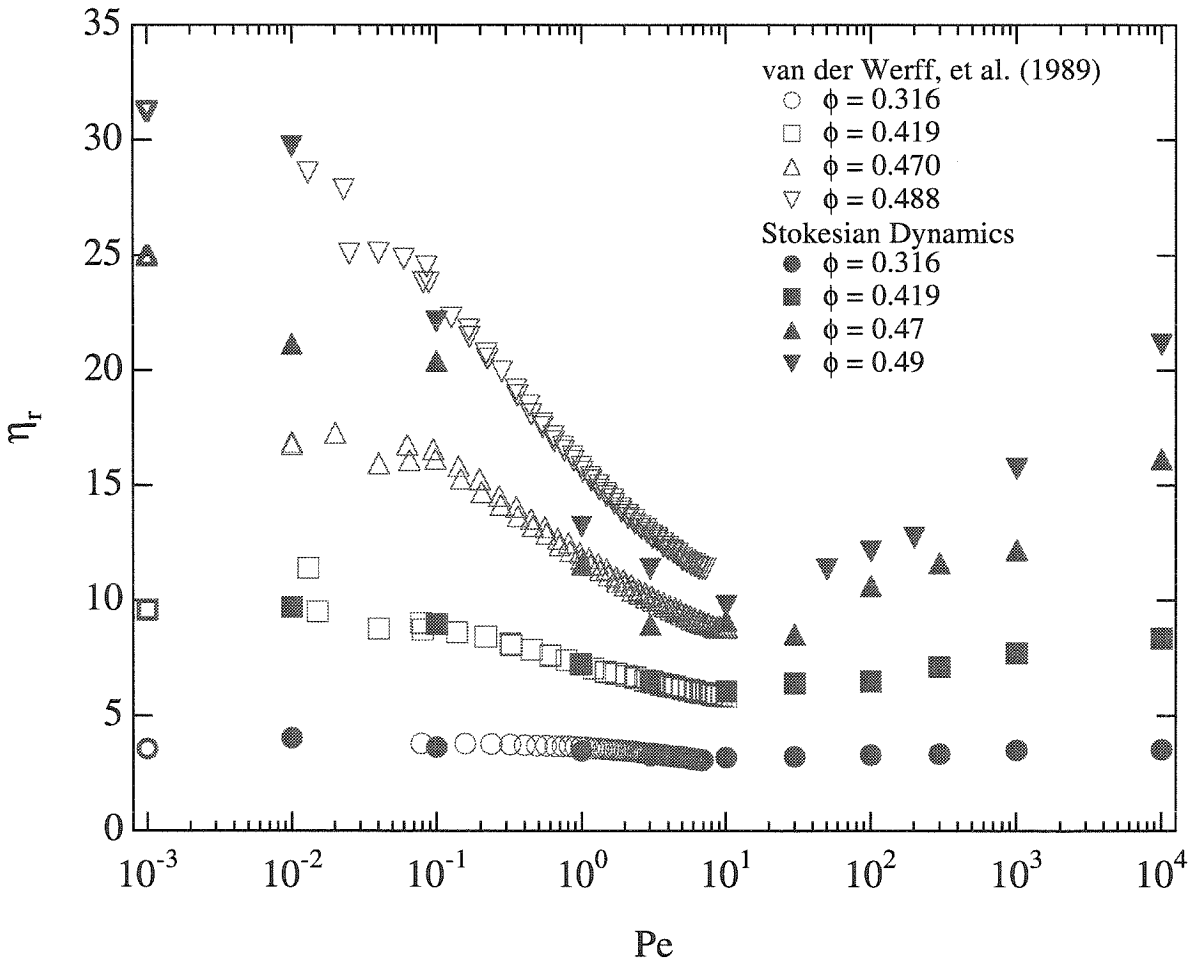

Figure 3.3: Comparison of the relative viscosity of hard-sphere suspensions determined by Stokesian Dynamics as a function of the Péclet number Pe with the experimental results (open symbols) of van der Werff & de Kruif (1989). The thick open symbols on the far left represent the $Pe \to 0$ limits independently determined by an equilibrium Green-Kubo analysis.

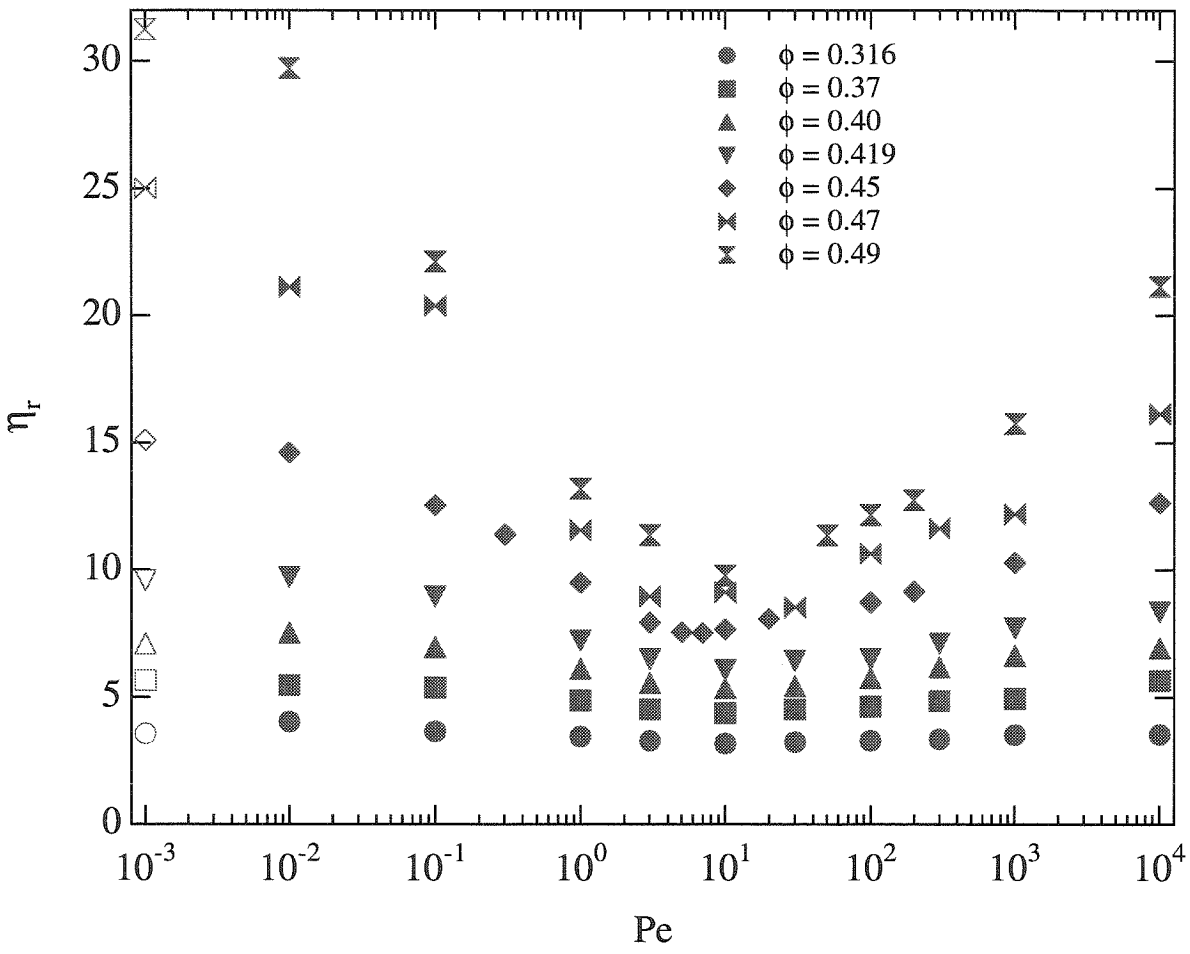

Figure 3.4: The relative viscosity, $\eta_r = 1 + \eta_r^B + \eta_r^H$, as a function of Peclet number Pe for the range of volume fraction, $0.316 \leq \phi \leq 0.49$ with $N = 27$. The open symbols on the far left represent the $Pe \to 0$ limits independently determined by an equilibrium Green-Kubo analysis.

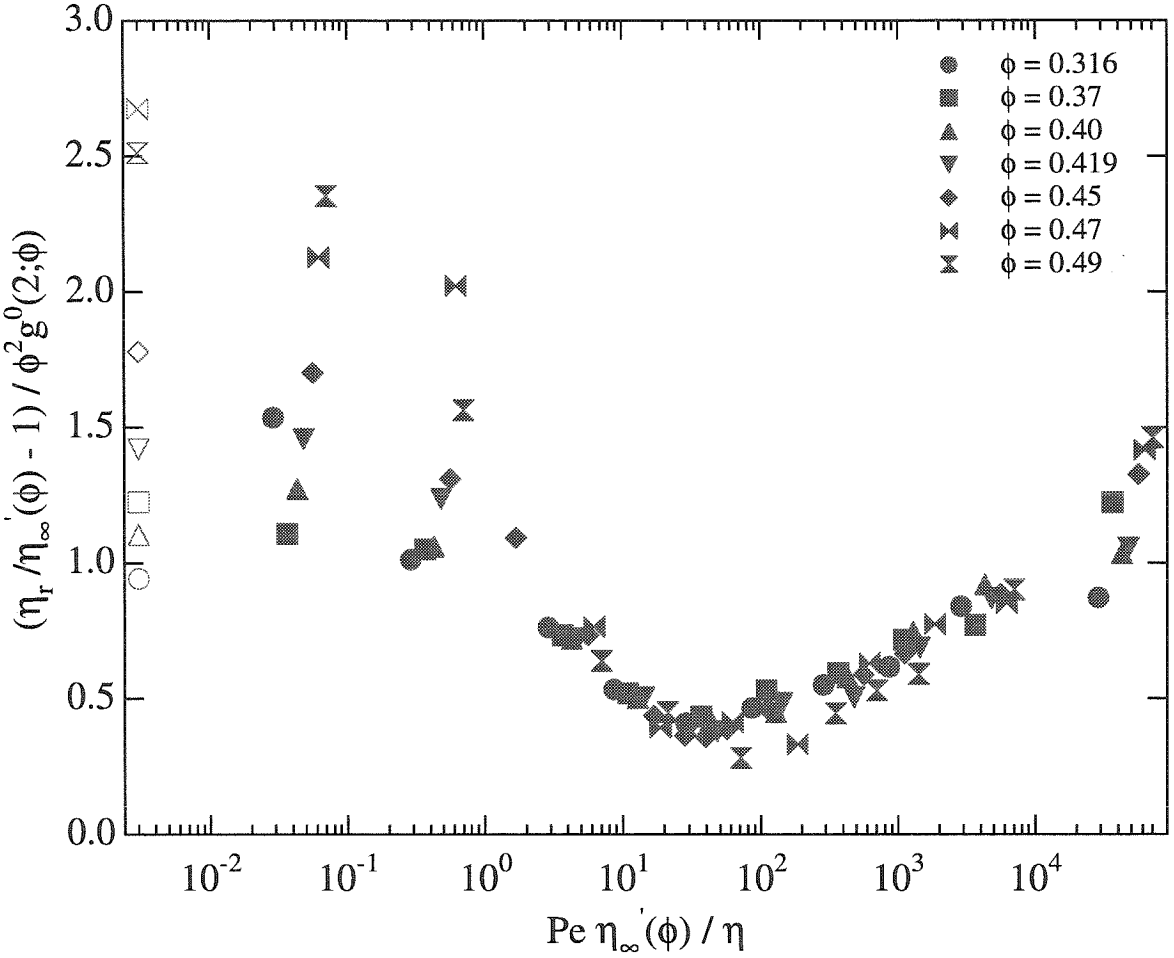

Figure 3.5: The difference of the total viscosity, η_r, from its equilibrium hydrodynamic contribution, η'_∞, scaled by $\eta'_\infty \phi^2 g^0(2)$ is plotted as a function of rescaled Péclet number $\bar{P}e = Pe\ \eta'_\infty/\eta$ for volume fractions $0.316 \leq \phi \leq 0.49$ with $N = 27$. The open symbols on the far left represent the $Pe \to 0$ limits independently determined by an equilibrium Green-Kubo analysis.

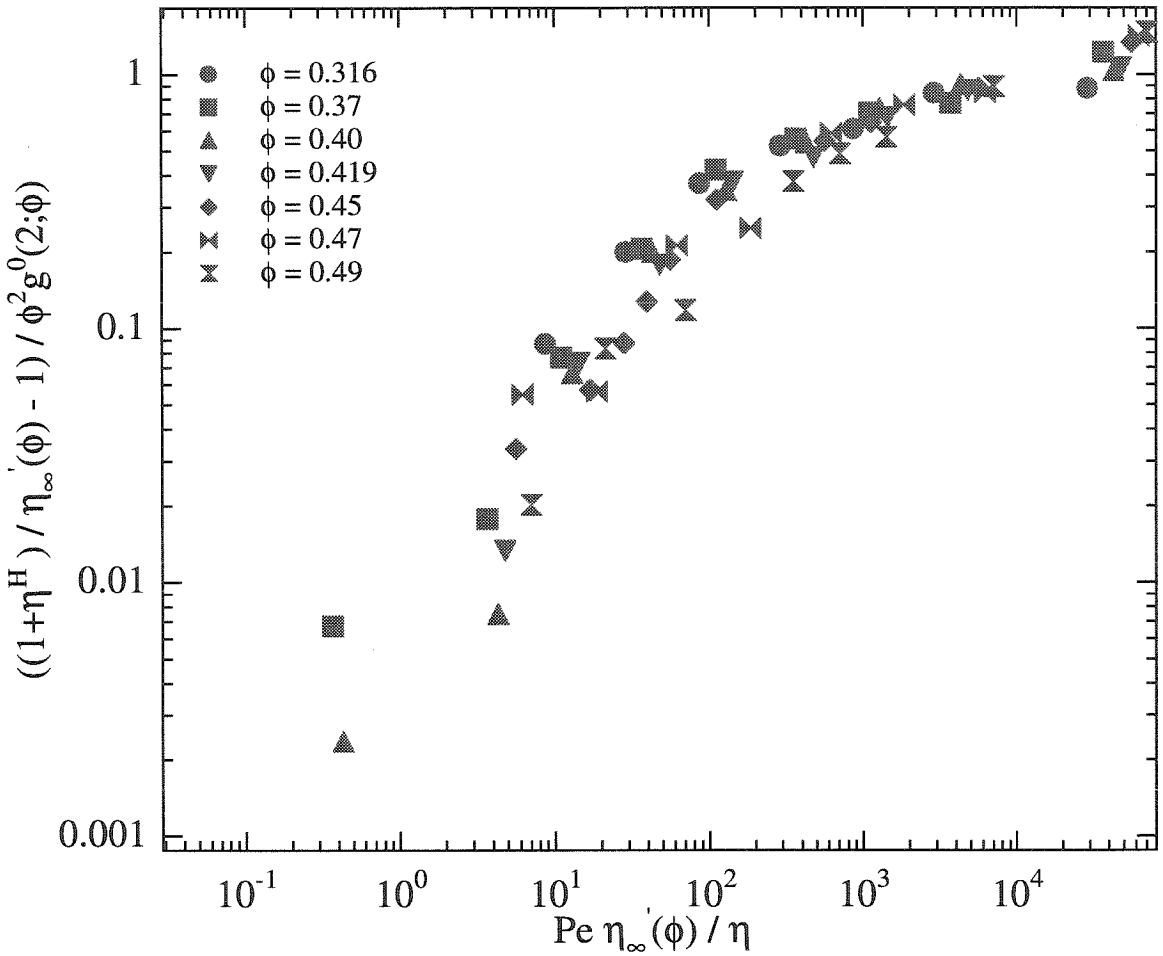

Figure 3.6: The difference of the total hydrodynamic contribution to the viscosity, $1 + \eta^H$, from its equilibrium contribution, η'_∞, scaled by $\eta'_\infty \phi^2 g^0(2)/\eta$ is plotted as a function of rescaled Péclet number $\bar{Pe} = Pe\ \eta'_\infty/\eta$ for volume fractions $0.316 \leq \phi \leq 0.49$ with $N = 27$.

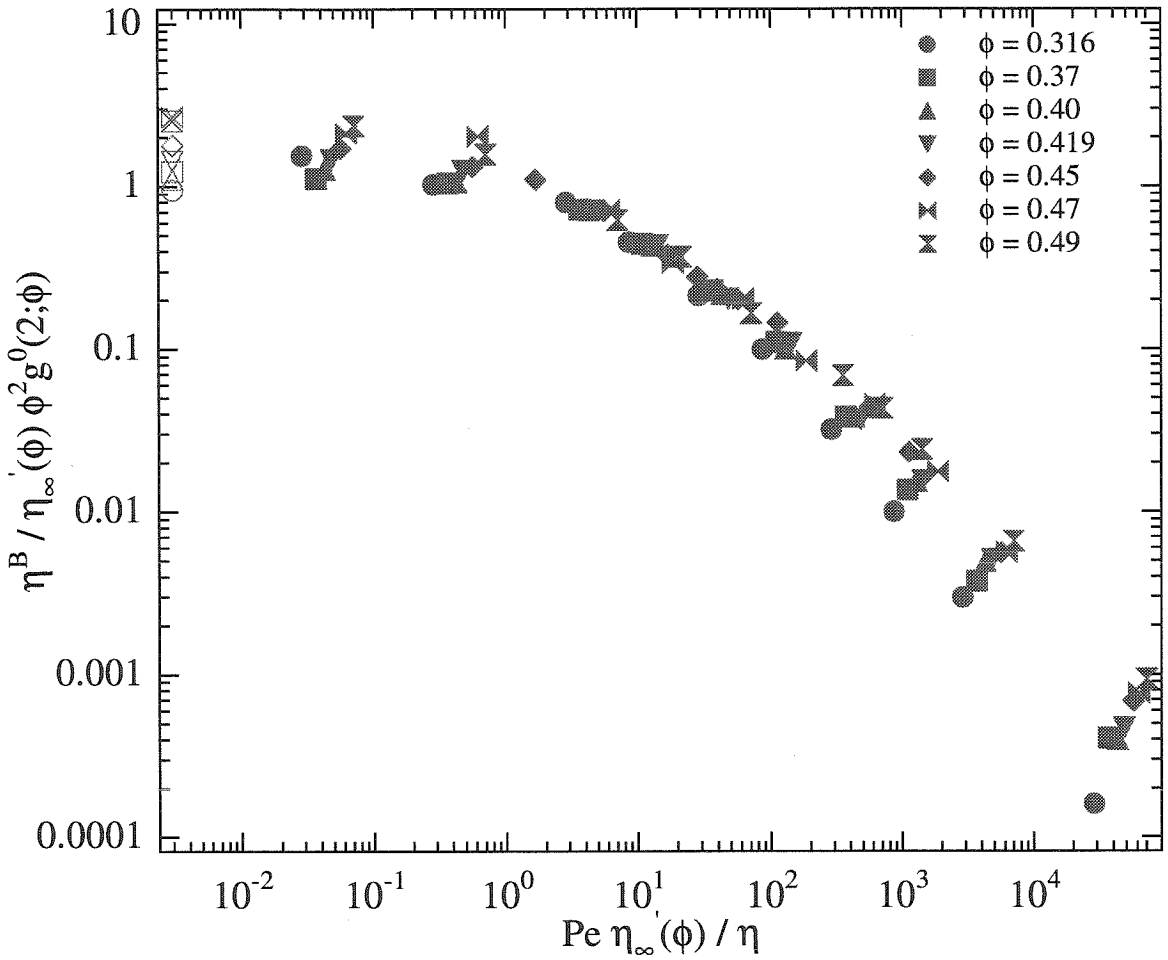

Figure 3.7: The Brownian contribution to the viscosity, η^B, scaled by $\eta'_\infty \phi^2 g^0(2)/\eta$ and plotted as a function of rescaled Péclet number $\bar{Pe} = Pe\ \eta'_\infty/\eta$ for volume fractions $0.316 \leq \phi \leq 0.49$ with $N = 27$. The open symbols on the far left represent the $Pe \to 0$ limits independently determined by an equilibrium Green-Kubo analysis.

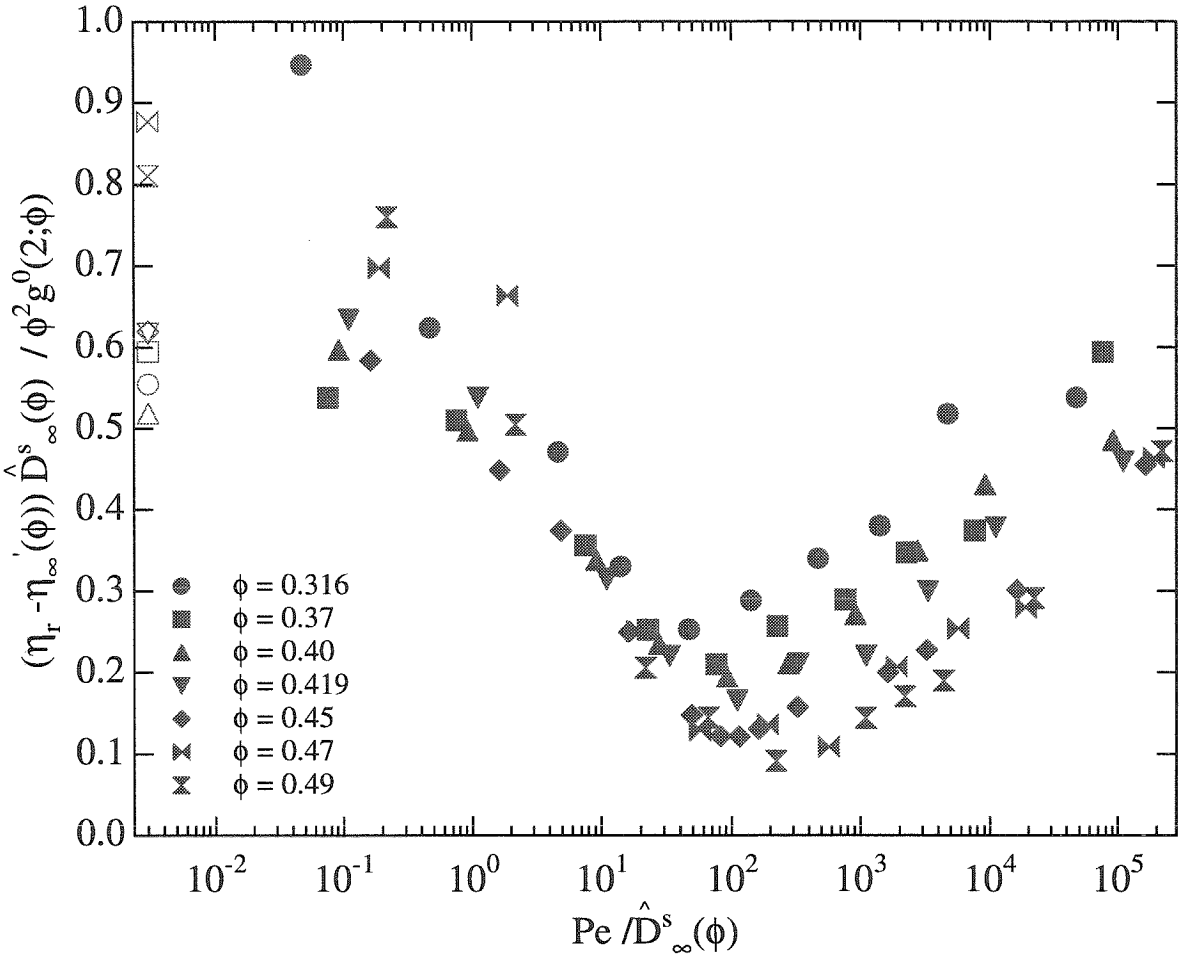

Figure 3.8: The difference of the total viscosity, η_r, from its equilibrium viscous contribution, η'_∞, scaled by $\phi^2 g^0(2)/\hat{D}^s_\infty$ and plotted as a function of rescaled Péclet number $Pe/\hat{D}^s_\infty$ for volume fractions $0.316 \leq \phi \leq 0.49$ with $N = 27$. $\hat{D}^s_\infty$ is the long-time self-diffusivity scaled by the Stokes Einstein value $D = kT/6\pi\eta a$. The open symbols on the far left represent the $Pe \to 0$ limits independently determined by an equilibrium Green-Kubo analysis.

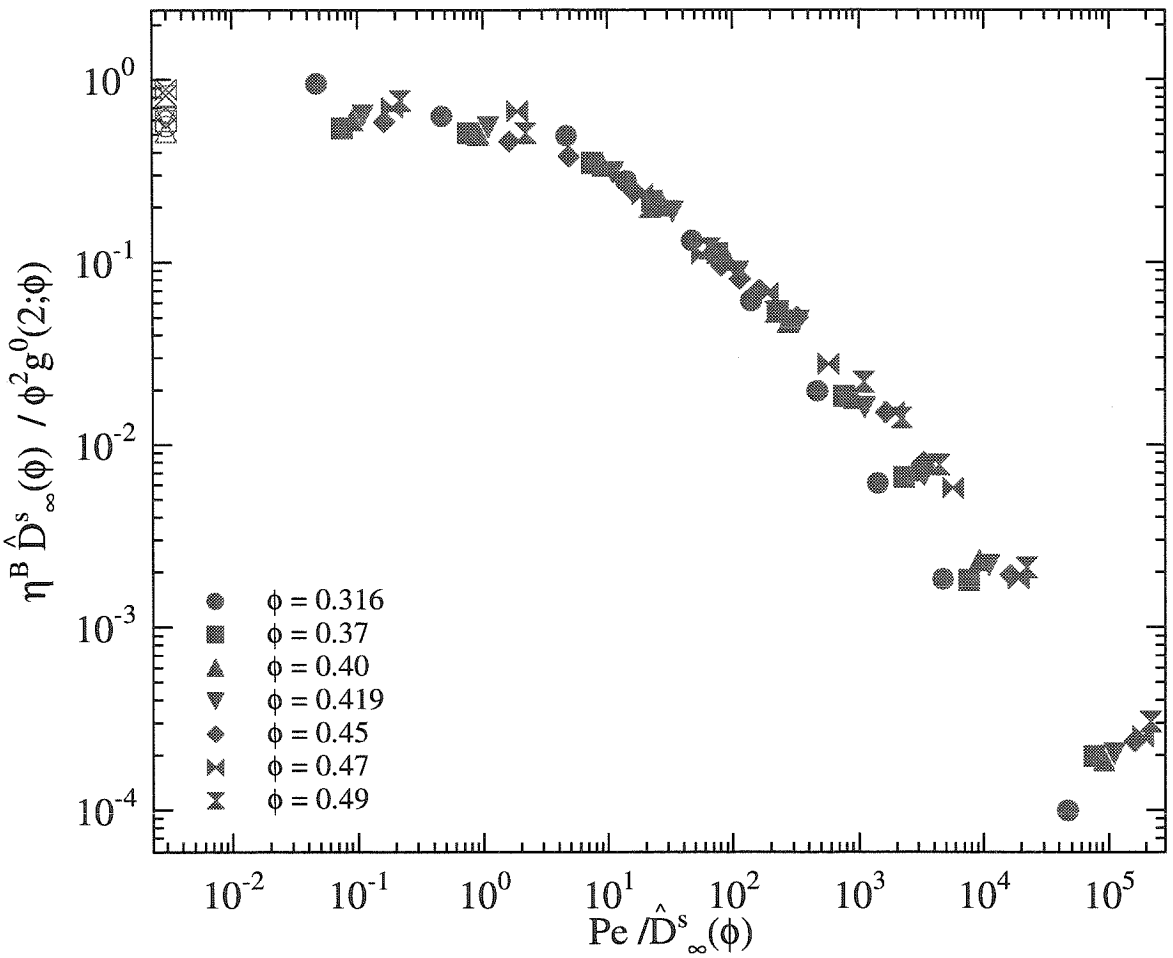

Figure 3.9: The Brownian contribution to the viscosity, η^B, scaled by $\phi^2 g^0(2)/\hat{D}^s_\infty$ and plotted as a function of rescaled Péclet number $Pe/\hat{D}^s_\infty$ for volume fractions $0.316 \leq \phi \leq 0.49$ with $N = 27$. $\hat{D}^s_\infty$ is the long-time self-diffusivity scaled by the Stokes Einstein value $D = kT/6\pi\eta a$. The open symbols on the far left represent the $Pe \to 0$ limits independently determined by an equilibrium Green-Kubo analysis.

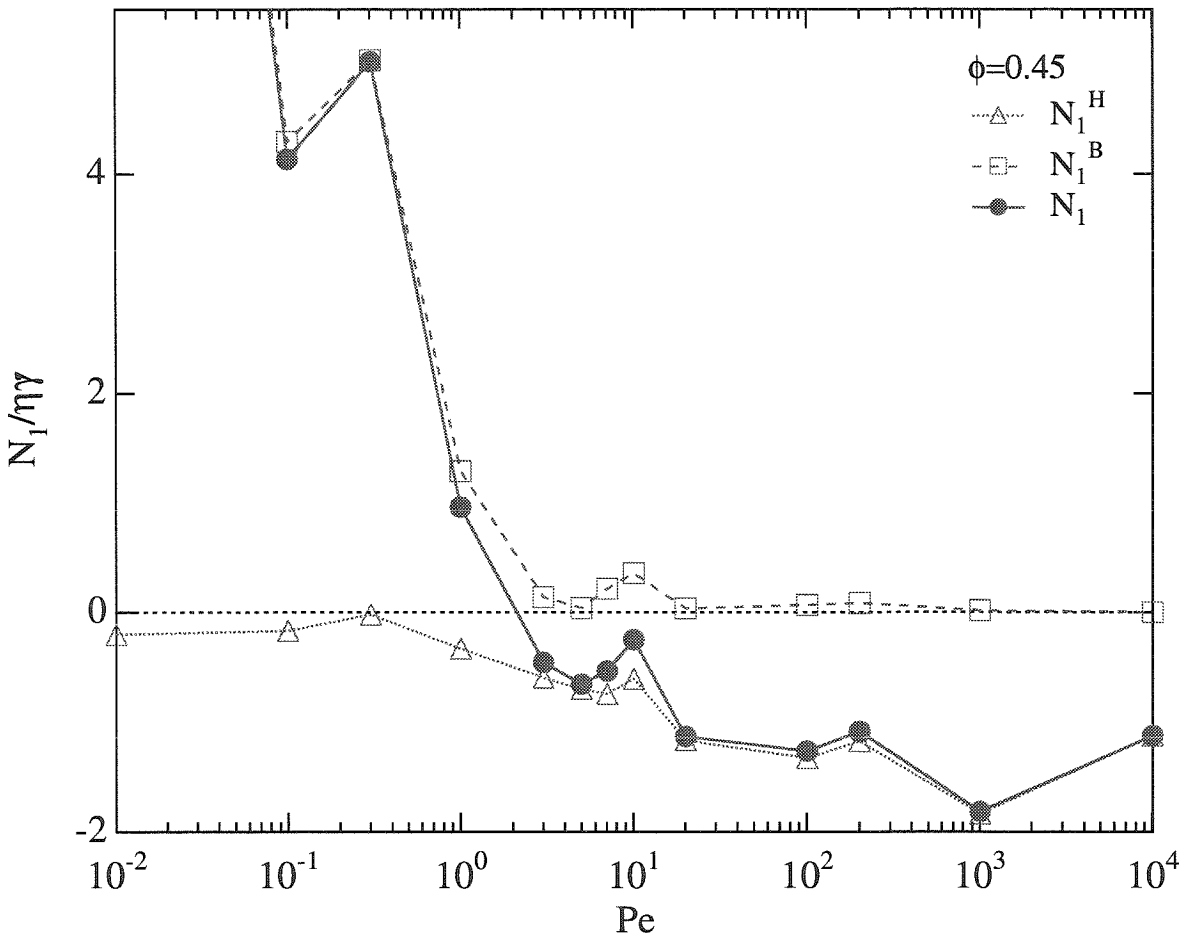

Figure 3.10: The hydrodynamic and Brownian contributions to the first normal stress difference for $N = 27$ and $\phi = 0.45$ as a function of the Peclet number.

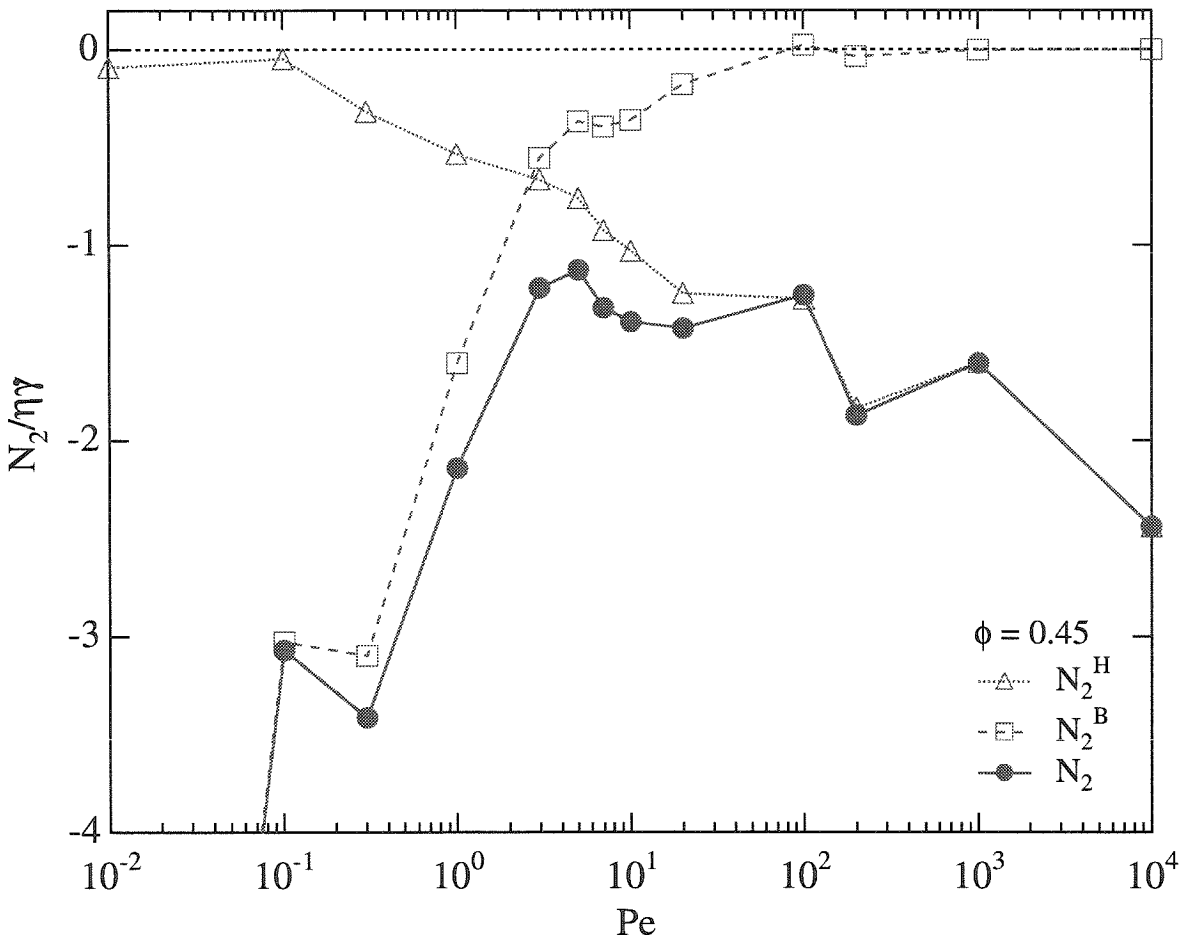

Figure 3.11: The hydrodynamic and Brownian contributions to the second normal stress difference for $N = 27$ and $\phi = 0.45$ as a function of the Peclet number.

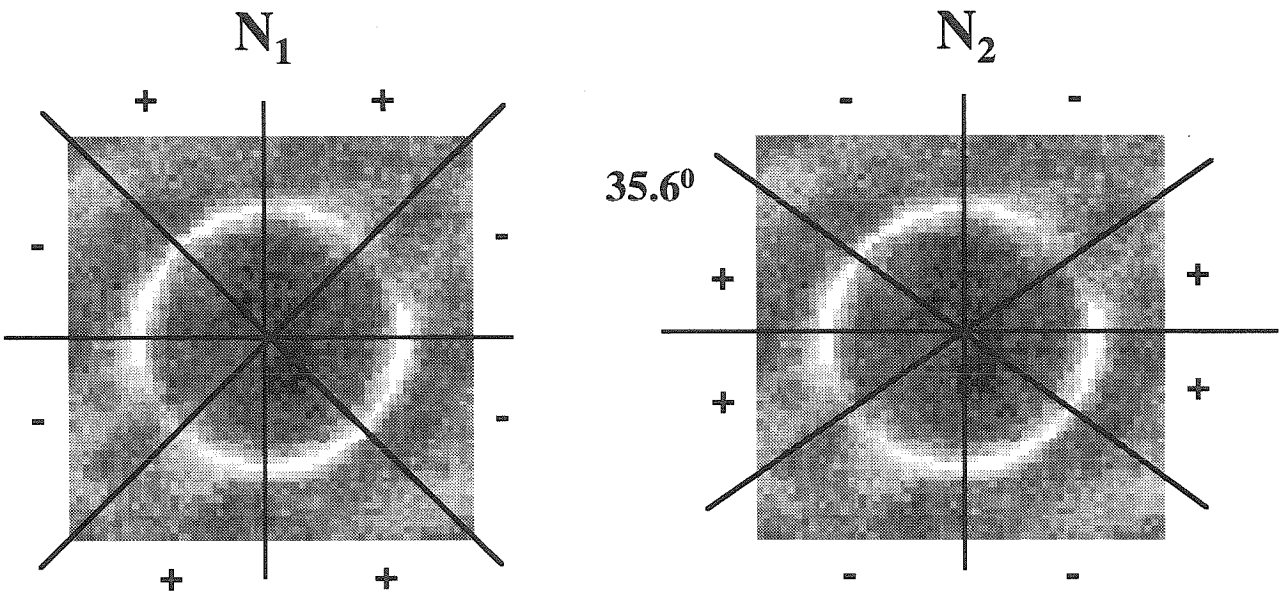

Figure 3.12: Projections of the pair distribution function, $g(\boldsymbol{r})$, into the xy-plane from $N = 27$, $\phi = 0.45$, and $Pe = 1$. The projections are divided into eight sections each denoting the sign of the contribution to the Brownian normal stress difference from a particle in that region. The projections on the left and right are divided and labelled for determining N_1 and N_2, respectively. The Brownian stress is assumed to be proportional to $-\hat{\boldsymbol{r}}\hat{\boldsymbol{r}}$ and $g(\boldsymbol{r})$ is assumed to be symmetric about the z-axis.

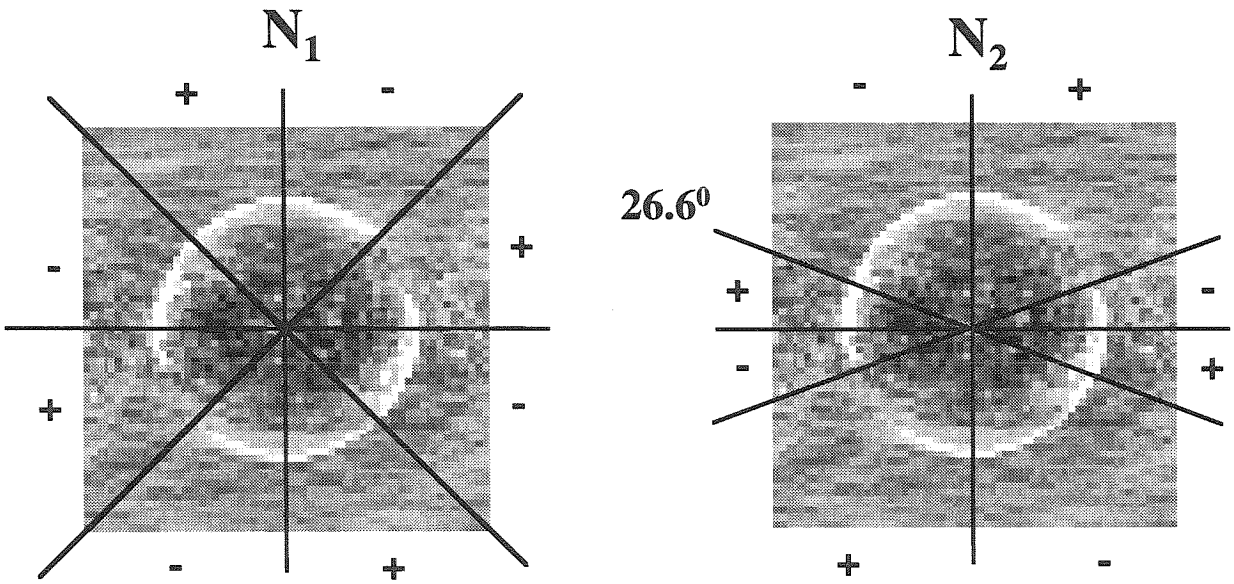

Figure 3.13: Projections of the pair distribution function, $g(\boldsymbol{r})$, into the xy-plane from $N = 27$, $\phi = 0.45$, and $Pe = 1000$. The projections are divided into eight sections each denoting the sign of the contribution to the hydrodynamic normal stress difference from a particle in that region. The projections and on the left and right are divided and labelled for determining N_1 and N_2, respectively. The Brownian stress is assumed to be proportional to $\hat{\boldsymbol{r}}\hat{\boldsymbol{r}}(\hat{\boldsymbol{r}}\cdot\hat{\boldsymbol{E}}\cdot\hat{\boldsymbol{r}})$ and $g(\boldsymbol{r})$ is assumed to be symmetric about the z-axis.

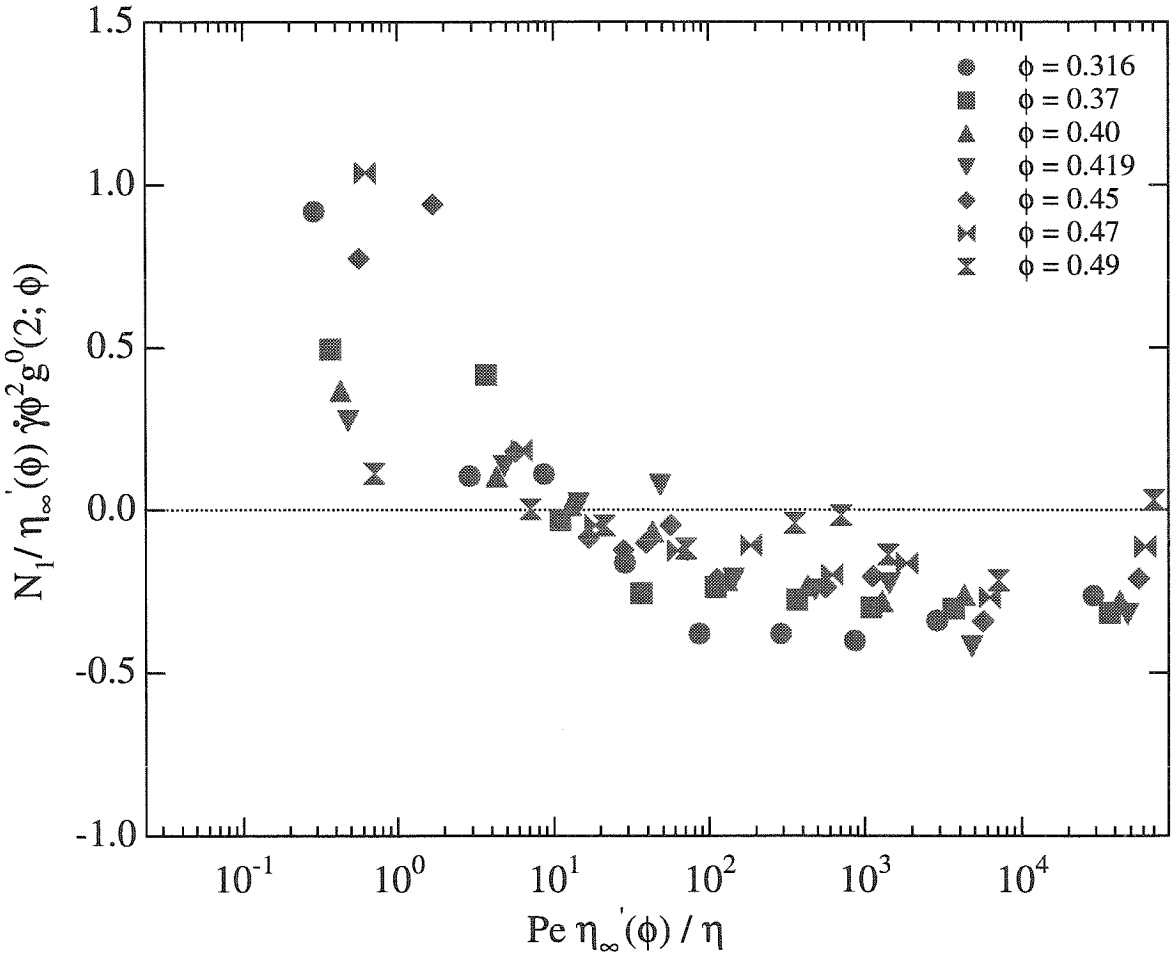

Figure 3.14: The first normal stress difference, N_1, scaled by $\eta'_\infty \dot{\gamma}\phi^2 g^0(2)$ and plotted as a function of rescaled Péclet number $\bar{Pe} = Pe\ \eta'_\infty/\eta$ for volume fractions $0.316 \leq \phi \leq 0.49$ with $N = 27$.

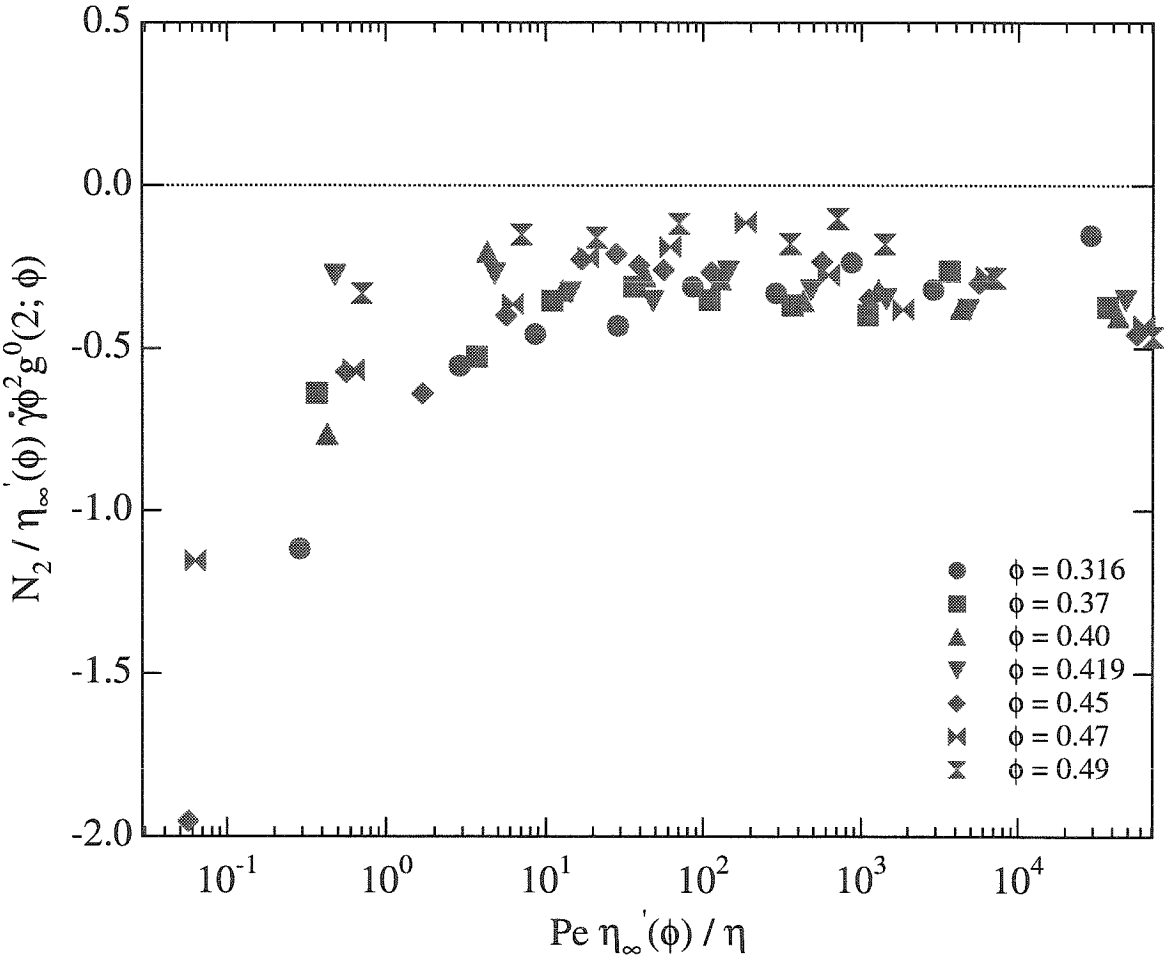

Figure 3.15: The second normal stress difference, N_2, scaled by $\eta'_\infty \dot{\gamma}\phi^2 g^0(2)$ and plotted as a function of rescaled Péclet number $\bar{Pe} = Pe\ \eta'_\infty/\eta$ for volume fractions $0.316 \leq \phi \leq 0.49$ with $N = 27$.

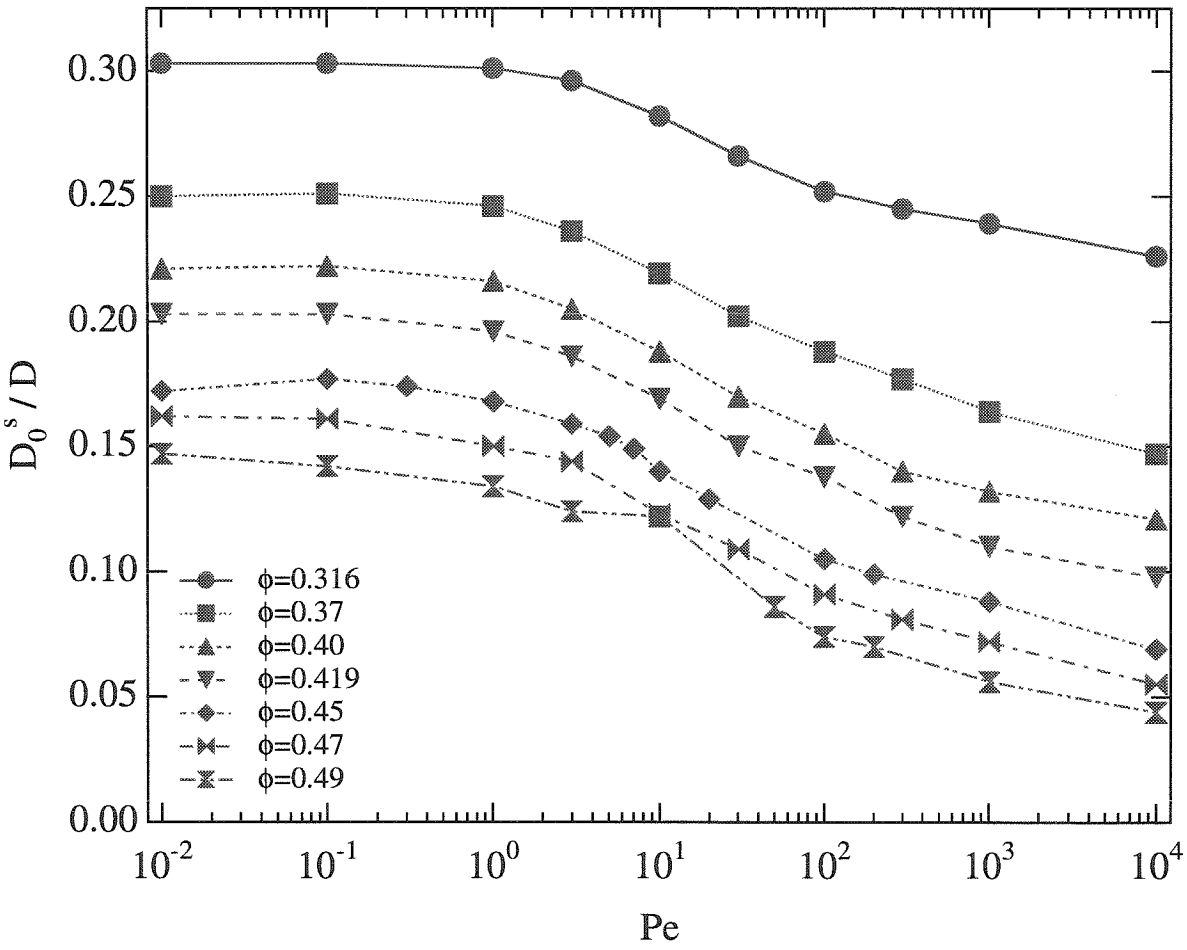

Figure 3.16: The average particle translational mobilities as a function of Pe for volume fractions $0.316 \leq \phi \leq 0.49$. At $Pe \equiv 0$ these instantaneous mobilities (multiplied by kT) correspond to the short-time self-diffusion coefficients. The mobilities have been normalized by the diffusion coefficient of an isolated Brownian particle, $kT/6\pi\eta a$.

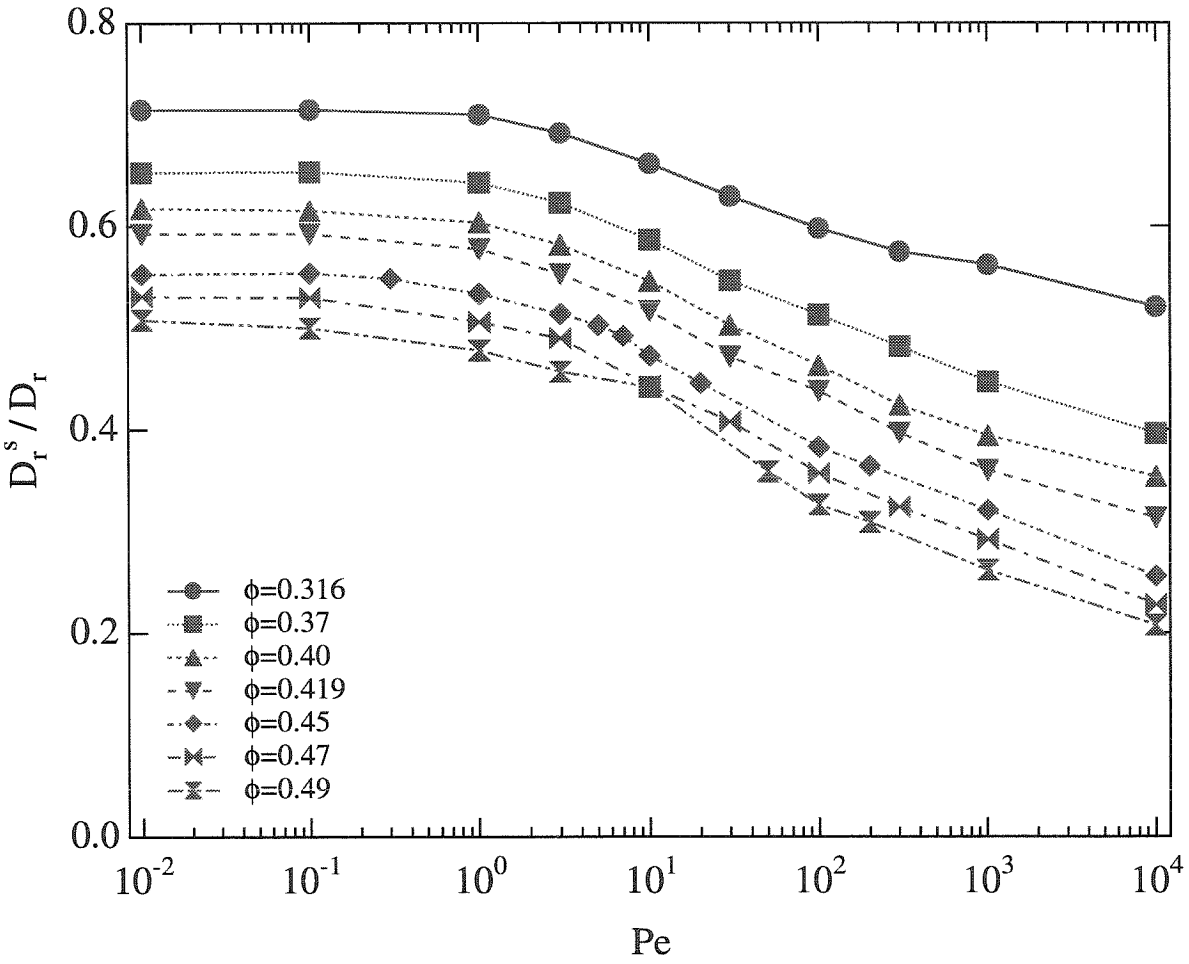

Figure 3.17: The average particle rotational mobilities as a function of Pe for volume fractions $0.316 \leq \phi \leq 0.49$. At $Pe \equiv 0$ these instantaneous mobilities (multiplied by kT) correspond to the short-time self-diffusion coefficients. The mobilities have been normalized by the diffusion coefficient of an isolated Brownian particle, $kT/8\pi\eta a^3$.

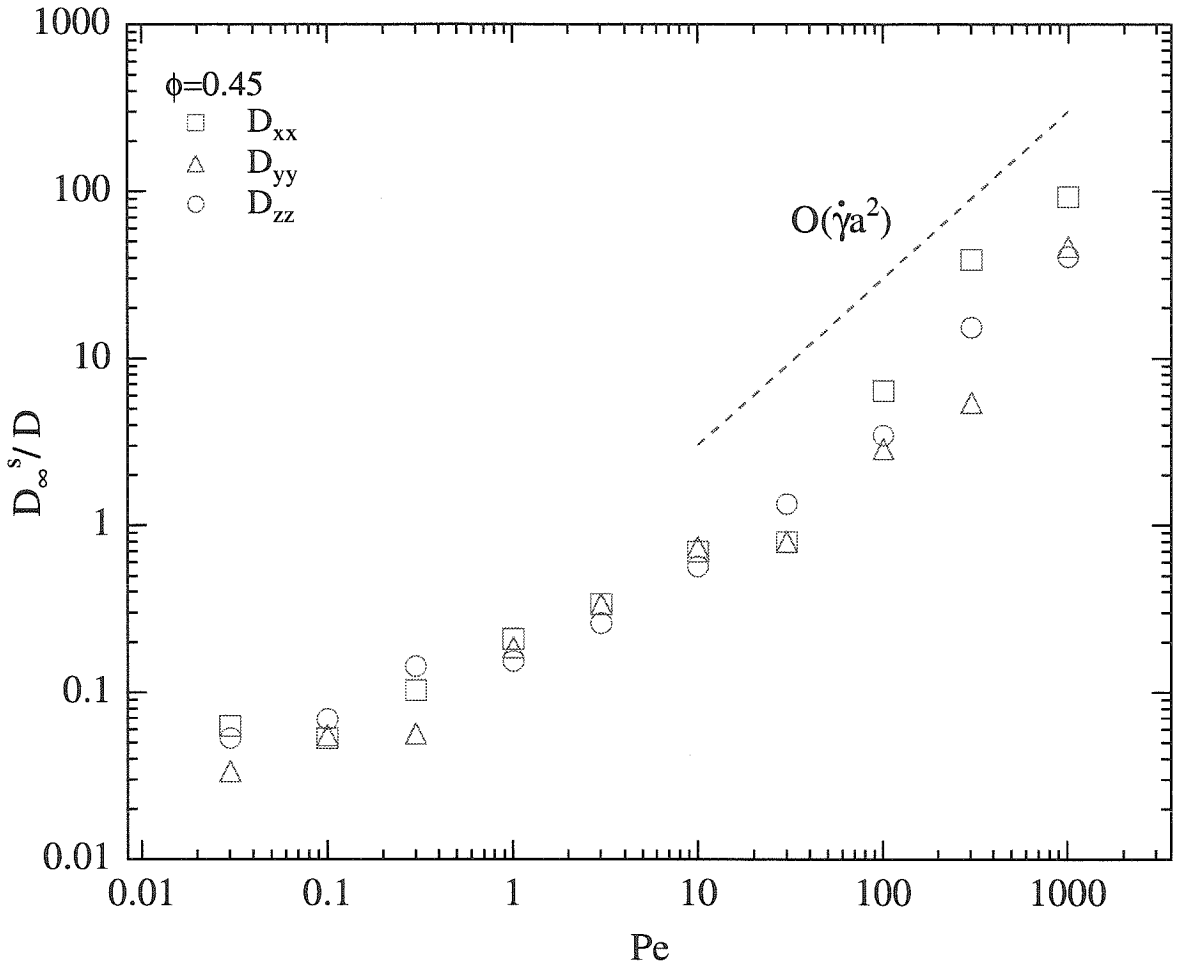

Figure 3.18: The long-time self-diffusivities in the velocity, D_{xx}, velocity-gradient, D_{yy}, and vorticity, D_{zz}, directions for $\phi = 0.45$ as a function of Pe. The diffusivities have been normalized by the diffusion coefficient of an isolated Brownian particle, $kT/6\pi\eta a$. At large Pe the dimensional long-time diffusivities scale hydrodynamically as $\dot{\gamma}a^2$.

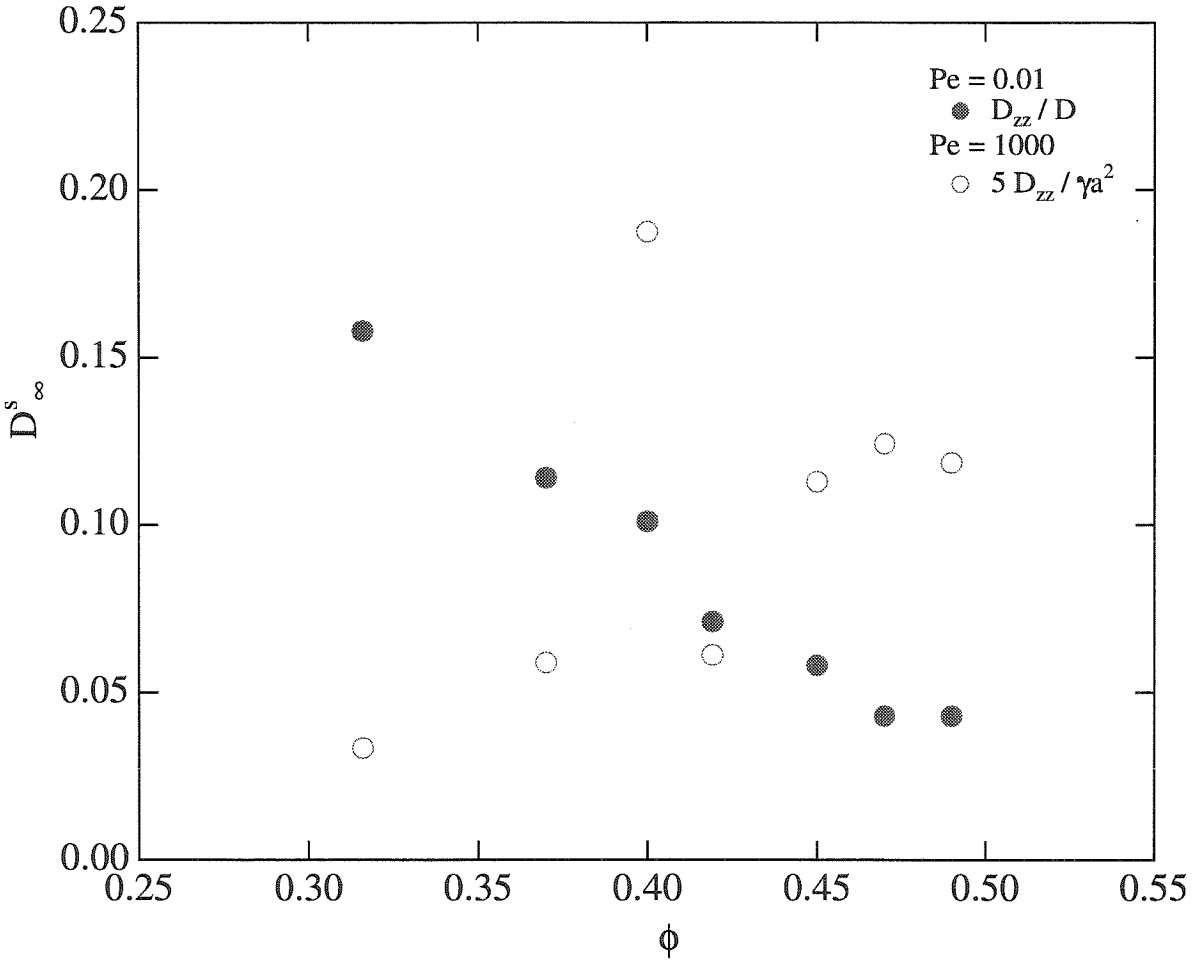

Figure 3.19: The zz-component of the long-time self-diffusivity tensor as a function of ϕ at both high and low Péclet numbers. The diffusivity is nondimensionalized by the Stokes-Einstein value $D = kT/6\pi\eta a$ for $Pe = 0.01$ and by $\frac{1}{5}\dot{\gamma}a^2$ for $Pe = 1000$.

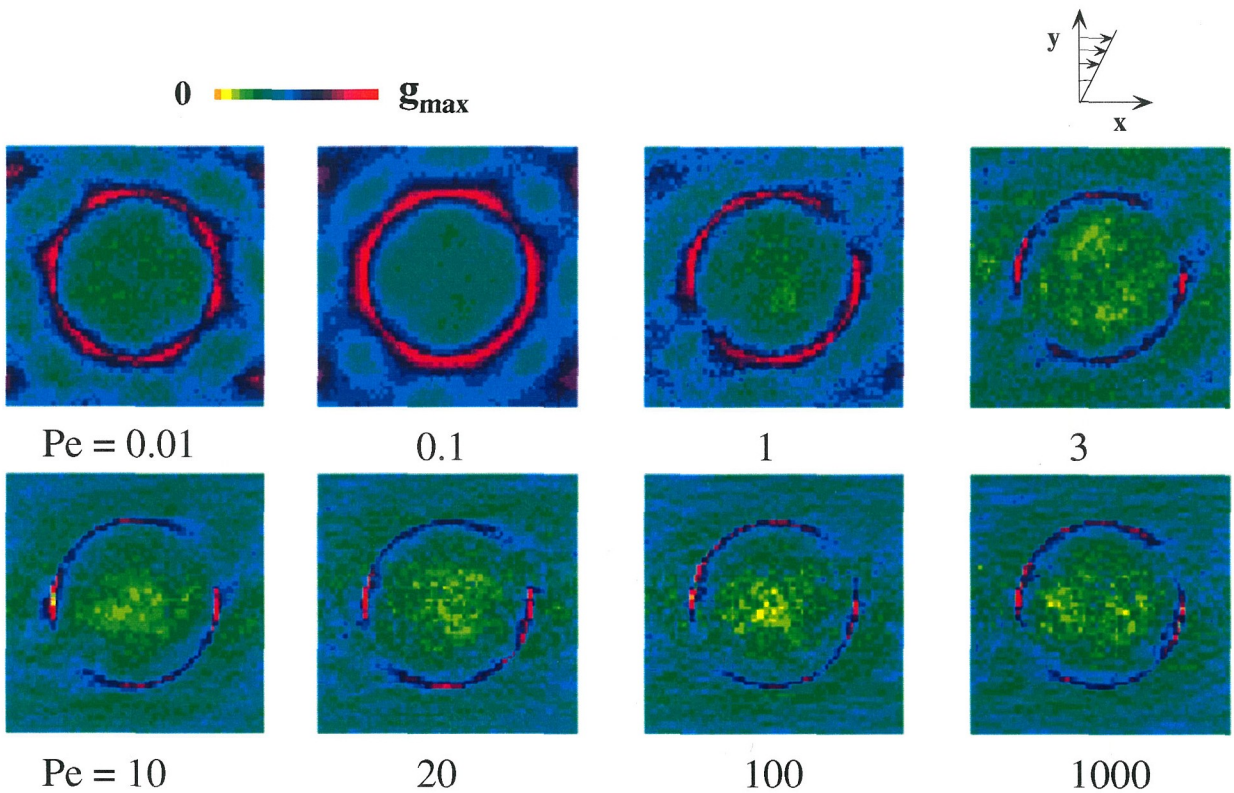

Figure 3.20: The pair-distribution function projected into the velocity–velocity-gradient plane for $N = 27$ and $\phi = 0.45$.

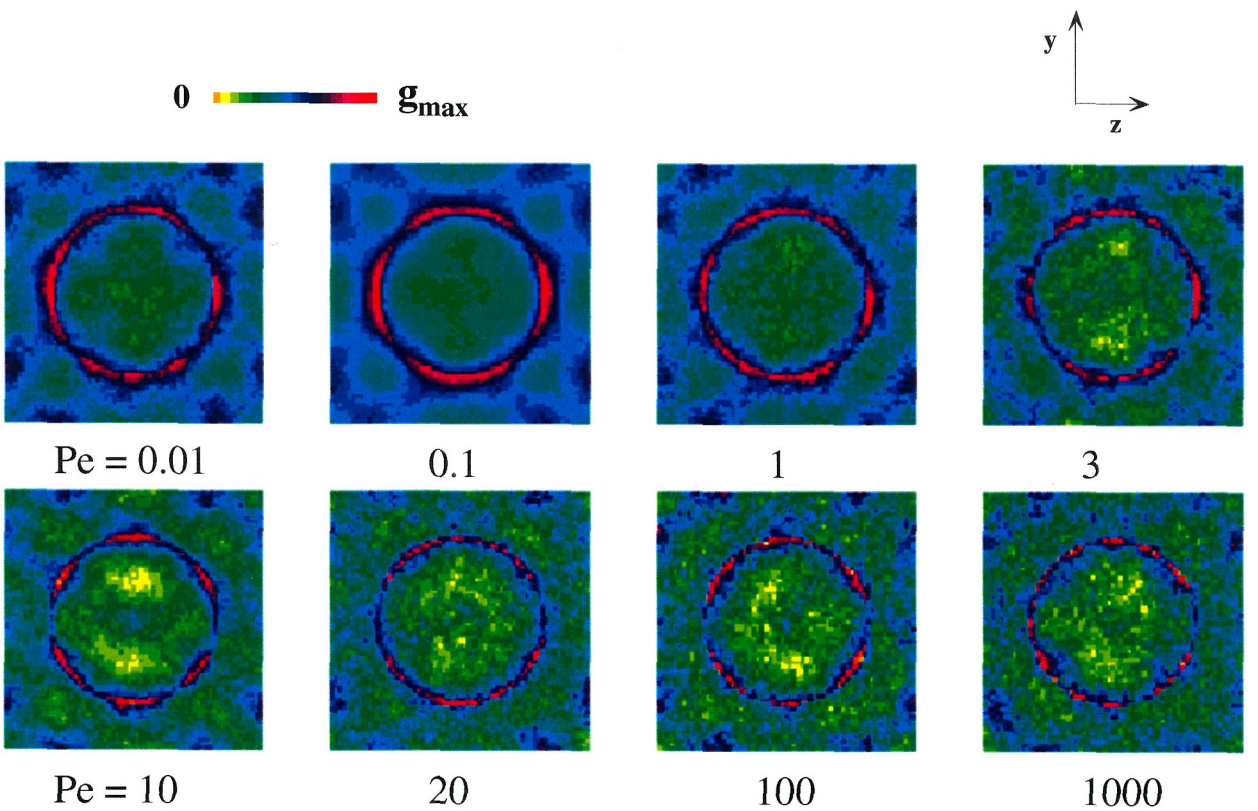

Figure 3.21: The pair-distribution function projected into the velocity-gradient–vorticity plane for $N = 27$ and $\phi = 0.45$.

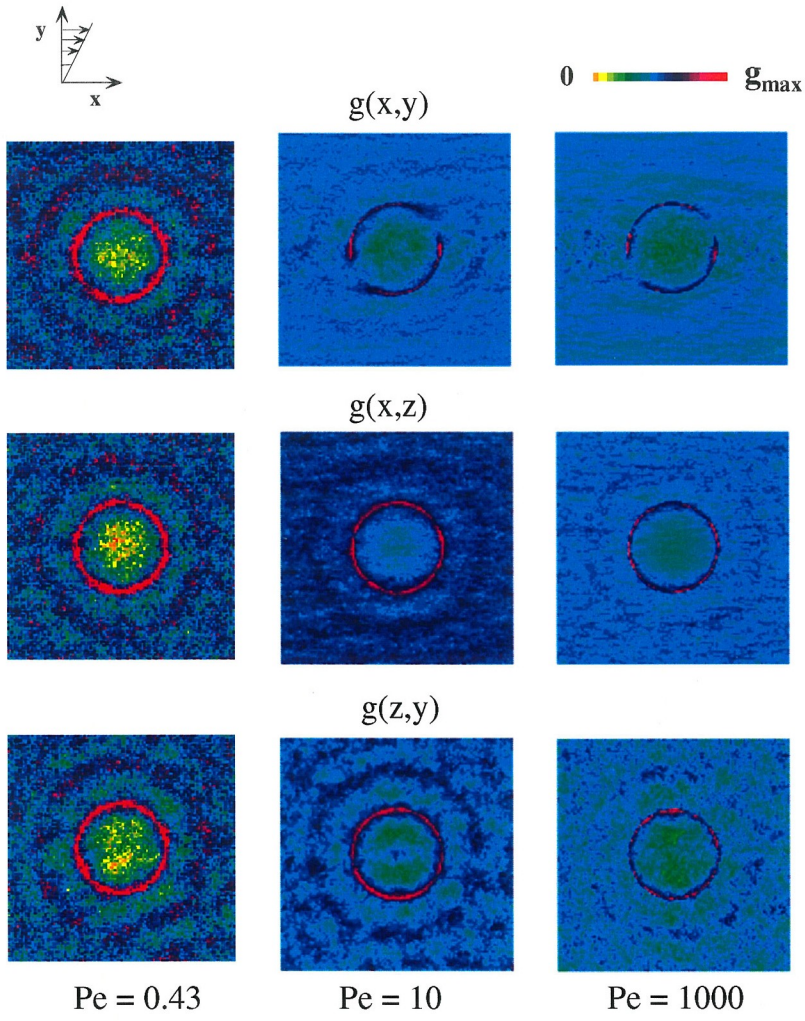

Figure 3.22: Projections of the pair-distribution function in all three planes for $N = 123$ at $Pe = 0.43, 10$, and 1000.

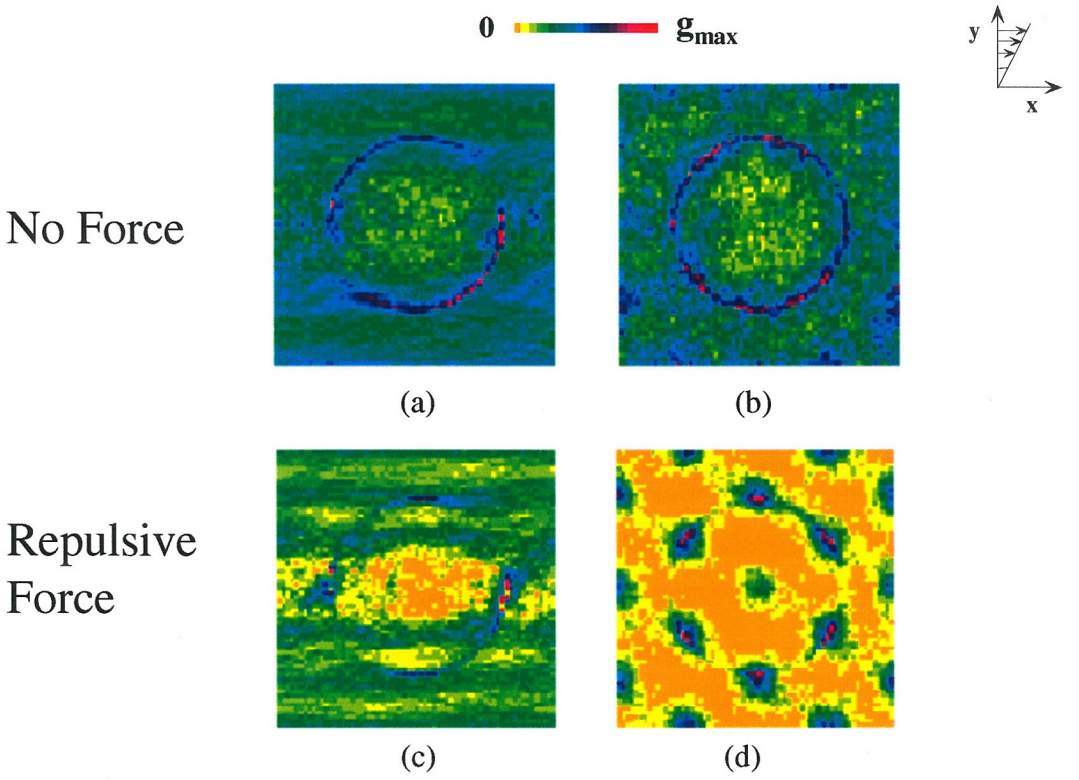

Figure 3.23: Pair distribution functions for $N = 27$, $\phi = 0.40$ and $Pe = 100$ for the hard-sphere case (a)–(b) shows no flow-induced ordering while using a DLVO-type repulsive force (c)–(d), $(\dot{\gamma}^* = 0.5, \tau = 100)$ shows hexagonally-packed string ordering. The pair-distribution function is projected into the velocity–velocity-gradient plane for (a), (c) and the velocity-gradient–vorticity plane for (b), (d).

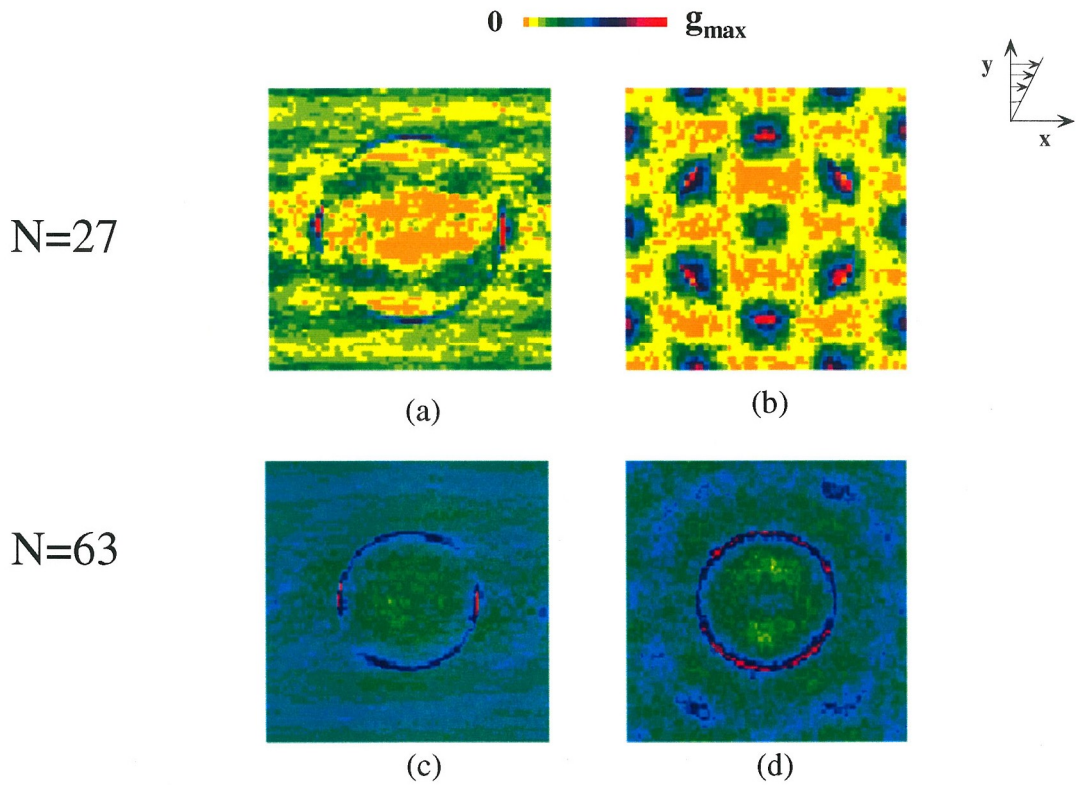

Figure 3.24: Pair distribution functions for $\phi = 0.49$ and $Pe = 100$ using $N = 27$ (a)–(b) shows hexagonally-packed string ordering while increasing the system size to $N = 63$ (c)–(d), shows no flow-induced ordering hexagonally-packed string ordering. The pair-distribution function is projected into the velocity–velocity-gradient plane for (a), (c) and the velocity-gradient–vorticity plane for (b), (d).

$\phi = 0.316$						
Pe	N	Δt	$NSTEPS$	η_r^H	η_r^B	η_r^T
0.01*	27	5×10^{-4}	200 000	1.87 ± 0.00	1.16 ± 0.67	4.03 ± 0.67
0.1*	27	10^{-3}	200 000	1.87 ± 0.00	0.77 ± 0.09	3.63 ± 0.09
1*	27	10^{-3}	200 000	1.85 ± 0.00	0.60 ± 0.01	3.45 ± 0.01
3.00	27	5×10^{-4}	200 000	1.93 ± 0.05	0.34 ± 0.04	3.27 ± 0.07
10.00	27	5×10^{-4}	200 000	2.02 ± 0.05	0.16 ± 0.01	3.18 ± 0.06
30.00	27	5×10^{-4}	200 000	2.15 ± 0.07	0.075 ± 0.010	3.22 ± 0.08
10^2	27	5×10^{-4}	200 000	2.26 ± 0.05	0.024 ± 0.001	3.28 ± 0.05
3×10^2	27	5×10^{-4}	200 000	2.33 ± 0.05	0.0075 ± 0.0013	3.33 ± 0.05
10^3	27	5×10^{-4}	200 000	2.50 ± 0.04	0.0022 ± 0.0004	3.50 ± 0.04
10^4	27	2.5×10^{-4}	400 000	2.53 ± 0.06	0.0001 ± 0.0000	3.53 ± 0.06

Table 3.5: Relative viscosity data as a function of Pe from Stokesian Dynamics at $\phi = 0.316$. *Data obtained from Phung (1993).

$\phi = 0.316$				
Pe	N	$N_1^H/\eta\dot{\gamma}$	$N_1^B/\eta\dot{\gamma}$	$N_1^T/\eta\dot{\gamma}$
0.01*	27	-0.024 ± 0.004	1.68 ± 1.04	1.65 ± 1.04
0.1*	27	-0.027 ± 0.008	0.69 ± 0.18	0.66 ± 0.18
1*	27	-0.054 ± 0.003	0.13 ± 0.02	0.076 ± 0.036
3.00	27	-0.16 ± 0.03	0.24 ± 0.05	0.072 ± 0.073
10.00	27	-0.21 ± 0.07	0.094 ± 0.077	-0.11 ± 0.15
30.00	27	-0.33 ± 0.08	0.057 ± 0.033	-0.27 ± 0.10
10^2	27	-0.30 ± 0.05	0.027 ± 0.006	-0.27 ± 0.06
3×10^2	27	-0.30 ± 0.07	0.011 ± 0.003	-0.29 ± 0.07
10^3	27	-0.25 ± 0.11	0.005 ± 0.001	-0.24 ± 0.12
10^4	27	-0.19 ± 0.08	4.9×10^{-4}	-0.19 ± 0.08

Table 3.6: First normal stress difference data as a function of Pe from Stokesian Dynamics at $\phi = 0.316$. *Data obtained from Phung (1993).

$\phi = 0.316$				
Pe	N	$N_2^H/\eta\dot{\gamma}$	$N_2^B/\eta\dot{\gamma}$	$N_2^T/\eta\dot{\gamma}$
0.01*	27	-0.008 ± 0.001	-2.51 ± 0.48	-2.52 ± 0.49
0.1*	27	-0.016 ± 0.003	-0.79 ± 0.18	-0.80 ± 0.18
1*	27	-0.13 ± 0.00	-0.27 ± 0.12	-0.40 ± 0.12
3.00	27	-0.12 ± 0.04	-0.21 ± 0.05	-0.34 ± 0.08
10.00	27	-0.23 ± 0.06	-0.082 ± 0.080	-0.31 ± 0.13
30.00	27	-0.20 ± 0.13	-0.025 ± 0.075	-0.23 ± 0.20
10^2	27	-0.23 ± 0.05	-0.009 ± 0.012	-0.24 ± 0.06
3×10^2	27	-0.17 ± 0.06	-0.001 ± 0.005	-0.17 ± 0.06
10^3	27	-0.23 ± 0.12	-0.0008 ± 0.0035	-0.23 ± 0.12
10^4	27	-0.11 ± 0.06	-7.6×10^{-5}	-0.11 ± 0.06

Table 3.7: Second normal stress difference data as a function of Pe from Stokesian Dynamics at $\phi = 0.316$. *Data obtained from Phung (1993).

$\phi = 0.316$							
Pe	N	$\langle g(2) \rangle_\Omega$	D_0^s	$D_0^{s,r}$	D_{xx}	D_{yy}	D_{zz}
0.00*	27		0.304	0.717		0.160	0.158
0.01*	27	2.38	0.303	0.715		0.187	0.126
0.1*	27	2.49	0.303	0.715		0.204	0.100
1*	27	2.71	0.301	0.710		0.326	0.179
3.00	27	3.64	0.296	0.692		0.600	0.191
10.00	27	5.78	0.282	0.662		0.774	0.425
30.00	27	11.0	0.266	0.630		1.181	0.353
10^2	27	18.6	0.252	0.598		2.099	1.639
3×10^2	27	24.5	0.245	0.575		5.895	2.038
10^3	27	27.7	0.239	0.562		21.84	6.651
10^4	27	32.9	0.226	0.521		108.7	85.94

Table 3.8: Data for the contact values of the radial distribution function, short- and long-time self-diffusivities from Stokesian Dynamics at $\phi = 0.316$. *Data obtained from Phung (1993). Simulations performed before method for calculating $D^s_{\infty,xx}$ was implemented into the code.

$\phi = 0.37$						
Pe	N	Δt	$NSTEPS$	η_r^H	η_r^B	η_r^T
0.01*	27	5×10^{-4}	400 000	2.66 ± 0.00	1.81 ± 0.67	5.47 ± 0.67
0.1*	27	10^{-3}	60 000	2.67 ± 0.01	1.70 ± 0.18	5.38 ± 0.18
1*	27	10^{-3}	60 000	2.69 ± 0.01	1.17 ± 0.01	4.86 ± 0.02
3.00	27	5×10^{-4}	200 000	2.78 ± 0.06	0.72 ± 0.04	4.51 ± 0.09
10.00	27	5×10^{-4}	200 000	2.99 ± 0.04	0.37 ± 0.04	4.37 ± 0.08
30.00	27	5×10^{-4}	200 000	3.34 ± 0.13	0.18 ± 0.02	4.52 ± 0.15
10^2	27	5×10^{-4}	200 000	3.57 ± 0.09	0.062 ± 0.006	4.63 ± 0.09
3×10^2	27	5×10^{-4}	200 000	3.80 ± 0.12	0.022 ± 0.002	4.83 ± 0.12
10^3	27	5×10^{-4}	200 000	3.91 ± 0.27	0.006 ± 0.001	4.92 ± 0.27
10^4	27	2.5×10^{-4}	400 000	4.66 ± 0.48	0.001 ± 0.000	5.66 ± 0.48

Table 3.9: Relative viscosity data as a function of Pe from Stokesian Dynamics at $\phi = 0.37$. *Data obtained from Phung (1993). Simulations performed before method for calculating $D^s_{\infty,xx}$ was implemented into the code.

$\phi = 0.37$				
Pe	N	$N_1^H/\eta\dot{\gamma}$	$N_1^B/\eta\dot{\gamma}$	$N_1^T/\eta\dot{\gamma}$
0.01*	27	-0.083 ± 0.002	24.2 ± 8.83	24.1 ± 8.85
0.1*	27	-0.032 ± 0.012	0.84 ± 0.28	0.81 ± 0.28
1*	27	-0.11 ± 0.01	0.79 ± 0.04	0.68 ± 0.03
3.00	27	-0.28 ± 0.11	0.23 ± 0.29	-0.057 ± 0.384
10.00	27	-0.46 ± 0.14	0.044 ± 0.076	-0.41 ± 0.21
30.00	27	-0.48 ± 0.05	0.093 ± 0.038	-0.39 ± 0.08
10^2	27	-0.50 ± 0.12	0.049 ± 0.012	-0.45 ± 0.13
3×10^2	27	-0.51 ± 0.05	0.023 ± 0.003	-0.49 ± 0.05
10^3	27	-0.50 ± 0.14	0.006 ± 0.003	-0.50 ± 0.14
10^4	27	-0.52 ± 0.28	0.001 ± 0.001	-0.52 ± 0.29

Table 3.10: First normal stress difference data as a function of Pe from Stokesian Dynamics at $\phi = 0.37$. *Data obtained from Phung (1993).

$\phi = 0.37$				
Pe	N	$N_2^H/\eta\dot{\gamma}$	$N_2^B/\eta\dot{\gamma}$	$N_2^T/\eta\dot{\gamma}$
0.01*	27	-0.024 ± 0.002	-23.3 ± 8.24	-23.31 ± 8.25
0.1*	27	-0.021 ± 0.005	-1.02 ± 0.23	-1.04 ± 0.24
1*	27	-0.22 ± 0.01	-0.64 ± 0.05	-0.86 ± 0.05
3.00	27	-0.27 ± 0.08	-0.31 ± 0.16	-0.59 ± 0.20
10.00	27	-0.42 ± 0.07	-0.088 ± 0.067	-0.50 ± 0.09
30.00	27	-0.52 ± 0.08	-0.054 ± 0.035	-0.58 ± 0.10
10^2	27	-0.58 ± 0.16	-0.022 ± 0.027	-0.60 ± 0.19
3×10^2	27	-0.64 ± 0.14	-0.010 ± 0.005	-0.65 ± 0.15
10^3	27	-0.43 ± 0.11	0.0007 ± 0.0048	-0.43 ± 0.12
10^4	27	-0.61 ± 0.15	3.1×10^{-4}	-0.61 ± 0.15

Table 3.11: Second normal stress difference data as a function of Pe from Stokesian Dynamics at $\phi = 0.37$. *Data obtained from Phung (1993).

$\phi = 0.37$							
Pe	N	$\langle g(2) \rangle_\Omega$	D_0^s	$D_0^{s,r}$	D_{xx}	D_{yy}	D_{zz}
0.01*	27	3.02	0.250	0.653		0.105	0.114
0.1*	27	3.06	0.251	0.654		0.131	0.124
1*	27	3.54	0.246	0.643		0.184	0.164
3.00	27	4.54	0.236	0.623		0.309	0.132
10.00	27	8.30	0.219	0.587		0.650	0.300
30.00	27	15.8	0.202	0.547		0.888	1.223
10^2	27	25.4	0.188	0.513		5.429	2.180
3×10^2	27	32.6	0.177	0.482		8.296	7.431
10^3	27	38.4	0.164	0.447		23.31	11.76
10^4	27	45.9	0.147	0.396		377.9	92.61

Table 3.12: Data for the contact values of the radial distribution function, short- and long-time self-diffusivities from Stokesian Dynamics at $\phi = 0.37$. *Data obtained from Phung (1993). Simulations performed before method for calculating $D^s_{\infty,xx}$ was implemented into the code.

$\phi = 0.40$						
Pe	N	Δt	$NSTEPS$	η_r^H	η_r^B	η_r^T
0.01*	27	5×10^{-4}	220 000	3.28 ± 0.01	3.22 ± 1.13	7.51 ± 1.13
0.1*	27	10^{-3}	60 000	3.29 ± 0.01	2.68 ± 0.12	6.97 ± 0.12
1*	27	10^{-3}	60 000	3.30 ± 0.01	1.81 ± 0.01	6.11 ± 0.02
3.00	27	5×10^{-4}	200 000	3.45 ± 0.10	1.10 ± 0.09	5.55 ± 0.18
10.00	27	5×10^{-4}	200 000	3.78 ± 0.06	0.55 ± 0.03	5.33 ± 0.09
30.00	27	5×10^{-4}	200 000	4.16 ± 0.26	0.25 ± 0.04	5.42 ± 0.31
10^2	27	5×10^{-4}	200 000	4.65 ± 0.15	0.097 ± 0.009	5.74 ± 0.16
3×10^2	27	5×10^{-4}	200 000	5.13 ± 0.15	0.038 ± 0.003	6.17 ± 0.15
10^3	27	5×10^{-4}	200 000	5.59 ± 0.52	0.012 ± 0.003	6.61 ± 0.53
10^4	27	2.5×10^{-4}	400 000	5.90 ± 0.24	0.001 ± 0.000	6.91 ± 0.24

Table 3.13: Relative viscosity data as a function of Pe from Stokesian Dynamics at $\phi = 0.40$. *Data obtained from Phung (1993).

$\phi = 0.40$				
Pe	N	$N_1^H/\eta\dot{\gamma}$	$N_1^B/\eta\dot{\gamma}$	$N_1^T/\eta\dot{\gamma}$
0.01*	27	-0.082 ± 0.011	38.4 ± 6.88	38.3 ± 6.89
0.1*	27	-0.018 ± 0.007	0.95 ± 1.01	0.93 ± 1.01
1*	27	-0.24 ± 0.01	0.50 ± 0.07	0.26 ± 0.08
3.00	27	-0.29 ± 0.13	0.33 ± 0.28	0.04 ± 0.40
10.00	27	-0.42 ± 0.13	0.25 ± 0.09	-0.17 ± 0.20
30.00	27	-0.64 ± 0.16	0.094 ± 0.083	-0.54 ± 0.24
10^2	27	-0.65 ± 0.52	0.062 ± 0.059	-0.59 ± 0.57
3×10^2	27	-0.74 ± 0.21	0.030 ± 0.011	-0.71 ± 0.22
10^3	27	-0.67 ± 0.15	0.011 ± 0.003	-0.66 ± 0.16
10^4	27	-0.71 ± 0.39	0.001 ± 0.000	-0.71 ± 0.39

Table 3.14: First normal stress difference data as a function of Pe from Stokesian Dynamics at $\phi = 0.40$. *Data obtained from Phung (1993).

$\phi = 0.40$				
Pe	N	$N_2^H/\eta\dot{\gamma}$	$N_2^B/\eta\dot{\gamma}$	$N_2^T/\eta\dot{\gamma}$
0.01*	27	-0.010 ± 0.013	-26.2 ± 1.53	-26.23 ± 1.53
0.1*	27	-0.052 ± 0.015	-1.89 ± 1.49	-1.94 ± 1.50
1*	27	-0.28 ± 0.01	-0.24 ± 0.04	-0.52 ± 0.05
3.00	27	-0.45 ± 0.12	-0.37 ± 0.37	-0.82 ± 0.49
10.00	27	-0.54 ± 0.20	-0.17 ± 0.11	-0.71 ± 0.30
30.00	27	-0.70 ± 0.16	-0.030 ± 0.084	-0.73 ± 0.21
10^2	27	-0.86 ± 0.20	-0.039 ± 0.027	-0.90 ± 0.23
3×10^2	27	-0.82 ± 0.22	0.002 ± 0.025	-0.82 ± 0.25
10^3	27	-0.96 ± 0.30	-0.0006 ± 0.0053	-0.96 ± 0.30
10^4	27	-1.02 ± 0.09	-1.6×10^{-4}	-1.02 ± 0.09

Table 3.15: Second normal stress difference data as a function of Pe from Stokesian Dynamics at $\phi = 0.40$. *Data obtained from Phung (1993).

$\phi = 0.40$							
Pe	N	$\langle g(2) \rangle_\Omega$	D_0^s	$D_0^{s,r}$	D_{xx}	D_{yy}	D_{zz}
0.00*	27		0.269	0.667		0.103	0.131
0.01*	27	3.70	0.221	0.618		0.115	0.101
0.1*	27	3.55	0.222	0.616		0.120	0.104
1*	27	4.06	0.216	0.604		0.135	0.144
3.00	27	5.56	0.205	0.582		0.444	0.162
10.00	27	9.76	0.188	0.546		0.805	0.616
30.00	27	18.4	0.170	0.503		0.837	1.475
10^2	27	29.6	0.155	0.463		5.065	2.270
3×10^2	27	38.2	0.140	0.424		6.245	9.709
10^3	27	44.0	0.132	0.394		37.72	37.51
10^4	27	47.7	0.121	0.354		572.4	180.7

Table 3.16: Data for the contact values of the radial distribution function, short- and long-time self-diffusivities from Stokesian Dynamics at $\phi = 0.40$. *Data obtained from Phung (1993). Simulations performed before method for calculating $D^s_{\infty,xx}$ was implemented into the code.

$\phi = 0.419$						
Pe	N	Δt	$NSTEPS$	η_r^H	η_r^B	η_r^T
0.01*	27	5×10^{-4}	200 000	3.78 ± 0.02	4.93 ± 3.92	9.71 ± 3.92
0.1*	27	10^{-3}	100 000	3.73 ± 0.07	4.24 ± 0.34	8.96 ± 0.35
1*	27	10^{-3}	100 000	3.82 ± 0.01	2.40 ± 0.01	7.23 ± 0.02
3.00	27	5×10^{-4}	200 000	4.02 ± 0.19	1.46 ± 0.15	6.49 ± 0.34
10.00	27	5×10^{-4}	200 000	4.38 ± 0.29	0.68 ± 0.12	6.06 ± 0.42
30.00	27	5×10^{-4}	200 000	5.05 ± 0.22	0.37 ± 0.04	6.41 ± 0.25
10^2	27	5×10^{-4}	200 000	5.36 ± 0.19	0.12 ± 0.01	6.49 ± 0.21
3×10^2	27	5×10^{-4}	200 000	6.06 ± 0.33	0.052 ± 0.006	7.11 ± 0.33
10^3	27	5×10^{-4}	200 000	6.70 ± 0.45	0.017 ± 0.002	7.71 ± 0.46
10^4	27	2.5×10^{-4}	400 000	7.35 ± 0.50	0.002 ± 0.000	8.35 ± 0.50

Table 3.17: Relative viscosity data as a function of Pe from Stokesian Dynamics at $\phi = 0.419$. *Data obtained from Phung (1993).

$\phi = 0.419$				
Pe	N	$N_1^H/\eta\dot{\gamma}$	$N_1^B/\eta\dot{\gamma}$	$N_1^T/\eta\dot{\gamma}$
0.01*	27	-0.139 ± 0.010	66.8 ± 21.1	66.5 ± 21.1
0.1*	27	-0.172 ± 0.008	1.10 ± 0.71	0.92 ± 0.71
1*	27	-0.28 ± 0.01	0.74 ± 0.07	0.47 ± 0.07
3.00	27	-0.34 ± 0.10	0.41 ± 0.21	0.07 ± 0.22
10.00	27	-0.26 ± 0.16	0.52 ± 0.16	0.26 ± 0.30
30.00	27	-0.83 ± 0.35	0.12 ± 0.14	-0.71 ± 0.47
10^2	27	-0.88 ± 0.15	0.058 ± 0.045	-0.82 ± 0.12
3×10^2	27	-0.80 ± 0.15	0.039 ± 0.011	-0.76 ± 0.15
10^3	27	-1.42 ± 0.31	0.007 ± 0.006	-1.42 ± 0.31
10^4	27	-1.08 ± 0.37	0.001 ± 0.002	-1.08 ± 0.37

Table 3.18: First normal stress difference data as a function of Pe from Stokesian Dynamics at $\phi = 0.419$. *Data obtained from Phung (1993).

$\phi = 0.419$				
Pe	N	$N_2^H/\eta\dot{\gamma}$	$N_2^B/\eta\dot{\gamma}$	$N_2^T/\eta\dot{\gamma}$
0.01^*	27	-0.109 ± 0.021	-72.9 ± 27.0	-73.01 ± 27.0
0.1^*	27	-0.056 ± 0.015	-0.88 ± 0.73	-0.93 ± 0.71
1^*	27	-0.29 ± 0.01	-0.63 ± 0.06	-0.92 ± 0.07
3.00	27	-0.58 ± 0.09	-0.53 ± 0.19	-1.10 ± 0.26
10.00	27	-0.82 ± 0.29	-0.38 ± 0.12	-1.21 ± 0.39
30.00	27	-0.85 ± 0.14	-0.045 ± 0.089	-0.89 ± 0.21
10^2	27	-1.04 ± 0.12	-0.046 ± 0.032	-1.09 ± 0.15
3×10^2	27	-1.17 ± 0.38	-0.009 ± 0.023	-1.17 ± 0.40
10^3	27	-1.29 ± 0.49	-0.001 ± 0.009	-1.29 ± 0.50
10^4	27	-1.19 ± 0.21	-4.5×10^{-4}	-1.19 ± 0.21

Table 3.19: Second normal stress difference data as a function of Pe from Stokesian Dynamics at $\phi = 0.419$. *Data obtained from Phung (1993).

$\phi = 0.419$							
Pe	N	$\langle g(2) \rangle_\Omega$	D_0^s	$D_0^{s,r}$	D_{xx}	D_{yy}	D_{zz}
0.01^*	27	3.84	0.203	0.593		0.074	0.071
0.1^*	27	3.87	0.203	0.593		0.085	0.087
1^*	27	4.57	0.196	0.578		0.210	0.153
3.00	27	6.62	0.186	0.553		0.368	0.239
10.00	27	11.2	0.169	0.517		0.394	0.522
30.00	27	21.6	0.150	0.472		1.543	0.514
10^2	27	32.1	0.138	0.438		3.548	3.229
3×10^2	27	41.3	0.122	0.397		18.07	9.305
10^3	27	47.3	0.110	0.360		63.51	12.22
10^4	27	53.1	0.098	0.313		622.5	171.5

Table 3.20: Data for the contact values of the radial distribution function, short- and long-time self-diffusivities from Stokesian Dynamics at $\phi = 0.419$. *Data obtained from Phung (1993). Simulations performed before method for calculating $D^s_{\infty,xx}$ was implemented into the code.

$\phi = 0.45$						
Pe	N	Δt	$NSTEPS$	η_r^H	η_r^B	η_r^T
0.01*	27	5×10^{-4}	1 000 000	4.61 ± 0.01	9.0 ± 9.1	14.61 ± 9.11
0.10	27	5×10^{-4}	1 000 000	4.54 ± 0.05	7.00 ± 1.11	12.54 ± 1.12
0.30	27	5×10^{-4}	200 000	4.60 ± 0.16	5.79 ± 0.69	11.39 ± 0.76
1.00	27	5×10^{-4}	200 000	4.78 ± 0.13	3.70 ± 0.27	9.48 ± 0.40
3.00	27	5×10^{-4}	200 000	4.91 ± 0.29	2.00 ± 0.27	7.90 ± 0.54
5.00	27	5×10^{-4}	200 000	5.07 ± 0.27	1.46 ± 0.21	7.52 ± 0.48
7.00	27	5×10^{-4}	200 000	5.28 ± 0.18	1.23 ± 0.07	7.51 ± 0.24
10.00	27	5×10^{-4}	200 000	5.59 ± 0.47	1.07 ± 0.21	7.66 ± 0.68
20.00	27	5×10^{-4}	200 000	6.30 ± 0.30	0.76 ± 0.09	8.07 ± 0.39
10^2	27	5×10^{-4}	200 000	7.56 ± 0.41	0.22 ± 0.03	8.78 ± 0.44
2×10^2	27	5×10^{-4}	200 000	8.02 ± 0.28	0.12 ± 0.01	9.14 ± 0.29
10^3	27	5×10^{-4}	200 000	9.25 ± 0.59	0.029 ± 0.004	10.28 ± 0.59
10^4	27	2.5×10^{-4}	400 000	11.64 ± 1.11	0.004 ± 0.001	12.64 ± 1.11

Table 3.21: Relative viscosity data as a function of Pe from Stokesian Dynamics at $\phi = 0.45$. *Data obtained from Phung (1993).

$\phi = 0.45$				
Pe	N	$N_1^H/\eta\dot{\gamma}$	$N_1^B/\eta\dot{\gamma}$	$N_1^T/\eta\dot{\gamma}$
0.01*	27	-0.204 ± 0.009	20.9 ± 14.9	20.7 ± 14.9
0.10	27	-0.161 ± 0.072	4.29 ± 3.04	4.13 ± 3.08
0.30	27	-0.015 ± 0.145	5.03 ± 2.65	5.01 ± 2.72
1.00	27	-0.33 ± 0.17	1.28 ± 0.51	0.95 ± 0.57
3.00	27	-0.59 ± 0.08	0.14 ± 0.11	-0.45 ± 0.17
5.00	27	-0.70 ± 0.20	0.042 ± 0.39	-0.65 ± 0.57
7.00	27	-0.74 ± 0.08	0.21 ± 0.14	-0.53 ± 0.12
10.00	27	-0.60 ± 0.37	0.36 ± 0.40	-0.25 ± 0.76
20.00	27	-1.16 ± 0.47	-0.037 ± 0.21	-1.20 ± 0.67
10^2	27	-1.43 ± 0.34	0.062 ± 0.055	-1.37 ± 0.38
2×10^2	27	-1.17 ± 0.37	0.087 ± 0.048	-1.09 ± 0.41
10^3	27	-1.83 ± 0.78	0.019 ± 0.013	-1.81 ± 0.79
10^4	27	-1.13 ± 1.27	0.003 ± 0.001	-1.12 ± 1.27

Table 3.22: First normal stress difference data as a function of Pe from Stokesian Dynamics at $\phi = 0.45$. *Data obtained from Phung (1993).

$\phi = 0.45$				
Pe	N	$N_2^H/\eta\dot{\gamma}$	$N_2^B/\eta\dot{\gamma}$	$N_2^T/\eta\dot{\gamma}$
0.01*	27	-0.092 ± 0.011	-10.34 ± 5.11	-10.43 ± 5.10
0.10	27	-0.041 ± 0.042	-3.03 ± 2.91	-3.07 ± 2.94
0.30	27	-0.317 ± 0.991	-3.09 ± 2.65	-3.41 ± 2.59
1.00	27	-0.54 ± 0.18	-1.59 ± 1.00	-2.12 ± 1.11
3.00	27	-0.66 ± 0.24	-0.55 ± 0.56	-1.21 ± 0.77
5.00	27	-0.76 ± 0.18	-0.37 ± 0.28	-1.13 ± 0.33
7.00	27	-0.92 ± 0.14	-0.40 ± 0.13	-1.32 ± 0.14
10.00	27	-1.03 ± 0.28	-0.36 ± 0.22	-1.39 ± 0.47
20.00	27	-1.25 ± 0.19	-0.18 ± 0.16	-1.43 ± 0.34
10^2	27	-1.60 ± 0.50	-0.014 ± 0.065	-1.62 ± 0.56
2×10^2	27	-1.84 ± 0.32	-0.038 ± 0.048	-1.87 ± 0.36
10^3	27	-1.60 ± 0.37	-0.003 ± 0.009	-1.61 ± 0.38
10^4	27	-2.44 ± 0.51	-6.2×10^{-4}	-2.44 ± 0.51

Table 3.23: Second normal stress difference data as a function of Pe from Stokesian Dynamics at $\phi = 0.45$. *Data obtained from Phung (1993).

$\phi = 0.45$							
Pe	N	$\langle g(2) \rangle_\Omega$	D_0^s	$D_0^{s,r}$	D_{xx}	D_{yy}	D_{zz}
0.00*	27		0.210	0.604		0.059	0.055
0.01*	27	4.20	0.172	0.553		0.068	0.058
0.10	27	4.47	0.177	0.554		0.069	0.096
0.30	27	4.82	0.174	0.549		0.115	0.083
1.00	27	5.80	0.168	0.534		0.146	0.151
3.00	27	7.73	0.159	0.514		0.311	0.257
5.00	27	9.22	0.154	0.503		0.636	0.425
7.00	27	10.9	0.149	0.492		0.846	0.405
10.00	27	13.6	0.140	0.473		0.688	0.452
20.00	27	20.8	0.129	0.446		1.247	0.885
10^2	27	39.0	0.105	0.383		2.349	5.457
2×10^2	27	43.1	0.099	0.364		6.788	3.374
10^3	27	49.9	0.088	0.321		47.27	22.58
10^4	27	59.2	0.069	0.256		644.5	230.6

Table 3.24: Data for the contact values of the radial distribution function, short- and long-time self-diffusivities from Stokesian Dynamics at $\phi = 0.45$. *Data obtained from Phung (1993). Simulations performed before method for calculating $D^s_{\infty,xx}$ was implemented into the code.

$\phi = 0.47$						
Pe	N	Δt	$NSTEPS$	η_r^H	η_r^B	η_r^T
0.01*	27	5×10^{-4}	400 000	5.19 ± 0.03	14.9 ± 10.2	21.1 ± 10.2
0.1*	27	5×10^{-4}	200 000	5.16 ± 0.01	14.2 ± 3.06	20.4 ± 3.10
1.00	27	10^{-3}	100 000	5.57 ± 0.25	4.99 ± 0.78	11.6 ± 1.03
3.00	27	5×10^{-4}	200 000	5.58 ± 0.58	2.36 ± 0.56	8.94 ± 1.14
10.00	27	5×10^{-4}	200 000	6.67 ± 0.46	1.43 ± 0.20	9.10 ± 0.65
30.00	27	5×10^{-4}	200 000	6.93 ± 0.34	0.59 ± 0.06	8.51 ± 0.40
10^2	27	5×10^{-4}	200 000	9.30 ± 0.45	0.32 ± 0.04	10.62 ± 0.49
3×10^2	27	5×10^{-4}	200 000	10.50 ± 0.39	0.12 ± 0.01	11.62 ± 0.40
10^3	27	5×10^{-4}	200 000	11.13 ± 0.49	0.040 ± 0.004	12.17 ± 0.50
10^4	27	2.5×10^{-4}	400 000	15.13 ± 0.59	0.005 ± 0.000	16.13 ± 0.59

Table 3.25: Relative viscosity data as a function of Pe from Stokesian Dynamics at $\phi = 0.47$. *Data obtained from Phung (1993).

$\phi = 0.47$				
Pe	N	$N_1^H/\eta\dot{\gamma}$	$N_1^B/\eta\dot{\gamma}$	$N_1^T/\eta\dot{\gamma}$
0.01*	27	-0.044 ± 0.001	103.2 ± 21.2	103.2 ± 21.2
0.1*	27	-0.188 ± 0.013	7.47 ± 1.18	7.28 ± 1.18
1.00	27	-0.38 ± 0.18	1.67 ± 0.64	1.29 ± 0.74
3.00	27	-0.57 ± 0.20	0.24 ± 0.58	-0.33 ± 0.64
10.00	27	-1.06 ± 0.25	0.18 ± 0.29	-0.88 ± 0.50
30.00	27	-0.97 ± 0.48	0.21 ± 0.26	-0.77 ± 0.72
10^2	27	-1.49 ± 0.65	0.10 ± 0.14	-1.39 ± 0.79
3×10^2	27	-1.22 ± 0.61	0.078 ± 0.020	-1.15 ± 0.63
10^3	27	-1.91 ± 1.02	0.019 ± 0.021	-1.89 ± 1.04
10^4	27	-0.79 ± 0.96	0.002 ± 0.001	-0.79 ± 0.96

Table 3.26: First normal stress difference data as a function of Pe from Stokesian Dynamics at $\phi = 0.47$. *Data obtained from Phung (1993).

$\phi = 0.47$				
Pe	N	$N_2^H/\eta\dot{\gamma}$	$N_2^B/\eta\dot{\gamma}$	$N_2^T/\eta\dot{\gamma}$
0.01*	27	-0.027 ± 0.013	-8.08 ± 0.81	-8.10 ± 0.82
0.1*	27	-0.244 ± 0.163	-3.75 ± 0.88	-3.99 ± 0.89
1.00	27	-0.69 ± 0.10	-1.88 ± 0.60	-2.57 ± 0.67
3.00	27	-0.81 ± 0.17	-0.74 ± 0.72	-1.55 ± 0.86
10.00	27	-1.03 ± 0.25	-0.30 ± 0.27	-1.34 ± 0.47
30.00	27	-0.83 ± 0.52	0.022 ± 0.135	-0.81 ± 0.64
10^2	27	-1.90 ± 0.66	-0.042 ± 0.135	-1.94 ± 0.79
3×10^2	27	-2.65 ± 0.57	-0.039 ± 0.028	-2.69 ± 0.60
10^3	27	-1.98 ± 0.62	0.0086 ± 0.0208	-1.98 ± 0.64
10^4	27	-3.03 ± 0.96	0.0016 ± 0.0026	-3.03 ± 0.96

Table 3.27: Second normal stress difference data as a function of Pe from Stokesian Dynamics at $\phi = 0.47$. *Data obtained from Phung (1993).

$\phi = 0.47$							
Pe	N	$\langle g(2) \rangle_\Omega$	D_0^s	$D_0^{s,r}$	D_{xx}	D_{yy}	D_{zz}
0.01*	27	4.79	0.162	0.531		0.042	0.043
0.1*	27	4.76	0.161	0.530		0.078	0.040
1.00	27	6.58	0.150	0.506		0.150	0.097
3.00	27	8.46	0.144	0.490		0.276	0.093
10.00	27	16.5	0.123	0.443		0.650	0.200
30.00	27	26.3	0.109	0.408		0.386	0.621
10^2	27	41.8	0.091	0.357		4.722	3.451
3×10^2	27	48.1	0.081	0.324		13.60	16.17
10^3	27	53.9	0.072	0.292		42.61	24.86
10^4	27	62.3	0.055	0.228		459.0	226.9

Table 3.28: Data for the contact values of the radial distribution function, short- and long-time self-diffusivities from Stokesian Dynamics at $\phi = 0.47$. *Data obtained from Phung (1993). Simulations performed before method for calculating $D^s_{\infty,xx}$ was implemented into the code.

$\phi = 0.49$						
Pe	N	Δt	$NSTEPS$	η_r^H	η_r^B	η_r^T
0.01*	27	5×10^{-4}	280 000	6.05 ± 0.50	22.7 ± 13.7	29.72 ± 13.8
0.1*	27	5×10^{-4}	100 000	6.01 ± 1.25	15.1 ± 5.01	22.12 ± 5.85
1*	27	10^{-3}	100 000	6.25 ± 0.03	5.95 ± 0.07	13.19 ± 0.10
3.00	27	5×10^{-4}	200 000	6.85 ± 0.50	3.52 ± 0.67	11.37 ± 1.17
10.00	27	5×10^{-4}	200 000	6.53 ± 1.15	1.31 ± 0.53	8.84 ± 1.68
50.00	27	5×10^{-4}	200 000	9.60 ± 0.28	0.65 ± 0.04	11.25 ± 0.32
10^2	27	5×10^{-4}	200 000	10.50 ± 1.20	0.40 ± 0.10	11.90 ± 1.29
2×10^2	27	5×10^{-4}	200 000	11.49 ± 0.71	0.23 ± 0.03	12.72 ± 0.74
10^3	27	5×10^{-4}	200 000	14.66 ± 1.25	0.063 ± 0.010	15.73 ± 1.26
10^4	27	2.5×10^{-4}	400 000	20.17 ± 1.96	0.009 ± 0.002	21.18 ± 1.96

Table 3.29: Relative viscosity data as a function of Pe from Stokesian Dynamics at $\phi = 0.49$. *Data obtained from Phung (1993).

$\phi = 0.49$				
Pe	N	$N_1^H/\eta\dot{\gamma}$	$N_1^B/\eta\dot{\gamma}$	$N_1^T/\eta\dot{\gamma}$
0.01*	27	-0.189 ± 0.015	67.9 ± 4.36	67.8 ± 4.37
0.1*	27	-0.212 ± 0.018	1.30 ± 0.67	1.09 ± 0.67
1*	27	-0.51 ± 0.02	0.54 ± 0.10	0.03 ± 0.08
3.00	27	-0.88 ± 0.35	0.42 ± 0.83	-0.47 ± 1.11
10.00	27	-0.82 ± 0.73	-0.32 ± 0.72	-1.14 ± 1.36
50.00	27	-0.75 ± 0.55	0.37 ± 0.24	-0.38 ± 0.79
10^2	27	-0.49 ± 0.72	0.33 ± 0.12	-0.16 ± 0.82
2×10^2	27	-1.46 ± 0.69	0.15 ± 0.05	-1.31 ± 0.73
10^3	27	-2.11 ± 1.03	0.033 ± 0.093	-2.08 ± 1.03
10^4	27	0.29 ± 3.45	0.007 ± 0.005	0.30 ± 3.46

Table 3.30: First normal stress difference data as a function of Pe from Stokesian Dynamics at $\phi = 0.49$. *Data obtained from Phung (1993).

$\phi = 0.49$				
Pe	N	$N_2^H/\eta\dot{\gamma}$	$N_2^B/\eta\dot{\gamma}$	$N_2^T/\eta\dot{\gamma}$
0.01*	27	-0.133 ± 0.006	-75.5 ± 9.31	-75.6 ± 9.31
0.1*	27	-0.278 ± 0.006	-2.91 ± 0.69	-3.19 ± 0.69
1*	27	-0.77 ± 0.01	-0.69 ± 0.09	-1.45 ± 0.10
3.00	27	-1.02 ± 0.23	-0.53 ± 1.00	-1.55 ± 1.19
10.00	27	-1.01 ± 0.15	-0.12 ± 0.74	-1.13 ± 0.76
50.00	27	-1.64 ± 0.45	-0.083 ± 0.153	-1.72 ± 0.55
10^2	27	-1.07 ± 0.31	0.087 ± 0.065	-0.99 ± 0.33
2×10^2	27	-1.78 ± 0.86	0.034 ± 0.085	-1.75 ± 0.93
10^3	27	-2.76 ± 0.91	0.011 ± 0.009	-2.75 ± 0.92
10^4	27	-4.49 ± 2.05	0.0016 ± 0.0067	-4.49 ± 2.06

Table 3.31: Second normal stress difference data as a function of Pe from Stokesian Dynamics at $\phi = 0.49$. *Data obtained from Phung (1993).

$\phi = 0.49$							
Pe	N	$\langle g(2) \rangle_\Omega$	D_0^s	$D_0^{s,r}$	D_{xx}	D_{yy}	D_{zz}
0.01*	27	4.91	0.147	0.508		0.023	0.043
0.1*	27	5.49	0.142	0.500		0.041	0.060
1*	27	7.25	0.134	0.478		0.160	0.089
3.00	27	10.5	0.124	0.457		0.361	0.311
10.00	27	15.0	0.122	0.442		0.403	0.378
50.00	27	36.6	0.086	0.359		1.107	1.449
10^2	27	45.2	0.074	0.326		2.510	1.638
2×10^2	27	49.5	0.070	0.309		8.187	4.880
10^3	27	58.0	0.056	0.262		28.32	23.72
10^4	27	64.6	0.044	0.208		307.0	583.2

Table 3.32: Data for the contact values of the radial distribution function, short- and long-time self-diffusivities from Stokesian Dynamics at $\phi = 0.49$. *Data obtained from Phung (1993). Simulations performed before method for calculating $D^s_{\infty,xx}$ was implemented into the code.

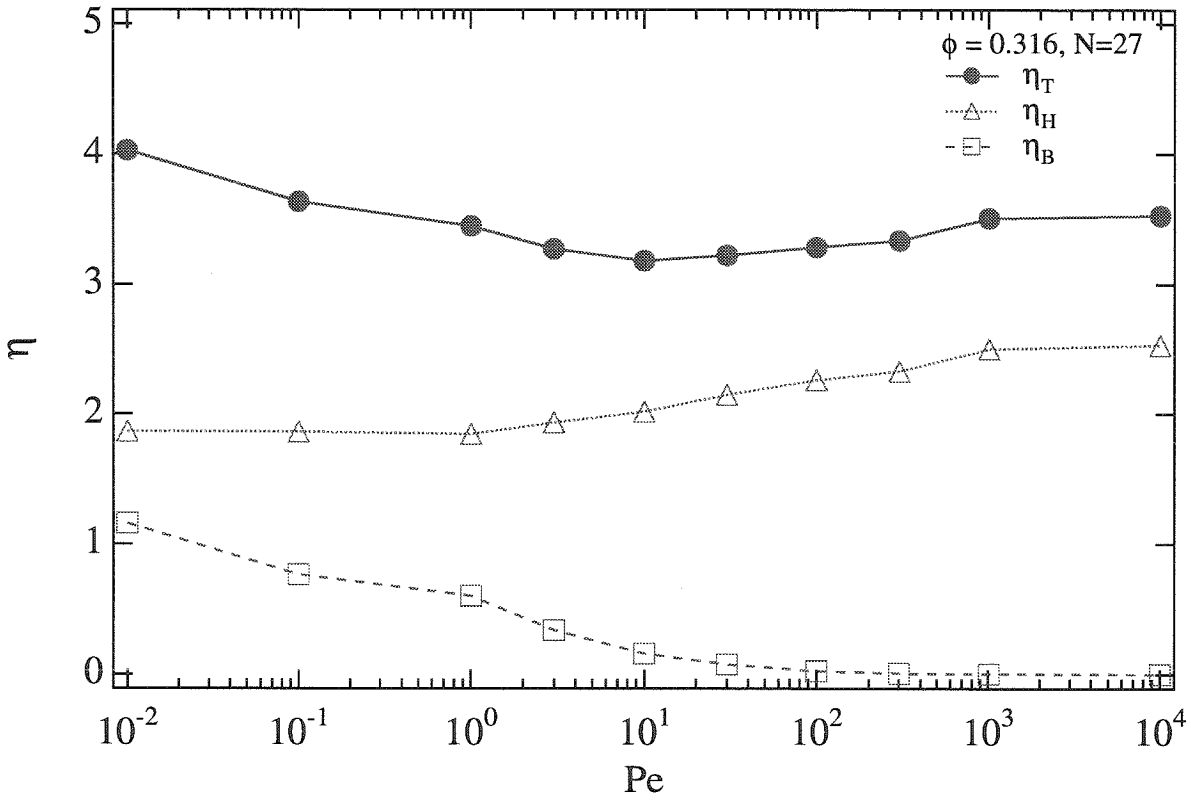

Figure 3.25: Hydrodynamic and Brownian contributions to the relative viscosity as a function of Pe from Stokesian Dynamics for $\phi = 0.316$, $N = 27$.

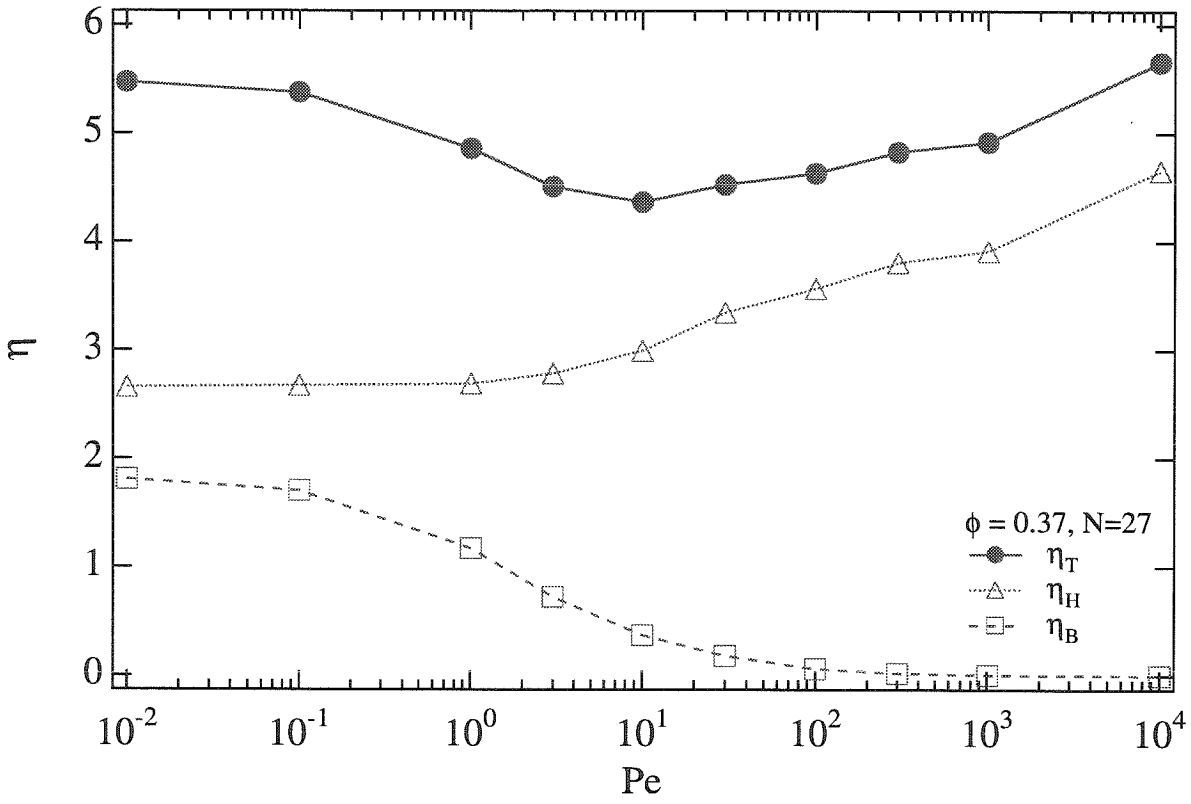

Figure 3.26: Hydrodynamic and Brownian contributions to the relative viscosity as a function of Pe from Stokesian Dynamics for $\phi = 0.37$, $N = 27$.

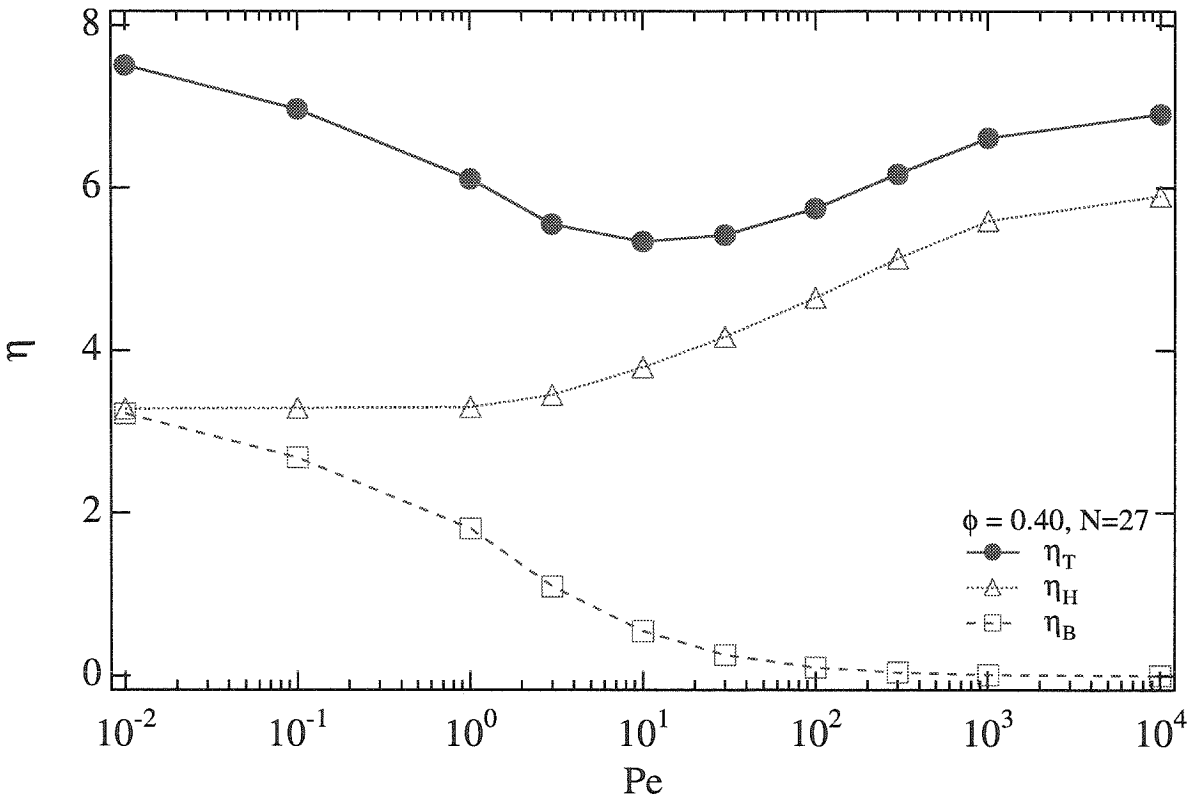

Figure 3.27: Hydrodynamic and Brownian contributions to the relative viscosity as a function of Pe from Stokesian Dynamics for $\phi = 0.40$, $N = 27$.

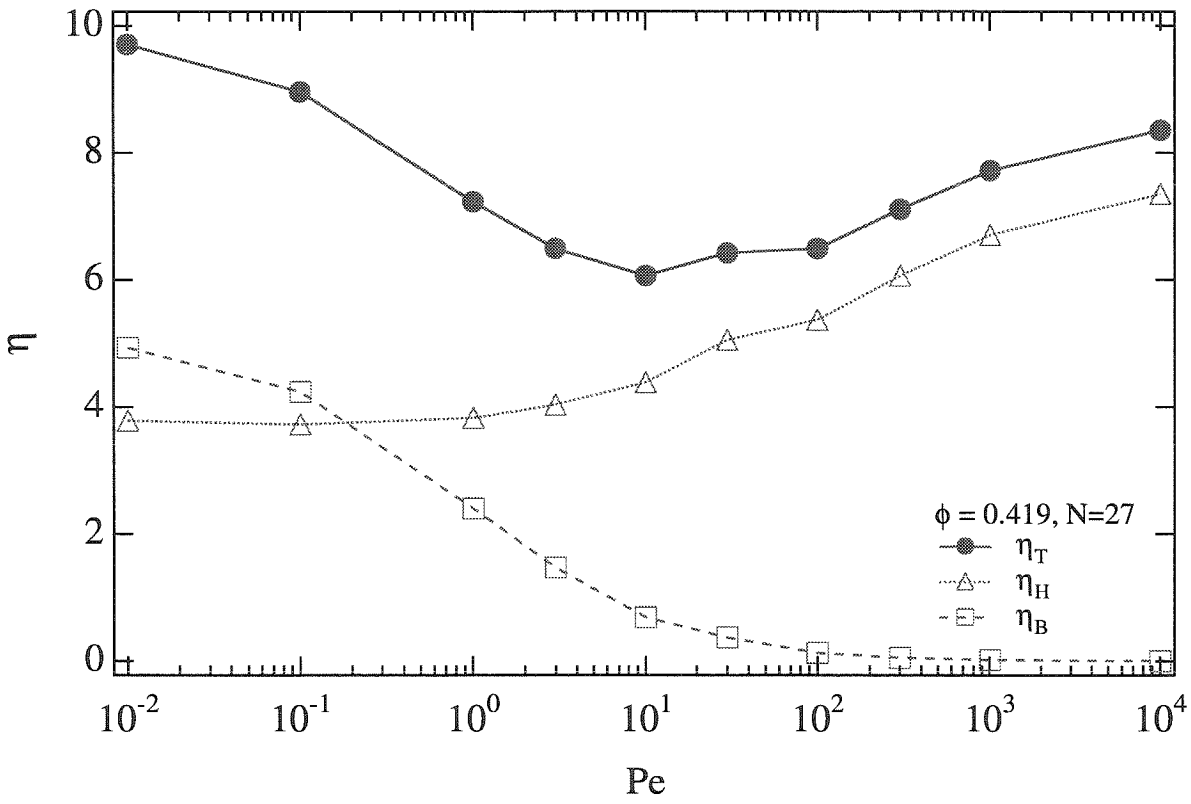

Figure 3.28: Hydrodynamic and Brownian contributions to the relative viscosity as a function of Pe from Stokesian Dynamics for $\phi = 0.419$, $N = 27$.

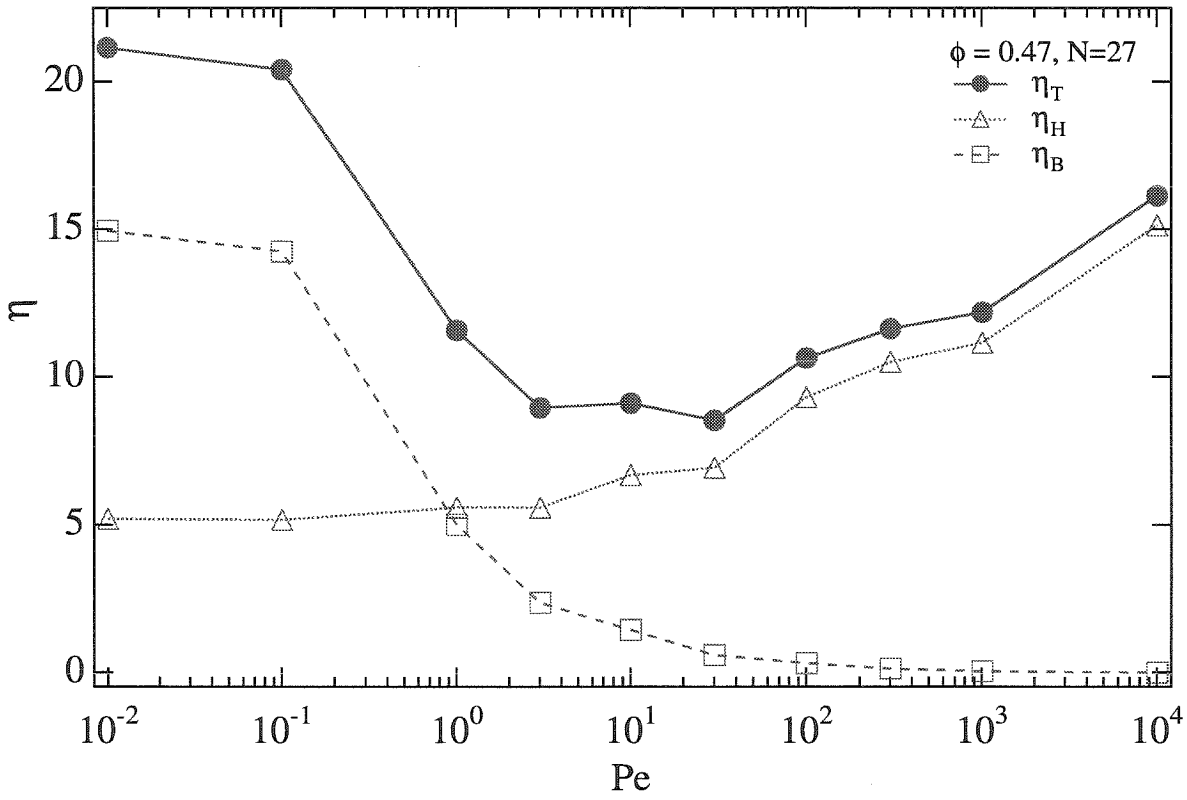

Figure 3.29: Hydrodynamic and Brownian contributions to the relative viscosity as a function of Pe from Stokesian Dynamics for $\phi = 0.47$, $N = 27$.

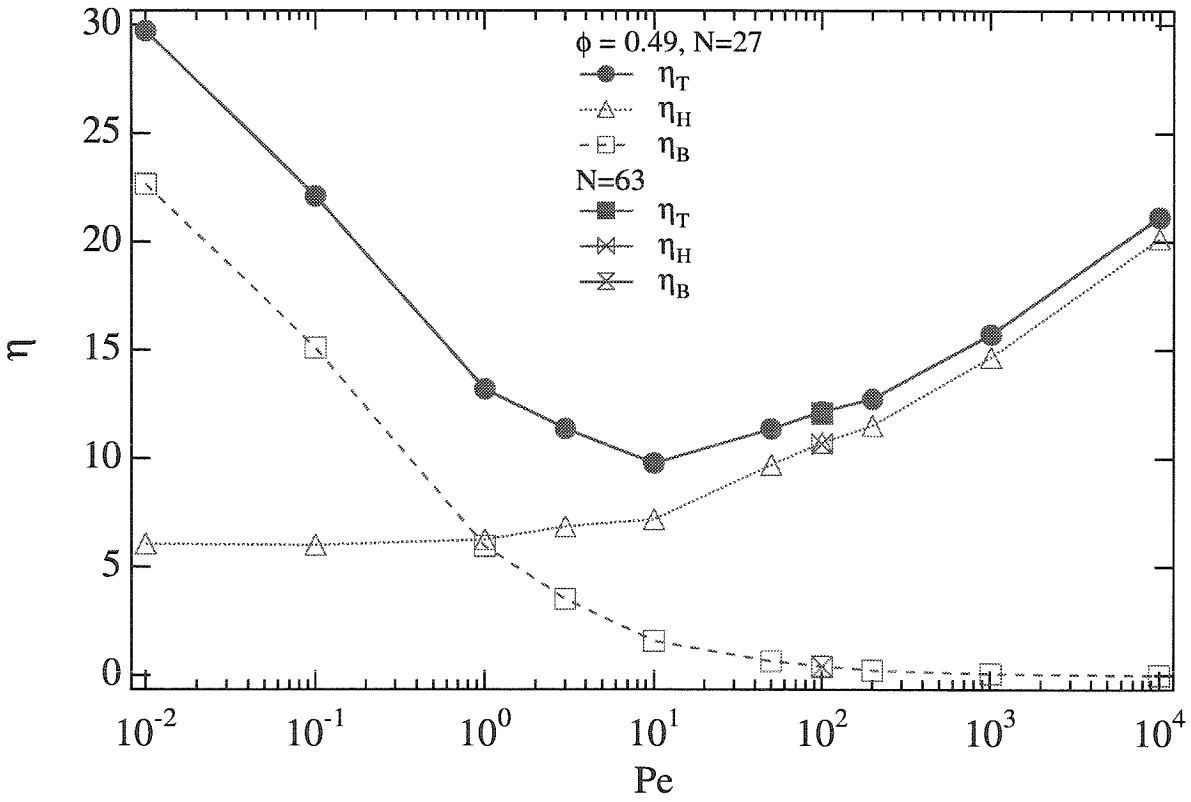

Figure 3.30: Hydrodynamic and Brownian contributions to the relative viscosity as a function of Pe from Stokesian Dynamics for $\phi = 0.49$, $N = 27$.

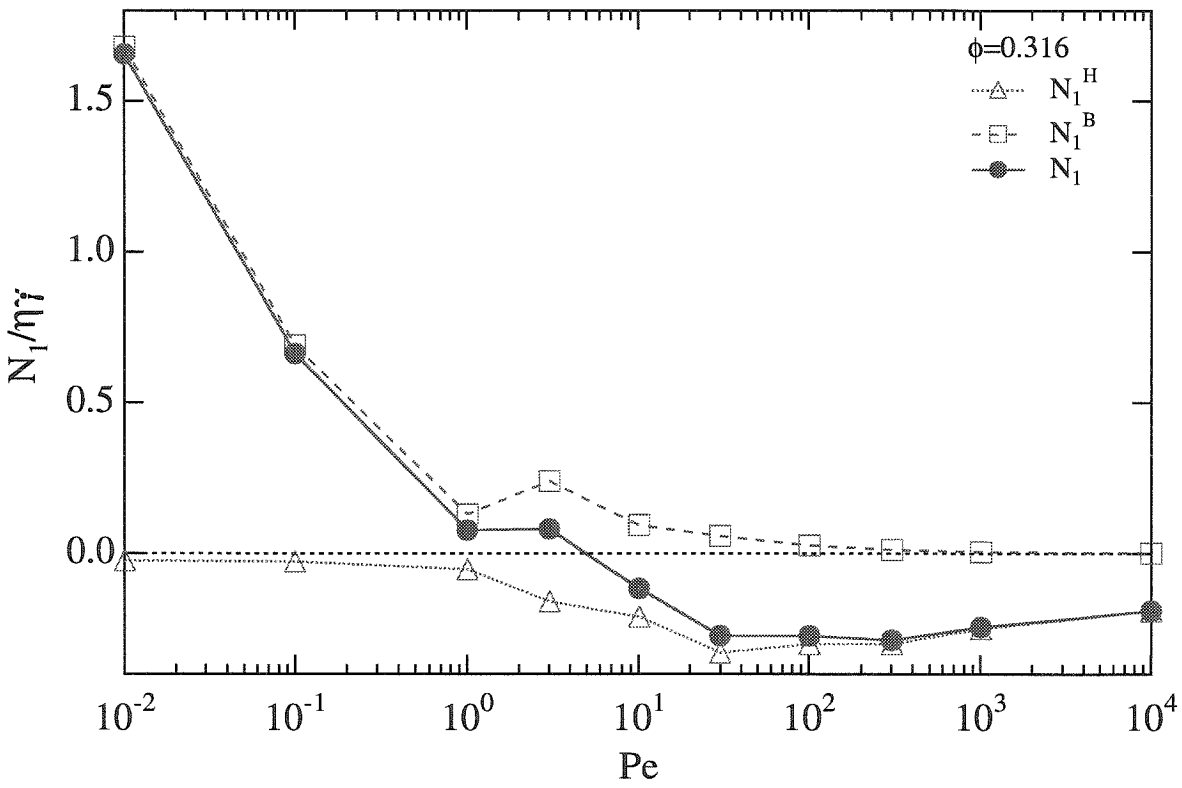

Figure 3.31: Hydrodynamic and Brownian contributions to the first normal stress difference, nondimensionalized by $\eta\dot{\gamma}$, as a function of Pe from Stokesian Dynamics for $\phi = 0.316$, $N = 27$.

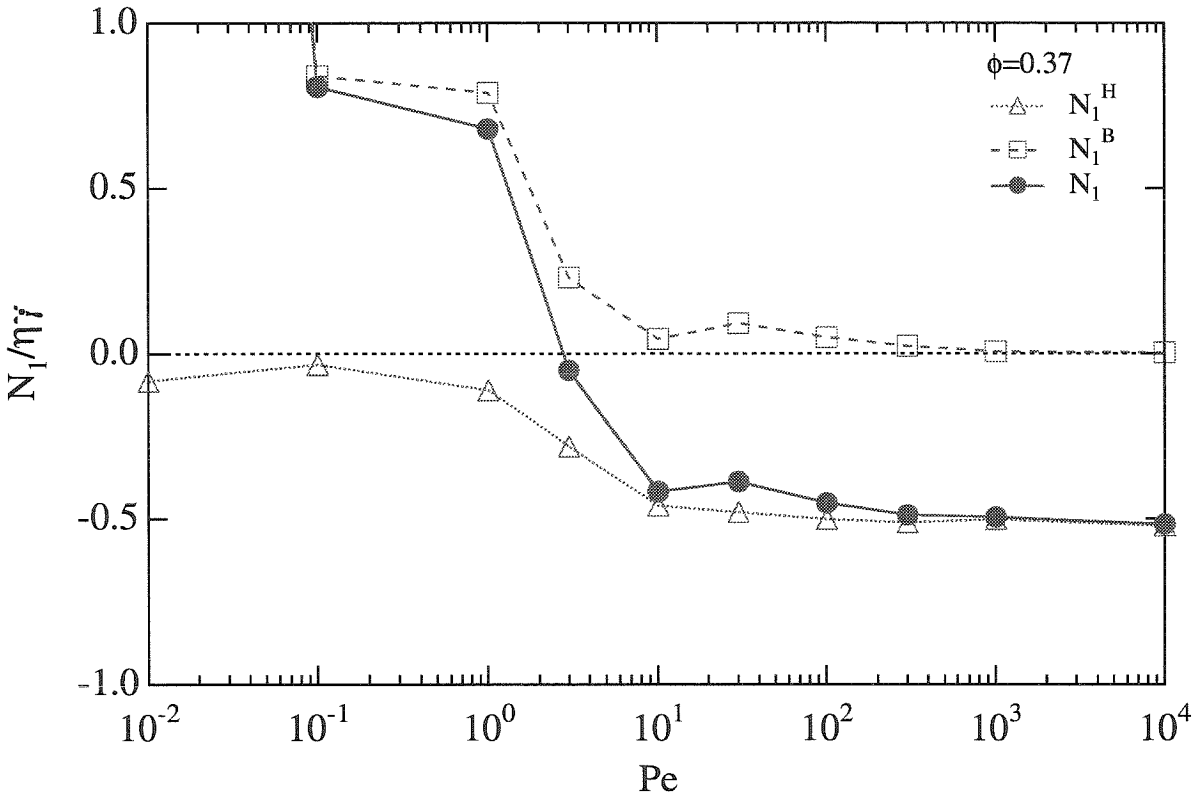

Figure 3.32: Hydrodynamic and Brownian contributions to the first normal stress difference, nondimensionalized by $\eta\dot{\gamma}$, as a function of Pe from Stokesian Dynamics for $\phi = 0.37$, $N = 27$.

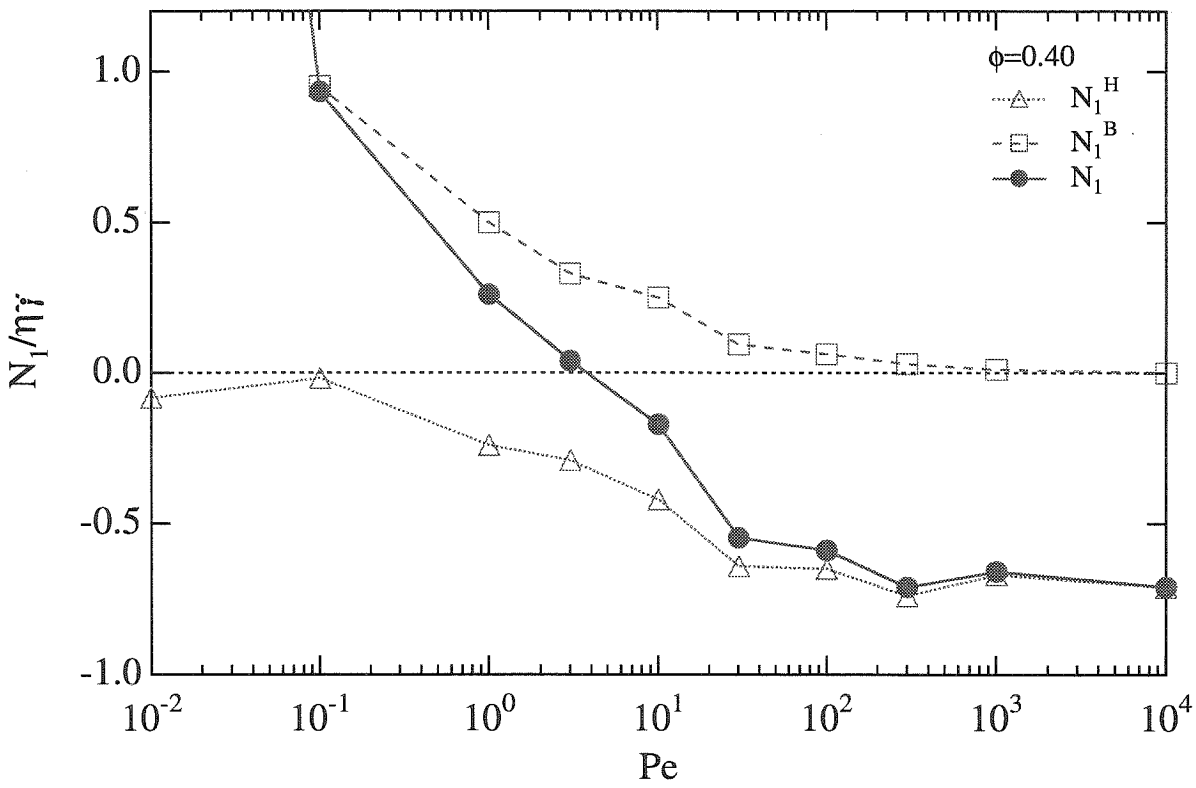

Figure 3.33: Hydrodynamic and Brownian contributions to the first normal stress difference, nondimensionalized by $\eta\dot{\gamma}$, as a function of Pe from Stokesian Dynamics for $\phi = 0.40$, $N = 27$.

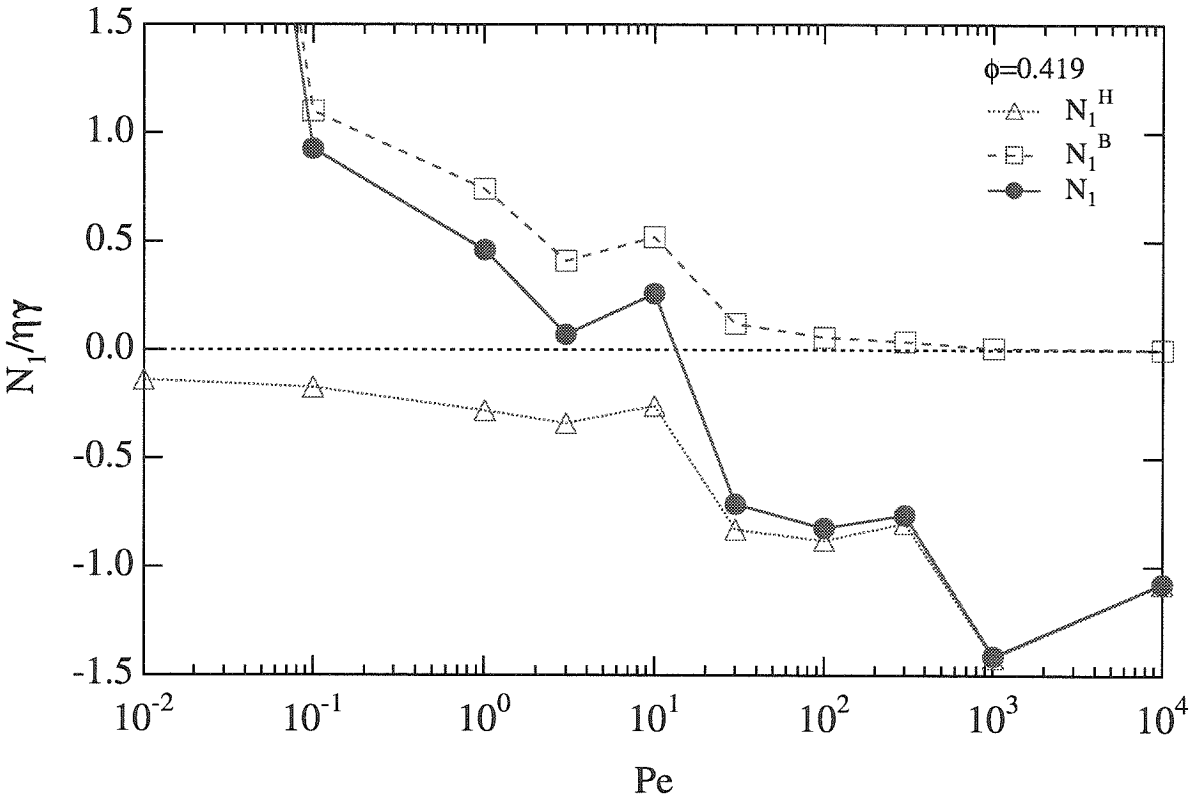

Figure 3.34: Hydrodynamic and Brownian contributions to the first normal stress difference, nondimensionalized by $\eta\dot{\gamma}$, as a function of Pe from Stokesian Dynamics for $\phi = 0.419$, $N = 27$.

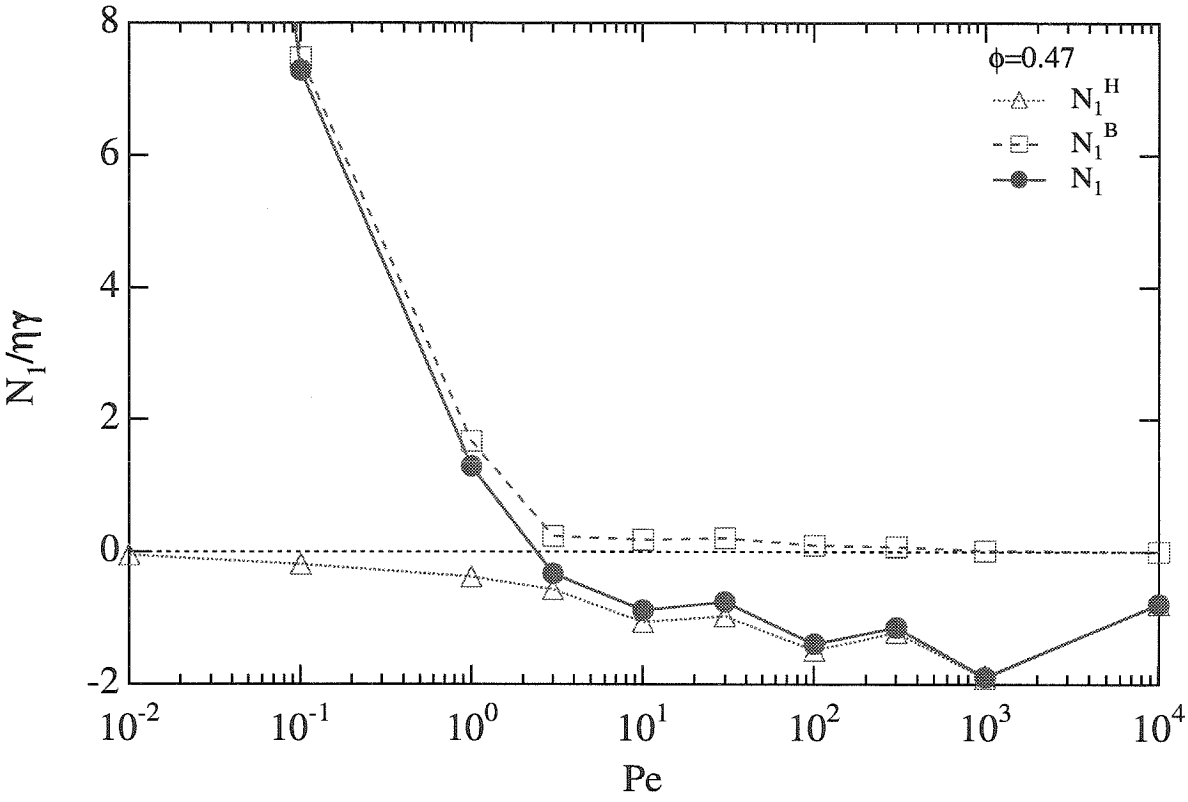

Figure 3.35: Hydrodynamic and Brownian contributions to the first normal stress difference, nondimensionalized by $\eta\dot{\gamma}$, as a function of Pe from Stokesian Dynamics for $\phi = 0.47$, $N = 27$.

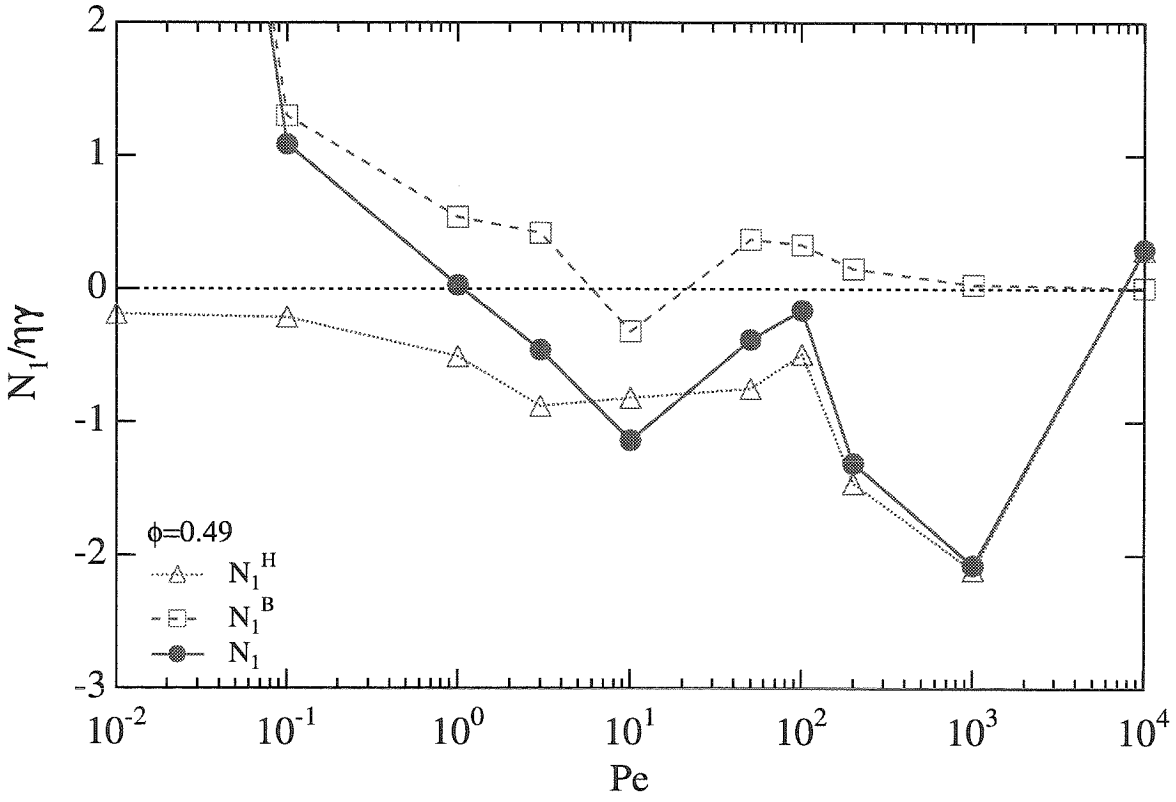

Figure 3.36: Hydrodynamic and Brownian contributions to the first normal stress difference, nondimensionalized by $\eta\dot{\gamma}$, as a function of Pe from Stokesian Dynamics for $\phi = 0.49$, $N = 27$.

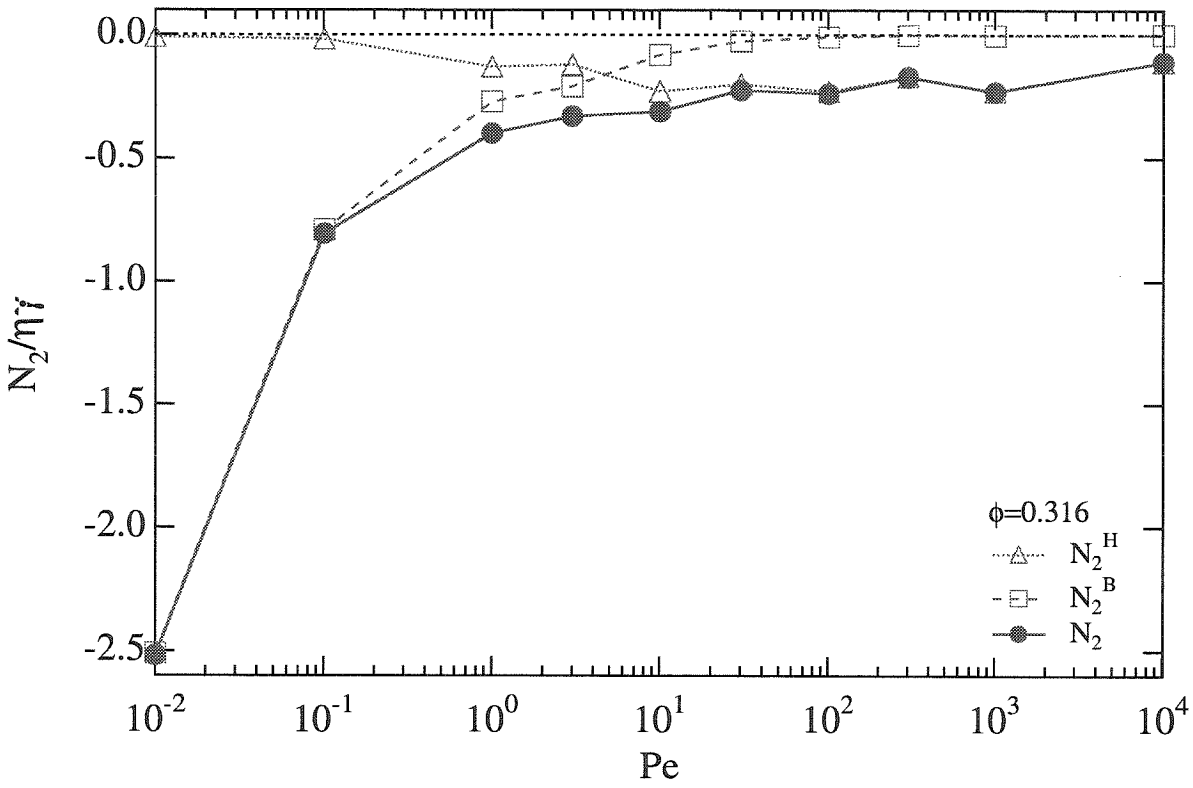

Figure 3.37: Hydrodynamic and Brownian contributions to the second normal stress difference, nondimensionalized by $\eta\dot{\gamma}$, as a function of Pe from Stokesian Dynamics for $\phi = 0.316$, $N = 27$.

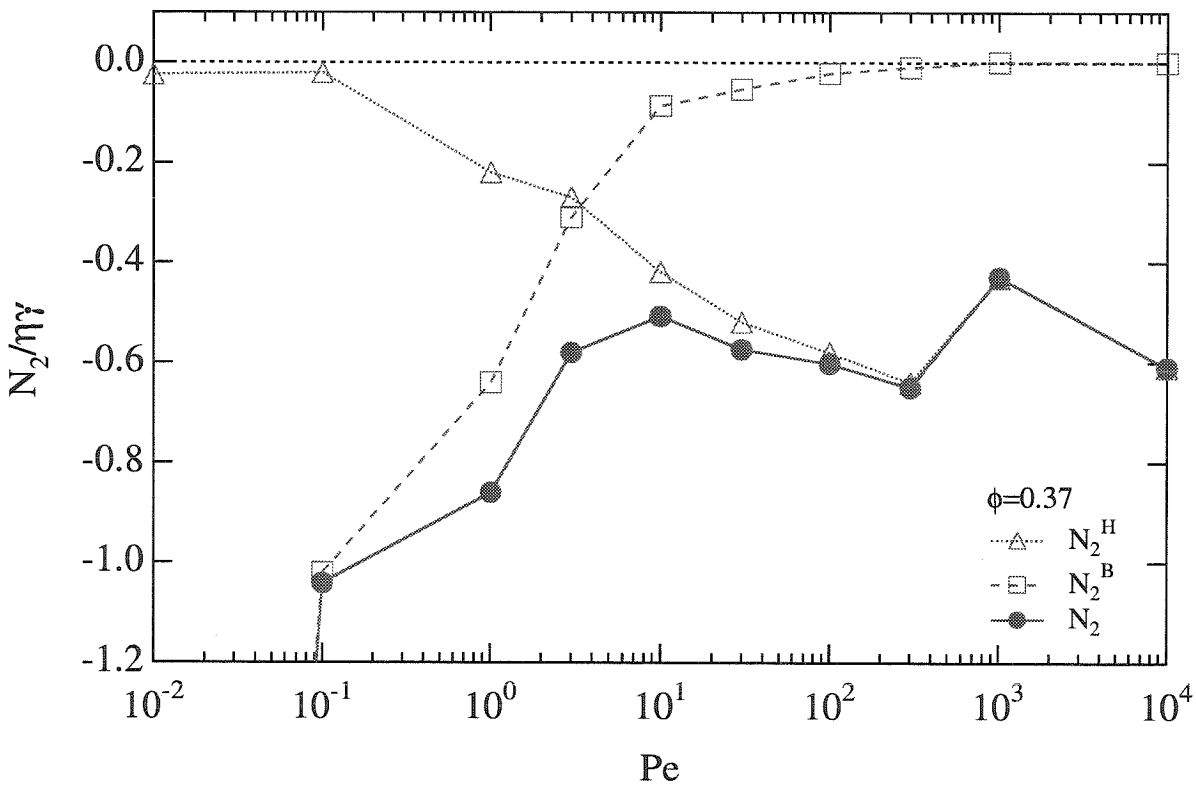

Figure 3.38: Hydrodynamic and Brownian contributions to the second normal stress difference, nondimensionalized by $\eta\dot{\gamma}$, as a function of Pe from Stokesian Dynamics for $\phi = 0.37$, $N = 27$.

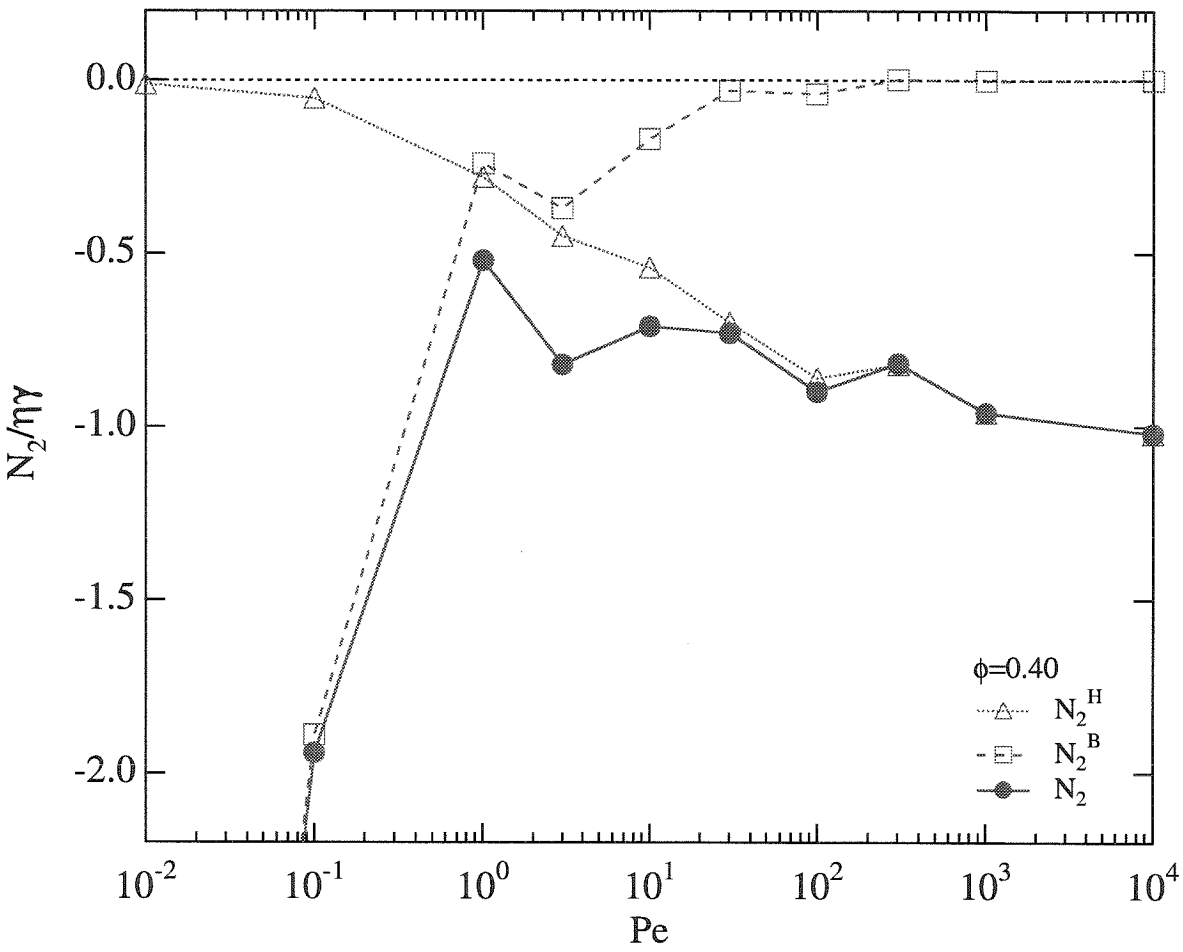

Figure 3.39: Hydrodynamic and Brownian contributions to the second normal stress difference, nondimensionalized by $\eta\dot{\gamma}$, as a function of Pe from Stokesian Dynamics for $\phi = 0.40$, $N = 27$.

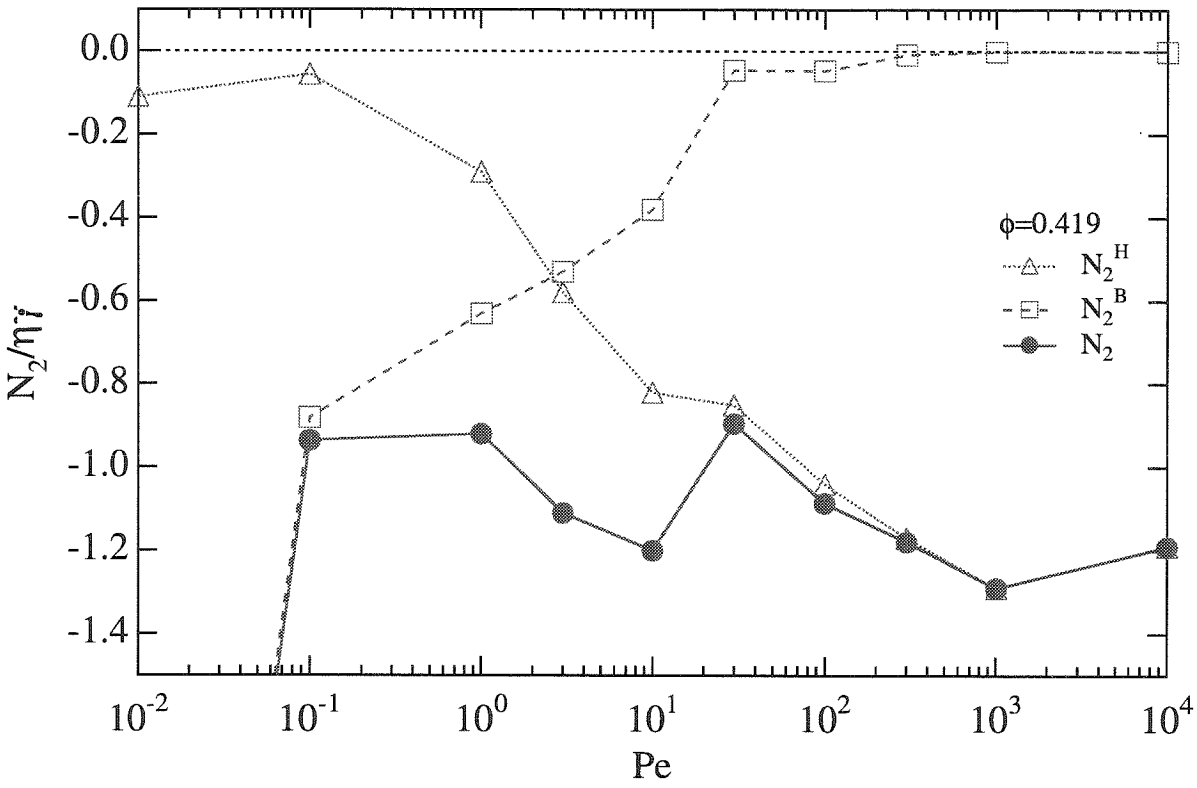

Figure 3.40: Hydrodynamic and Brownian contributions to the second normal stress difference, nondimensionalized by $\eta\dot{\gamma}$, as a function of Pe from Stokesian Dynamics for $\phi = 0.419$, $N = 27$.

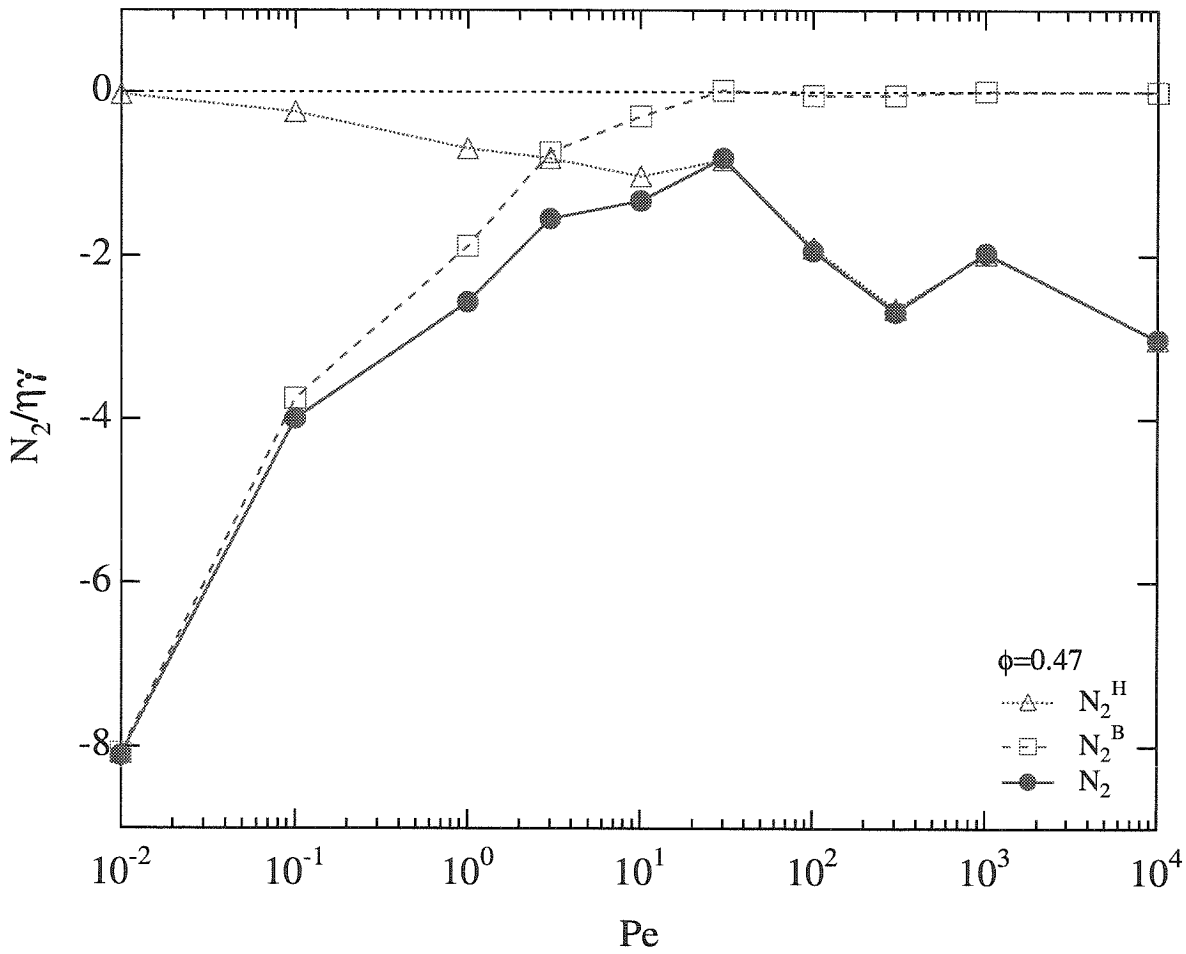

Figure 3.41: Hydrodynamic and Brownian contributions to the second normal stress difference, nondimensionalized by $\eta\dot{\gamma}$, as a function of Pe from Stokesian Dynamics for $\phi = 0.47$, $N = 27$.

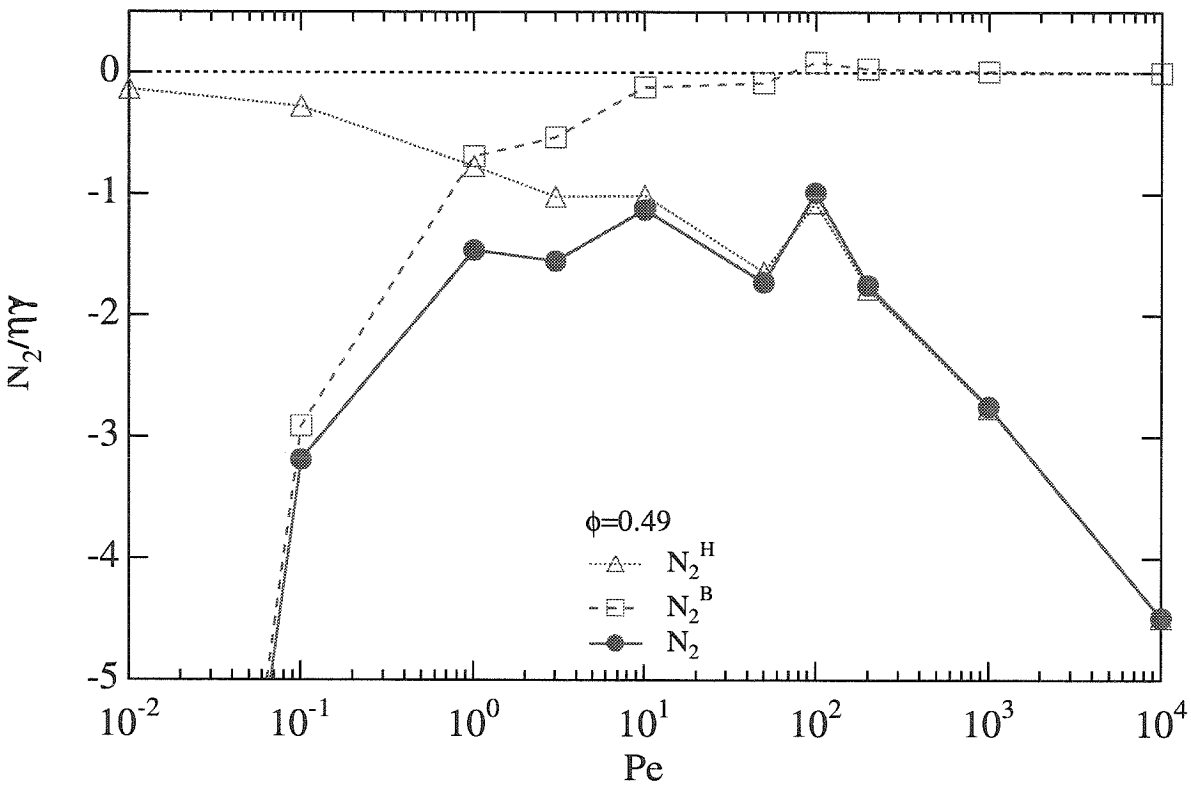

Figure 3.42: Hydrodynamic and Brownian contributions to the second normal stress difference, nondimensionalized by $\eta\dot{\gamma}$ as a function of Pe from Stokesian Dynamics for $\phi = 0.49$, $N = 27$.

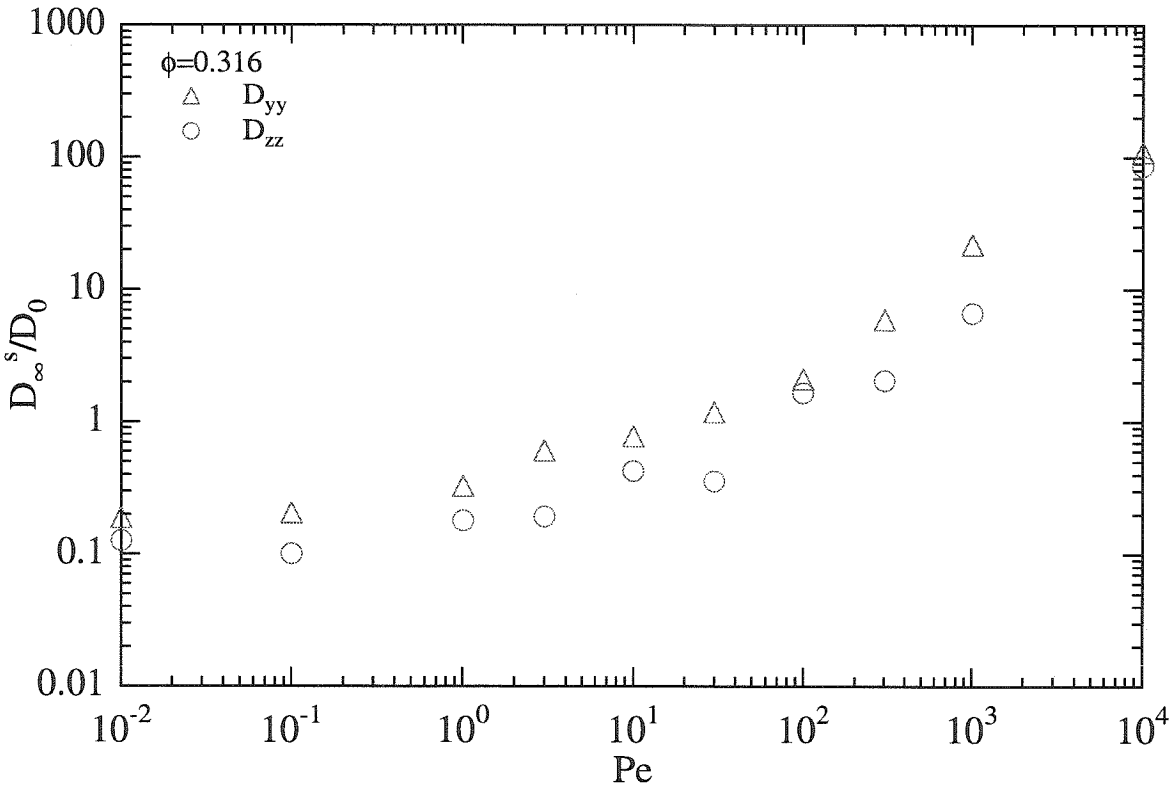

Figure 3.43: The yy- and zz-components of the long-time self-diffusion tensor as a function of Pe from Stokesian Dynamics for $\phi = 0.316$, $N = 27$.

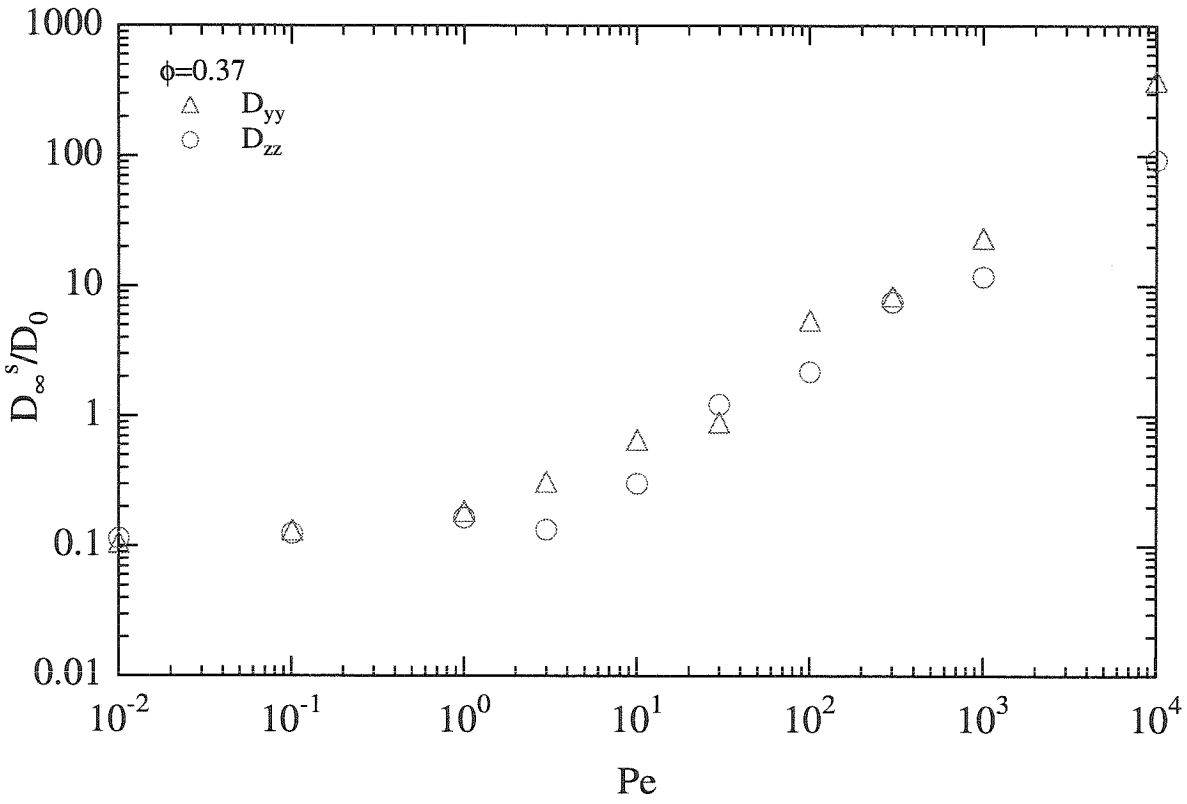

Figure 3.44: The yy- and zz-components of the long-time self-diffusion tensor as a function of Pe from Stokesian Dynamics for $\phi = 0.37$, $N = 27$.

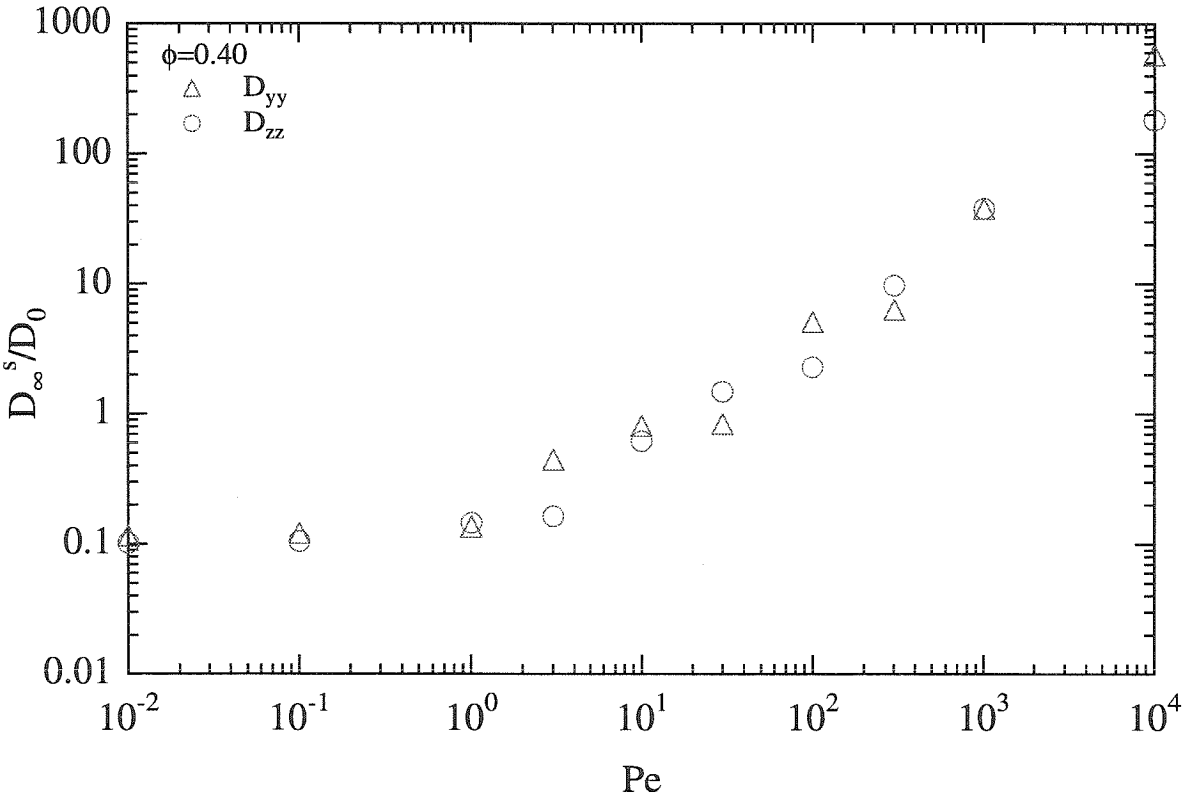

Figure 3.45: The yy- and zz-components of the long-time self-diffusion tensor as a function of Pe from Stokesian Dynamics for $\phi = 0.40$, $N = 27$.

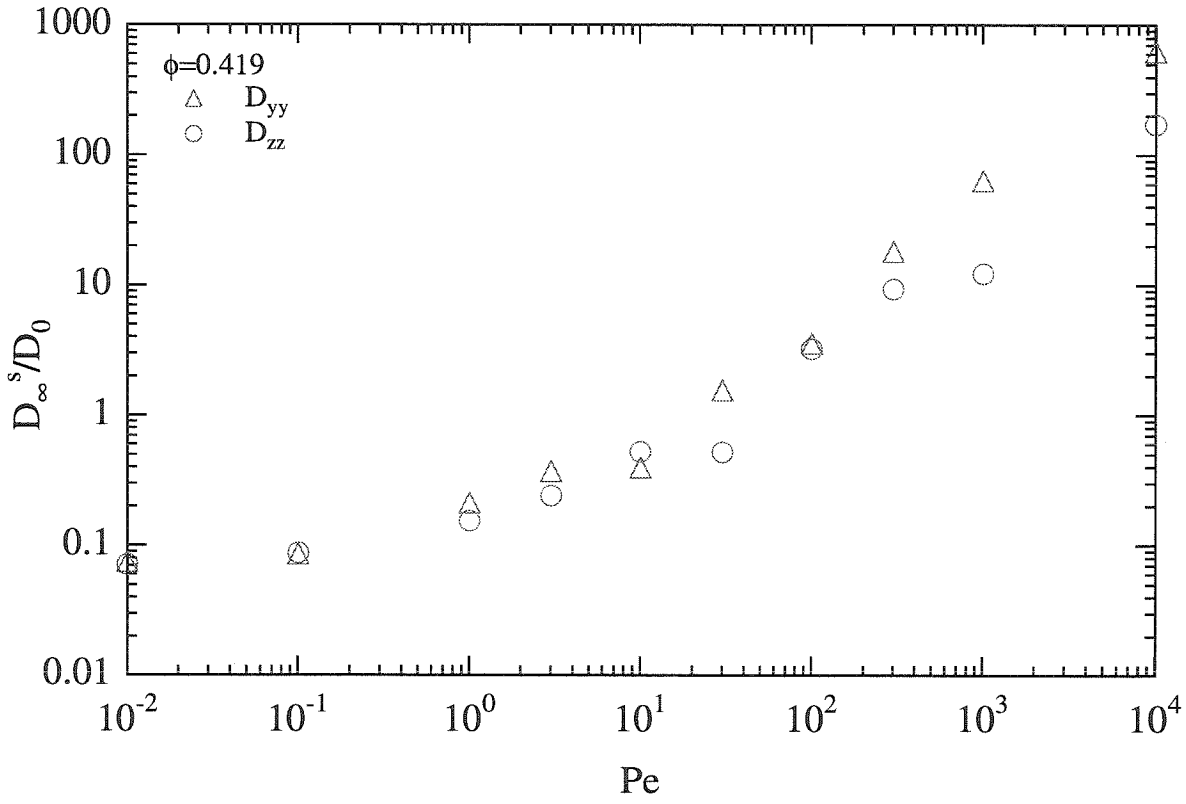

Figure 3.46: The yy- and zz-components of the long-time self-diffusion tensor as a function of Pe from Stokesian Dynamics for $\phi = 0.419$, $N = 27$.

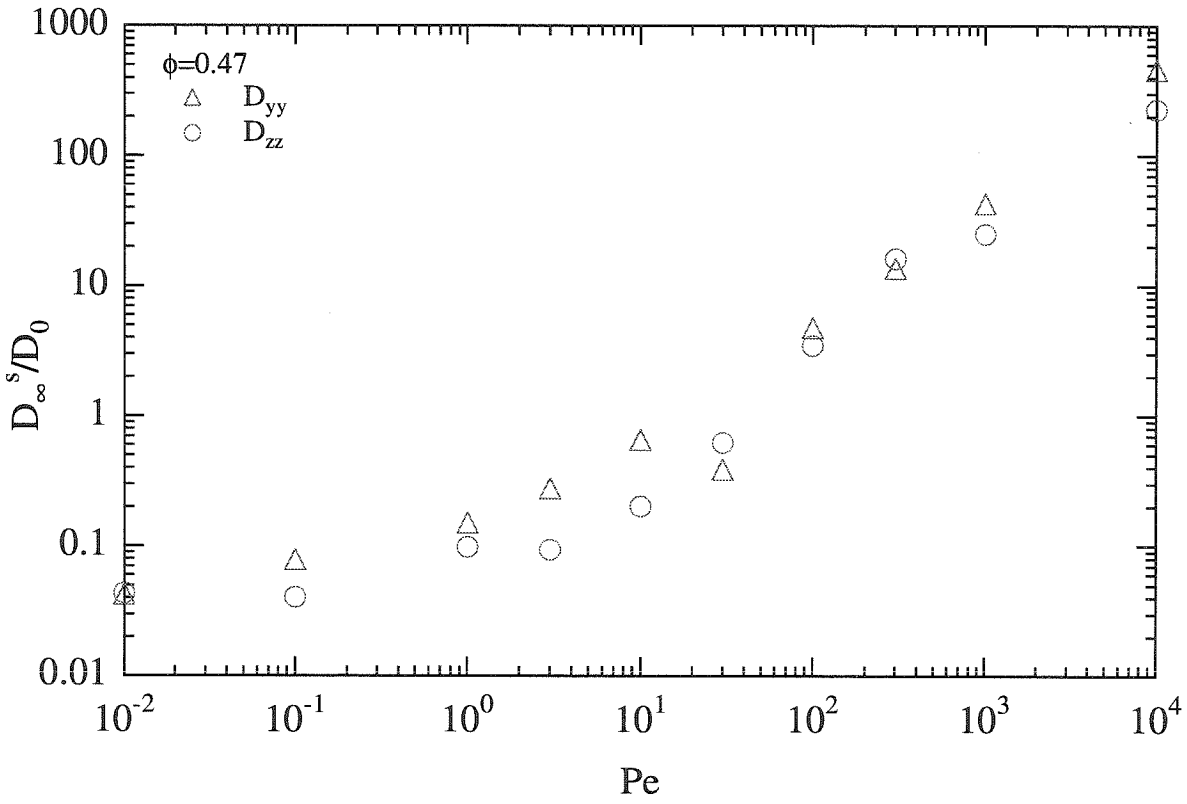

Figure 3.47: The yy- and zz-components of the long-time self-diffusion tensor as a function of Pe from Stokesian Dynamics for $\phi = 0.47$, $N = 27$.

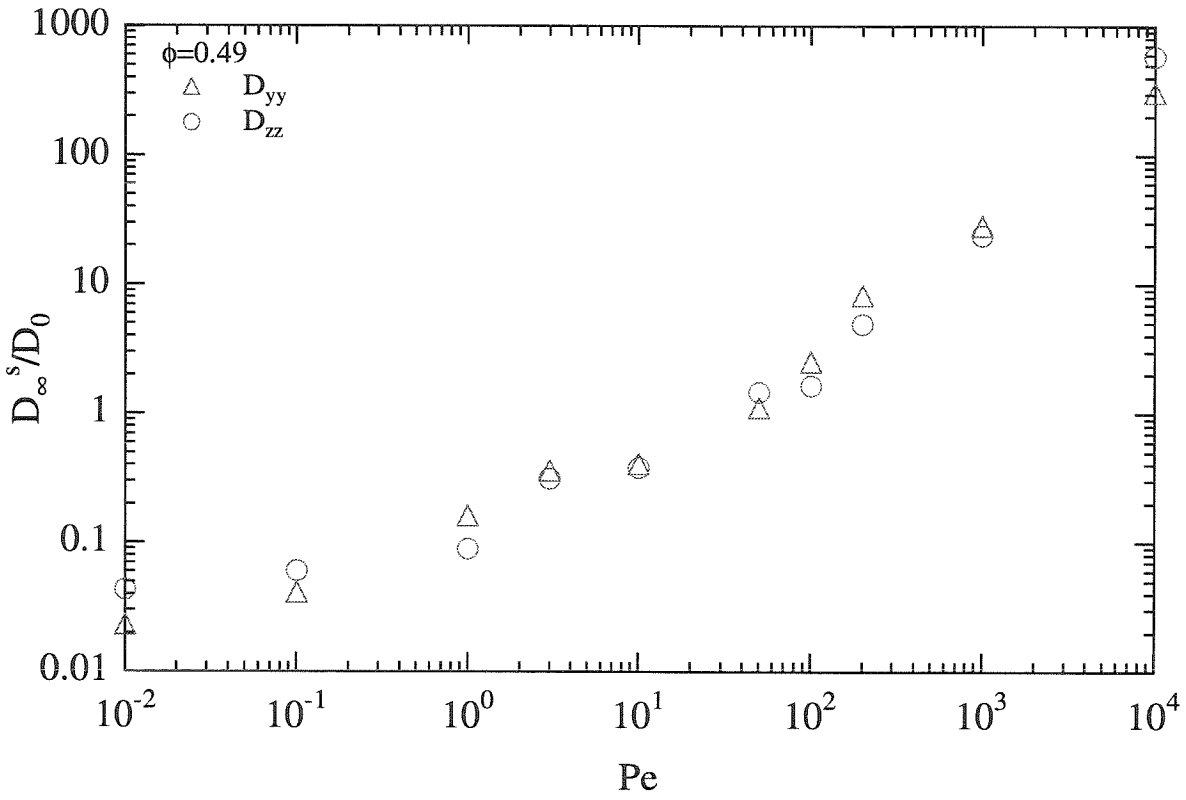

Figure 3.48: The yy- and zz-components of the long-time self-diffusion tensor as a function of Pe from Stokesian Dynamics for $\phi = 0.49$, $N = 27$.

Chapter 4

Stress relaxation in colloidal dispersions

4.1 Introduction

This paper examines several different modes of stress relaxation that occur in a colloidal dispersion. The behavior of the stress responce in a colloidal dispersion can be explained through an analysis of the dynamics of the microstructure — the spatial distribution of the particles. The microstructure is affected by Brownian, hydrodynamic and interparticle forces. Brownian forces originate from thermal fluctuations in the solvent, give rise to the familiar phenomenon of Brownian motion, and act to restore a distorted microstructure to equilibrium. Hydrodynamic forces arise from the particles' motion through the fluid and can act to both deform the microstructure, for example, when an external shearing motion is imposed, and to set the rate of microstructural relaxation through viscous damping. Other interparticle forces of nonhydrodynamic origin may be attractive or repulsive, short- or long-ranged in nature and due to a variety of effects, *e.g.*, electrostatic, van der Waals, or even a combination of multiple types of interactions. For simplicity, this work we are interested in the the simplest dispersion — monodisperse hard spheres suspended in a Newtonian solvent at low Reynolds number. Hard-sphere particles only have excluded volume interactions and then the essential generic elements of size and flow can be studied.

Brownian forces are included in all the work performed here. For the hydrodynamic forces, we consider two cases. The first case is a suspension with no hydrodynamic interactions; single-body effects such as the stokes drag force and the single-particle stresslet are still present, but all two-particle and higher effects are neglected. This case is associated with the Brownian Dynamics simulation technique. The other case is a suspension with full hydrodynamic interactions, that is all of the many-body far-field interactions as well as the pairwise additive lubrication interactions are included which necessitates use of computationally-intensive Stokesian Dynamics simulations.

In the absence of flow the stress and microstructure are isotropic, but the presence of Brownian motion results in temporary structural anisotropies that form and

dissipate with time. These fluctuations have been extensively studied using stress autocorrelation functions and related to near equilibrium quantities such as linear viscoelastic behavior by way of Green-Kubo formulae. A review of these formulae and how they relate to stress relaxation is presented in §4.3.

At nonequilibrium conditions, the structure is no longer isotropic. Fluctuations around the steady-state microstructure are still present. In this work, we are interested in the larger responses due to step changes in the shear rate, *i.e.*, start-up flow and flow cessation.

Experimental work has recently been performed in the area of transient nonequilibrium rheology. Flow cessation experiments (Mackay & Kaffashi 1995, Kaffashi, *et al.* 1997) have been able separate out the hydrodynamic contribution, which decays 'instantly', and observe the decay of the Brownian stress towards equilibrium. Some amount of data extrapolation is necessary due limitations in the ability of their instrumentation to monitor the stress immediately following cessation. Both start-up and cessation have also been studied experimentally by Watanabe *et al.* (1996, 1997, 1999) examining the effects of shear thinning as well as shear thickening on the nonlinear time-dependent rheology.

In the next section we present the governing equations for the suspension microstructure. In section 4.3, we review previously published theories and their relevance to Green-Kubo stress autocorrelations. In section 4.3, we repeat the nonequilibrium steady-state boundary layer analysis of Brady & Morris (1997) and extend it to include transient start-up flow and flow cessation. The Brownian Dynamics and Stokesian Dynamics simulation methods used in this work are outlined in §4.5. Simulation results are presented in section 4.6 followed by a concluding remarks and suggestions for further studies in §4.7.

4.2 Governing equations

We first start with a discussion of the equations governing the microstructure in order to understand the types of relaxation behavior we may expect to see. Consider a

suspension of N identical spheres homogeneously dispersed in a Newtonian fluid. The suspension is subjected to a linear incompressible flow with constant velocity gradient tensor $\langle \dot{\boldsymbol{\Gamma}} \rangle$, so that the imposed flow $\langle \boldsymbol{U} \rangle = \langle \dot{\boldsymbol{\Gamma}} \rangle \cdot \boldsymbol{x}$. The probability distribution for the N-particle configuration, $\boldsymbol{x}^N$, is denoted $P_N(\boldsymbol{x}^N, t)$ and satisfies the Smoluchowski equation

$$\frac{\partial P_N}{\partial t} + \sum_{\alpha=1}^{N} \nabla_\alpha \cdot \boldsymbol{j}_\alpha = 0, \tag{4.1}$$

with the flux of particle α given by

$$\boldsymbol{j}_\alpha = \boldsymbol{U}_\alpha P_N - \sum_{\beta=1}^{N} \boldsymbol{D}_{\alpha\beta} P_N \cdot \nabla_\beta (\ln P_N + V), \tag{4.2}$$

where $\boldsymbol{U}_\alpha$ is the velocity of particle α, V is the potential energy made dimensionless by kT, and the relative Brownian diffusivity is given by $\boldsymbol{D}_{\alpha\beta} = kT\boldsymbol{M}_{\alpha\beta}$, where $\boldsymbol{M}_{\alpha\beta}$ is the hydrodynamic mobility of particle α due to a force exerted on particle β. The particle velocity is given by

$$\boldsymbol{U}_\alpha = \langle \dot{\boldsymbol{\Gamma}} \rangle \cdot \boldsymbol{x}_\alpha + (\boldsymbol{R}_{FU}^{-1} \cdot \boldsymbol{R}_{FE} : \langle \boldsymbol{E} \rangle)_\alpha,$$

where $\boldsymbol{R}_{FU}$ and $\boldsymbol{R}_{FE}$ are the many-body hydrodynamic resistance tensors that give the hydrodynamic force on a particle due to its motion relative to the fluid and due to an imposed shear flow, respectively. Here, $\langle \boldsymbol{E} \rangle$ is the rate of strain tensor of the bulk linear flow. We take V to be an interparticle potential depending only upon the relative configuration of the particles.

Equation (4.1) can be integrated with respect to the center-of-mass coordinate of a pair of particles and the positions of the remaining $N-2$ particles to arrive at the equation for $P_{1|1}(\boldsymbol{r})$, the probability distribution for finding a particle at $\boldsymbol{r}$ given that a particle lies at the origin:

$$\frac{\partial P_{1|1}}{\partial t} + \nabla_r \cdot (\langle \boldsymbol{U} \rangle_2 P_{1|1}) - \nabla_r \cdot [P_{1|1} \langle \boldsymbol{D} \cdot \nabla_r (\ln P_N + V) \rangle_2]$$

$$- \nabla_r \cdot P_{1|1} \int P_{3|2}(\boldsymbol{x}_3 | \boldsymbol{r}) \langle (\boldsymbol{D}_{13} - \boldsymbol{D}_{23}) \cdot \nabla_3 (\ln P_N + V) \rangle_3 d\boldsymbol{x}_3 = 0, \tag{4.3}$$

where $\nabla_r = \nabla_2 = -\nabla_1$, and $P_{3|2}$ is the probability of finding a third particle at $\boldsymbol{x}_3$ given the positions of two particles. In (4.3), the relative velocity and relative diffusivity are given by

$$\boldsymbol{U} = \boldsymbol{U}_2 - \boldsymbol{U}_1, \quad \text{and} \quad \boldsymbol{D} = \boldsymbol{D}_{11} - \boldsymbol{D}_{12} - \boldsymbol{D}_{21} + \boldsymbol{D}_{22}, \tag{4.4}$$

respectively, and $\langle \quad \rangle_2$ indicates a conditional average with two particles fixed.

Quantities are made dimensionless by scaling as

$$\boldsymbol{r} \sim a, \quad \boldsymbol{U} \sim \dot{\gamma} a, \quad \boldsymbol{D} \sim 2D_0, \quad \text{and} \quad t \sim a^2/2D_0,$$

where $\dot{\gamma}$ is a characteristic magnitude of the velocity gradient tensor $\dot{\boldsymbol{\Gamma}}$, and the scaling of the relative diffusivity is with the far-field asymptotic value for isolated particles $2D_0$, with $D_0 = kT/6\pi\eta a$ the diffusivity of an isolated particle of radius a and thermal energy kT in a fluid of viscosity η. The relative importance of shearing flow and Brownian motion is given by the Péclet number

$$Pe \equiv \frac{\dot{\gamma} a^2}{2D_0} = \frac{3\pi\eta a^3 \dot{\gamma}}{kT}. \tag{4.5}$$

The qualitative features of the suspension dynamics can be obtained from a dilute, two-particle analysis and the dimensionless equation and associated boundary conditions governing the pair-distribution function $g(\boldsymbol{r})$, defined by $P_{1|1}(\boldsymbol{r}) = ng(\boldsymbol{r})$, are

$$\frac{\partial g}{\partial t} + Pe\nabla\cdot(\boldsymbol{U}g) - \nabla\cdot(\boldsymbol{D}\cdot\nabla g) = 0, \tag{4.6a}$$

$$\hat{\boldsymbol{r}}\cdot\boldsymbol{D}\cdot\nabla g(\boldsymbol{r}) = Pe\ \hat{\boldsymbol{r}}\cdot\boldsymbol{U}g(\boldsymbol{r}) \quad \text{at} \quad r = 2, \tag{4.6b}$$

$$g \sim 1 \quad \text{as} \quad r \to \infty, \tag{4.6c}$$

where $\hat{\boldsymbol{r}} = \boldsymbol{r}/r$ is the unit vector projecting from particle 1 to particle 2. To simplify notation in (4.6a) and hereafter, we write ∇ for ∇_r and the angle brackets indicating averaging are not needed in the dilute limit.

From the microstructure, we can determine the particle contribution to the bulk stress given by (Brady 1993a)

$$\langle \boldsymbol{\Sigma}_p \rangle = -nkT\boldsymbol{I} + n(\langle \boldsymbol{S}^B \rangle + \langle \boldsymbol{S}^P \rangle + \langle \boldsymbol{S}^H \rangle), \tag{4.7}$$

where $nkT\boldsymbol{I}$ is the kinetic contribution that yields the dilute osmotic pressure, and

$$\langle \boldsymbol{S}^B \rangle = -kT\langle \nabla\cdot(\boldsymbol{R}_{SU}\cdot\boldsymbol{R}_{FU}^{-1}) \rangle, \tag{4.8a}$$

$$\langle \boldsymbol{S}^P \rangle = -\langle (\boldsymbol{x}\boldsymbol{I} + \boldsymbol{R}_{SU}\cdot\boldsymbol{R}_{FU}^{-1})\cdot\boldsymbol{F}^P \rangle, \tag{4.8b}$$

$$\langle \boldsymbol{S}^H \rangle = -\langle \boldsymbol{R}_{SU}\cdot\boldsymbol{R}_{FU}^{-1}\cdot\boldsymbol{R}_{FE} - \boldsymbol{R}_{SE} \rangle : \langle \boldsymbol{E} \rangle, \tag{4.8c}$$

are, respectively, expressions for the Brownian, interparticle force, and hydrodynamic stresslets. The particle stress may be rewritten as (Brady 1993a)

$$\langle \boldsymbol{\Sigma}_p \rangle = -nkT\boldsymbol{I} - n^2kTa \oint_{r=2a} \hat{\boldsymbol{r}}\hat{\boldsymbol{r}} g(\boldsymbol{r}) dS - n\langle \boldsymbol{x}\boldsymbol{F}^P \rangle$$

$$- n\langle \boldsymbol{R}_{SU}\cdot\boldsymbol{R}_{FU}^{-1}\cdot\boldsymbol{R}_{FE} - \boldsymbol{R}_{SE} \rangle : \langle \boldsymbol{E} \rangle + nkT\langle \boldsymbol{R}_{SU}\cdot\boldsymbol{R}_{FU}^{-1}\cdot\nabla[V + \ln P_N] \rangle, \tag{4.9}$$

by decomposing $\langle \boldsymbol{S}^B \rangle$ into the contact integral and the final term involving $\nabla \ln P_N$. In (4.8) and (4.9), the subscripts on the configurationally dependent hydrodynamic resistance tensors $\boldsymbol{R}_{FU}$ and $\boldsymbol{R}_{SE}$ denote the relation of force to velocity and stress to rate of strain, respectively, and the others should be clear from these.

The bulk stress of the entire suspension — particles plus fluid — is simply

$$\langle \boldsymbol{\Sigma} \rangle = -\langle p \rangle_f \boldsymbol{I} + 2\eta\langle \boldsymbol{E} \rangle + \langle \boldsymbol{\Sigma}_p \rangle, \tag{4.10}$$

where $\langle p \rangle_f$ is the average pressure in the suspending fluid, which is arbitrary for an incompressible fluid.

4.3 Near-equilibrium Green-Kubo theory

We first consider the relaxation behavior at equilibrium through the decay of the stress autocorrelation function, and in particular its behavior at short time both with and without hydrodynamic interactions. The steady-state solution to (4.6) in the absence of flow is simply $g = 1$ everywhere. Thus, the sole contribution to the particle stress is an isotropic contribution, the osmotic pressure. Although the time-average structure at equilibrium is constant, Brownian motion produces fluctuations that cause temporary deviations in the microstructure from isotropy. Thus, the shear stress in the system at any specific instant in time is not necessarily zero, although the time-average shear stress most certainly is due to the absence of an imposed shear flow. The temporal behavior of these stress fluctuations at equilibrium is described by the shear-stress autocorrelation function,

$$C_s(t) = \langle \sigma_{xy}(t)\sigma_{xy}(0) \rangle. \tag{4.11}$$

Here, $\langle \quad \rangle$ denotes an ensemble average over all particles in suspension of volume, V, and σ_{xy} represents a shear stress due to an equilibrium fluctuation. We use the subscript xy for clarity, but since there is no preferred direction at equilibrium, we could also use xz, or yz or any other subscript that would represent a quadrupolar stress. Note that in terms of the stresses in (4.8), σ_{xy} could represent either the interparticle force or Brownian contribution; the hydrodynamic contribution is strictly proportional to an imposed rate of strain.

The relationship between the autocorrelation function in (4.11) and the suspension rheology by Green-Kubo formulae are well established (Boon & Yip 1980, Hansen & McDonald 1986). Specifically, the frequency-dependent complex viscosity due to an oscillatory shear flow is related to $C_s(t)$ by (Nägele & Bergenholtz, 1998)

$$\eta(\omega) = \eta'(\omega) - i\eta''(\omega) = \eta'_\infty + \frac{V}{kT}\int_0^\infty C_s(t)e^{-i\omega t}dt, \tag{4.12}$$

where the real part corresponds to dissipation and the imaginary part corresponds to

elasticity. Here, $\eta'_\infty(\phi)$ is the high-frequency dynamic viscosity, which is the hydrodynamic viscosity in an equilibrium microstructure. The complex modulus can also be calculated from (4.12) by

$$G'(\omega) = \omega\eta''(\omega) \quad \text{and} \quad G''(\omega) = \omega\eta'(\omega). \tag{4.13}$$

Thus, the high-frequency elastic shear modulus, $G'_\infty = G'(\omega \to \infty)$ is given by

$$G'_\infty = \frac{V}{kT} C_s(0). \tag{4.14}$$

Other properties of $C_s(t)$ can be found by analyzing the microstructure in the presence of a small-amplitude oscillatory shear flow characterized by the time-dependent rate of strain tensor

$$\langle \boldsymbol{E} \rangle = \hat{\boldsymbol{E}} e^{i\alpha t},$$

where $\alpha = \omega a^2/2D_0$ is the frequency nondimensionalized by the diffusive time, $a^2/2D_0$ and $\hat{\boldsymbol{E}}$ is a constant tensor giving the type of linear flow. The resultant perturbation to the equilibrium structure, $f = g - 1$, for small-oscillatory shear amplitudes, must be linear in the tensor $\hat{\boldsymbol{E}}$:

$$f(r,t) = -\frac{1}{2} Pe f(r) e^{i\alpha t} \hat{\boldsymbol{r}} \cdot \hat{\boldsymbol{E}} \cdot \hat{\boldsymbol{r}}, \tag{4.15}$$

where $Pe \ll 1$ due to the small amplitude of the shear. Substitution of (4.15) into the (4.6) gives, to leading order in Pe, the following system

$$-i\alpha f + \nabla \cdot \boldsymbol{D} \cdot \nabla f = \nabla \cdot (\boldsymbol{U} g), \tag{4.16a}$$

$$\hat{\boldsymbol{r}} \cdot \boldsymbol{D} \cdot \nabla f = Pe \hat{\boldsymbol{r}} \cdot \boldsymbol{U} (1 + f) \quad \text{at} \quad r = 2, \tag{4.16b}$$

$$f \sim 0 \quad \text{as} \quad r \to \infty, \tag{4.16c}$$

whose solution has been discussed at great length elsewhere (Brady 1993b, Cichocki & Felderhof 1991). Here, we are interested in the short-time behavior of $C_s(t)$ which

corresponds to the high-frequency behavior of f.

As $\alpha \to \infty$, the solution is simply $f = 0$ as the frequency is so high and the amplitude so small that the suspension is not disturbed from its equilibrium state. The perturbation around infinite frequency is singular, however, with in a boundary layer where unsteadiness balances diffusion in order to satisfy the no-flux boundary-condition at contact. In the absence of hydrodynamic interactions, the relative diffusivity between two particles is simply $\boldsymbol{I}$ in dimensionless form. Thus, at high frequencies there is a balance between scaled frequency α and two spatial derivatives of f, resulting in a balance between the scaled frequency, α, and two spatial derivatives of f necessitating a boundary layer near contact that scales as $a\alpha^{-1/2}$. The result of this thin boundary layer near the surface is a contact value of the perturbation function f, and thus a complex viscosity, that decays at high frequencies as $\alpha^{-1/2}$. From (4.13), this results in an elastic modulus, G', that grows as $\alpha^{1/2}$ as $\alpha \to \infty$ as widely reported in the literature (Brady 1993b, Lionberger & Russel 1994). Thus, from (4.12) it can be determined that $C_s(t)$ diverges at short times like $t^{-1/2}$ (Cichocki & Felderhof 1991).

Inclusion of hydrodynamic interactions produces a qualitatively different behavior. There is still a boundary layer at contact in which frequency balances diffusion, but since the relative diffusivity vanishes at contact as $r-2a$, the boundary layer thickness now scales as $a\alpha^{-1}$, rather than $a\alpha^{-1/2}$. The different scaling of the boundary layer results in qualitatively different rheological behavior. Now the contact value of f and the complex viscosity both decay at high frequencies as α^{-1}. The stronger decay of the complex viscosity means that the elastic modulus, G', now approaches a constant, G'_∞, as $\alpha \to \infty$. And thus, $C_s(t)$ approaches a constant as $t \to 0$ and its initial decay is linear with time as in the case with a soft, but steep, interaction potential (Verberg *et al.* 1997). We will see in §4.6.1 that these scaling predictions are borne out by dynamic simulations. The reader who is not interested in the details of the simulation methods may skip to §4.6.1 now. As a final note, the long-time (or low frequency) decay is predicted as $t^{-7/2}$ (Cichocki & Felderhof 1991) both with and without hydrodynamic interactions; only the coefficent changes with hydrodynamics.

This $t^{-7/2}$ behavior is simply the diffusive decay of the quadrupolar (cf. eq. (4.15)) disturbance caused by the weak shear flow.

4.4 High shear rate boundary layer: no hydrodynamics

We now turn our attention to the other limit of far from equilibrium behavior and analyze the beahavior for large Pe, where another baoundary layer is present and analytic progress is possible. We shall see in 4.6 that the behavior for all Pe can be understood form these two limits of small and large Pe.

4.4.1 Steady-state analysis

We are interested in the behavior far from equilibrium where $Pe \gg 1$ in the absence of hydrodynamic interactions. In this regime the relative velocity is equal to that of the imposed shear flow, $\boldsymbol{U} = \dot{\boldsymbol{\Gamma}} \cdot \boldsymbol{r}$ and the pair diffusivity is a constant equal to $2D_0$; thus equations (4.6a-4.6c) reduce to

$$\frac{\partial g}{\partial t} - \nabla^2 g + Pe\ \dot{\boldsymbol{\Gamma}} \cdot \boldsymbol{r} \cdot \nabla g = 0, \tag{4.17a}$$

$$\frac{\partial g}{\partial r} = 2Pe\ \gamma_r g \quad \text{at} \quad r = 2, \tag{4.17b}$$

$$g \sim 1 \quad \text{as} \quad r \to \infty. \tag{4.17c}$$

As shown by Brady & Morris (1997), at large Péclet number and at steady state, (4.17a) reduces to $\dot{\boldsymbol{\Gamma}} \cdot \boldsymbol{r} \cdot \nabla g = 0$, *i.e.*, on a streamline g is a constant, which (4.17c) dictates to be unity. This constant solution does not satisfy the no-flux boundary condition at contact, however, and there is a boundary layer in which the effects of Brownian motion balance those of advection similar to the boundary layer at high frequency considered in §4.3. The relevant length Scale is no longer the particle radius, but the size of the boundary layer, $\delta \sim aPe^{-1}$. Also, the time scale is shortened as the proper diffusive time scale is based on the ability for a particle to diffuse the

length of the boundary layer, $\delta^2/2D_0$, rather than the particle size $a^2/2D_0$. Thus, we stretch r and t according to

$$y = Pe(r-2) \quad \text{and} \quad \tau = tPe^2, \tag{4.18}$$

The governing equation and boundary conditions for g in the stretched coordinates are

$$\frac{\partial g}{\partial \tau} - \frac{\partial^2 g}{\partial y^2} + 2\gamma_r[1 - Pe^{-1}\frac{1}{2\gamma_r}(1-\gamma_r y)]\frac{\partial g}{\partial y} = -Pe^{-1}[\gamma_\theta \frac{\partial g}{\partial \theta} + \frac{\gamma_\varphi}{\sin\theta}\frac{\partial g}{\partial \varphi}] + O(Pe^{-2}), \tag{4.19a}$$

$$\frac{\partial g}{\partial y} = 2\gamma_r g \quad \text{at} \quad y = 0, \tag{4.19b}$$

$$g \sim 1 \quad \text{as} \quad y \to \infty, \tag{4.19c}$$

where θ is the azimuthal angle measured from the z-axis, and φ is the polar angle measured from the x-axis. In (4.17a)-(4.19b), γ_r, γ_θ, and γ_φ are defined by

$$\gamma_r = \hat{\boldsymbol{r}}\cdot\hat{\boldsymbol{\Gamma}}\cdot\hat{\boldsymbol{r}} = \hat{\boldsymbol{r}}\cdot\hat{\boldsymbol{E}}\cdot\hat{\boldsymbol{r}}, \quad \gamma_\theta = \hat{\boldsymbol{\theta}}\cdot\hat{\boldsymbol{\Gamma}}\cdot\hat{\boldsymbol{r}}, \quad \gamma_\varphi = \hat{\boldsymbol{\varphi}}\cdot\hat{\boldsymbol{\Gamma}}\cdot\hat{\boldsymbol{r}}, \tag{4.20}$$

where $\hat{\boldsymbol{\theta}}$ and $\hat{\boldsymbol{\varphi}}$ are the unit vectors in the θ- and φ-directions, respectively, and $\hat{\boldsymbol{\Gamma}}$ is the non-dimensional velocity gradient tensor.

Brady & Morris (1997) show that terms of $O(Pe^{-1})$ must be retained in the equation for g, and simplify the problem by keeping only those terms on the left-hand side of (4.19a) in a 'radial balance approximation' as the competition between radial advection and diffusion is what generates the large gradients in g characteristic of the boundary layer. The steady-state solution to the radial balance approximation is

$$g_{ss}(y) = \frac{1 + 2\gamma_r \int_0^y e^{s(z)}dz}{1 + 2\gamma_r \int_0^\infty e^{s(z)}dz}, \tag{4.21}$$

where $s(z)$ is given by

$$s(z) = 2\gamma_r[(1 - \frac{1}{2\gamma_r}Pe^{-1})z + \frac{1}{4}Pe^{-1}z^2]. \tag{4.22}$$

Here, $g_{ss}(y)$ is valid only for $\gamma_r < 0$, *i.e.* in the compressional quadrants; in the extensional quadrants, where $\gamma_r > 0$, g remains $O(1)$ and there is no boundary layer. Rewriting g as

$$g_{ss}(y) = g_{ss}(0)[1 + 2\gamma_r \int_0^y e^{s(z)} dz],$$

with

$$g_{ss}(0) = -\frac{4}{3} Pe\gamma_r + O(1) \quad \text{as} \quad Pe \to \infty \tag{4.23}$$

shows that there is an $O(Pe)$ excess of particles in the compressional quadrants.

Using this result for the pair-distribution function, the stress in the absence of hydrodynamic interactions for a hard-sphere potential is just the contact integral in (4.9)

$$\langle \boldsymbol{\Sigma}_p \rangle = -nkT\boldsymbol{I} + \eta\dot{\gamma}\phi^2 \frac{9}{\pi} \int_{\gamma_r<0} \hat{\boldsymbol{r}}\hat{\boldsymbol{r}}\gamma_r d\Omega + O(Pe^{-1}). \tag{4.24}$$

Even though the hard-sphere force is of magnitude kT, the large $O(Pe)$ build up of pair probability along the compressive axes results in a viscous ($O(\eta\dot{\gamma})$) stress independent of kT as $Pe \to \infty$.

Although we have neglected $O(Pe^{-1})$ terms on the right-hand side of (4.19a) in the radial balance approximation, these terms have only a slight quantitative effect on the results (Bergenholtz, Vicic & Brady 1999).

4.4.2 Start-up flow

We now turn our attention to the unsteady boundary-layer problem, using the same radial balance approximation as analytic progress is possible. We consider two cases: (1) Start-up flow in which the quiescent suspension is suddenly subjected to a strong steady shearing motion at large Pe, and (2) flow cessation in which a steady shearing flow is suddenly stopped. One could consider other time-dependent behavior, including an oscillating shearing motion superimposed on the steady motion, but the analytical complexity increases. The basic physical aspects of structural development and relaxation are captured by start-up and flow-cessation.

For start-up flow, the initial condition is the isotropic equilibrium structure, $g = 1$

and it is useful to analyze the problem in terms of the deviation from this structure denoted by $f = g - 1$. On taking Laplace transform, which we denote by $\tilde{}$, and with s conjugate to τ, the problem becomes

$$\frac{\partial^2 \tilde{f}}{\partial y^2} - 2\gamma_r(1 - \frac{1}{2\gamma_r}Pe^{-1} + \frac{1}{2}Pe^{-1}y)\frac{\partial \tilde{f}}{\partial y} - s\tilde{f} = 0, \tag{4.25a}$$

$$\frac{\partial \tilde{f}}{\partial y} - 2\gamma_r \tilde{f} = \frac{2\gamma_r}{s} \quad \text{at} \quad y = 0, \tag{4.25b}$$

$$\tilde{f} \sim 0 \quad \text{as} \quad y \to \infty. \tag{4.25c}$$

The factor of $1/s$ in (4.25b) is a result of the Heaviside step function in time necessary because $\gamma_r = 0$ before the inception of the flow. A change of variables transforms (4.25) to

$$\frac{\partial^2 \tilde{f}}{\partial x^2} + 2x\frac{\partial \tilde{f}}{\partial x} - \sigma\tilde{f} = 0 \tag{4.26a}$$

$$\frac{\partial \tilde{f}}{\partial x} + 2\beta\tilde{f} = -\frac{8Pe^2}{\beta\sigma} \quad \text{at} \quad x = x_0 = \frac{\beta^2 + 1}{\beta}, \tag{4.26b}$$

$$\tilde{f} \sim 0 \quad \text{as} \quad x \to \infty, \tag{4.26c}$$

where

$$\beta = (-2\gamma_r Pe)^{\frac{1}{2}},$$

$$x = \beta(1 - \frac{1}{2\gamma_r}Pe^{-1} + \frac{1}{2}Pe^{-1}y),$$

and

$$\sigma = s\frac{4Pe^2}{\beta^2}.$$

This problem has two linearly independent solutions in terms of the confluent hypergeometric function (Abramowitz & Stegun):

$$xe^{-x^2}M(1 + \frac{\sigma}{4}, \frac{3}{2}, x^2) \quad \text{and} \quad xe^{-x^2}U(1 + \frac{\sigma}{4}, \frac{3}{2}, x^2). \tag{4.27}$$

For calculation of the rheological properties, only the value at contact, $y = 0$ or $x = x_0$, is necessary and this simplifies the analysis. Once the boundary conditions

are applied, the contact value of g is

$$g(0,\tau) = 1 + \mathcal{L}^{-1}[\tilde{f}(0,s)], \tag{4.28a}$$

$$\tilde{f}(0,s) = \frac{\beta^2(\beta^2+1)}{1+\frac{1}{2}\beta^2 - (\beta^2+1)^2\frac{U'}{U}|_{x_0}}\frac{1}{s}. \tag{4.28b}$$

In (4.28), $\mathcal{L}^{-1}$ represents an inverse Laplace Transform and the arguments of U are the same as in (4.27) and are evaluated at $x = x_0$ with the prime representing differentiation with respect to the third argument. We have not been able to carry out the inverse analytically for all times, but the short- and long-time asymptotic behavior can be extracted.

At short times (4.28a) has the following assymptotic form

$$g(0,t) \sim 1 - \frac{16}{\pi^{\frac{1}{2}}}\gamma_r^3 Pe^3 t^{\frac{1}{2}} \quad \text{as} \quad t \to 0, \tag{4.29}$$

showing that the initial growth of the boundary-layer microstructure scales as $t^{\frac{1}{2}}$, similar to the behavior near equilibrium (cf. §4.3). The large exponent on Pe in (4.29) indicates that this limit is only strictly valid at very short times, of $O(tPe^{-4})$ or smaller. We have not been able to determine whether the $t^{\frac{1}{2}}$ behavior persists to longer more rheologically significant time scales.

At long times, the system reaches the steady-state solution (4.23) exponentially as

$$g(0,t) \sim 1 - \frac{4}{3}\gamma_r Pe(1 - e^{3\gamma_r Pe\ t}) \quad \text{as} \quad t \to \infty. \tag{4.30}$$

It is also evident from (4.30) that the appropriate time scale at long times is $(a^2/2D_0)Pe^{-1}$, or simply the flow time $\dot{\gamma}^{-1}$. To determine the stress at long times, one simply replaces γ_r in (4.24) with $\gamma_r(1 - e^{3\gamma_r Pe\ t})$.

4.4.3 Flow Cessation

Flow-cessation is a simpler calculation than start-up flow as the steady-state solution decays in the absence of an imposed flow, *i.e.*, γ_r is zero once the flow stops and only

enters as a parameter in the initial condition. Diffusion is the mode of structural decay, and the relevant time scale is the time it takes for a particle to diffuse the length of the boundary layer. Thus, again we analyze the problem in terms of the deviation from this structure denoted by $f = g - 1$, which to leading order in Pe is

$$\frac{\partial^2 f}{\partial y^2} - \frac{\partial f}{\partial \tau} = O(Pe^{-1}), \tag{4.31a}$$

$$\frac{\partial f}{\partial y} = 0 \quad \text{at} \quad y = 0, \tag{4.31b}$$

$$f \sim 0 \quad \text{as} \quad y \to \infty, \tag{4.31c}$$

$$f_0(y,0) = g_{ss}(y) - 1 = 2\gamma_r g_{ss}(0) \int_{\infty}^{y} e^{s(z)} dz. \tag{4.31d}$$

On taking Laplace transform, which we denote by $\tilde{}$, and with s conjugate to τ, the problem becomes

$$\frac{\partial^2 \tilde{f}}{\partial y^2} - s\tilde{f} = -f_0(y) \tag{4.32a}$$

$$\frac{\partial \tilde{f}}{\partial y} = 0 \quad \text{at} \quad y = 0, \tag{4.32b}$$

$$\tilde{f} \sim 0 \quad \text{as} \quad y \to \infty. \tag{4.32c}$$

The solution of this problem is straightforward using variation of parameters. Due to the delta-function nature of the hard-sphere interparticle force, we need only find the contact value,

$$\tilde{f}(0,s) = -g_{ss}(0) \frac{1}{\sqrt{s}(\sqrt{s} - 2\gamma_r)}, \tag{4.33}$$

to obtain the rheological behavior. The inverse Laplace transform of (4.33) can be found for all time (Abramowitz & Stegun, chap. 29) and is given by

$$f(0,\tau) = -g_{ss}(0) e^{4\gamma_r^2 \tau} \operatorname{erfc}(\sqrt{4\gamma_r^2 \tau}). \tag{4.34}$$

Assymptotic analysis of (4.34) shows that at short times after cessation, the pair distribution function in the boundary layer departs from its steady-shear value as $\tau^{\frac{1}{2}}$ consistent with the start-up flow behavior as any flow transition starts at short

times like an equilibrium fluctuation. The boundary-layer microstructure is far from equilibrium, however, and the short-time behavior does not persist for long. At long times, the structure decays as $\tau^{-\frac{1}{2}}$, consistent with boundary-layer relaxation being a one dimensional diffusion problem. Also, the relavant time scale for structural decay is τ indicating the rescaling of time in (4.18) based on a particle's ability diffuse the width of the boundary layer, δ, instead of the particle radius, a, is indeed appropriate. This simple temporal behavior will be seen to occur in the Brownian Dynamics simulations discussed in §4.6.2 even for volume fractions as large as 45%.

4.5 Simulation method

The time-dependent behavior of the stress in a suspension with and without hydrodynamic interactoins is examined with Stokesian Dynamics and Brownian Dynamics simulations, respectively. The details of these techniques can be found elsewhere; the following is a brief overview of each. The theoretical results apply to any linear flow; the simulations will be for simple shear flow.

The Brownian dynamics algorithm used here is based on the method of Heyes & Melrose (1993) for simulation of hard spheres in the absence of hydrodynamic interactions. Motion of the particles in this system is governed by the particle evolution equation:

$$\Delta \boldsymbol{x} = \boldsymbol{U}\Delta t + \Delta \boldsymbol{x}^{HS} + \boldsymbol{X}(\Delta t),$$

$$\overline{\boldsymbol{X}} = 0, \quad \text{and} \quad \overline{\boldsymbol{X}(\Delta t)\boldsymbol{X}(\Delta t)} = 2D_0 \boldsymbol{I}\Delta t. \tag{4.35}$$

Here, $\Delta \boldsymbol{x}$ is the change in particle position during the time step Δt, $\boldsymbol{U}\Delta t = \dot{\boldsymbol{\Gamma}}\cdot\boldsymbol{x}\Delta t = \dot{\gamma} y \hat{\boldsymbol{i}}\Delta t$ for simple shear flow and $\boldsymbol{X}(\Delta t)$ is a random displacement due to Brownian motion that has zero mean and covariance related to the Stokes-Einstein diffusivity for a single particle alone in the fluid. After the Brownian and affine displacements are applied, the simulation checks for particle overlaps and displaces them along their

lines of centers according to

$$\Delta \boldsymbol{x}^{HS} = \frac{1}{2}(\Delta r - 2a)\hat{\boldsymbol{r}} H(2a - \Delta r), \tag{4.36}$$

where $\Delta \boldsymbol{x}^{HS}$ is the hard-sphere displacement, and Δr is the interparticle separation after the affine and Brownian displacements. The Heaviside step function is included to ensure that the displacement is only applied to overlapping particle pairs and the coefficient $\frac{1}{2}$ is chosen to return the particles back into contact. These displacements are intended to duplicate the effects of a hard-sphere interparticle force. Due to the pairwise fashion in which they applied, however, there are some residual overlaps that cannot be resolved due to three particle effects. As shown by the temporal decay of the stress autocorrelation function, these residual overlaps do not contaminate the hard-sphere behavior.

Heyes & Melrose (1993) proceed to determine the suspension stress tensor by calculating $\langle \hat{\boldsymbol{r}}\hat{\boldsymbol{r}} g(\boldsymbol{r}) \rangle$ at contact over the course of a simulation as a way of measuring the contact integral in (4.9). This method ensures that an equilibrium distribution recovers the known theoretical value for the interparticle stress, $-4\phi g(2a)\boldsymbol{I}$. Here, we use a different method that involves calculating pairwise interparticle forces, $\boldsymbol{F}^P$, that would result in the hard-sphere displacements in (4.36). In the absence of hydrodynamic interactions, the force associated with each displacement is given by

$$\boldsymbol{F}^P = 6\pi\eta a \frac{\Delta \boldsymbol{x}^{HS}}{\Delta t}, \tag{4.37}$$

which is simply the average Stokes drag on the particle over the course the hard-sphere displacement.

After the interparticle forces have been calculated, it is straightforward to determine the bulk stress. In the absence of hydrodynamic interactions (4.10) reduces to

$$\langle \boldsymbol{\Sigma} \rangle = -\langle p \rangle_f \boldsymbol{I} - nkT\boldsymbol{I} + 2\eta(1 + \frac{5}{2}\phi)\langle \boldsymbol{E} \rangle - n\langle \boldsymbol{x}\boldsymbol{F}^P \rangle. \tag{4.38}$$

Here, the Brownian contribution to the stress is zero, while the hydrodynamic contri-

bution reduces to the dilute-limit Einstein correction to the viscosity, $\frac{5}{2}\phi$. This plus the isotropic stresses represent a Newtonian rheology. All of the interesting rheological behavior is due to the interparticle force contribution, $n\langle \boldsymbol{x}\boldsymbol{F}^P \rangle$. For simplicity, only this contribution is included in all stress results presented for the Brownian Dynamics system. The simplicity of this algorithm enables large systems to be studied. All Brownian Dynamics simulations in this work use the same number of particles, $N = 1331$.

Inclusion of hydrodynamic interactions involves the many-body far-field interactions and the pairwise additive lubrication forces present in the Stokesian Dynamics algorithm. Details of this technique are described elsewhere (Bossis & Brady 1987, Brady & Bossis 1988); here we proceed quickly. Conventional Stokesian Dynamics requires the inversion of large hydrodynamic mobility and resistance matrices at a high computational cost of $O(N^3)$, and thus we are limited to relatively small system sizes. All Stokesian Dynamics simulations in this work use the same number of particles, $N = 27$.

Dynamics of the simulation are governed by the particle-evolution equation,

$$\Delta \boldsymbol{x} = \Delta \boldsymbol{x}^a + \Delta \boldsymbol{x}^H + \Delta \boldsymbol{x}^B, \tag{4.39}$$

where we have broken the evolution equation into its affine, hydrodynamic and Brownian contributions. The affine displacement,

$$\Delta \boldsymbol{x}^a = \boldsymbol{U}\Delta t = \dot{\gamma} y \hat{\boldsymbol{i}} \Delta t, \tag{4.40}$$

simply convects the particle along with the bulk shear flow. The hydrodynamic displacement,

$$\Delta \boldsymbol{x}^H = \boldsymbol{R}_{FU}^{-1} \cdot \boldsymbol{R}_{FE} : \langle \boldsymbol{E} \rangle \Delta t, \tag{4.41}$$

represents the deviation in particle trajectories from the affine flow due to hydrodynamic interactions. The third contribution is the Brownian displacement given

by

$$\Delta \boldsymbol{x}^B = kT\nabla\cdot\boldsymbol{R}_{FU}^{-1}\Delta t + \boldsymbol{X}(\Delta t),$$

$$\overline{\boldsymbol{X}} = 0 \quad \text{and} \quad \overline{\boldsymbol{X}(\Delta t)\boldsymbol{X}(\Delta t)} = 2kT\boldsymbol{R}_{FU}^{-1}\Delta t, \tag{4.42}$$

which is similar to the Brownian contribution to (4.35) except that the short-time self-diffusion tensor, $kT\boldsymbol{R}_{FU}^{-1}$, is complicated by the introduction of hydrodynamic interactions. A higher order deterministic term involving the spatial gradient of the short-time diffusion tensor is also included to account for changes in the hydrodynamic mobility in the course of a random step. This term acts as a radially repulsive term that prevents particle overlaps due to the random displacements, and no hard-sphere force or hard-sphere-like displacements are needed with hydrodynamics.

Both the hydrodynamic and Brownian contribution to the stress can be determined at each instant in time from the particle configuration using (4.8). Nondimensionalizing $\boldsymbol{x}$ by the particle radius a, the rate of strain tensor, $\langle \boldsymbol{E} \rangle$, by its magnitude $\dot{\gamma}$, the imposed velocity $\boldsymbol{U}$ by $\dot{\gamma}a$ and the hydrodynamic resistance tensors $\boldsymbol{R}_{FU}$ and $\boldsymbol{R}_{FE}$ by $6\pi\eta a$ and $6\pi\eta a^2$, respectively, one finds two charactistic time scales. The time scale for the hydrodynamic displacements in (4.41) is the flow time scale, $\dot{\gamma}^{-1}$, whereas the relevant time scale for the Brownian displacements in (4.42) is the diffusive time scale, $a^2/2D_0 = 3\pi\eta a^3/kT$. The ratio of the diffusive time scale to the flow time scale is the Péclet number, $Pe = \dot{\gamma}a^2/2D_0$, which we use as the nondimensional shear rate for this work for both the Brownian Dynamics and Stokesian Dynamics systems. Note that this Péclet number has been chosen to match the accompanying theoretical work and differs from that Péclet number used in the other chapters by a factor of two.

Two types of simulations are performed for this work. The first type involves performing a single simulation at equilibrium ($Pe = 0$) for a long period of time in order to obtain the shear-stress autocorrelation function $C_s(t)$. During this long simulation, three independent stresses for the system are monitored: Σ_{xy}, Σ_{xz} and Σ_{yz}. The time average of each is zero at equilibrium and fluctuations are measured by the autocorrelation function $C_s(t)$. Because we are interested in the total system

stress — and not the individual particle contributions, as is necessary for other correlation functions, such as the mean-square displacements — it is straightforward to keep a record of the values of the three shear stresses for all time to maximize the data available for calculating $C_s(t)$. From the data, three separate autocorrelation functions are calculated for fluctuating shear stress which are simply averaged to obtain the full function, $C_s(t)$. Because the simulation is run at equilibrium, time is nondimensionalized by the diffusive time, a^2/D_0. The time step for the Brownian dynamics system was set to be $\Delta t = 2.5 \times 10^{-4}$ and is set to be $\Delta t = 5 \times 10^{-4}$ for the Stokesian Dynamics system. Simulations are performed at several volume fractions, ϕ. Because of the small system sizes ($N = 27$) involved in Stokesian Dynamics simulations, we are limited to studying suspensions below the equilibrium phase boundary at $\phi = 0.494$. The large systems used in Brownian Dynamics enabled study at higher densities. We are interested in studying suspensions in the metastable disordered state at volume fractions above the phase boundary. Starting configurations of this type are obtained using a density quenching technique (Rintoul & Torquato 1996, Clarke & Wiley 1987). The osmotic pressure was monitored during the run to ensure that crystallization does not occur.

The second type of simulation is used for monitoring the transient stress due to an abrupt change in the flow conditions. Relatively short runs are needed as the time it takes for the suspension to move from one steady-state condition to the next scales with the boundary-layer diffusion time and are therefore relatively small. For this work, we are interested in studying the stress response during both start-up and flow cessation. To do this, we start the simulation with an equilibrium configuration and undergo a step increase in the shear rate, or Pe. The shear rate is held constant while the stress response during start-up flow is monitored. At low shear rates, ($Pe \leq 1$), the diffusive time, a^2/D_0 is used to scale time in the simulations, while at high shear rates, the flow time, $\dot{\gamma}^{-1}$, is used. The time step for all Brownian Dynamics simulations is $\Delta t = 2.5 \times 10^{-4}$ and the number of time steps the shear rate is held constant is 4000. This sets the length of the start-up flow regime to be one particle diffusive time at low shear rates and one strain at high shear rates. At this point,

the flow is abruptly stopped by no longer including the affine displacements in the evolution equation (4.35) for 4000 more time steps while the nondimensionalization of time is not changed. At high shear rates, this continued nondimensionalization with the flow time, $\dot{\gamma}^{-1} = (a^2/D_0)Pe^{-1}$, despite the fact that it is diffusion that drives particle motion following cessation, enables us to study the immediate post-cessation behavior in greater detail. This technique is repeated 91 times and transient stress data from each of the individual runs are averaged together to reduce statistical noise.

Start-up flow and flow cessation are also studied using Stokesian Dynamics in the same manner, but with a few changes. Hydrodynamic interactions have the effect of slowing down the dynamics of the system, thus a larger time step, $\Delta t = 5 \times 10^{-4}$ can be used. The lengths of the flow regimes remain at 4000 time steps which sets the length of the start-up regime to be two diffusive times near equilibrium and two strains at high shear rates. With Stokesian Dynamics, both the affine (4.40) and hydrodynamic (4.41) displacements are set to zero. Also, the technique is repeated 182 times instead of 91 times in an attempt to partly compensate for the much smaller system sizes involved.

4.6 Results

4.6.1 Equilibrium Fluctuations: Green-Kubo

Relaxation behavior of equilibrium fluctuations, as measured by the shear-stress autocorrelation function $C_s(t)$, for the Brownian Dynamics system at various volume fractions, ϕ, is shown in figure 4.1. The decay of $C_s(t)$ with time is strictly monotonic. At short times, $C_s(t)$ apppears to be diverging like $t^{-1/2}$ in agreement with the theoretical discussion in §4.3. The reason for the divergent behavior is due to the delta-function nature of the hard-sphere interparticle force. The suspension stress at any particular instant in time is either zero or infinite depending on whether or not a particle-particle collision is occuring at that precise moment. The time average of such a stress profile is finite (in this case, it is zero), but the variance, and thus

the zero-value of the autocorrelation function, is infinite. This divergent behavior implies that there is an infinite high freqency limit to the elastic modulus, G'_∞, also as predicted by theory. In this work, the 'instantaneous' stress from the simulation is actually a time-step-averaged stress, and thus the delta-function nature of the stress is removed. Despite this, $C_s(t)$ still appears divergent at times as short as one time step, $\Delta t = 2.5 \times 10^{-4}$. Examination of shorter times requires smaller time steps, which one can see from (4.37) results in larger 'instantaneous' forces and stresses, enabling $C_s(t)$ to increase further at the shorter times being probed. The $t^{-1/2}$ behavior of $C_s(t)$ serves as a good check of the hard-sphere interparticle force algorithm used in this work. A soft interparticle potential would result in a finite modulus. The long-time behavior of $C_s(t)$ is hard to discern from the data; it relaxes to zero, but the precise form of the decay is not evident due to statistical noise. Theoretically, the long-time decay should be as $t^{-7/2}$ coming from the three dimensional diffusive response to a quadrupolar $\langle \boldsymbol{E} \rangle$ forcing. Long-time autocorrelations in a complex system such as this are very difficult to measure, as the system becomes more and more uncorrelated as time progresses and it becomes increasingly difficult to measure such small correlations.

Inclusion of hydrodynamic interactions produces qualitatively different behavior. Figure 4.2 shows the time-dependent behavior of $C_s(t)$ at various volume fractions for the Stokesian Dynamics system. Again, relaxation of $C_s(t)$ is monotonic. Unlike in the situation in the absence of hydrodynamic interactions, $C_s(t)$ approaches a constant at short times, indicative of the existence of a finite high-frequency modulus, G'_∞. The hard-sphere delta-function interparticle force is still present, but is never implemented to keep the particles from overlapping as the strong lubrication interactions between the particles are sufficient. The stress present at equilibrium is no longer the interparticle stress, but the Brownian stress as defined by (4.8a). This stress does have a finite instantaneous value associated with each particle configuration. Therefore the variance of the stress, and thus also G'_∞, is finite. The value of $C_s(t)$ subtracted from its constant zero-time value is shown in figure 4.3. It is clear from the figure that the initial decay is linear with time in agreement with the

discussion in §4.3. As is the case with Brownian Dynamics, the precise nature of the long-time decay cannot be extracted from the data due to statistical noise; theory predicts $t^{-7/2}$.

The values of the high-frequency modulus, G'_∞, from Stokesian Dynamics are shown as a function of ϕ in figure 4.4. Also on the figure are experimental data on model hard-sphere systems by Shikata & Pearson (1994) showing some degree of agreement. The experimental data are consistently larger than the simulation data which could be due to some residual effect of the steric stabilization necessary in these silica dispersions. The error in the simulation data is about 1%. The simulation results here are obtained from the zero-time value of the shear-stress autocorrelation funtion. One could also obtain G'_∞ by calculating the variance of the stresses associated with numerous independent random configurations without evolving these configurations over time.

4.6.2 Nonequilibrium Behavior: Start-up / Flow-Cessation

No hydrodynamic interactions: Brownian Dynamics

Start-up flow

At this point, we shift our focus toward the response of the stress to start-up and flow cessation. Figure 4.5 shows the instantaneous stress during start-up flow at various Pe for the Brownian Dynamics system at one volume fraction $\phi = 0.45$. This plot shows that nondimensionalizing the stress by $\eta\dot{\gamma}$ — plotting the viscosity — and nondimensionalizing the time by the diffusive time a^2/D_0 collapses the data for small Pe. The viscosity is seen to grow as $t^{1/2}$ at short times as predicted in the theory in §4.4.2. At longer times, one can see the shear thinning behavior as the curves peel off towards their steady-state values that are decreasing functions of Pe.

Also on the plot is the time integral of $C_s(t)$ which is obtained by performing the integral in (4.12) at zero frequency with t used as the upper limit of integration instead of ∞. At short times, this integral increases like $t^{1/2}$, corresponding to the $t^{-1/2}$ behavior at of $C_s(t)$ at short times. At long times, this integral asymptotes to

the zero shear viscosity, η_0. The agreement of the transient stress data with this time integral is good, and to be expected in that at very low Pe or at short times at other Pe the systems response to the step change in shear rate is indistinguishable from an equilibrium fluctuation and should behave in the same manner.

At higher Pe, the system deviates from the near equilibrium behavior, particularly at long times. There is still a discernable $t^{1/2}$ growth at short times in the viscosity for all Pe, but the curves appear to be shifting to the left with Pe on figure 4.5 indicating that the characteristic time scale at short times is changing to a smaller time scale, perhaps the flow time $\dot{\gamma}^{-1}$, but we cannot be sure from the data. The $t^{1/2}$ behavior does not persist for very long at high Pe. It shifts to a more linear growth behavior that scales with the flow time $\dot{\gamma}^{-1}$. This is more clearly seen in figure 4.6 which shows the same data as in figure 4.5 but the time is nondimensionalized by the flow time, $\dot{\gamma}^{-1}$. Here, the initial $t^{1/2}$ behavior can barely be seen at high Pe and is represented by a cusp near zero time. Viscosities for all Pe reach a plateau value within one strain, which is in agreement with the theoretical development in §4.4.2 that shows that the structure during start-up flow reaches steady-state exponentially on the time scale of $\dot{\gamma}^{-1}$ (Equation (4.30)). There appears to be an overshoot in the viscosity with time at the higher shear rates. We do not expect such nonmonotonic behavior to be present in the two-body analysis presented in §4.4.2 and is most likely an effect of many-body interactions at high ϕ.

Also one notes from the data that the response to start-up flow becomes independent of Pe at the highest shear rates. The curves for the three highest Pe numbers are all coincident when time is nondimensionalized by $\dot{\gamma}^{-1}$. This is consistent with the high-Pe assymptotic limit in (4.30) and also in Brady & Morris (1997). The fact that the viscosity reaches a non-zero high-Pe plateau is also in agreement with Brady & Morris (1997).

Flow cessation

The flow is abruptly stopped after 4000 time steps and the shear stress is monitored as the structure relaxes back towards equilibrium. Figure 4.7 shows the stress as a

function of time after cessation from flows at various values of Pe (before cessation). We choose a shear-rate independent nondimensionalization of the stress, nkT, in order to measure the degree of deformation to the microstructure. Because of this, the stress at the moment of cessation scales as Pe as all the pre-cessation viscosities are of the same magnitude. After an initial decay, all the relaxation curves become coincident at intermediate and long times. It is expected that relaxation to equilibrium from any configuration should take place on an $O(a^2/D_0)$ time, as particles need to diffuse a length on order of their size to completely relax the microstructure. Figure 4.7 makes a stronger statement, however, showing that each nonequilibrium microstructure takes the same relaxation path towards equilibrium. At intermediate times a region of $t^{-1/2}$ decay is evident from the simulation data. The precise nature of the stronger terminal decay is not evident due to statistical noise present and small magnitudes of the shear stress; theory predicts $t^{-7/2}$.

Figure 4.8 more closely examines the behavior immediately following cessation of the flow. Here, we nondimensionalize the stress by the precessation value of $\eta\dot{\gamma}$. Using this scaling is more appropriate for the short time behavior as the viscosities before the flow is stopped are roughly equal. Time has been nondimensionalized by the time necessary for a particle to diffuse the width of the boundary layer, $\delta^2/D_0 = (a^2/D_0)Pe^{-2}$, as this is the relevant time scale for the initial relaxation. Our theoretical prediction, equation (4.34) is also shown on figure 4.8. Here, we use $\gamma_r = -\frac{1}{2}$ as this is the minimum value on the compressional axis and select $g_{ss}(0)$ to match the pre-cessation value of the viscosity. Excellent agreement is found between simulation data for $Pe \geq 15$ where the high-Pe boundary layer analysis is most appropriate. The $t^{-1/2}$ decay present at intermediate times in figure 4.7 is present here at long times. This represents a typical long-time tail in a one-dimensional diffusion problem, such as diffusion out of a boundary layer. Relaxation behavior from lower Pe show some deviation from the theory at longer times, but only after the stress has dropped by an order of magnitude. The theoretical boundary-layer solution is only supposed to be valid in the high-Pe limit and the mode of relaxation at low Pe may have switched to its stronger terminal behavior, which involves decay of the

microstructure outside the boundary layer.

We are able to analyze the microstructure during start-up and cessation directly from the simulation data. Figure 4.9 shows projections of the pair-distribution function $g(\boldsymbol{r})$ onto the plane of shear during eight points in the flow; four during start-up and four during flow-cessation. Here, $g(\boldsymbol{r})$ measures the probability of finding a particle at a point in the plane given that another particle in the center of the figure. Figure 4.10 shows the corresponding plot of the instantaneous viscosity versus time for this particular run performed at $\phi = 0.45$ and $Pe = 15$. Point (1) shows the equilibrium structure with isotropic first and second nearest-neighbor rings of high probability around the test particle in the center. After the flow is turned on (2) we see the rings appearing more like ovals, with the probability distribution narrowing in the compressional quadrants and being convected away from the test particle in the extensional quadrants. At (3), the maximum of the stress, a further thinning of the boundary layer in the compressional zone is evident and one can see separation of probability from particle contact in the extensional zone. At the moment of cessation (4), the thickness of the boundary layer has stabilized and there is evidence of a trailing wake in the extensional zone.

Just after cessation, (5), one sees no noticeable change in the microstructre despite the fact that figure 4.10 shows a precipitous drop in the suspension stress. All of the relaxation of the microstructure occurs inside the small boundary layer region in the compressional zones, which cannot be seen on this scale of resolution. The structure at later times (6)-(8) bears this out. The boundary layer of particle probability in the compressional zones continues to relax back to equilibrium (1) thickness. While the structure of the boundary layer has completely relaxed — it requires only an $O([a^2/D_0]Pe^{-2})$ time — there is still anisotropy outside the boundary layer as evident in the depletion of particles near contact in the extensional zone. Structural relaxation outside the boundary layer requires a longer $O(a^2/D_0)$ time as particles need to diffuse on order their size, a, rather than simply the boundary layer thickness, δ. Note that this figure shows that the stress-optical rule will fail for these colloids, as the stress has almost completely relaxed while the structure on the particle scale, which is what

optical measurements would probe, has hardly relaxed by time (8).

Hydrodynamic interactions: Stokesian Dynamics

The transient behavior of the stress is also examined in suspensions with hydrodynamic interactions. Using Stokesian Dynamics we monitor both the hydrodynamic and Brownian stress during start-up and following cessation. The hard-sphere interparticle force is not necessary in this system and thus the contribution to the viscosity due to interparticle forces is zero.

Start-up flow

The instantaneous Brownian stress during start-up flow in the Stokesian Dynamics system at $\phi = 0.45$ and various Pe is shown in figure 4.11. Due to the much smaller sizes of the Stokesian Dynamics system, we have difficulties precisely measuring a zero Brownian shear stress at equilibrium. The error was rather small — always less than $0.15nkT$, or about $0.6\eta\dot{\gamma}Pe^{-1}$ — but even small errors tend to destroy the quality of logarithmic plots. For this reason, the zero-time value of the Brownian stress is subtracted from its instantaneous value in order to more closely examine the growth of the stress during start-up. Here we only examine data from $Pe \geq 1.5$ as small errors in the stress are quite significant at low shear rates. Figure 4.11 shows that the growth of the viscosity from its zero-time value is clearly linear in time in contrast with $t^{1/2}$ growth seen in the Brownian Dynamics system. Also shown in figure 4.11 is the time-integral of the shear stress autocorrelation function, $C_s(t)$. As was the case with the Brownian Dynamics system, this integral does an excellent job of predicting the transient behavior of the viscosity during start-up. The agreement seems to hold for the growth portion of the curves for all Pe. There is no leftward shift of the curves at high Pe evident in the Brownian Dynamics system. The linear growth at short times of the Brownian stress can thus be related to the high-frequency behavior at equilibrium

At long times the Brownian viscosity curves peel off towards their steady-state values in inverse order of shear rate. Each data set contains 4000 times steps which

translates to two strains, or $2\dot{\gamma}t$. A steady-state is attained within each data set which compares well with the values obtained from long time-averages during steady-state simulations (Foss & Brady 1999 (ch. 3)). There is evidence of an overshoot in most of the curves in figure 4.11, although the evidence is not conclusive as there is a fair amount of noise present in this portion the data.

The hydrodynamic viscosity is also measured during start-up flow and shown in figure 4.12. At zero time, the viscosity is non-zero and equal to the high-frequency dynamic viscosity, η'_∞. The value of η'_∞ shown here agrees well with those obtained from time averages of long steady-state simulations performed at or near equilibrium (Foss & Brady 1999 (ch. 3)). The hydrodynamic viscosity grows with time indicative of shear thickening behavior and, following what appears to be an overshoot in several of the curves, reaches a fairly noisy steady-state within two strains.

In contrast to the Brownian viscosity, the growth of the hydrodynamic viscosity does not appear to be linear at short times as is evident by the the zero slope of the curve near $t = 0$. This is clearer in figure 4.13 where the zero-value of the hydrodynamic viscosity has been subtracted. The data is quite noisy at very short times, but starting at about $t = 0.05\dot{\gamma}t$ one can discern algebraic growth that is definitely stronger than linear, and perhaps quadratic in time. The slower growth of the hydrodynamic viscosity compared to the Brownian viscosity is due perhaps to the fact that the hydrodynamic viscosity is not as sensitive to small changes in the microstructure as is evident by the fact that it is constant, and equal to η'_∞ during a small-amplitude oscillatory shear flow. Also, in steady-shear flow, the hydrodynamic viscosity is constant at low shear rates and shear thickening is not noticeable until Péclet numbers of about 5. Behavior at short-times is not unlike behavior near equilibrium and thus, the Brownian viscosity may react earlier start-up flow.

Flow cessation

Following cessation, the hydrodynamic stress vanishes 'instantly' as it is proportional to $\boldsymbol{E}$, which is zero in the absence of flow. Hydrodynamic stresses decay on the much faster inertial relaxation time, a^2/ν, where ν is the kinematic viscosity of the solvent.

Relaxation of the Brownian stress in the Stokesian Dynamics system as a function of time is shown in figure 4.14. As with the case with no hydrodynamic interactions (figure 4.7), we use a shear-rate independent nondimensionalization of the stress, nkT, which gives a measure of the degree of the deformation of the microstructure. From figure 4.14, it is clear that after an initial period of decay each nonequilibrium microstructure follows the same path to equilibrium on the diffusive, a^2/D_0, time scale.

Note that in figure 4.14, we are able to use a linear scale for the Brownian stress as the pre-cessation values are not a strong function of Pe at high Pe. So far, we have not been able to collapse of the data at short times following cessation as is done in the case with no hydrodynamic interactions (figure 4.8). According to Brady & Morris (1997), the microstructure at high Pe is still dominated by an $O(Pe^{-1})$ boundary layer. However, the stress and microstructure are not as intimately connected as they are without hydrodynamics, where all the stress is due to a delta-function force at contact. With hydrodynamics, the Brownian stress is not singular at contact — as is evident by the finite G'_∞ — and the contribution to the stress from two particles not in contact is nonzero. This may cause the stress to relax in a different manner than the relaxation of microstructure. Also, one cannot rule out possible effects of system size. The simulation size is quite small ($N = 27$) in the Stokesian Dynamics system and although the results represent an average over many runs, there may be effects due to the small size of the periodic cell.

4.7 Summary and concluding remarks

In this work, we examine the time-dependent stress behavior in hard-sphere colloidal suspensions in both equilibrium and nonequilibrium situations theoretically and via dynamic simulation. Suspensions with and without hydrodynamic interactions are studied using Stokesian Dynamics and Brownian Dynamics, respectively. Relaxation of microstructural fluctuations at equilibrium can be examined by analysis of the shear-stress autocorrelation function $C_s(t)$. A review of previous theoretical work

relates this function directly to the linear viscoelastic complex viscosity, and thus also the complex modulus. Short-time behavior of $C_s(t)$ is analagous to the behavior of the microstructure in oscillatory shear flow at high frequencies.

The behavior at high frequencies is singular with a boundary layer forming near contact where frequency-dependent convection balances Brownian diffusion. This boundary layer scales as $\omega^{-1/2}$ in the absence of hydrodynamic interactions. The presence of hydrodynamic interactions, specifically lubrication forces, weakens the effects of Brownian motion resulting in a thinner ω^{-1} boundary layer near particle contact. From this analysis, the behavior of $C_s(t)$ at short times can be extracted: Divergent $t^{-1/2}$ behavior is found in the absence of hydrodynamic interactions indicating an infinite high frequency limit to the elastic modulus, G'_∞. With hydrodynamic interactions $C_s(t)$ assymptotes linearly at short times to a constant indicating a finite G'_∞. Simulation results in this work show agreement with these previous theoretical predictions. The divergent $t^{-1/2}$ behavior in the Brownian Dynamics system as well as the linear decay from a constant zero-time value in the Stokesian Dynamic system. Stokesian Dynamics results for G'_∞ are reported showing fair agreement with experiment.

Transient stress behavior is analyzed during nonequilibrium start-up and flow cessation simulations with the Brownian Dynamics system. The viscosity is found to grow at short times during start-up flow like $t^{1/2}$. A stronger relationship between the time integral of $C_s(t)$ and the stress growth during start-up flow at all times for low Pe is suggested by the simulation results.

At high Pe, behavior is dictated by a different boundary layer near contact where convection balances diffusion than that present at equilibrium which scales as Pe^{-1}. Theoretical analysis is performed which extends the steady-state boundary layer analysis of Brady & Morris (1997) to include start-up and flow cessation. Formation of the boundary layer during start-up flow is found to occur on the flow time scale, $\dot{\gamma}^{-1}$, while relaxation following cessation occurs on a shorter time scale, $(a^2/D_0)Pe^{-2} = \delta^2/D_0$, given by diffusion in the boundary layer.

Brownian Dynamics simulations verify the above theoretical claims. After the

$t^{1/2}$ growth at very short times, start-up flow at high Pe approaches steady-state on the flow time scale, $\dot{\gamma}^{-1}$. Relaxation of the stress following cessation is found to occur on the predicted time scale $(a^2/D_0)Pe^{-2} = \delta^2/D_0$ with excellent functional agreement with the theoretical result. At long times, relaxation shifts to the regular diffusive time scale, a^2/D_0, for the final decay of anisotropies present outside the boundary layer. Snapshots of the microstructure obtained from simulation at various points during start-up and cessation are in agreement with the relaxation mechanisms proposed from analysis of the stress data.

The behavior during start-up and following cessation is also examined with hydrodynamic interactions using Stokesian Dynamics. Both the Brownian and hydrodynamic stress are monitored. The Brownian viscosity during start-up is found to grow linearly at short times. The strong relationship between start-up flow at all times for low Pe and the time integral of $C_s(t)$ is also found for the Stokesian Dynamics system. The hydrodynamic viscosity also increases with time, but with different functional behavior. Steady-state for both stresses is attained with two strains.

Several questions remain. Although relaxation behavior at short times for both $C_s(t)$ at equilibrium and the stress following cessation is quite clear, the precise long-time decay of the functions could not be obtained due to statistical noise. Also, due to the relation between $C_s(t)$ and the complex viscosity, a precise volume fraction analysis of the relaxation of the function would provide insight into the relevant time scales involved in various rheological theories such as those for the low-shear viscosity.

Acknowledgements

The authors would like to thank Johan Bergenholtz for many thoughtful discussions pertaining to this work. This work is supported in part from grants CTS-9420415 from NSF and NAG8-1237 from NASA.

References

Abramowitz, M. & Stegun, I.A. 1972 *Handbook of Mathematical Functions.* Dover.

Bergenholtz, J.B., Vicic, M. & Brady, J.F. 1999 Personal communication.

Boon, J.-P. & Yip, S. 1980 *Molecular Hydrodynamics* Dover.

Bossis, G. & Brady, J.F. 1987 Self-diffusion of Brownian particles in concentrated suspensions under shear. *J. Chem. Phys.* **83**, 97.

Brady, J.F. 1993a Brownian motion, hydrodynamics, and the osmotic pressure. *J. Chem. Phys.* **98**, 3335.

Brady, J.F. 1993b The rheological behavior of concentrated colloidal dispersions. *J. Chem. Phys.* **99**, 567.

Brady, J.F. & Bossis, G. 1988 Stokesian Dynamics. *Ann. Rev. Fluid Mech.* **20**, 111.

Brady, J.F. & Morris, J.F. 1997 Microstructure of strongly sheared suspensions and its impact on rheology and diffusion. *J. Fluid Mech.* **348**, 103.

Cichocki, B. & Felderhof 1991 Linear viscoelasticity of semi-dilute hard-sphere suspensions. *Phys. Rev. A* **43**, 5405.

Clarke, A.S. & Wiley, J.D. 1987 Numerical simulation of the dense random packing of a binary mixture of hard spheres: Amorphous metals. *Phys. Rev. B* **35**, 7350.

Foss, D.R. & Brady, J.F. 1999 Structure, diffusion and rheology of Brownian suspensions by Stokesian Dynamics simulation. *J. Fluid Mech.* (submitted).

Hansen, J.-P. & McDonald, I.R. 1986 *Theory of Simple Liquids* Academic.

Heyes, D.M. & Melrose, J.R. 1993 Brownian dynamics simulations of model hard-sphere suspensions, *J. Non-Newtonian Fluid Mech.* **46**, 1.

Kaffashi, B., O'Brien, V.T., Mackay, M.E. & Underwood, S.M. 1997 Elastic-like and viscous-like components of the shear viscosity for nearly hard sphere, Brownian suspensions, *J. Colloid Int. Sci.* **187**, 22.

Lionberger, R.A. & Russel, W.B. 1994 High frequency modulus of hard sphere colloids, *J. Rheol.* **38**, 1885.

Mackay, M.E. & Kaffashi, B. 1995 Stress jumps of charged colloidal suspensions, measurement of the elastic-like and viscous-like stress components, *J. Colloid Int. Sci.* **174**, 117.

Nägele, G. & Bergenholtz, J. 1998 Linear viscoelasticity of colloidal mixtures. *J. Chem. Phys.* **108**, 9893.

Rintoul, M.D. & Torquato, S. 1996 Computer simulations of dense hard-sphere systems. *J. Chem. Phys* **105**, 9258.

Shikata, T. & Pearson, D.S. 1994 Viscoelastic behavior of concentrated spherical dispersions. *J. Rheol.* **38**, 601.

Verberg, R., de Schepper, I.M., Feigenbaum, M.J. & Cohen, E.G.D. 1997 Square root singularity in the viscosity of neutral colloidal suspensions at large frequencies, *J. Stat. Phys.* **87**, 1037.

Watanabe, H., Yao, M-.L., Osaki, K., Shikata, T., Niwa, H. & Morishima, Y. 1996 Nonlinear rheology of a concentrated spherical silica suspension. *Rheol. Acta* **35**, 433.

Watanabe, H., Yao, M-.L., Osaki, K., Shikata, T., Niwa, H. & Morishima, Y. 1997 Nonlinear rheology of a concentrated spherical silica suspension: 2. Role of strain in shear-thickening. *Rheol. Acta* **35**, 433.

Watanabe, H., Yao, M-.L., Osaki, K., Shikata, T., Niwa, H. & Morishima, Y. 1999 Nonlinear rheology of a concentrated spherical silica suspension: 3. Concentration dependence. *Rheol. Acta* (to be submitted).

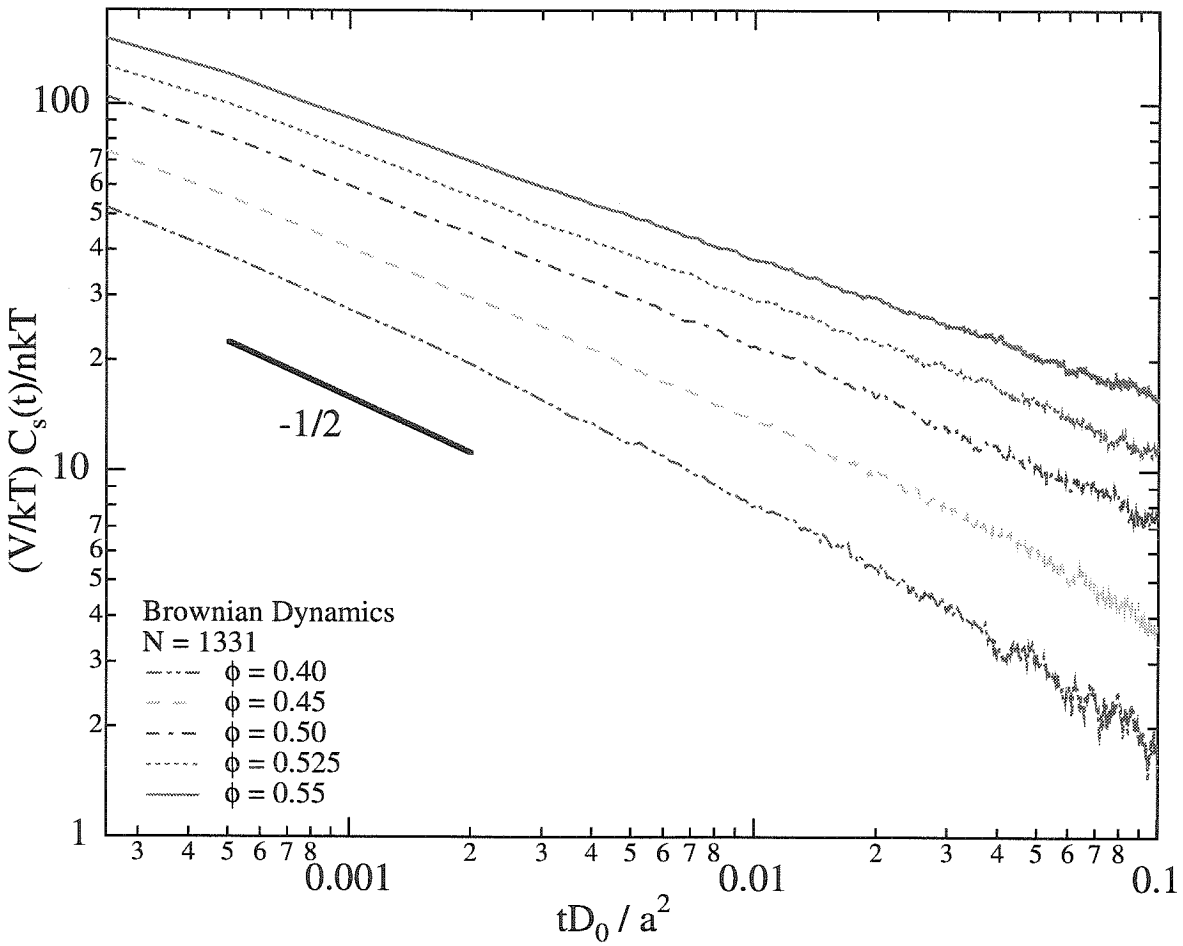

Figure 4.1: Shear stress autocorrelation function, $C_s(t)$, from the Brownian Dynamics system nondimensionalized by $n(kT)^2/V$ as a function of time, nondimensionalized by the diffusive time, a^2/D_0, for several values of volume fraction, ϕ.

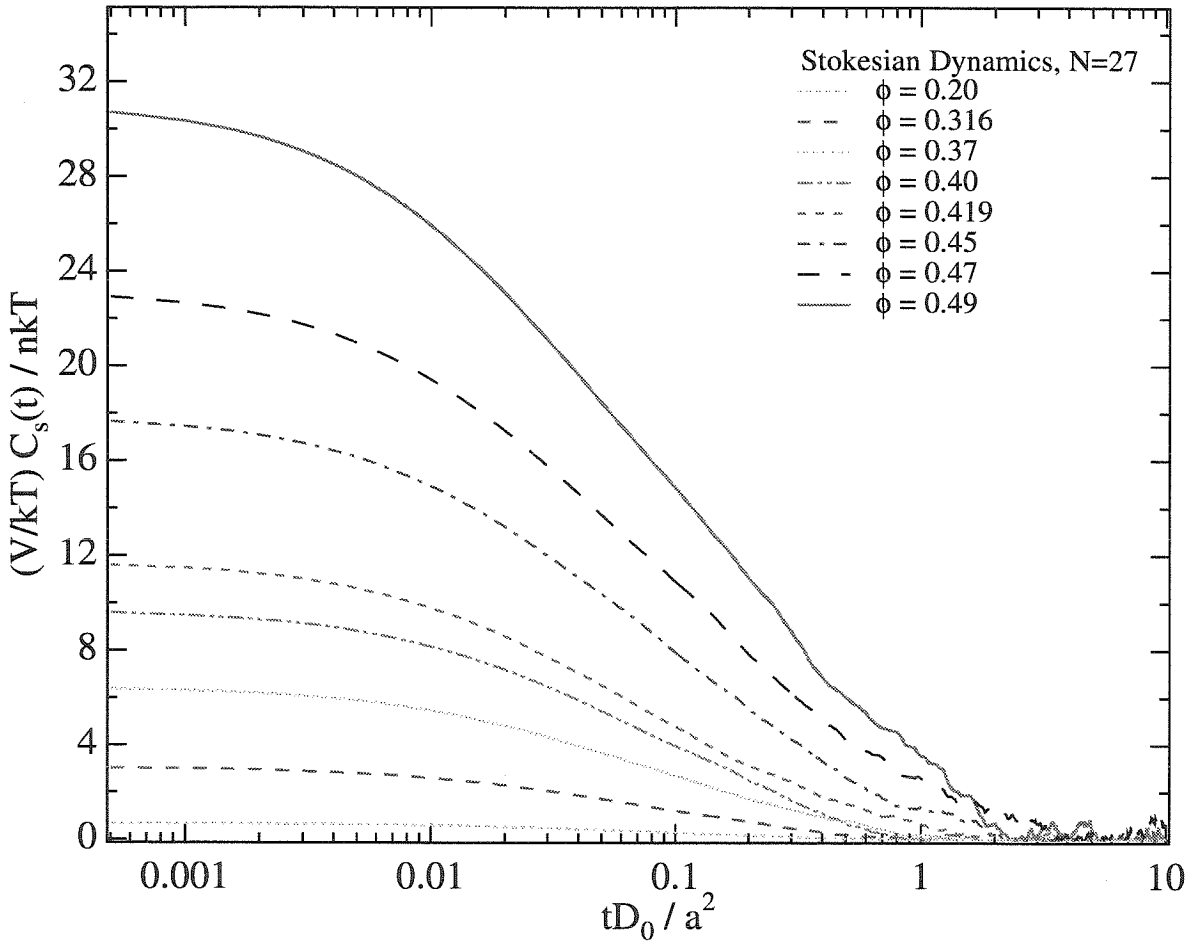

Figure 4.2: Shear stress autocorrelation function, $C_s(t)$, from the Stokesian Dynamics system nondimensionalized by $n(kT)^2/V$ as a function of time, nondimensionalized by the diffusive time, a^2/D_0, for several values of volume fraction, ϕ.

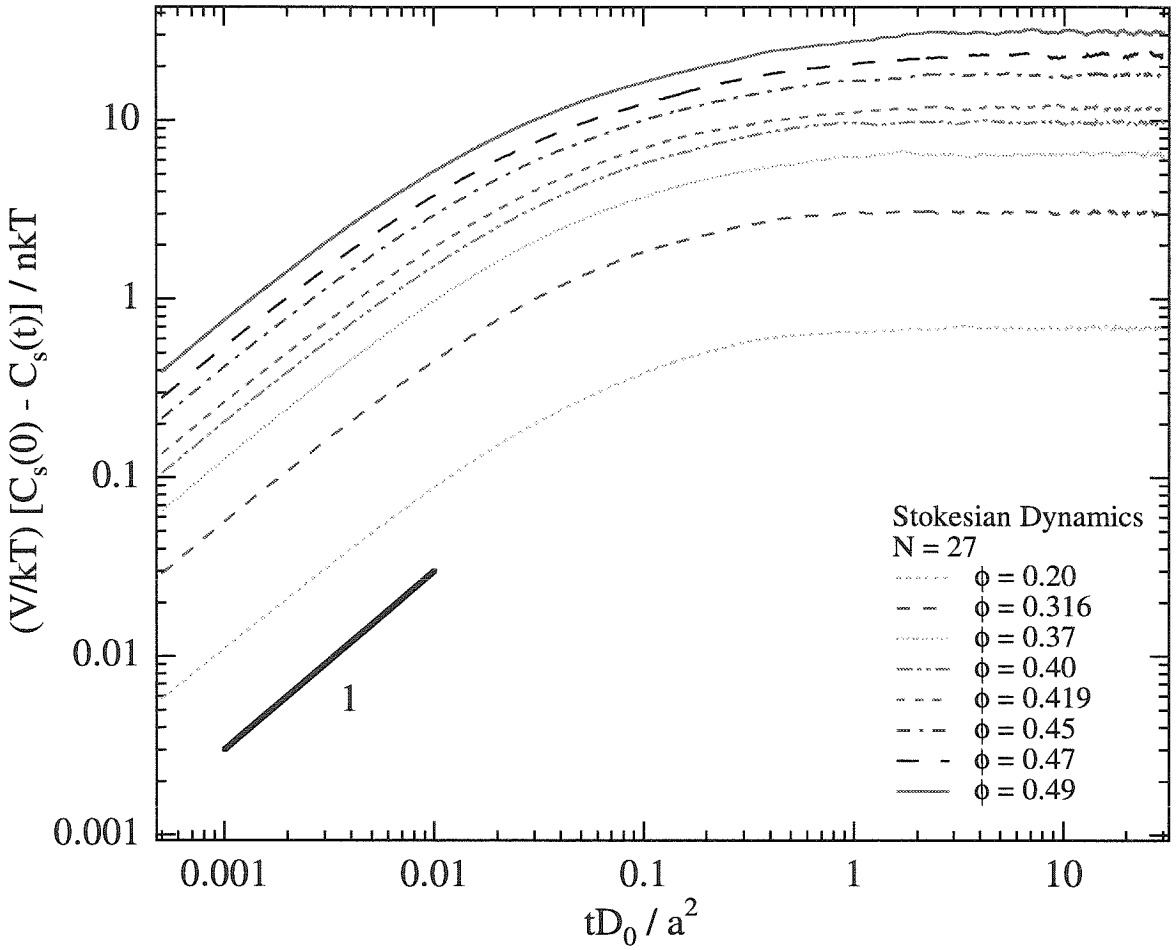

Figure 4.3: Shear stress autocorrelation function, $C_s(t)$, from the Stokesian Dynamics system subtracted from its zero-time value, nondimensionalized by $n(kT)^2/V$, as a function of time to show the nature of the intial decay of $C_s(t)$. Here, time is nondimensionalized by the diffusive time, a^2/D_0. Curves are shown for several values of volume fraction, ϕ.

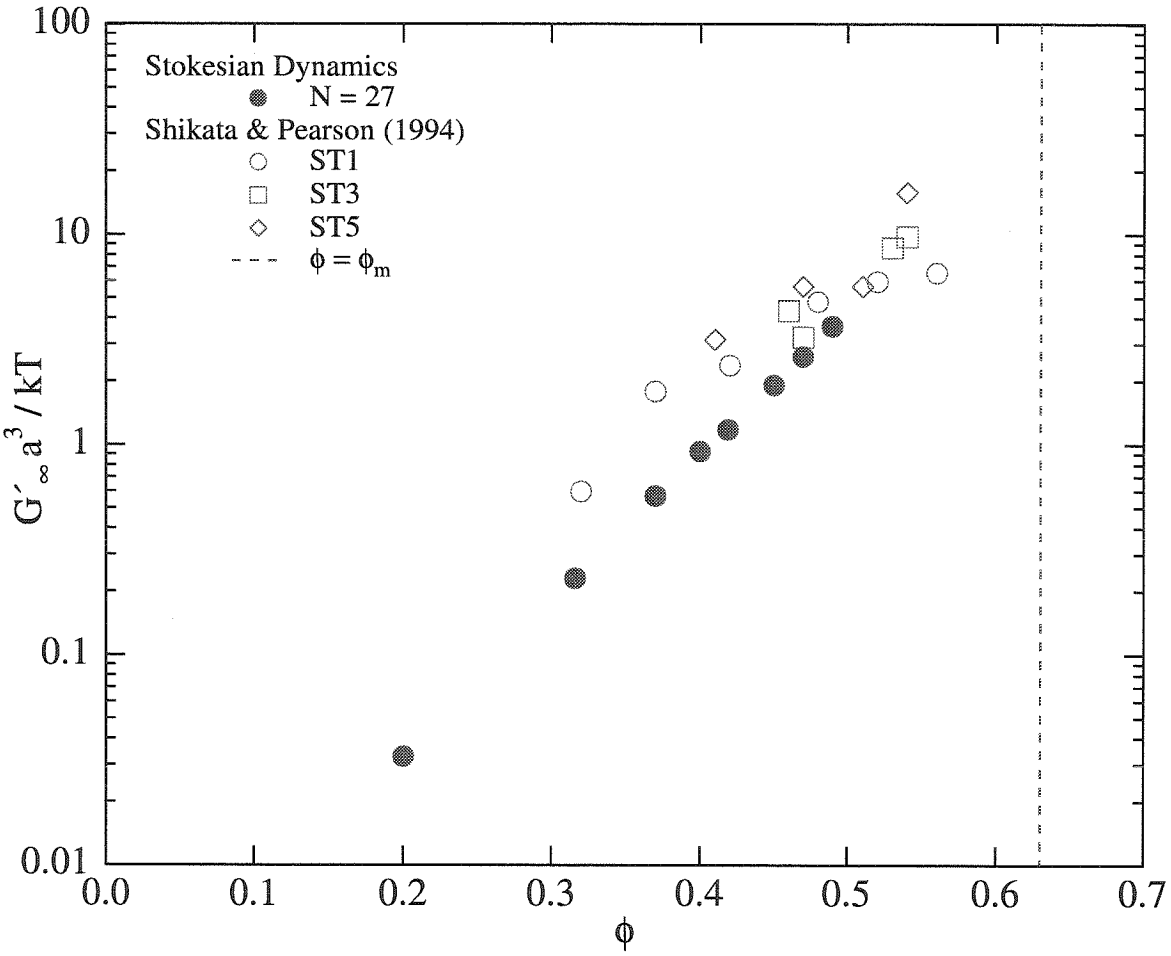

Figure 4.4: High frequency elastic modulus, G'_∞, nondimensionalized by kT/a^3, obtained from Stokesian Dynamics, $N = 27$. Data plotted as a function of volume fraction, ϕ.

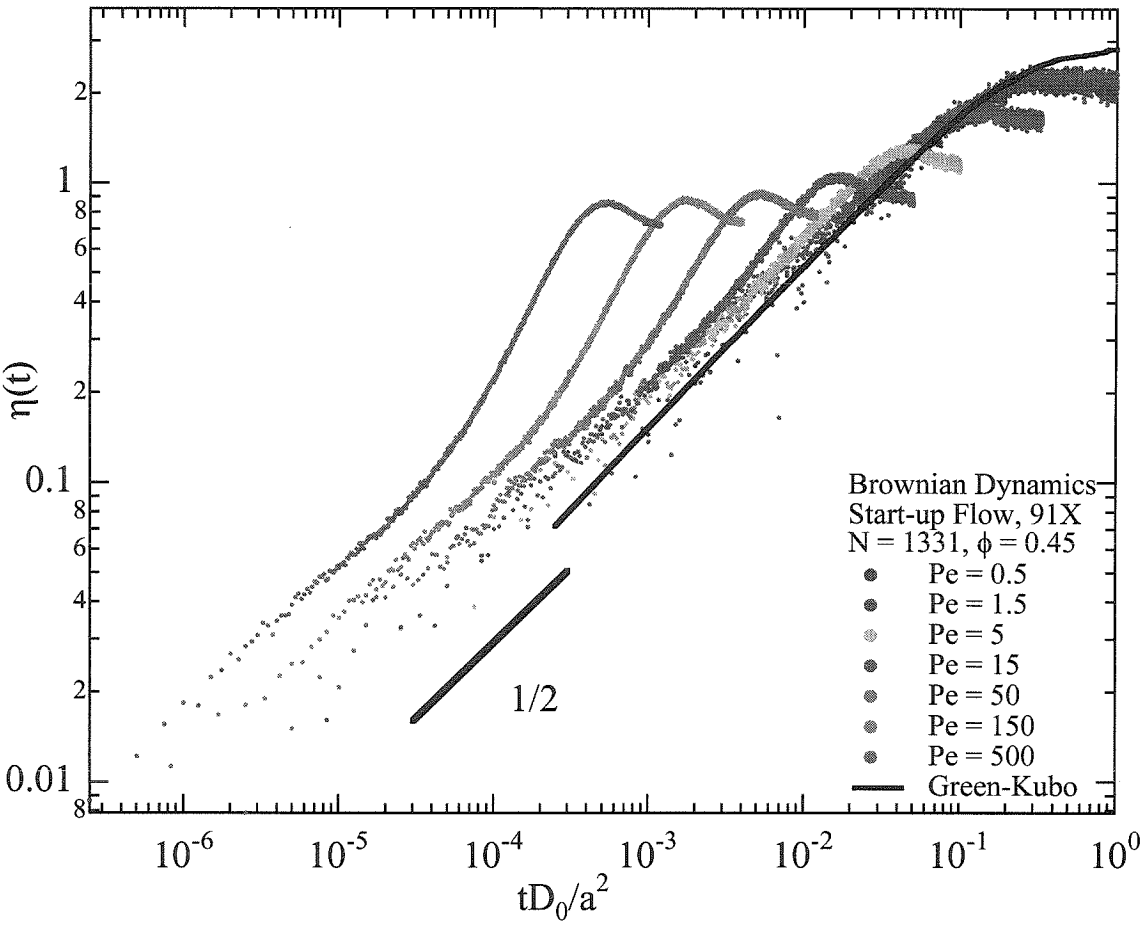

Figure 4.5: Start-up flow: Instantaneous relative viscosity as a function of time, nondimensionalized by a^2/D_0, at various values of Pe for the Brownian Dynamics system at $\phi = 0.45$.

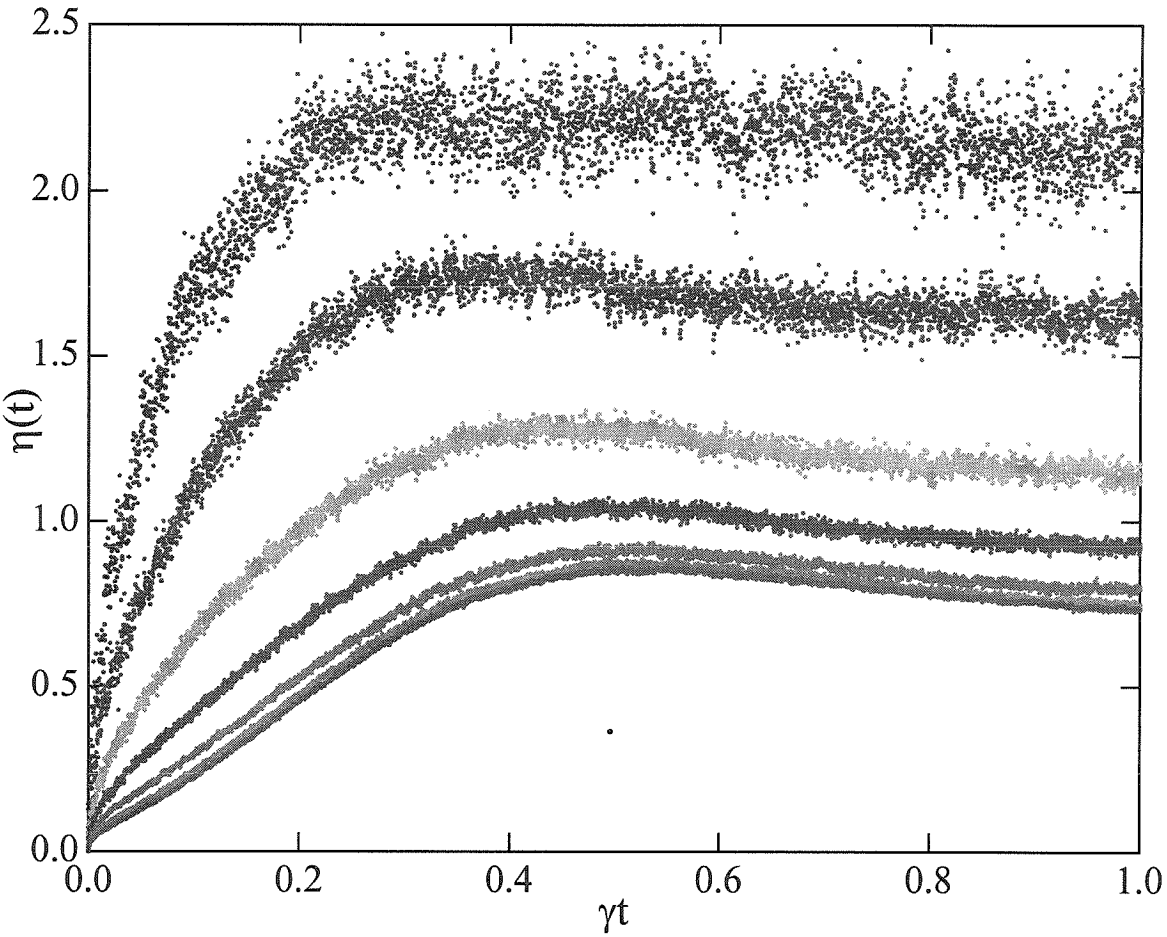

Figure 4.6: Start-up flow: Instantaneous relative viscosity as a function of time, nondimensionalized by $\dot{\gamma}^{-1}$, at various values of Pe for the Brownian Dynamics system at $\phi = 0.45$.

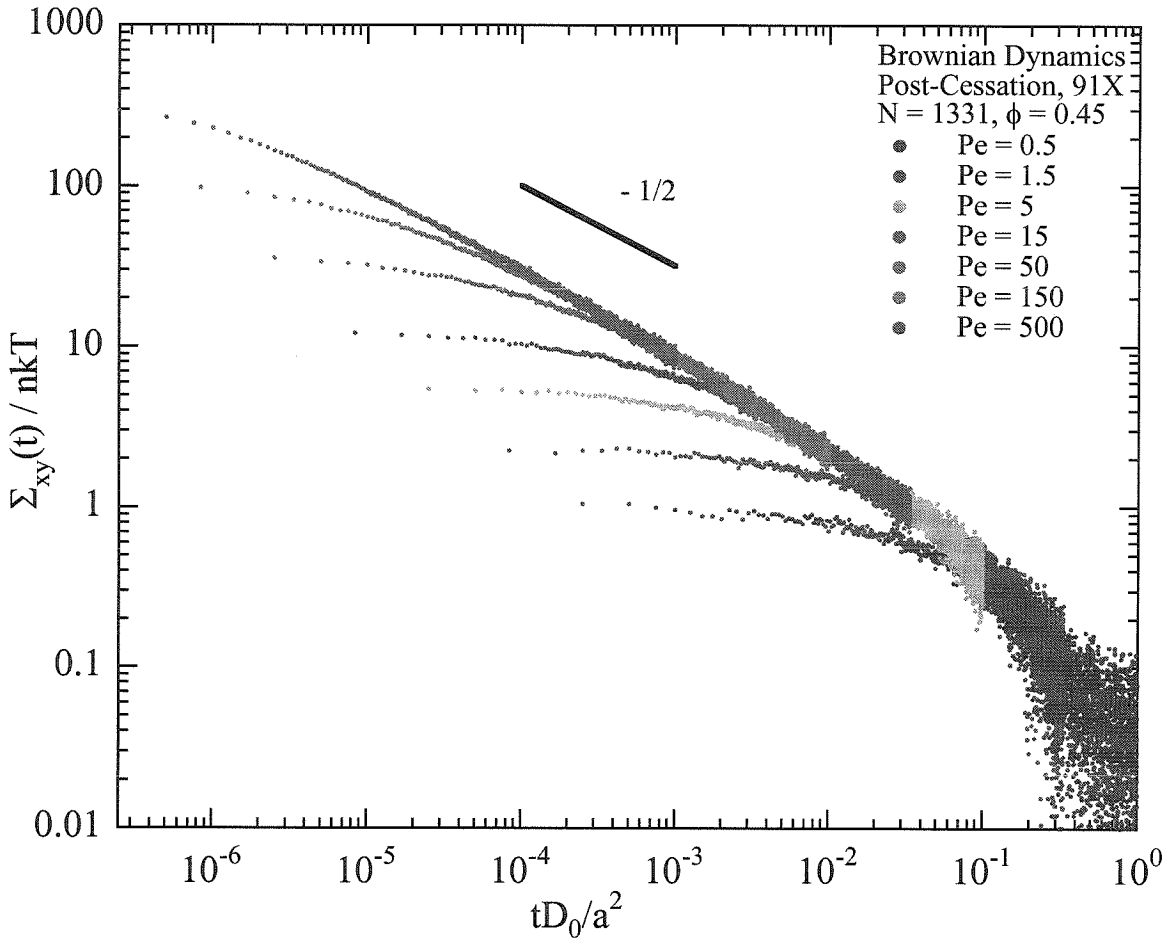

Figure 4.7: Flow cessation: Instantaneous suspension stress nondimensionalized by nkT as a function of time, nondimensionalized by a^2/D_0, at various values of Pe for the Brownian Dynamics system at $\phi = 0.45$.

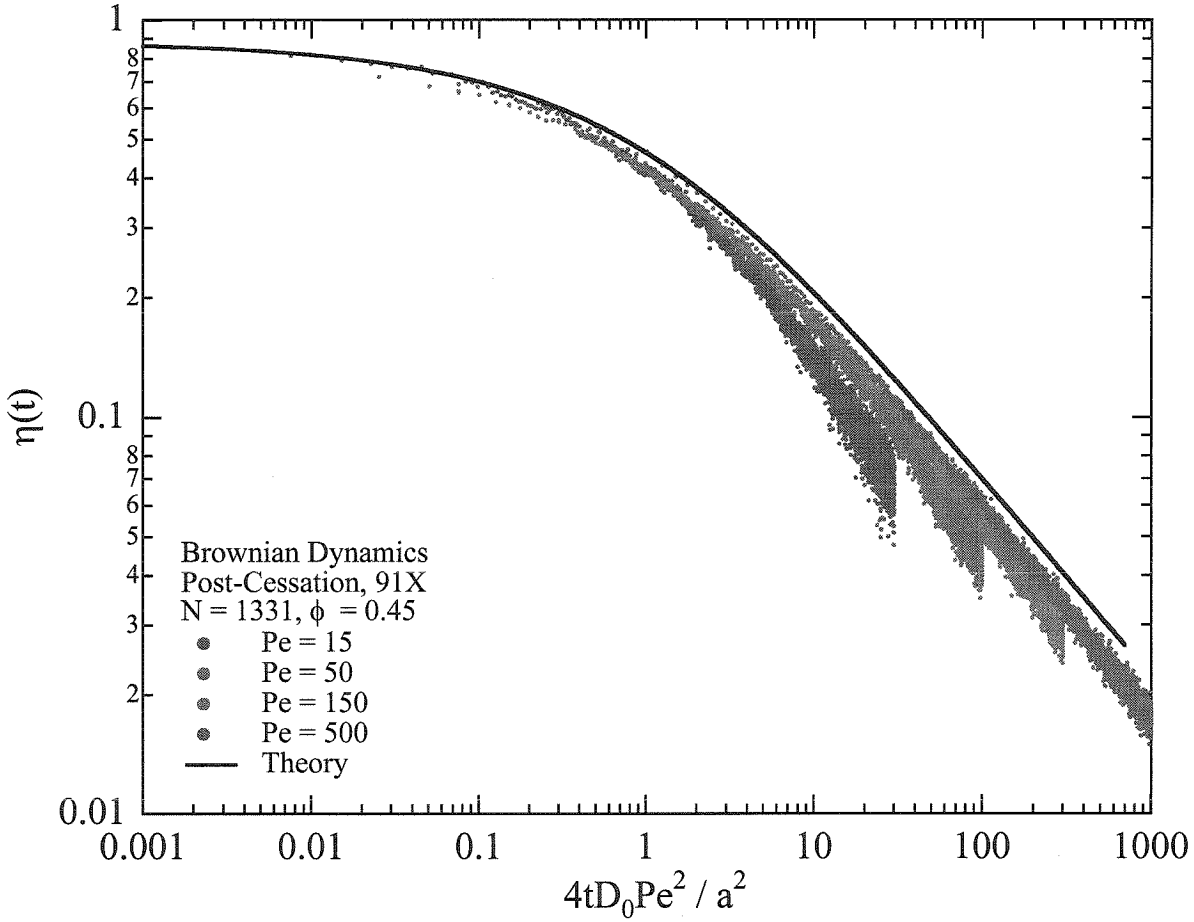

Figure 4.8: Flow cessation: Instantaneous suspension stress nondimensionalized by pre-cessation $\eta\dot{\gamma}$ as a function of time, nondimensionalized by $\delta^2/D_0 = (a^2/D_0)/Pe^2$, at various pre-cessation values of Pe for the Brownian Dynamics system at $\phi = 0.45$. The solid curve is the theoretical result (equation 4.34) using $\gamma_r = -\frac{1}{2}$, its value on the compressive axis, and fitting $g_{ss}(0)$ to the pre-cessation stress value.

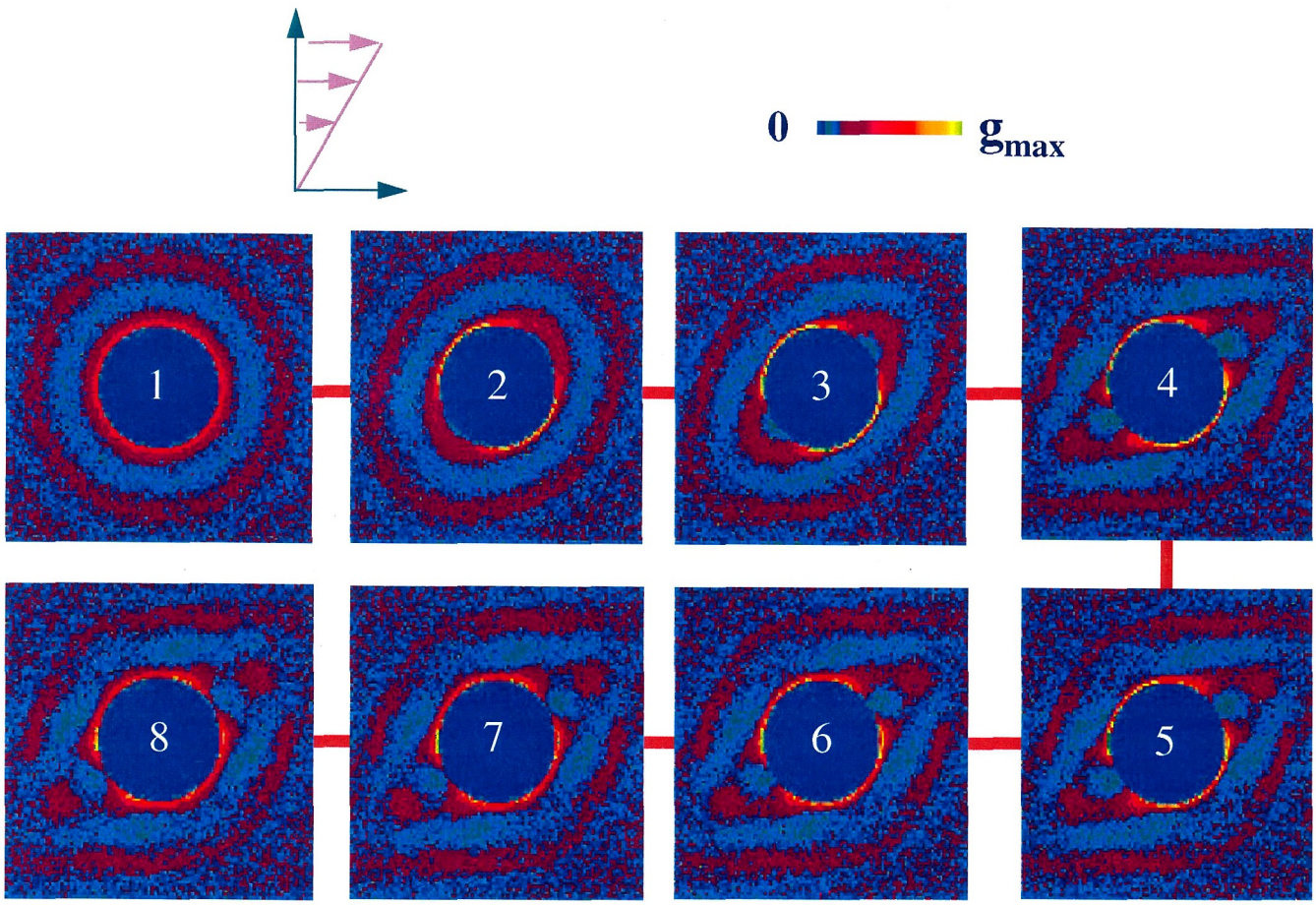

Figure 4.9: Projection of the pair-distribution function $g(\boldsymbol{r})$ into the xy-(velocity-gradient)-plane at different times during start-up and flow cessation. Here, $\phi = 0.45$ and $Pe = 15$. Times nondimensionalized by the pre-cessation $\dot{\gamma}^{-1}$ for the eight projections are at 0, 0.25, 0.50, 0.75, 1.0, 1.05, 1.1, 1.2, 1.5, 1.9. Dark represents high probability and light low.

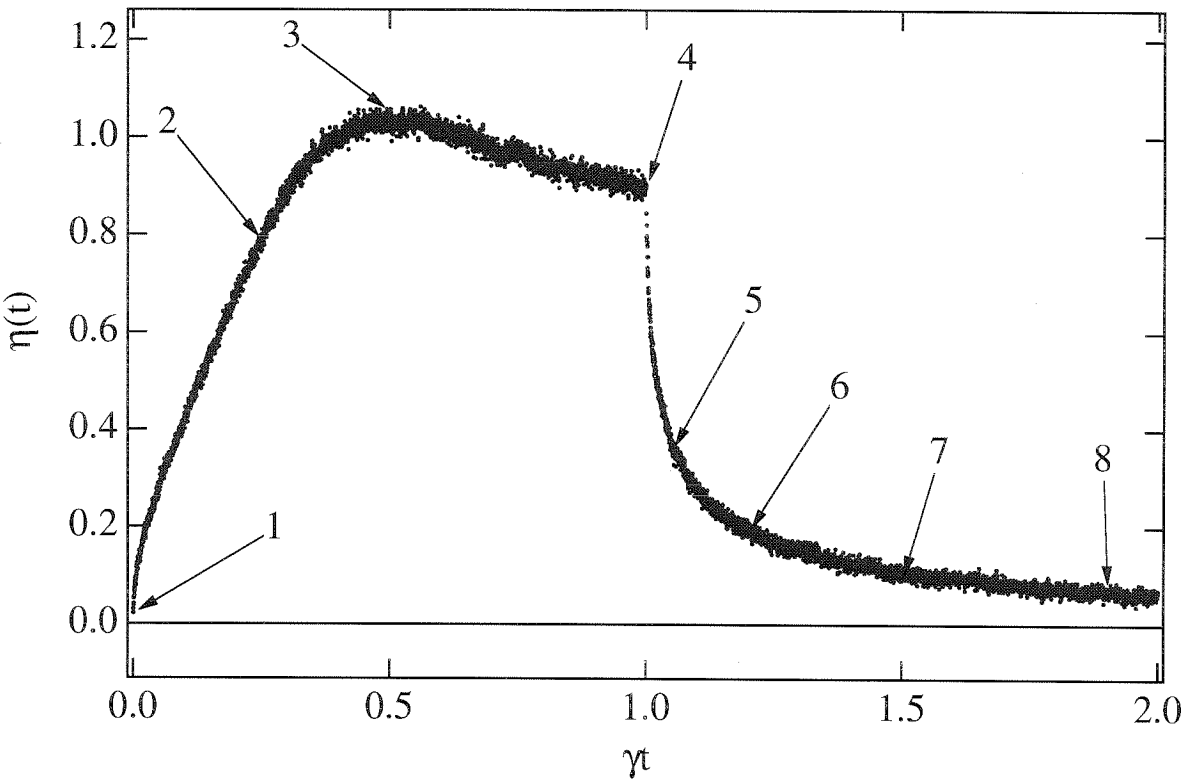

Figure 4.10: Plot of stress nondimensionalized by the pre-cessation $\eta\dot{\gamma}$ as a function of time, nondimensionalized by precessation $\dot{\gamma}^{-1}$ for start-up and flow cessation at $\phi = 0.45$ and $Pe = 15$ for the Brownian Dynamics system. Labels 1-8 show the times of the eight projections of the pair distribution function in figure 4.9.

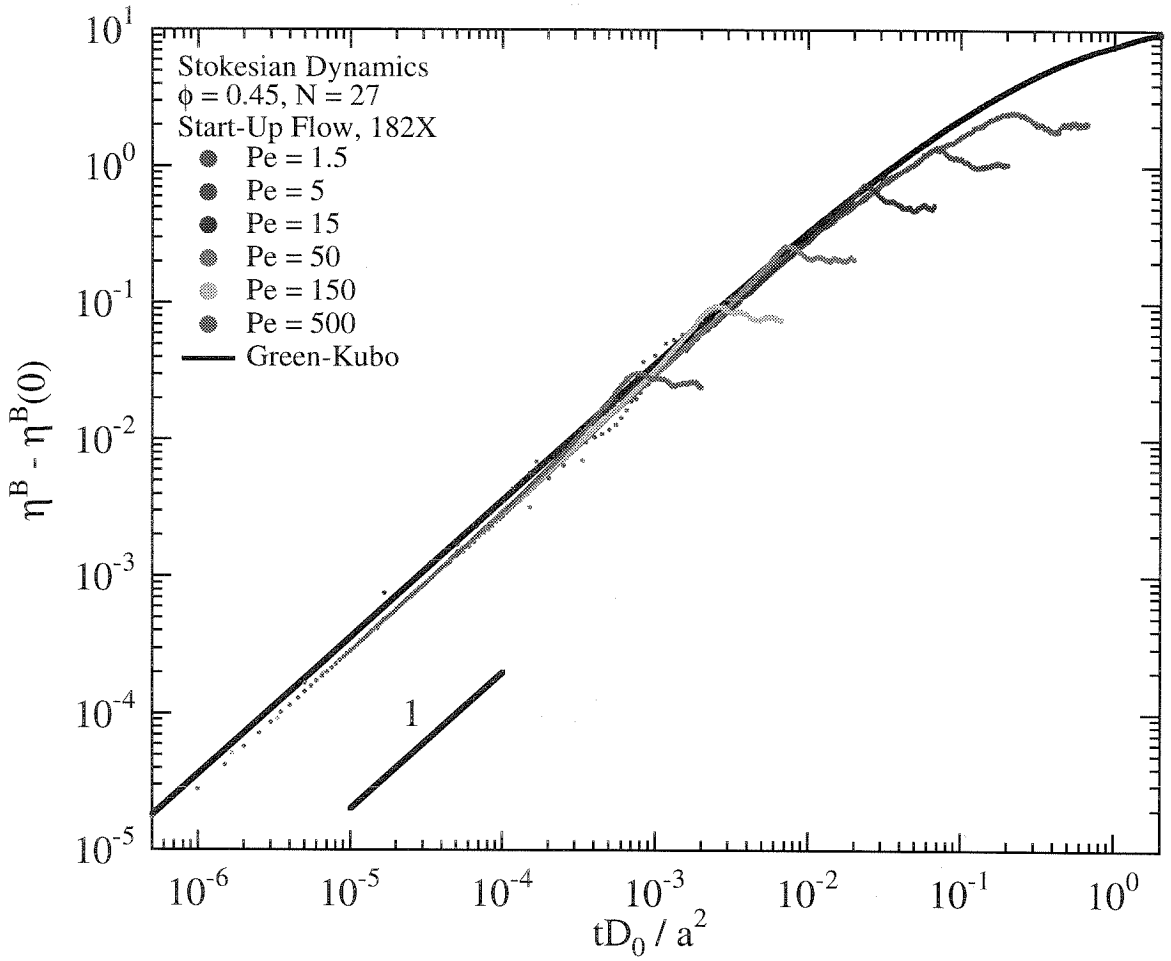

Figure 4.11: The Brownian viscosity, after subtraction of its zero-time value, as a function of time, nondimensionalized by the diffusive time, a^2/D_0, during start-up flow for the Stokesian Dynamics system with $\phi = 0.45$ and various values of Pe.

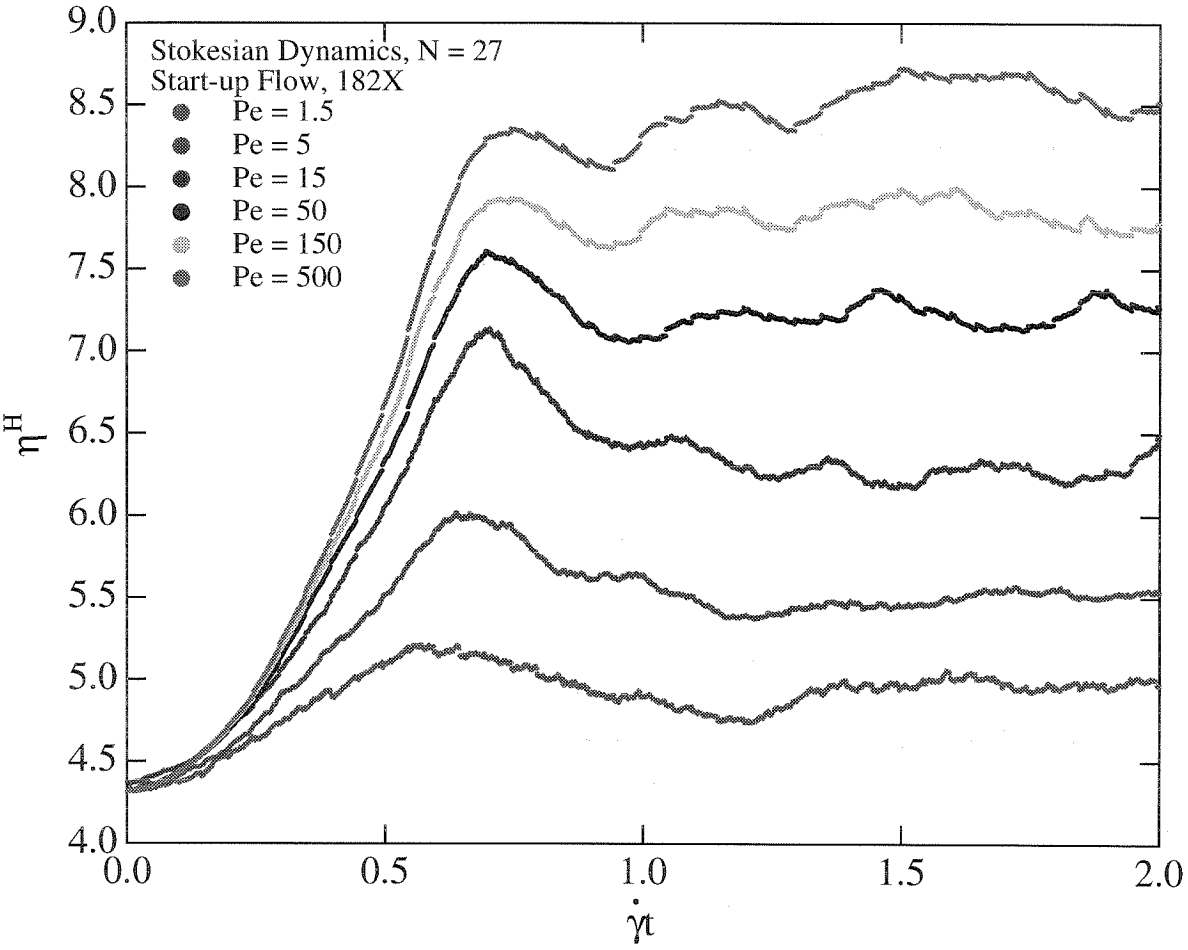

Figure 4.12: The hydrodynamic viscosity as a function of time, nondimensionalized by the flow time $\dot{\gamma}^{-1}$, during start-up flow for the Stokesian Dynamics system with $\phi = 0.45$ and various values of Pe.

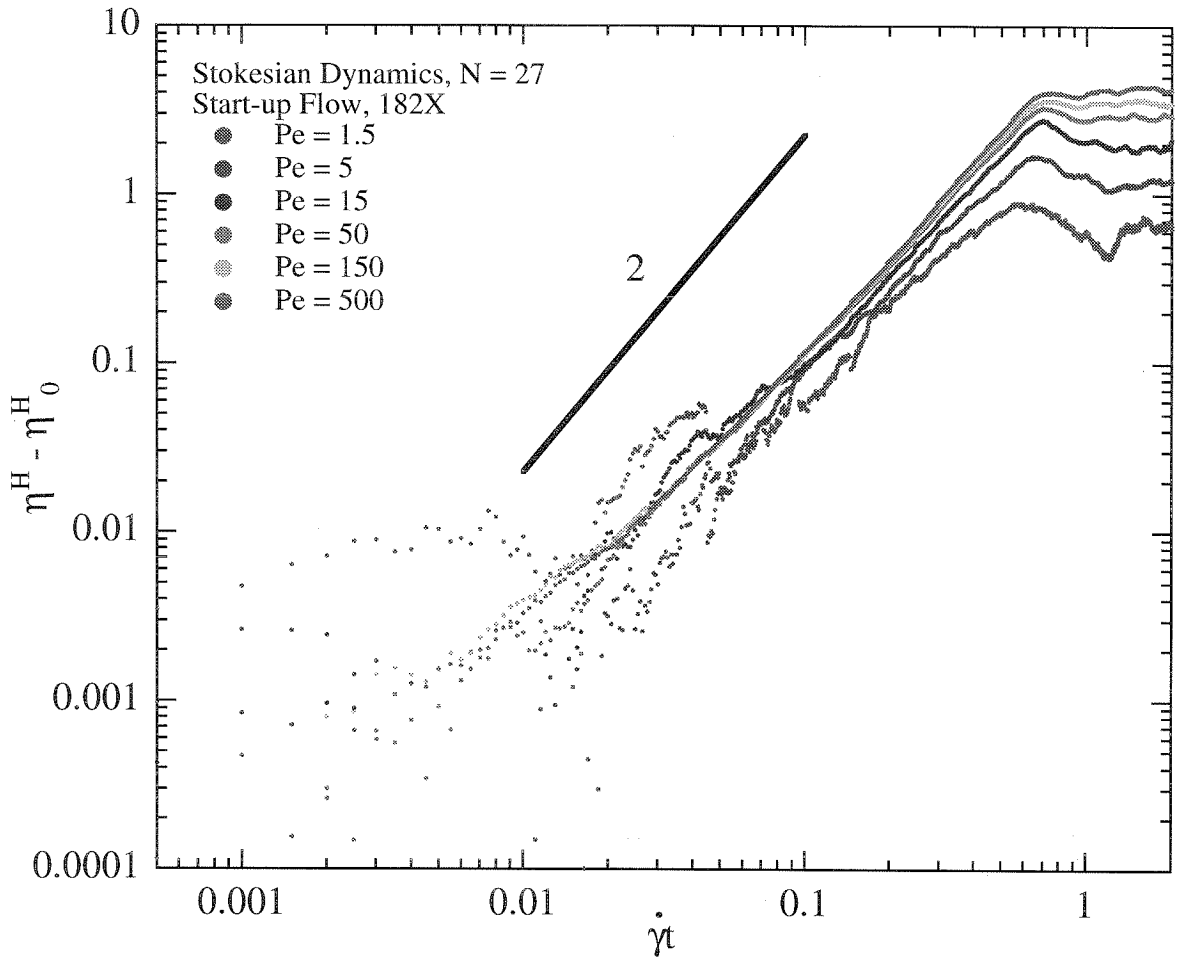

Figure 4.13: The hydrodynamic viscosity, after subtraction of its zero-time value, as a function of time, nondimensionalized by the flow time $\dot{\gamma}^{-1}$, during start-up flow for the Stokesian Dynamics system with $\phi = 0.45$ and various values of Pe.

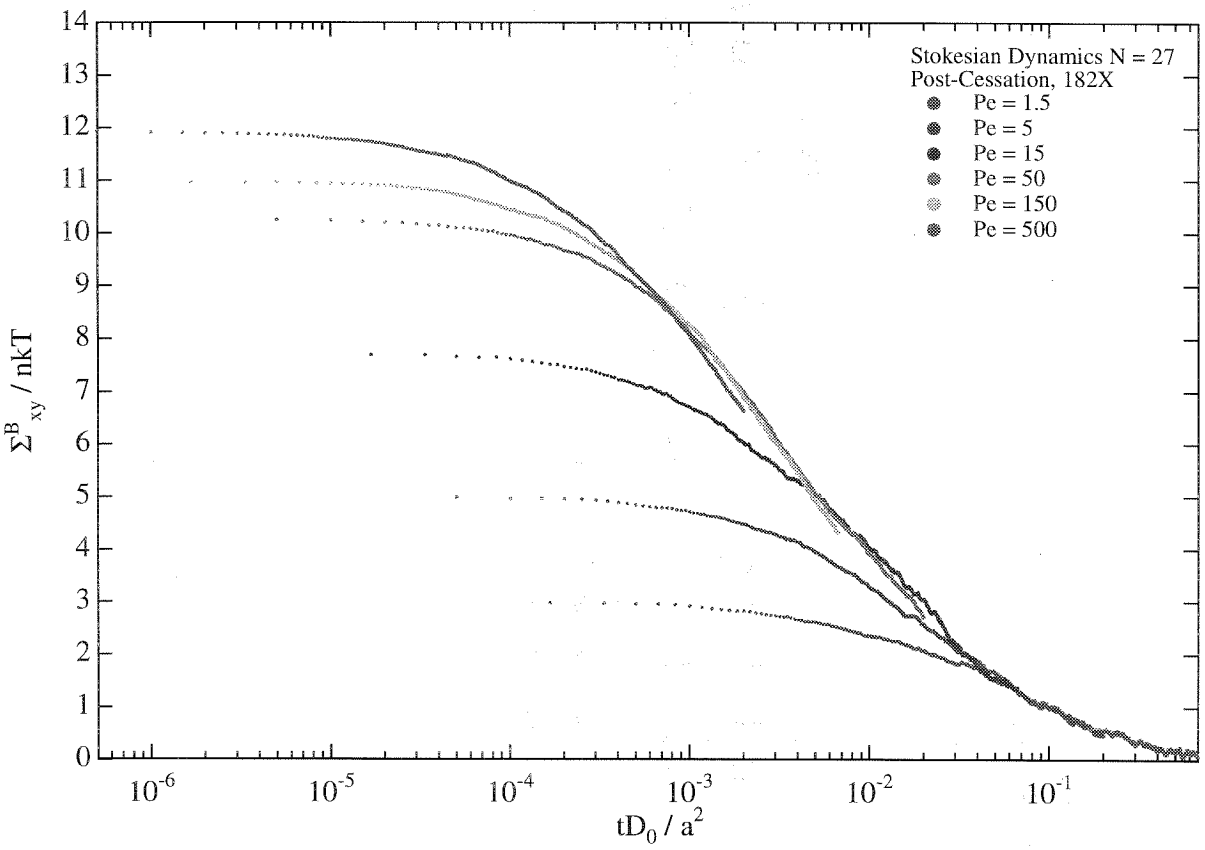

Figure 4.14: The Brownian stress, nondimensionalized by nkT, as a function of time after flow cessation, nondimensionalized by a^2/D_0 for the Stokesian Dynamics system with $\phi = 0.45$ and various pre-cessation values of Pe.

Chapter 5

Self-diffusion in sheared suspensions by dynamic simulation

5.1 Introduction

This work addresses the problem of determining the long-time self-diffusivity in a monodisperse low-Reynolds-number suspension of spherical particles at both equilibrium and steady shear conditions via dynamic simulation. Self-diffusion is one of the most basic transport processes occurring in a suspension and is related to a number of tranport and relaxation mechanisms. There are three well-defined diffusive processes in a colloidal suspension: the short-time self-diffusivity, D_0^s, the long-time self-diffusivity, D_∞^s, and the gradient or collective diffusivity, D^c. At infinite dilution all three diffusivities are the same and equal to the Stokes-Einstein diffusivity of an isolated particle: $D_0 = kT/6\pi\eta a$ for translational self-diffusion and $D_0^r = kT/8\pi\eta a^3$ for its rotational analog. Here, k is Boltzmann's constant, T is the absolute temperature, η is the viscosity of the continuum suspending fluid, and a is the characteristic particle size, which for a monodisperse suspension of spheres is simply the particle radius.

As the concentration is increased and the effects of particle interactions become important, the three diffusivities behave quite differently as they represent three distinct physical processes. The short-time self-diffusivity measures the local particle mobility on time-scales long compared to the momentum relaxation time, $\tau_I = m/6\pi\eta a$, but small compared to the time it takes for a particle to move a fraction of its size, which is the diffusive timescale, $\tau_D = a^2/D_0$; here, m is the mass of the particle. The long-time self-diffusivity is related to diffusion on times long compared to a^2/D_0, so that a particle has wandered far from its starting point. Finally, the gradient or collective diffusivity results from a flux down a macroscopic concentration gradient. This work focuses on the long-time self-diffusivity.

While the short-time self-diffusivity depends only on the particle mobility, which is a purely time-independent hydrodynamic quantity, the long-time self-diffusivity is affected by both the particle mobility and the dynamic microstucture of particles exchanging places with their neighbors. Often researchers have simplified the system by excluding hydrodynamic interactions, which sets the mobility of each particle to unity

and independent of microstuctural variations, effectively isolating the contribution of the dynamic microstructure to the long-time self-diffusivity. A Brownian Dynamics algorithm is employed for the simplified system of hard-spheres interacting in the absence of hydrodynamic interactions. For the complete system, the computationally intensive Stokesian Dynamics algorithm that includes the many-body hydrodynamic interactions into the Brownian Dynamics framework is used. A goal of this work is to compare and contrast results from these two systems to provide insight to the relevant mechanisms for long-time self-diffusion.

Much work has been done on the long-time self-diffusivity at both equilibrium and in the high-shear limit. Dynamic light scattering can be used to measure the self-diffusivity at equilibrium, while tracer experiments, where a small fraction of the particles are tagged and their motion monitored, can be used, in principle, at any shear rate, although only experiments at high shear rates have been performed to date. Out of equilibrium, structural anisotropies arise due to the shearing flow and the long-time self-diffusivity is properly represented in full tensoral form, $\boldsymbol{D}^s_\infty$, whose components are defined using a cartesian coordinate system, (x, y, z), with principle axes corresponding to the velocity, velocity-gradient, and vorticity directions in simple shear flow, respectively.

Theoretical work on self-diffusion at high shear rates is complicated by the fact that two particles acting solely under the influence of hydrodynamics exhibit no diffusive behavior due to the symmetry properties of low-Reynolds number flow. Wang *et al.* (1996) examined self-diffusion in dilute suspensions theoretically using three-particle interactions. da Cunha & Hinch (1996) examined the two-particle problem, adding surface roughness to create diffusive motion. Brady & Morris (1997) used residual Brownian motion to break the symmetry of the pure hydrodynamic limit. Effects of weak shear on self-diffusion were studied by Morris & Brady (1996). The previous two studies are referred to many times throughout this paper and will be discussed in more detail in §5.2. One interesting prediction of these works is the appearance of a non-zero xy-component of the long-time self-diffusivity tensor in shear flow. This quantity is difficult to measure both experimentally and via simulation as it

involves examining motion in the direction of the bulk flow. The current work makes use of a method for calculating the diffusivity that enables us to obtain meaningful results for this quantity.

We also present results for the long-time rotational diffusivity. Theoretical work by Jones (1989) and Degiorgio *et al.* (1995) predict behaviour for dilute suspensions at equilibrium considering two- and three-body hydrodynamic interactions. Short-time rotational diffusivities at equilibrium for all volume fractions were determined by Stokesian Dynamics simulations by Phillips, *et al.* (1988). Many advances have been made recently in experimentally measuring rotational self-diffusion using techniques ranging from dynamic depolarized light scattering (Degiorgio *et al.* 1995), forced Rayleigh scattering (Kanetakis & Sillescu 1996), and nuclear magnetic resonance spectroscopy (Barell *et al.* 1996, Kanetakis *et al.* 1996). To date, work has been performed at equilibrium with extensive focus on the behavior of the short-time rotational self-diffusivity over a wide range of volume fraction, ϕ.

In the next section we discuss the theoretical results of Morris & Brady (1996) and Brady & Morris (1997), analyzing what behavior is to be expected in shear flow. Section 5.3 outlines the simulation method, discussing the two simulation techniques used, how the diffusion coefficients are calculated, and a new way of splitting the diffusivity into its hydrodynamic and Brownian contributions. In section 5.4, results for the diagonal components of the long-time self-diffusion tensor are presented showing their dependence on both density and shear rate. The simulation results are shown to compare well with experimental data. Section 5.5 is devoted to discussing the off-diagonal components of the self-diffusion tensor and presenting possible physical mechanisms for this mode of diffusion. Finally, we conclude in section 5.6 with a summary and suggestions for future studies.

5.2 Theoretical background

According to the theoretical results of Morris & Brady (1996), at small shear rates in the absence of hydrodynamic interactions, the long-time self-diffusion tensor of

colloidal suspensions has the following form

$$\boldsymbol{D}^s_\infty = D_0[(1-2\phi)\boldsymbol{I} + \frac{46}{15}\phi(\tfrac{1}{2}Pe)\hat{\boldsymbol{E}} + 0.65\phi(\tfrac{1}{2}Pe)^{3/2}\boldsymbol{I} + O(\phi^2, Pe^2)], \qquad (5.1)$$

where the Péclet number $Pe = \dot{\gamma}a^2/D_0 = 6\pi\eta a^3\dot{\gamma}/kT$ and $\dot{\gamma}$ is the shear rate. The nondimensional rate of strain tensor is $\hat{\boldsymbol{E}} = \boldsymbol{E}/\dot{\gamma}$, and $\boldsymbol{I}$ is the isotropic tensor. This result is strictly valid to leading order in volume fraction, ϕ, but the general form may be applicable at higher concentrations. The $O(Pe)$ contribution is valid for a general linear flow and represents a correction to the diffusion due to a perturbed microstructure. For weak flows, there is an $O(Pe)$ deformation to the equilibrium microstructure that scales as $Pe\hat{\boldsymbol{E}}$. This perturbation causes a volume fraction fluctuation of $-\phi Pe\hat{\boldsymbol{E}}$ around a particle; there is a buildup of particles in the compressional zones and a depletion of particles in the extensional zones (Batchelor 1977). For a simple random walk in the perturbed microstructure, we obtain the $\phi Pe\hat{\boldsymbol{E}}$ correction to the diffusivity. The $O(Pe^{3/2})$ term for simple shear flow is isotropic, and represents the first contribution to the normal components of the long-time self-diffusion tensor. This term results from a singular effect of weak advection at large separations, $r/a \sim O(Pe^{-1/2})$ (Leal 1973).

Morris & Brady (1996) also studied the effect of including hydrodynamic interactions on diffusion. For small Pe, the long-time self-diffusion tensor in a dilute suspension behaves as

$$\boldsymbol{D}^s_\infty = D_0[(1-2.07\phi)\boldsymbol{I} + 0.30\phi(\tfrac{1}{2}Pe)\hat{\boldsymbol{E}} + +\mathcal{D}\phi(\tfrac{1}{2}Pe)^{3/2} + O(\phi^2, Pe^2)], \qquad (5.2)$$

where, for simple shear flow,

$$\mathcal{D} = \begin{pmatrix} 3.96 & 0.93 & 0 \\ 0.93 & 1.87 & 0 \\ 0 & 0 & 0.52 \end{pmatrix}.$$

Equation (5.2) has the same general form as (5.1) with a few exceptions. The equi-

librium isotropic term and the $O(Pe)$ term valid for general linear flow have different coefficients and show a hindrance of the diffusion process on the inclusion of hydrodynamic interactions. Also, the $O(Pe^{3/2})$ contribution is no longer isotropic, not only showing different contributions along the diagonal but also a significant positive contribution to the off-diagonal xy component.

The behavior at high Pe has also been analyzed theoretically by Brady & Morris (1997) and da Cunha & Hinch (1996). Brady & Morris (1997) find that the long-time diffusivity for monodisperse hard-spheres in the absence of hydrodynamic interactions is related to the particle contribution to the stress, $\boldsymbol{\Sigma}$, by the following relation:

$$\boldsymbol{D}^s_\infty = -\frac{a^2}{\eta}\frac{1}{\phi}\frac{2}{27}\boldsymbol{\Sigma}, \tag{5.3}$$

which agrees with the idea of self-diffusion being driven by the osmotic, or partial, pressure: the self-diffusivity is the product of the particle mobility, which is $O(1)$ in the absence of hydrodynamic interactions, and the osmotic pressure gradient $\partial\boldsymbol{\Sigma}/\partial\phi$. The coefficent $\frac{2}{27}$ in (5.3) is strictly valid only for dilute suspensions, but the origin of the asymmetry that gives rise to the diffusion process is in a singular boundary layer at particle contact and thus the proportionality in (5.3) should be valid for all ϕ. From this relation we can come to several conclusions about the long-time diffusivity. First, since all components of the stress tensor scale as $\eta\dot{\gamma}$ in the high shear limit, all diffusivities scale as $\dot{\gamma}a^2$, as simple dimensional reasoning would suggest. Second, although the simple radial-balance approximation used by Brady & Morris (1997) predicts a zero first normal stress difference, $N_1 = \Sigma_{xx} - \Sigma_{yy}$, as well as a negative second normal stress difference, $N_2 = \Sigma_{yy} - \Sigma_{zz}$. The normal stress differences lead to the inequality $\Sigma_{zz} > \Sigma_{yy} \approx \Sigma_{xx}$ which, due to the minus sign in (5.3), gives long-time self-diffusivities of the following relative magnitudes, $D_{xx} \approx D_{yy} > D_{zz}$. Also, there is a positive off-diagonal component to the stress tensor Σ_{xy} — the shear stress is nonzero — resulting in a negative value of D_{xy}.

The inclusion of hydrodynamic interactions complicates matters in an important way. The pure-hydrodynamic limit corresponding to hydrodynamic interaction only,

no Brownian motion nor interparticle forces, is a singular limit and exhibits no diffusion due to the symmetry and reversibility of low-Reynolds-number flow. The symmetry can easily be broken, however, by the presence of other forces, whether they are due to Brownian motion or to a repulsive interparticle force of nonhydrodynamic origin, no matter how small in magnitude. The simple relationship between diffusivity and stress in (5.3) no longer holds due to the complexity of the hydrodynamic interactions. However, the diffusivity can still be thought of as a particle mobility times an osmotic pressure gradient, but the particle mobility is no longer a constant due to the presence of lubrication forces near contact. Apart from the special case of the pure hydrodynamic limit where there is no diffusive motion, the principle effect of hydrodynamic interactions is the quantitative dependence of the diffusivity on the volume fraction ϕ. The first normal stress difference, N_1, is no longer zero and has been shown by simulation to be negative. This leads the inequality, $\Sigma_{zz} > \Sigma_{yy} > \Sigma_{xx}$, which results in diffusivities of the following magnitudes, $D_{xx} > D_{yy} > D_{zz}$. As before, the sole off-diagonal contribution is a negative D_{xy}.

5.3 Simulation method

Long-time self-diffusivities were determined with and without hydrodynamics using the aid of Stokesian Dynamics and Brownian Dynamics simulations, respectively. Here we shall not focus on the details of these techniques, as they are found elsewhere, but rather give a brief overview of each, and then discuss how they were implemented to compute the long-time self-diffusivities.

The Brownian Dynamics algorithm used here is based on the method of Heyes & Melrose (1993) and Schaertl & Sillescu (1994). Measurement of the long-time self-diffusivities involves calculation of the mean-square displacements of each particle over time and are calculated from the individual particle trajectories. These trajectories are governed by the particle evolution equation for this system:

$$\Delta \boldsymbol{x} \quad = \quad \Delta \boldsymbol{x}^a + \Delta \boldsymbol{x}^{HS} + \boldsymbol{X}(\Delta t), \tag{5.4a}$$

$$\overline{\boldsymbol{X}} = 0 \qquad \text{and} \qquad \overline{\boldsymbol{X}(\Delta t)\boldsymbol{X}(\Delta t)} = 2D_0\boldsymbol{I}\Delta t. \tag{5.4b}$$

Here, $\Delta\boldsymbol{x}^a = \boldsymbol{U}\Delta t$ is the affine contribution due to the bulk shear flow and is simply $\dot{\gamma}y\hat{\boldsymbol{i}}\Delta t$ for simple shear flow. The random Brownian step, $\boldsymbol{X}$, has zero mean (denoted by the overbar) and variance equal to the single-particle Stokes-Einstein diffusivity, D_0, in the absence of hydrodynamic interactions. After the affine and Brownian contributions are added, the algorithm searches for particle pairs that have overlapped during the time step Δt and displaces each particle $\Delta\boldsymbol{x}^{HS}$ along their line of centers returning the particles to contact in response to a hard-sphere-like interparticle force. There is a small inherent 'softness' to the interparticle potential due to three-body effects that are not resolved using this method, but these systems have been shown to mimic the behavior of hard spheres in several regards. The shear stress autocorrelation function is found to diverge at short times as $t^{-1/2}$, the osmotic pressure as a function of ϕ shows good agreement with the hard-sphere equation of state, and the equilibrium radial-distribution function agrees with the known form for hard spheres. The simplicity of the algorithm used in this work allows for systems with large numbers of particles ($N = 1331$, in this study) reducing the statistical noise. Hard-sphere suspensions can also be approximated using a steep, continuous, interparticle potential, such as r^{-n}, where n is made very large. These algorithms produce very large values of the interparticle force near contact which necessitates the use of an extremely small time step in order to prevent an unrealistically large particle displacement during a typical particle collision.

In simple-shear flow, the mean-square displacements are expected to grow with time according to those for diffusion from a point source (Elrick 1962, Morris & Brady 1996):

$$\langle x^2(t)\rangle = 2D_{xx}t + 2D_{yy}t\,[1 + \tfrac{1}{3}(\dot{\gamma}t)^2], \tag{5.5a}$$

$$\langle y^2(t)\rangle = 2D_{yy}t, \tag{5.5b}$$

$$\langle z^2(t)\rangle = 2D_{zz}t, \tag{5.5c}$$

$$\langle x(t)y(t)\rangle = 2D_{xy}t + D_{yy}t(\dot{\gamma}t), \tag{5.5d}$$

as $t \to \infty$. Here the angle brackets $\langle \quad \rangle$ denote an average over all particles in the system. The diffusivity in the velocity-gradient direction, D_{yy}, provides not only the normal diffusive behavior in the y-direction, but also couples with the motion in the x-direction, resulting in $\langle x^2(t) \rangle$ growing cubically with time and $\langle x(t)y(t) \rangle$ growing quadratically in time, both with a proportionality constant given by D_{yy}. The underlying linear growth represented by the presence of D_{xx} and D_{xy} is dominated by the convectively enhanced stronger growths of the $\langle x^2(t) \rangle$ and $\langle x(t)y(t) \rangle$ displacements, making these diffusivities computationally difficult to measure. To circumvent this problem, we can take advantage of the fact that in simulation we know precisely the affine displacement at each time step, $\Delta \boldsymbol{x}^a$ in (5.4a). By subtracting off the affine displacement at each instant as far as the mean square displacement is concerned, we can remove this nonlinear temporal growth and extract all components, D_{yy}, D_{xx}, D_{zz} and D_{xy}. Note, as far as the suspension structure and dynamics are concerned, the affine displacement is, of course, added; it is only removed to compute $\boldsymbol{D}^s_\infty$. Thus, the long-time self-diffusivity is given by

$$\boldsymbol{D}^s_\infty = \lim_{t\to\infty} \frac{1}{2}\frac{d}{dt}\langle (\boldsymbol{x}(t) - \boldsymbol{x}^a(t))(\boldsymbol{x}(t) - \boldsymbol{x}^a(t)) \rangle, \tag{5.6}$$

where $\boldsymbol{x}^a(t)$ represents the affine contribution to a particle's displacement. This approach of subtracting off the affine displacement was also used successfully by Sami (1996) in extensional flow, where the temporal growth of the convectively enhanced dispersion is now exponential rather than a power law.

The inclusion of hydrodynamics, which include both the many-body far-field interactions and the pairwise-additive lubrication forces between particles, necessitates the use of the Stokesian Dynamics simulation technique described in detail elsewhere (Bossis & Brady 1987, Brady & Bossis 1988). The computational cost of calculating all the hydrodynamic interactions in conventional Stokesian Dynamics is $O(N^3)$, and thus we are limited to relatively small system sizes ($N = 27$). As before, the particle-evolution equation contains all the vital information for calculating the mean-square displacements. Previously, the particle stress was shown to consist of both hydrody-

namic and Brownian contributions (Bossis & Brady 1989), and the particle trajectories are no different. For Stokesian Dynamics, it is useful to write the evolution equation as

$$\Delta \boldsymbol{x} = \Delta \boldsymbol{x}^{a} + \Delta \boldsymbol{x}^{H} + \Delta \boldsymbol{x}^{B}. \tag{5.7}$$

Here, we have broken the evolution equation into three contributions. The first is the affine displacement:

$$\Delta \boldsymbol{x}^{a} = \boldsymbol{U}\Delta t = \dot{\gamma} y \hat{\boldsymbol{i}} \Delta t, \tag{5.8}$$

which simply convects the particle along with the bulk shear flow. The second contribution, the hydrodynamic displacement, is given as

$$\Delta \boldsymbol{x}^{H} = \mathbf{R}_{FU}^{-1} \cdot \mathbf{R}_{FE} : \boldsymbol{E}\Delta t. \tag{5.9}$$

Here, $\mathbf{R}_{FU}$ and $\mathbf{R}_{FE}$ are configuration-dependendent hydrodynamic resistance tensors. These displacements describe the deviation in particle paths from the affine motion solely due to hydrodynamic interactions. The remaining contribution to the particle evolution equation is the Brownian displacement, originally given by Ermak & McCammon (1978) as

$$\Delta \boldsymbol{x}^{B} = kT\nabla \cdot \mathbf{R}_{FU}^{-1}\Delta t \; + \; \boldsymbol{X}(\Delta t),$$

$$\overline{\boldsymbol{X}} = 0 \qquad \text{and} \qquad \overline{\boldsymbol{X}(\Delta t)\boldsymbol{X}(\Delta t)} = \; 2kT\mathbf{R}_{FU}^{-1}\Delta t. \tag{5.10}$$

Here, the short-time self-diffusion tensor enters as $kT\mathbf{R}_{FU}^{-1}$ (which is just the Stokes-Einstein diffusivity using the many-body hydrodynamic mobility, $\mathbf{R}_{FU}^{-1}$, instead of the single-particle inverse Stokes drag) as the variance of the random step $\boldsymbol{X}$. Also, because the random step is large, $O(\Delta t^{1/2})$, compared to the $O(\Delta t)$ size of the hydrodynamic and affine displacements, a higher order term including the spatial gradient of the short-time diffusion tensor must be included to account for changes in the particle mobility during the random step. This deterministic term acts as a radially repulsive force and helps to prevent particles from overlapping during a random step.

Nondimensionalizing $\boldsymbol{x}$ by the particle radius a, the rate of strain tensor, $\hat{\boldsymbol{E}}$, by its magnitude $\dot{\gamma}$, the imposed velocity $\boldsymbol{U}$ by $\dot{\gamma}a$ and the hydrodynamic resistance tensors $\mathbf{R}_{FU}$ and $\mathbf{R}_{FE}$ by $6\pi\eta a$ and $6\pi\eta a^2$, respectively, one finds two charactistic time scales. The time scale for the hydrodynamic displacements in (5.9) is the flow time scale, $\dot{\gamma}^{-1}$, whereas the relevant time scale for the Brownian displacements in (5.10) is the diffusive time scale, $a^2/D_0 = 6\pi\eta a^3/kT$. The ratio of the diffusive time scale to the to the flow time scale is the Péclet number, $Pe = \dot{\gamma}a^2/D_0$. Thus, one can think of the Brownian displacements as those that are present at equilibrium in the absence of flow ($Pe = 0$), and the hydrodynamic displacements as those that accompany the affine flow in the pure hydrodynamic limit ($Pe^{-1} \equiv 0$). In each limit, no interparticle forces of nonhydrodynamic origin are required in order to prevent particle overlaps and no such forces are included in this work. The Péclet number is also the appropriate nondimensional shear rate for the Brownian Dynamics system (5.4a).

The pure hydrodynamic limit is singular and in order to resolve the strong lubrication forces between the particles an infinitessimally small time-step is required resulting in prohibitive computational cost (Ball & Melrose 1995, Dratler & Schowalter 1996). Inclusion of a nonhydrodynamic interparticle repulsive force is often used to study non-Brownian suspensions (Yurkovetsky 1998); here, we shall limit ourselves to large, but finite, Pe, where residual Brownian motion is sufficient in preventing particle overlaps with a serviceably finite simulation time step. The fact that there are no interparticle forces may have implications for the resulting diffusivity, however, for as $Pe \to \infty$ there should be no diffusive motion for pure hydrodynamics.

As with Brownian Dynamics, the particle mean-square displacements are calculated as a function of time ignoring the affine displacements to eliminate nonlinear temporal behavior. Here, we have the advantage of separating the hydrodynamic and Brownian contributions,

$$\langle(\boldsymbol{x} - \boldsymbol{x}^a)(\boldsymbol{x} - \boldsymbol{x}^a)\rangle = \langle \boldsymbol{x}^H \boldsymbol{x}^H \rangle + \langle \boldsymbol{x}^B \boldsymbol{x}^B \rangle + [\langle \boldsymbol{x}^H \boldsymbol{x}^B \rangle + \langle \boldsymbol{x}^B \boldsymbol{x}^H \rangle]. \tag{5.11}$$

Unlike the particle displacements, the square displacements are not additive and a symmetric cross-correlation term between hydrodynamic and Brownian displacements appears. Comparing (5.11) to (5.6) we can define

$$\boldsymbol{D}^s_\infty = \boldsymbol{D}^s_{\infty,h} + \boldsymbol{D}^s_{\infty,b} + \boldsymbol{D}^s_{\infty,hb}, \tag{5.12}$$

providing useful knowledge of the individual contributions to the long-time self-diffusion tensor. This division of diffusivities is not possible in Brownian Dynamics due to the inclusion of the hard-sphere-like interparticle force which acts in the same manner in response to both Brownian and affine motion and thus cannot itself be separated into Brownian and nonBrownian components.

One might question the validity of dividing the displacements in such a manner. In separating the hydrodynamic and Brownian displacements we do not claim that each one is acting independent of the other. Clearly, the two are acting together to create a dynamic microstructure that in turn affects the temporal behavior of the trajectories of each particle. Separation of the displacements is a relatively simple matter to do in the context of a computer simulation, however, and provides some insight into the mechanisms for self-diffusion.

Calculation of the mean-square displacement curves for both Brownian Dynamics and Stokesian Dynamics is done with the aid of a novel method. First, the simulations are kept relatively short, that is, for a time sufficient enough for the system to reach a steady state and for the mean-square displacements to enter the linear regime for an appreciable length of time. Second, many of these short simulations are performed independently from separate initial hard-sphere equilibrium configurations creating a large number of mean-square displacement curves. All of these curves are then averaged together point by point to form one smooth mean-square displacement curve. This method works well for three reasons. First, averaging over many runs effectively increases the size of the system and reduces the costly $N^{-1/2}$ noise present in random walk calculations. This is especially advantageous when using Stokesian Dynamics as the cost of increasing the system size is high. Second, although averag-

ing over long times is useful in obtaining good data in finite systems for properties with well-defined instantaneous values such as stresses and spatial distribution functions, it often creates problems in time-dependent correlations such as Green-Kubo auto-correlation functions and mean-square displacements. These quantities continue to directly depend on — instead of becoming independent of — the initial condition of the system. For this reason the statistical noise in these functions will grow with time. More realizations, *i.e.*, averaging over many correlations from different starting points, is used to obtain better quality autocorrelation functions, but the long-time 'tails' of these functions are very difficult to measure accurately. This is true with mean-square displacements for the same physical reasons. As a particle has diffused far from its starting point the instantaneous random fluctuations of the particle have very little dependence on the initial particle position and thus show large fluctuations in the mean-square displacement curve. The use of many realizations can delay the onset of this noise, whether it be by frequently resetting the starting point, or by increasing the number of particles, but the noise will always persist at long times. This brings us to the third point, analysis of the mean-square displacement curves at very long times is not necessary because it does not require a very long time for the mean-square displacements to reach their linear, long-time assymptote. This may seem counterintuitive due to the infinite time limit present in (5.6), but a particle does not have to travel long distances in order to reach its long-time assymptote; it simply has to encounter enough particle-particle interactions to sample the dynamic microstructure present. In the familiar cage-diffusion model, the particle does not have to leave the cage and travel far from its starting point, it simply has to interact with enough of its neighboring cage members until all the information necessary for long-time diffusion has been attained. This idea has been borne out by the recent experimental work of Breedveld *et al.* (1998) who measured long-time diffusivities at high Pe and found adequate agreement with previous measurements despite the fact that their mean-square displacement data is limited to times less than $0.6\dot{\gamma}^{-1}$. (cf. figures 5.17 & 5.18).

In the absence of hydrodynamic interactions, the rotation of the particles is not

coupled with the flow or the microstructure and each particle rotates freely under the influence of rotary Brownian motion exhibiting isotropic rotational self-diffusion governed by the Stokes-Einstein equation, $D_0^{s,r} = kT/8\pi\eta a^3$ for both short- and long-time scales. Inclusion of hydrodynamic interactions couples rotation and translation resulting in a long-time rotational self-diffusion tensor that varies as a function of ϕ and Pe. Calculating this tensor is done in exactly the same manner as the translational self-diffusion tensor except the particle angular displacements are used in lieu of the translational displacements. One notable difference is the affine angular displacement, $-\frac{1}{2}\dot{\gamma}\hat{\boldsymbol{k}}\Delta t$, is directed along the vorticity axis in simple shear flow and, due to the fact that it has no spatial dependence, does not create any convectively enhanced angular dispersion. For consistency, the affine angular displacements have been subtracted off when calculating the mean square angular displacements.

5.4 Results

This work will focus on the equilibrium and non-equilibrium behavior of the long-time self-diffusivity of a suspension of monodisperse spheres in the presence of Brownian motion with and without hydrodynamic interactions. As discussed earlier, the Péclet number, Pe, is the parameter we shall use to determine the relative magnitudes of Brownian motion and the imposed shear flow. The other important parameter of interest in a hard-sphere suspension is the volume fraction, ϕ, which is a measure of the density of the suspension. In order to reduce the number of parameters in the system, we limit our study in the following manner: To study the effects of Pe, we focus on one volume fraction, $\phi = 0.45$, and vary Pe from 0 to 1000 in order to capture the full range of equilibrium and non-equilibrium behavior. This volume fraction represents a relatively concentrated system, but remains below the equilibrium phase transition at $\phi = 0.494$. Then, to examine the role of the volume fraction, we focus on two Péclet numbers, $Pe = 0$ and $Pe = 1000$, in order to examine the equilibrium and high-shear limits, respectively.

As stated in the previous section, two separate simulation techniques were used

in this work. For the Brownian Dynamics simulations, a large system was studied, $N = 1331$, and the number of independent repetitions of each run from different starting configurations was set to be 91. To explain the length of each run, we must discuss the nondimensionalizations for time in the regimes being studied. At equilibrium and low shear rates, ($Pe \leq 1$), the diffusive time, a^2/D_0, is used, while at high shear rates, the flow time, $\dot{\gamma}^{-1}$, is used. The time step for all the simulations is $\Delta t = 2.5 \times 10^{-4}$ and the number of time steps used is 4000. This sets the length of the simulation to be one particle diffusive time at low shear rates, and one strain at high shear rates. At high shear rates, systems in the absence of hydrodynamics are known to order into strings that are aligned in the flow direction which results in a significant decrease in the diffusivities. While the mean-square displacements reach their long-time linear assymptote in less than one strain, as shown in figure 5.1, the disorder-order transition generally takes approximately twenty strains to form from an equilibrium starting configuration. This allows us to examine the mechanisms for diffusion in the intermediate disordered suspension that exists before the transition to the ordered phase. Although this disordered phase is unstable, it is worth studying because it provides a simple, useful model to compare to the system with hydrodynamic interactions, which does not exhibit order at high shear rates.

The Stokesian Dynamics simulations were performed in the same manner but with a few changes. Computational costs limited us to a smaller system, $N = 27$. This was partially compensated for by increasing the number of repetitions to 182. However, for a given run the simulation cell with $N = 27$ is substantially smaller than a cell from a run for Brownian Dynamics with $N = 1331$ and this finite simulation cell may affect the final values for the diffusivities — the results may not give the large N limit. The same nondimensionalizations for time are used, but the presence of hydrodynamics has the effect of slowing down the dynamics of the system. For this reason, we used a larger time step of $\Delta t = 5.0 \times 10^{-4}$ while maintaining the total number of steps used at 4000. This sets a longer simulation length of two particle diffusive times near equilibrium, and two strains at high shear rates.

To give the reader an idea of the statistical noise in the results, the following

process was performed wherever possible. Each of the 91 (or 182) simulations for each system produces a mean-square displacement curve and a value for the long-time self-diffusivity. These values can then be grouped into subsets of N_v values and averaged. The standard deviation of the subset averages can be used as a measure of the amount of uncertainty in the data. Of course, the measured uncertainty decreases as the number of values chosen to be in each subset, N_v, increases. Figure 5.2 shows the size of the uncertainty as a function of N_v showing that the error decays like $N_v^{-1/2}$ as one would expect from independent subsets of data. At first, the best choice for N_v would seem to be taking the standard deviation of the diffusivities obtained from each individual simulation, $N_v = 1$. This produces the largest error as the uncertainty in each individual run is determined by the number of particles used and does not take advantage of any averaging over independent realizations and often results in large error bars on data with high internal consistency. In contrast, grouping all of the realizations into one or two subsets might be construed as an attempt to unfairly minimize the uncertainties. We choose an intermediate condition of 6 subsets of 15 (or 30) simulations for use in determining the uncertainty represented by the error bars on our graphs. For the Brownian Dynamics simulations, the error bars are always less than the symbol size and are not shown. No attempt was made to simulate systems with varying N in order to extrapolate for large N because of the large computational cost. This should not be a problem for the Brownian Dynamics system, but the Stokesian Dynamics results may be impacted by the small system size used.

5.4.1 Shear-rate dependence of diffusivities

The Pe-dependence of the diagonal components of the long-time self-diffusivity from the Brownian Dynamics simulations are shown in figure 5.3. The diffusivities tend to their constant isotropic equilibrium values at low Pe, while they grow linearly with Pe, indicating a $\dot{\gamma}a^2$ scaling, at high shear rates. As predicted in §5.2, D_{zz} is clearly the smallest of the diagonal components. D_{xx} and D_{yy} are predicted to roughly

equal due to a zero first normal stress difference, but the data in figure 5.3 appears to show that $D_{xx} > D_{yy}$. Figure 5.4 represents the same data after subtraction of the equilibrium values clearly showing that the first correction to the diagonal components of the long-time diffusion tensor scales as $Pe^{3/2}$ as predicted by theory. The xx- and yy-components are roughly equal at low Pe, both being greater than the zz-component.

Inclusion of hydrodynamic interactions results in similar behavior. The Pe-dependence of the normal components to the long-time self-diffusivity from the Stokesian Dynamics simulations are shown in figure 5.5. Again, the diffusivities approach their isotropic equilibrium values at low Pe and grow linearly with Pe at high shear rates. The relative sizes of the normal components at high Pe is governed by the same inequality, $D_{xx} > D_{yy} > D_{zz}$, as predicted in §5.2. Figure 5.6 shows the same data after subtraction of the equilibrium diffusivities showing the enhancement to the normal components of the long-time diffusion tensor by the flow. One can see that the xx-component is clearly the largest of the three in agreement with (5.2), with D_{yy} being slightly larger than D_{zz}. Unfortunately, the $Pe^{3/2}$ scaling predicted in section 5.2 is not evident as the quality of the data is not high enough. There are several possible reasons for this. The addition of hydrodynamic interactions slows the system down, the diffusivities are smaller, which necessitates a higher degree of accuracy in the measurement. The mean-square-displacements require a longer time to reach their long-time assymptote increasing the effect of the noise that enters at long times. Also, the characteristic Péclet number for systems involving hydrodynamic interactions is $\bar{Pe} = Pe/D_0^s(\phi)$, which necessitates the use of even smaller Pe when examining the near equilibrium behavior. Moreover, one cannot stress enough the difference in the sizes of the systems. Multiplying the number of particles in the system by the number of independent realizations gives an effective system size of 4914 particles for the Stokesian Dynamics system compared to 121,121 particles for the Brownian Dynamics system. Random noise scales with the system size as $N^{-1/2}$ showing the advantages of the larger Brownian Dynamics systems. In addition to reducing the statistical noise, larger systems reduce the effects of the periodic unit

cell.

It is very interesting to note that the shear-induced diffusivities with and without hydrodynamics at high Péclet number are very comparable in magnitude, in agreement with the prediction of Brady & Morris (1997).

The different contributions to the diffusivities with hydrodynamic interactions are examined in figures 5.7–5.9 for the xx-, yy-, and zz-components, respectively. At equilibrium, the only displacements present are Brownian and the long-time self-diffusivity is solely defined by its Brownian contribution, $D^s_{\infty,b}$. Here, it is useful to subtract the equilibrium value from the Brownian contribution in order to study the effects of the flow on diffusion. $D^s_{\infty,b} - D^s_{\infty,eq}$ represents the enhancement to the random-walk-type diffusion due to the presence of the imposed flow. At low-Pe the main enhancement to the diffusivity is from $D^s_{\infty,b}$, which indicates that the first correction is due to random-walk-type diffusion that is facilitated by the external flow. We propose the following mechanism for the enhancement of the Brownian contribution to the diffusivity. Imagine the particles in the suspension occupying sites on a lattice. In a Brownian random walk a particle moves from one site to a neighboring unoccupied site. In the dilute limit, the particle is free to step in any direction at any time because none of the other sites are occupied. As the concentration is increased, the chances of a neighboring site being occupied increase, reducing the ability of a particle to make a step. The number of occupied neighbor sites is not a constant with time as all particles are undergoing the same random-walk process producing local density fluctuations. A particle diffusing over long distances in a dense suspension will often be trapped in a region of high density and be forced to wait until that fluctuation dissipates, resulting in a low value of the diffusivity. Now, apply a shear flow to the lattice. Particles are still confined to the lattice sites, but these sites are convected along with the flow. All motion in the velocity-gradient direction is still caused by the random walk, but the neighboring sites are changing with time due to the shear flow. The effect of this is that a high density fluctuation hindering the motion of a tagged particle can — in addition to dissipating as a result of random-walk-type diffusion — be convected away from the tagged particle

enabling random-walk motion in the velocity-gradient direction. This results in a larger value of $D^s_{\infty,b}$ relative to equilibrium. Note that $D^s_{\infty,b}$ is never greater than its dilute-limit value, D_0, as the easiest random walk is one in the absence of any other particles. The shearing motion simply lessens the hindering effects of neighboring particles to random-walk diffusion. This effect increases as the shear rate increases and ultimately saturates. At high Pe particles are driven into near contact by the shearing motion and the lubrication forces reduce the particle mobility, or short-time self-diffusivity. At smaller Pe, the reduction is rather small, but for $Pe > 10$ this clustering intensifies, the hydrodynamic viscosity increases and the drop in particle mobility becomes quite significant resulting in smaller random displacements and a decrease in $D^s_{\infty,b}$. Indeed, our results show that $D^s_{\infty,b}$ reaches at maximum at $Pe \approx 10$ where the effects of decreased mobility begin to cancel the effects of the enhanced random walk in a shearing microstructure.

The hydrodynamic diffusivity $D^s_{\infty,h}$, also shown in figure 5.8, is the dominant contribution at high Pe and grows linearly with Pe, or in dimensional form as $\dot{\gamma}a^2$, the shear-induced diffusivity scaling. At low Pe, this contribution is very small, apparently vanishing as Pe^2. The behavior of the hydrodynamic diffusivity can be explained by noting that the diffusion constant can be defined as a time integral of the velocity autocorrelation function. Fluctuations in the hydrodynamic velocity scale like $\dot{\gamma}a$; thus, the velocity autocorrelation scales as $\dot{\gamma}^2a^2$. Near equilibrium the correlation time for the velocity fluctuation is the diffusive time, a^2/D_0, resulting in an $O(D_0Pe^2)$ hydrodynamic contribution. At high shear rates, the correlation time is the flow time $\dot{\gamma}^{-1}$, giving a hydrodynamic diffusivity of $O(D_0Pe)$. It should be noted that the behavior at high Pe is qualitatively different than the behavior in the pure hydrodynamic limit ($Pe^{-1} \equiv 0$). The pure hydrodynamic limit exhibits no self-diffusion due to symmetry properties present in the low-Reynolds-number microstructure. The Brownian displacements do more than produce $D^s_{\infty,b}$ which, by itself, is a negligible part of the total diffusivity. The Brownian displacements break the symmetry producing a microstructure suitable for hydrodynamic diffusion to occur.

The cross-correlation between the hydrodynamic and Brownian displacements, $D^s_{\infty,hb}$, is also shown in figure 5.8. It is slightly less than the geometric mean of $D^s_{\infty,b}$ and $D^s_{\infty,h}$ at intermediate Péclet numbers indicating a strong cross-correlation and less at extreme values of Pe. It is important to note that $D^s_{\infty,hb}$ is greater than zero for all Pe indicating that the total diffusivity is always greater than the sum of the Brownian and hydrodynamic contributions, and that at no point are the two displacements negatively correlated and act against each other.

Results for the diagonal components of the rotational long-time self-diffusion tensor with hydrodynamics are shown in figure 5.10. As is the case with the translational analogs, the rotational diffusivities, when nondimensionalized by the Stokes-Einstein rotational diffusion coefficient, $D_0^{s,r}$, approach their constant equilibrium value at low Pe and grow linearly, indicating a $\dot{\gamma}$ scaling, at high shear rates. The largest of the three diagonal components is D_{zz} for the entire range of Pe. The difference is small near equilibrium as the suspension microstructure is close to isotropic, and quite large at high Pe where the zz-component is over three times greater than the other two components as this is the direction of the affine angular displacements. One intriguing difference in the rotational diffusivities as compared to their translational counterparts is that there is a slight decrease in the diffusivity with Pe at low Pe. Figure 5.11 for the Brownian contribution to the diffusivity shows that $D^{s,r}_{\infty,b}$ clearly has its maximum at equilibrium and there is no evidence of any enhancement of 'random-spin-type' diffusion in nonequilibrium configurations. The hydrodynamic contribution to the diffusivities in figure 5.12 is scaled by $\dot{\gamma}$ showing linear growth (Pe^2 growth when scaled by $D_0^{s,r}$) at low Pe, and approaching a constant at high Pe quite similar to the translational counterparts. The transition from low-shear to high-shear behavior occurs at higher Pe for the rotational diffusivities. The $D^{s,r}_{\infty,hb}$ contribution (not shown) to the diffusivity is small for all Pe indicating little correlation between the hydrodynamic and Brownian angular displacements.

5.4.2 Volume-fraction dependence of the diffusivities

We now turn our discussion to the effects of volume fraction ϕ on the high- and low-Pe limits of the diagonal components of the long-time self-diffusion tensor. At $Pe = 0$, the suspension is isotropic and all the diagonal components are equal; thus, all the components can be averaged together effectively tripling the amount of data and decreasing the amount of noise present in the results. Figure 5.13 shows the long-time diffusivity at equilibrium as a function of ϕ with and without hydrodynamics. Also in the figure are previous simulation results of hard spheres in the absence of hydrodynamic interactions. Schaertl & Sillescu (1994) employed the same simulation method used in this work and studied only the equilibrium behavior. This method allows for some particle overlap due to a finite-size time step and thus exhibits a diffusivity that may be slightly larger than the true hard-sphere value. Cichocki & Hinsen (1992) used a method in which particles take small random steps and if an overlap occurs, the steps leading to the overlap are rejected and another random step is chosen. This method should produce a diffusivity slightly smaller than the true hard-sphere diffusivity. Nonetheless, the three sets of data are in good agreement with each other suggesting that errors due to finite-size time steps are small. The diffusivity with hydrodynamics is smaller due to the decrease in the short-time diffusivity from a reduced particle mobility which decreases the size of the random Brownian steps. The mode of diffusion at equilibrium is of random-walk type, which is hindered by the presence of other particles causing the diffusion constant to decrease monotonically as ϕ is increased. Indeed, Brady (1994) showed that the long-time self-diffusivities with and without hydrodynamics are simply related by the hydrodynamically-determined short-time self-diffusion cofficient; $(D^s_\infty)_{hydro} = D^s_0(\phi)(D^s_\infty)_{nohydro}$; the data in figure 5.13 agree with this scaling behavior. Brady (1994) showed that Stokesian Dynamics results agree very well with experimental data.

Rotational self-diffusivities are plotted in figure 5.14 along with their short-time counterparts, which are simply the particles' average instantaneous hydrodynamic rotational mobility. Unlike tranlational diffusion, there is no hindrance to rotational

diffusion without the presence of hydrodynamic lubrication forces, which are also less singular at contact than their translational lubrication counterparts. This results in rotational self-diffusivities that are much larger in comparison to their translational counterparts. Also, the long-time rotational diffusivities are only slightly less than their short-time counterparts indicating that the dynamic microstructure plays only a small role in the diffusive behavior. The experimental results of Digiorgio *et al.* (1995) for the rotational short-time self-diffusivities are also included in figure 5.14 for comparison with the simulation data. There are no corresponding results for Brownian Dynamics simulation because in the absence of hydrodynamic interactions particle rotational mobility is unity and unaffected by the dynamics of the microstructure and the long- and short-time rotational self-diffusivities are equal to each other and equal to the dilute limit Stokes-Einstein diffusivity $D_0^{s,r}$.

At high Pe, the mechanisms for diffusion are markedly different from those at equilibrium. Diffusion is driven by particle-particle interactions that prevent coincident particles on neighboring streamlines in shear flow from passing through one another. The frequency of these interactions increases with volume fraction. Data was not available at dilute volume fractions as particle collisions are so infrequent that the mean-square displacements do not reach their long-time assymptote in the time of the simulation runs. The normal components of $\boldsymbol{D}_\infty^s$ at $Pe = 1000$, scaled by $\dot{\gamma}a^2$, the appropriate scale for high-Pe diffusion, are shown for the Brownian Dynamics system in figure 5.15 and the Stokesian Dynamics system in figure 5.16. For the Brownian Dynamics system, all three diffusivities are monotonic increasing functions of ϕ; D_{zz} is clearly the smallest of the three diffusivities with D_{xx} slightly greater than D_{yy} for all except for the highest volume fraction where D_{yy} is larger. The Stokesian Dynamics results show somewhat different behavior. As before, the inequality $D_{xx} > D_{yy} > D_{zz}$ holds for all ϕ, but only D_{zz} clearly appears to be monotonically increasing in this range of ϕ. Of the other terms, D_{yy} increases at first and reaches a plateau, and D_{xx} appears to be constant over the entire range studied here. This differs from the Brownian Dynamics result and is not in agreement with the theoretical results of Brady & Morris (1997) who predict that all components are strictly increasing functions of

ϕ, with and without hydrodynamic interactions. Due to system size constraints, we were not able to study larger and more dense systems to validate these behaviors. It should be noted that for the Stokesian Dynamics system, the characteristic Péclet number is $\bar{Pe} = Pe/D_0^s(\phi)$, and since D_0^s is a monotonically decreasing function of ϕ, $Pe = 1000$ represents a different $\bar{Pe}$ for each value of ϕ, which may lead to the nonmonotonic behavior. A more accurate study would be to fix $\bar{Pe}$, which would involve knowing D_0^s *a priori*. The high shear values of the yy- and zz-components of the long-time self-diffusion tensor are compared with the experimental data of Eckstein *et al.* (1977), Leighton & Acrivos (1987), Phan & Leighton (1993) and Breedveld *et al.* (1998) in figures 5.17 and 5.18, respectively. Note that the shear-induced diffusivities with and without hydrodynamics are of roughly the same magnitude in keeping with the theory of Brady & Morris (1997).

Although the diffusivity at high Pe is dominated by its hydrodynamic contribution, there is a small Brownian contribution that scales like D_0 and is shown in figure 5.19. This contribution is a monotonically decreasing function of ϕ, exhibiting the same qualitative behavior at both high and low Pe as random walks are always hindered by the presence of other particles. The magnitudes are the same as at equilibrium.

Rotational self-diffusities are shown in figure 5.20. Again, there appears to be an increase in the values of the diffusivity at lower ϕ which reaches a plateau at higher ϕ. The zz-component is by far the largest of the three diagonal components, with $D_{yy} > D_{xx}$ being true at the lower volume fractions and those two components being roughly equal at higher ϕ. Rotational diffusion is dominated by its hydrodynamic contribution at high Pe. The Brownian contributions in figure 5.21 show similar magnitudes and behavior to the equilibrium rotational diffusivities as Brownian diffusion is hindered as the concentration is increased.

5.5 Off-diagonal components of the self-diffusion tensor

The long-time self-diffusion tensor, being symmetric, has six independent components. The three diagonal components have been discussed in the previous section. Of the three off-diagonal components all are zero with the exception of $D_{xy} = D_{yx}$ for both translational and rotational diffusion in simple shear flow. Here, we shall discuss the results for this interesting component and also possible physical mechanisms for off-diagonal diffusion.

The diagonal components of $\boldsymbol{D}^s_\infty$ are straightforward to interpret in terms of the macroscopic flux of tagged particles given by Fick's law; D_{xx} represents a particles ability to diffuse in the x-direction and so forth. To understand the D_{xy} component requires examination of its corresponding mean-square displacement, $\langle x(t)y(t)\rangle$. As shown in figure 5.22, the positive and negative xy-axes correspond to the extensional and compressional directions in shear flow, respectively. Motion in the extensional direction, whether it be outward or inward, results in positive xy-displacements and diffusivities. Similarly, motion in the compressional direction results in negative xy-displacements and diffusivities. Therefore, the sign and magnitude of D_{xy} show which direction is more conducive to diffusion and by how much.

The Pe-dependence of D_{xy} at $\phi = 0.45$ in the absence of hydrodynamic interactions is shown in figure 5.23. At low shear rates, the diffusivity is positive and grows linearly with Pe. The diffusivity reaches a maximum at $Pe \approx 10$ followed by an abrupt decrease and sign change. At high Pe, D_{xy} is negative and its absolute value grows linearly with Pe. All of this behavior is in agreement with the theoretical predictions of Morris & Brady (1996) and Brady & Morris (1997).

According to (5.1), at low Pe the first correction to the diffusivity is $O(Pe\hat{\boldsymbol{E}})$, resulting in a D_{xy} that grows linearly with Pe. Morris & Brady (1996) show two contributions to this term. The first comes from random-walk, equilibrium-type diffusion occuring in the $O(Pe\hat{\boldsymbol{E}})$ deformed microstructure first calculated by Batchelor (1977). The pair probability, and therefore effectively the volume fraction, in the

compressional zones is higher than in the extensional zones due the perturbation of the structure by the flow. Since long-time self-diffusion at equilibrium is a strictly decreasing function of volume fraction, there is greater diffusion along the extensional axis than the compressional axis, resulting in a positive D_{xy}. The second contribution involves examining the $O(Pe)$ effects of the flow on the diffusion process in an equilibrium microstructure (noted by the function $\boldsymbol{b}_1$ in Morris & Brady (1996)). Motion of a tagged particle in the compressional direction will increase the probability that a particle-particle collision, which hinders random-walk-type diffusion, will take place due to the relative motion of the other particles in the shear flow. Conversely, particles in the extensional zone are being convected away from a marked particle and motion along the extensional axis is less likely to result in a particle-particle collision. This facilitates motion in the extensional direction compared to the compressional direction. Thus, each process scales as Pe and results in a positive contribution to D_{xy}.

The behavior of D_{xy} at high shear rates in the absence of hydrodynamic interactions can be explained by the relationship between diffusion and stress given in (5.3). In contrast to the behavior at low shear rates where particle-particle collisions are a hindrance to random walks, collisions are the principal mechanism producing diffusion at high Pe. The arrows in figure 5.22 show the effects of these collisions on the motion of the test particle in the center of the figure. There is a high probability of particles near contact in the compressional zone at high shear rates (Brady & Morris 1997), as shown by our simulations in figure 5.24. This high probability density in a boundary layer at contact is the origin of the $O(\eta\dot{\gamma})$ stresses seen in these systems, and increases the number of collisions — and therefore the particle motion — along the compressional axis resulting in a negative value of D_{xy}. Inclusion of hydrodynamic interactions produces qualitatively similar behavior.

Figure 5.25 shows D_{xy} and its main contributions as a function of Pe for the Stokesian Dynamics system. As with the diagonal components, the data is best at higher Pe where negative diffusivities of magnitude $\dot{\gamma}a^2$ are clearly seen in agreement with the theoretical work of Brady & Morris (1997). Near equilibrium, where

D_{xy} is predicted to vanish linearly with Pe, the small Stokesian Dynamics system proves unable to resolve the behavior. What is clear from the data, however, is that D_{xy} is indeed positive and dominated by the Brownian contribution validating the mechanism proposed above.

The collective or Fickian diffusion coefficient measures a particles ability to diffuse down a concentration gradient and is determined from Fick's law,

$$\boldsymbol{j} = -\boldsymbol{D}\cdot\nabla n, \tag{5.13}$$

where $\boldsymbol{j}$ is the particle flux and n is the particle concentration. Self-diffusion, which we have studied here, corresponds to the Fickian flux of a tracer or tagged particle as it diffuses down its (weak) concentration gradient. From this perspective of flux down a concentration gradient, what do off-diagonal terms in the diffusion tensor mean? Can a gradient in one direction cause a flux in another? To analyze this, we will look at high-Pe simple shear flow with the cases of a concentration gradient in either the x- or y-directions.

The case of a positive concentration gradient in the x-direction is shown in figure 5.26. At large Pe, the diffusive motion of particles is driven by the formation of particle doublets that exhibit solid-body-like clockwise rotation with the vorticity of the simple shear flow. In the absence of lubrication interactions, these doublets do not form and the the suspension orders (Bossis & Brady 1984, Dratler *et al.* 1997). (Note we have specifically limited the Brownian Dynamics simulations to times before ordering to probe the diffusive behavior in the disordered microstructure.) For the doublet in figure 5.26, the particle on the left is in a region of lower concentration and therefore rotates more easily than the particle to its right. The net result is a flux of particles in the positive y-direction, and from (5.13) a negative D_{yx}.

The other case of a positive concentration gradient in the y-direction is shown in figure 5.27. Here, the particle on the right is 'freer' to rotate because it is moving into a region of lower concentration, causing a flux downward into a leftward-moving streamline. At first glance this would appear to result in flux in the negative x-

direction, but when the affine motion is taken into account, this is not the case. As the doublet is rotating downward, the leftward motion of the particle on the right is impeded by the presence of the other particle in its compressional zone. This causes a 'lag' in the particle's leftward motion resulting in a net flux in the positive x-direction. To show this more explicitly, one can take the time dependent positions of the particle, $(x(t), y(t))$, and calculate the affine displacements along the path to calculate the affine contribution:

$$\boldsymbol{x}_a(t) = \int \dot{\gamma} y(t) dt.$$

Since the pariticle is hindered by its contacting neighbor on the compressional axis, the actual x-displacement is less than the affine displacement resulting in a net positive x-displacement. From Fick's law (5.13) we have $D_{xy} < 0$.

This gradient or Fickian diffusion can also be approached by looking at relative displacements of particles in the different quadrants of the xy-plane. Figure 5.28 is similar to figure 5.22 except the arrows have been made larger on the side of the test-particle with higher concentration. This is done intuitively on the basis that the the higher concentration of particles causes a larger impact on the test pariticle in the center of the figure due to a relative increase in the number of particle-particle collisions in these regions compared to the regions of lower concentration. Noting again the boundary layer in the compressional zones in figure 5.24, one can see the positive y- and x-fluxes that will result from positive x- and y-gradients, respectively.

The long-time rotational self-diffusivity also has a non-zero off-diagonal component, D^r_{xy}, in the presence of hydrodynamic interactions. Values of D^r_{xy} as a function of Pe in figure 5.29 show behavior that is quite similar to the translational case except each contribution has the opposite sign. At high Pe, the hydrodynamic contribution dominates showing a positive contribution that grows linearly with Pe. Near equilibrium, the negative Brownian contribution dominates, but the data is too noisy to obtain a definitive low-Pe assymptote.

The mechanisms for off-diagonal rotational diffusion are related to those of the

translational case in that they are dependent on a higher probability of a tagged particle having a neighbor in the compressional, rather the than extensional, zones. Consider first the near equilibrium case where Brownian motion dominates. For two particles near contact with each other, the ability to rotate is easiest along an axis of rotation coincident with the center-to-center vector between the particles and is most hindered along any direction perpendicular to this vector. In a shearing suspension, there is a surplus of particles in the compressional zones, thus the favored axis for rotational diffusion is the compressional axis, while unfavored axes lie in the extensional-vorticity plane. The preference for rotation along the compressional rather than extensional axis results in a negative Brownian contribution to D^r_{xy}.

At high Pe, the hydrodynamic contribution dominates. Hydrodynamic rotations are caused by a rolling motion that neighboring particles exhibit as they are convecting past each other in the flow. Most of the rotation occurs in the plane of shear, explaining the much larger values of D^r_{zz} compared to the other diagonal components. But, when particles convecting past each other have an offset in the z-direction, hydrodynamic rotations occur on other axes. Particles translating in the compressional direction with an offset in the z-direction would rotate along the extensional axis, while similar particles translating along the extensional axis would rotate along the compressional axis. The surplus of particles in the compressional zone causes more particles to translate in the compressional direction — as noted by the negative sign of the translational D_{xy} in this regime — resulting in preferred rotation along the extensional axis, or a positive hydrodynamic contribution to D^r_{xy}. This is an important observation as it verifies the results for the translational D_{xy} with an argument that does not involve exclusion of the affine motion which is unimportant for rotational motion and occurs along the z-axis in shear flow.

5.6 Summary and concluding remarks

Results for the long-time self-diffusivity have been presented with and without hydrodynamic interactions. Without hydrodynamic interactions, large systems were used

enabling accurate results to be obtained for all values of Pe, including verification of the $O(Pe)$ and $O(Pe^{3/2})$ corrections to the equilibrium long-time self-diffusivity predicted by Morris & Brady (1996). Qualitative agreement with the theoretical work of Brady & Morris (1997) was achieved at high Pe, with diffusivities scaling like $\dot{\gamma}a^2$. The ϕ-dependence of the diffusivity was also examined. Equilibrium self-diffusivities are decreasing functions of ϕ and agree with the previous results of Cichocki & Hinsen (1992) and Schaertl & Sillescu (1994). Diffusivities at $Pe = 1000$ were found to be strictly increasing functions of ϕ with relative sizes of the diagonal components consistent with the analogy that diffusion is directly related to the stress in this regime.

Inclusion of hydrodynamic interactions adds a configurational- and concentration-dependent particle mobility. We examined the diffusive behavior in the presence of hydrodynamic interactions, in which we were able to split the diffusivity into its Brownian and hydrodynamic contributions giving insight into the mechanisms for diffusion over the full range of Pe. Brownian diffusion, dominant at low Pe, is a random walk process that is hindered by the presence of other particles. At high shear rates, the prevalent diffusive mechanism is hydrodynamic in origin consisting of displacements due to interactions between neighboring particles and is thus enhanced by the presence of other particles. Thus, near equilibrium, the diffusivity, scaled by D_0, is found to be a monotonically decreasing function of ϕ, with lower values than in the Brownian Dynamics system. At high Pe, each diagonal component of the diffusivity, scaled by $\dot{\gamma}a^2$, grows with ϕ up to a point and then appears to reach a plateau near $\phi \approx 0.50$. It is unclear how this property will behave at higher volume fractions. We were limited to $\phi < 0.50$ due to system size restraints imposed by the computationally intensive Stokesian Dynamics algorithm. Note that the size limitations may affect the values of the diffusivities due to issues associated with fitting the proper microstructure in the small periodic cell even if a very large number of independent runs reduces the statistical noise to near zero.

For the Pe-dependence in the Stokesian Dynamic system, very good data was obtained at high shear rates, but we were unable to obtain a good measure of the first correction of the self-diffusivity from equilibrium due to shear. The diffusivity

is enhanced by the flow at low Pe mainly due to an increase in Brownian diffusion. The hydrodynamic contribution clearly vanishes like Pe^2 at low Pe in contrast to the predicted $Pe^{3/2}$ scaling.

Rotational self-diffusivites are also reported in this work showing similar behavior to the translational self-diffusivities. The zz-component is much larger than the other two components as rotation along the z-axis represents rotation in the plane of shear. Another notable exception is an initial decrease from its equilibrium value at low shear before the linear growth at high shear due to hydrodynamic interactions. Unlike the translational diffusivity, the Brownian rotational diffusivity is never enhanced by the flow, being a decreasing function of Pe for all Pe.

This work presents the first known data for colloidal suspensions on the xy-component to the long-time self-diffusion tensor. Two underlying factors dictate the behavior of this component. First, in shear flow there is a build-up of particles in the compressional zone relative to the extensional zone. Second, as discussed before, Brownian diffusion is hindered by the presence of other particles whereas hydrodynamic diffusion is enhanced. Thus, at low Pe both translation along the compressional axis and rotation around the extensional axis are relatively hindered leading to a positive D_{xy} and a negative D^r_{xy}, respectively. At high Pe, hydrodynamic diffusion takes over but the surplus in the compressional zone remains, thus reversing the signs of both D_{xy} and D^r_{xy}.

The data for the Brownian Dynamics system is of higher quality and more internally consistent than the Stokesian Dynamics system particularly at high volume fractions and low shear rates. The main reason for this is the size limitations put on the Stokesian Dynamics system due to the high computational cost of this algorithm. In the future, as hardware computational speed increases and Stokesian Dynamics algorithms are improved, it would be interesting to apply the method used to this work to study larger systems at high ϕ and/or low Pe in the presence of hydrodynamic interactions to clarify some issues raised here.

References

Ball, R.C. & Melrose, J.R. 1995 Lubrication breakdown in hydrodynamic simulations of concentrated colloids. *Adv. Colloid Interface Sci.* **59** 19.

Barrall, G.A., Schmidt-Rohr, K., Lee, Y.K., Landfester, K., Zimmerman, H., Chingas, G.C. & Pines, A. 1996 Rotational diffusion measurements of suspended colloidal particles using two-dimensional exchange nuclear magnetic resonance. *J. Chem. Phys.* **104** 509.

Batchelor, G.K. 1977 The effect of Brownian motion on the bulk stress in a suspension of spherical particles. *J. Fluid Mech.* **83**, 97.

Bossis, G. & Brady, J.F. 1984 Dynamic simulation of sheared suspensions. I. General method. *J. Chem. Phys.* **80**, 5141.

Bossis, G. & Brady, J.F. 1987 Self-diffusion of Brownian particles in concentrated suspensions under shear. *J. Chem. Phys.* **87**, 5437.

Bossis, G. & Brady, J.F. 1987 The rheology of Brownian suspensions. *J. Chem. Phys.* **91**, 1866.

Brady, J.F. 1994 The long-time self-diffusivity in concentrated colloidal dispersions. *J. Fluid Mech.* **272**, 109.

Brady, J.F. & Bossis, G. 1988 Stokesian dynamics. *Ann. Rev. Fluid Mech.* **20**, 111.

Brady, J.F. & Morris, J.F. 1997 Microstructure of strongly sheared suspensions and its impact on rheology and diffusion. *J. Fluid Mech.* **348**, 103.

Breedveld, V., van den Ende, D., Tripathi, A. & Acrivos, A. 1998 The Measurement of the Shear-Induced Particle and Fluid Tracer-Diffusivities in Concentrated Suspensions by a Novel Method. *J. Fluid Mech.* **375**, 297.

Cichocki, B. & Hinsen, K. 1992 Dynamic computer simulation of concentrated hard sphere suspensions. *Physica A* **187**, 145.

da Cunha, F.R. & Hinch, E.J. 1996 Shear-induced dispersion in a dilute suspension of rough spheres. *J. Fluid Mech.* **309**, 211.

Degiorgio, V., Piazza, R. & Jones, R.B. 1995 Rotational diffusion in concentrated colloidal dispersions of hard spheres. *Phys. Rev. E* **52**, 2707.

Dratler, D.I. & Schowalter, W.R. 1996 Dynamic simulation of suspensions of non-Brownian hard spheres. *J. Fluid Mech.* **325**, 53.

Dratler, D.I., Schowalter, W.R. & Hoffman, R.L. 1997 Dynamic Simulation of shear thickening in concentrated colloidal suspensions. *J. Fluid Mech.* **353**, 1.

Eckstein, E.C., Bailey, D.G. & Shapiro, A.H. 1977 Self-diffusion of particles in shear flow of a suspension. *J. Fluid Mech.* **79**, 191.

Elrick, D.E. 1962 Source functions for diffusion in uniform shear flow. *Aust. J. Phys.* **15**, 283.

Ermak, D.L. & McCammon, J.A. 1978 Brownian dynamics with hydro dynamic interactions. *J. Chem. Phys.* **69**, 1352.

Heyes, D.M. & Melrose, J.R. 1993 Brownian dynamics simulations of model hard-sphere suspensions. *J. Non-Newtonian Fluid Mech.* **46**, 1.

Jones, R.B. 1989 Rotational diffusion of a tracer colloidal particle. II. Long time orientational correlations. *Physica A* **157**, 752.

Kanetakus, J. & Sillescu, H. 1996 Simultaneous measurement of rotational and translational diffusion by forced Rayleigh scattering. Colloid spheres in suspension. *Chem. Phys. Lett.* **252**, 127.

Kanetakus, J., Tölle, A. & Sillescu, H. 1997 Rotational diffusion of colloid spheres in concentrated suspensions studied by deuteron NMR. *Phys. Rev. E* **55**, 3006.

Leal, L.G. 1973 On the effective conductivity of a dilute suspension of spherical drops in the limit of low particle Péclet number. *Chem. Engng Commun.* **1**, 21.

Leighton, D.T. & Acrivos, A. 1987 Measurement of shear-induced self-diffusion in concentrated suspensions of spheres. *J. Fluid Mech.* **177**, 109.

Morris, J.F. & Brady, J.F. 1996 Self-diffusion in sheared suspensions. *J. Fluid Mech.* **312**, 223.

Phan, S.E. & Leighton, D.T. 1993 Measurement of the shear-induced tracer diffusivity in concentrated suspensions. *J. Fluid Mech.*, submitted.

Phillips, R.J., Brady, J.F. & Bossis, G. 1988 Hydrodynamic transport properties of hard-sphere dispersions. I. Suspensions of freely mobile particles. *Phys. Fluids* **31**, 3462.

Sami, S. 1996 *Stokesian Dynamics simulations of Brownian suspensions in extensional flow.* M.S. Thesis, California Institute of Technology.

Schaertl, W. & Sillescu H. 1994 Brownian Dynamics Simulations of Colloidal Hard Spheres. Effects of Sample Dimensionality on Self-Diffusion. *J. Stat. Phys.* **74**, 687.

Wang, Y., Mauri, R. & Acrivos, A. 1996 Transverse shear-induced diffusion of spheres in a dilute suspension. *J. Fluid Mech.* **327**, 255.

Yurkovetsky, Y. 1998 *I. Statistical Mechanics of Bubbly Liquids. II. Behavior of Sheared Suspensions of Non-Brownian Particles.* Ph.D. Thesis, California Institute of Technology.

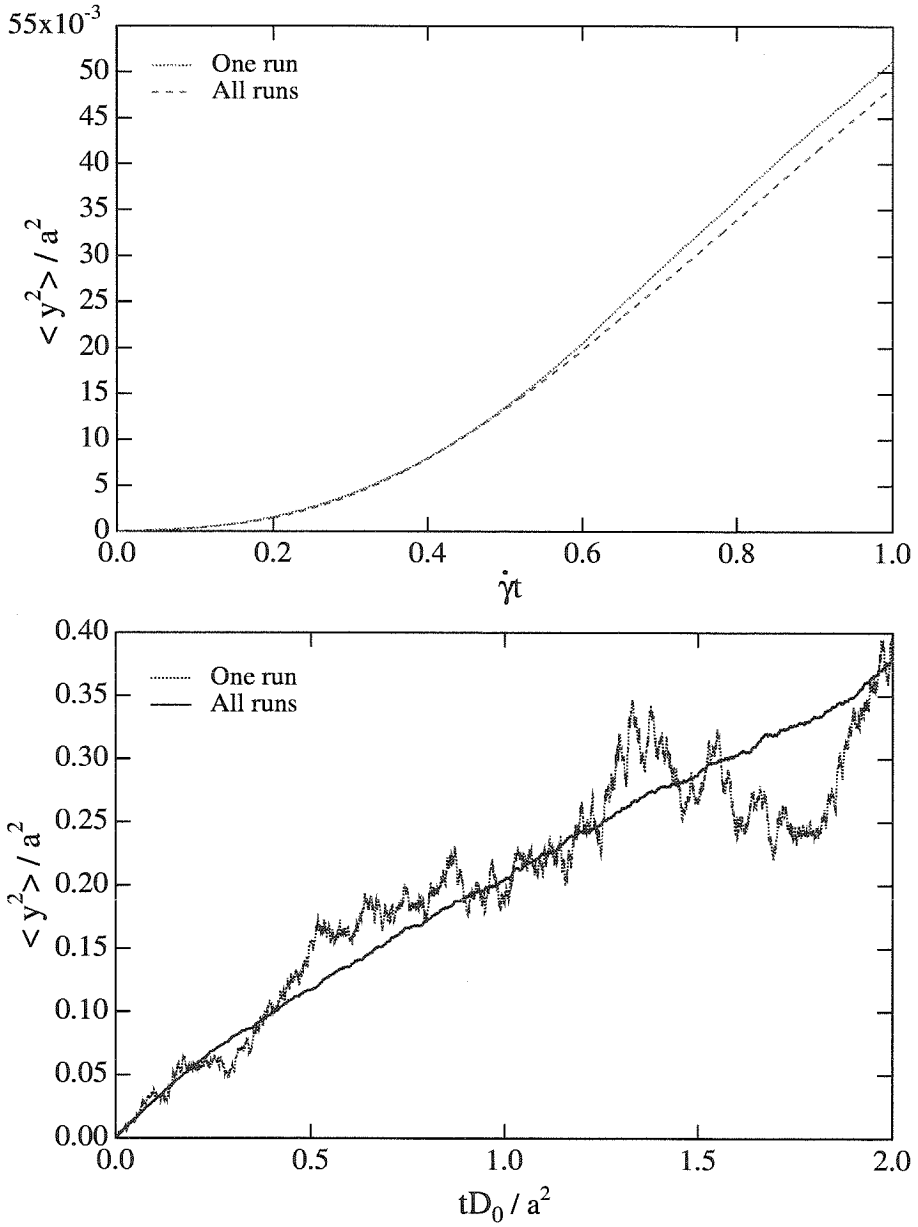

Figure 5.1: Mean square displacements as a functions of time for the Brownian Dynamics system (a) for $\phi = 0.45$, $Pe = 1000$ and Stokesian Dynamics system (b) for $\phi = 0.45$, $Pe = 0.3$ comparing data using both one and all realizations.

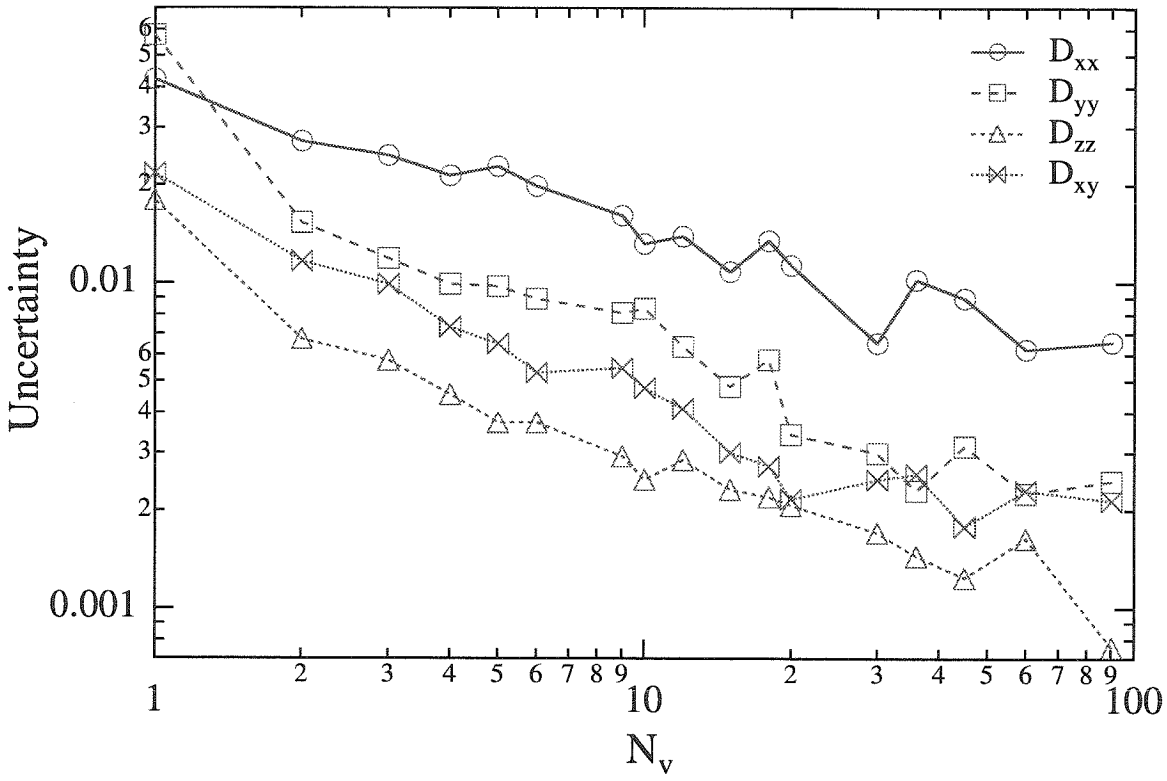

Figure 5.2: Standard deviations calculated from subset averages as a function of the number of data points included in each subset, N_v. This data is from the Stokesian Dynamics system, $\phi = 0.20$, $Pe = 1000$, $N = 27$, and 182 total independent realizations.

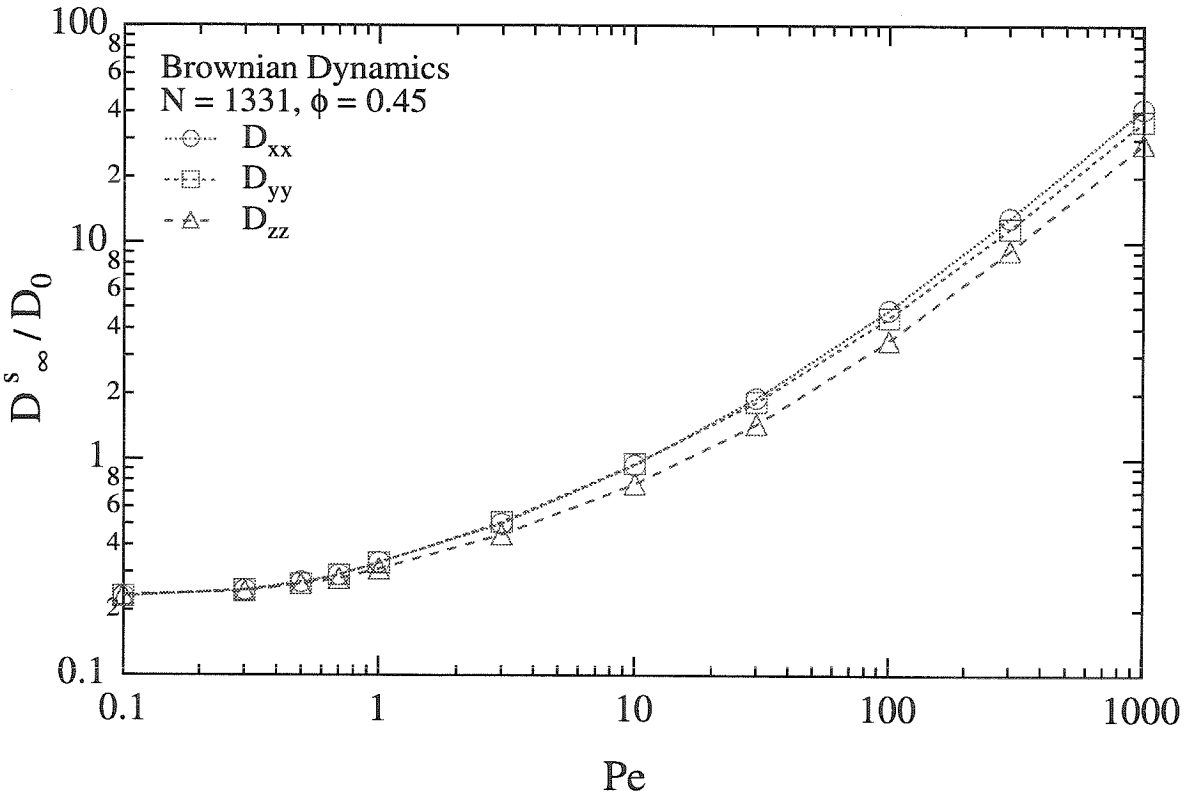

Figure 5.3: Diagonal components of the long-time self-diffusion tensor as a function of Pe for the Brownian Dynamics system.

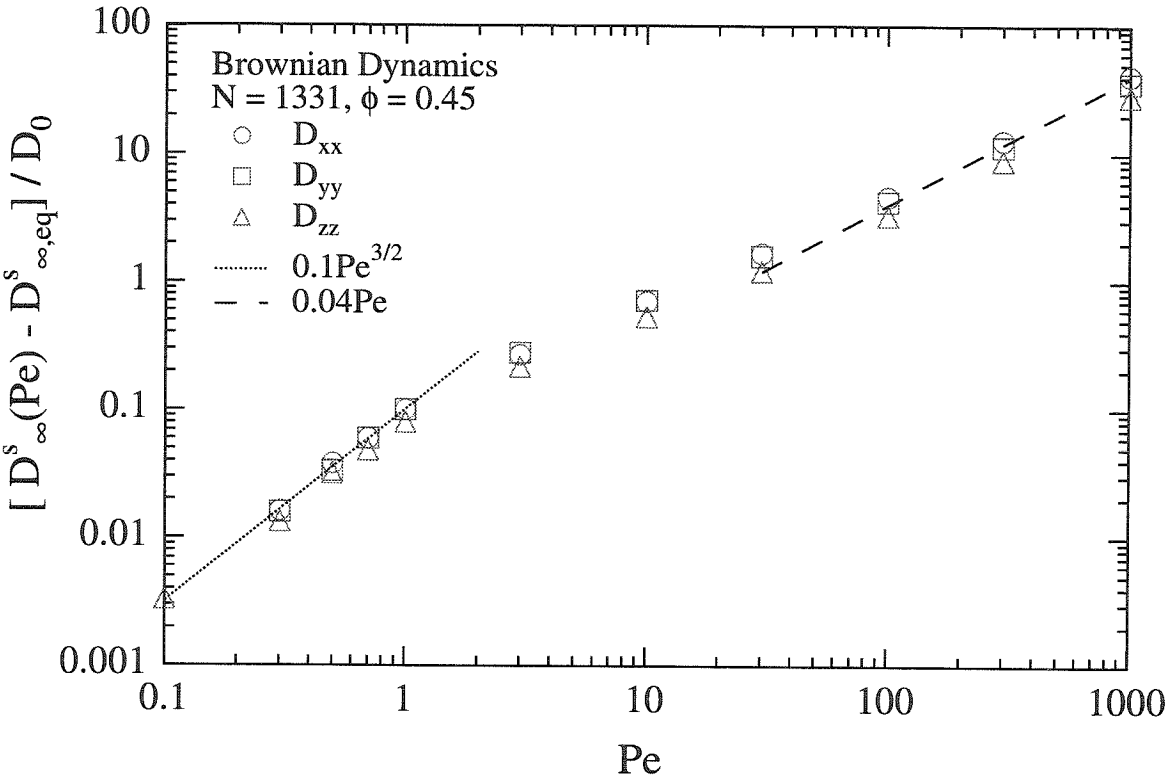

Figure 5.4: Diagonal components of the long-time self-diffusion tensor minus the equilibrium value as a function of Pe for the Brownian Dynamics system showing the functional dependence of the first correction of the diffusivity due to the shear flow.

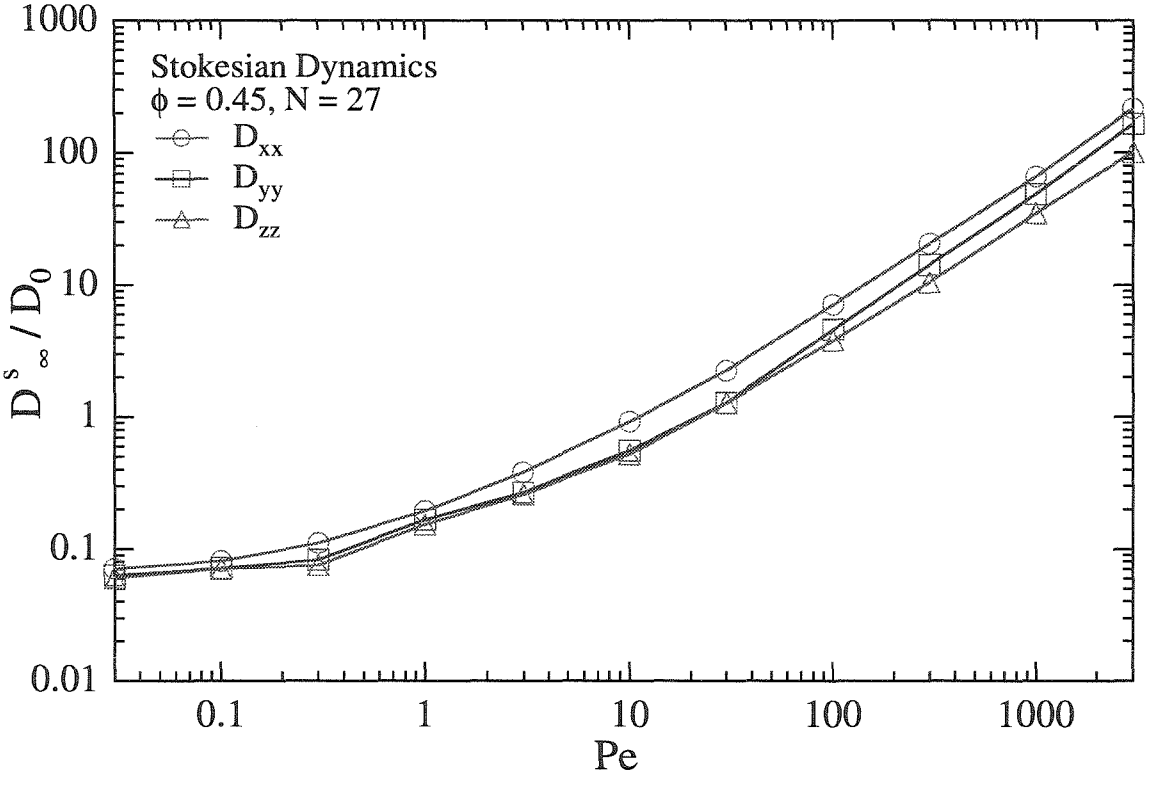

Figure 5.5: Diagonal components of the long-time self-diffusion tensor as a function of Pe for the Stokesian Dynamics system.

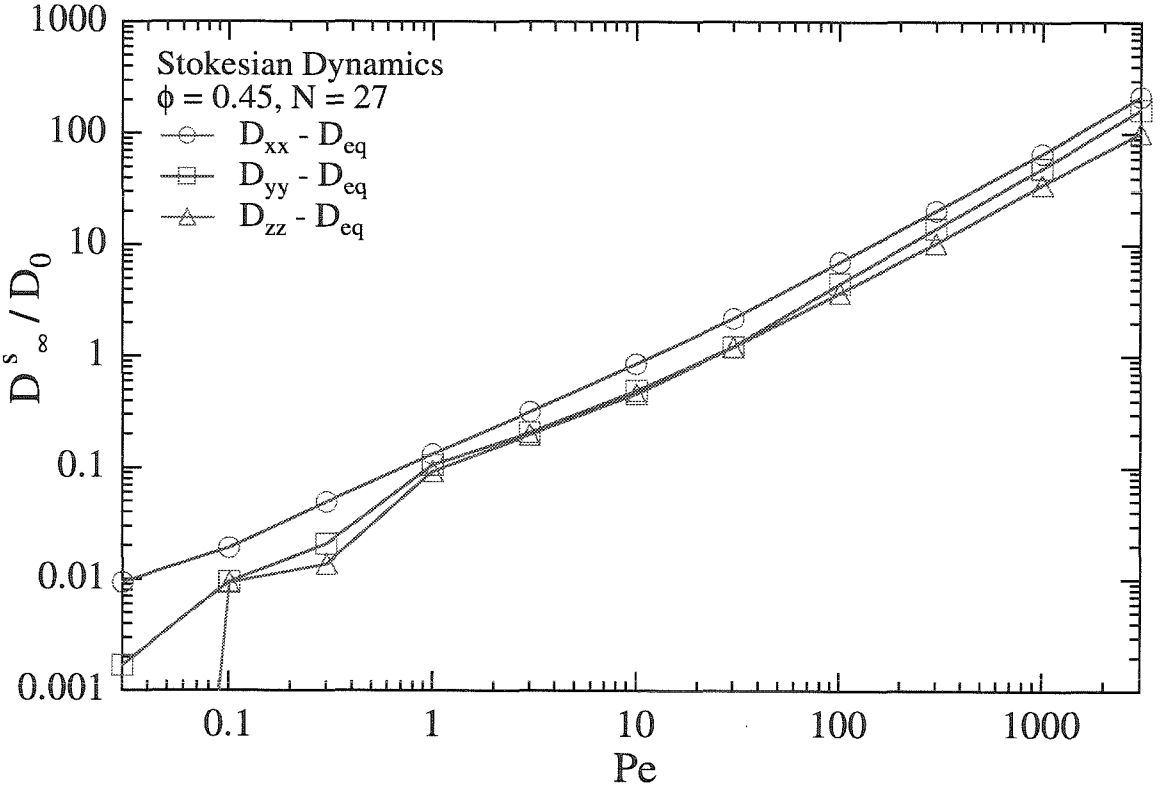

Figure 5.6: Diagonal components of the long-time self-diffusion tensor minus the equilibrium value as a function of Pe for the Stokesian Dynamics system showing the functional dependence of the first correction of the diffusivity due to the shear flow.

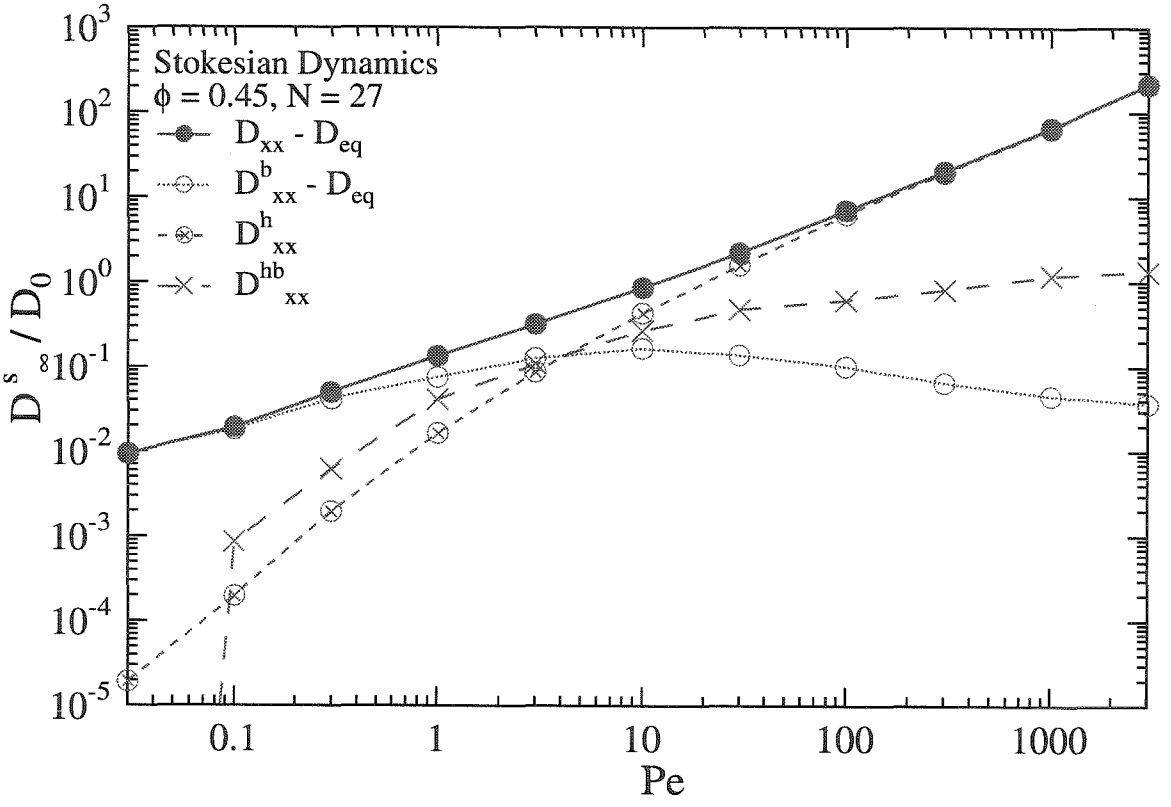

Figure 5.7: The different contributions to the xx-component of the long-time self-diffusion tensor as a function of Pe for the Stokesian Dynamics system. The equilibrium value of the self-diffusivity is subtracted from the Brownian contribution and total diffusivity to focus on the effects of the shear flow.

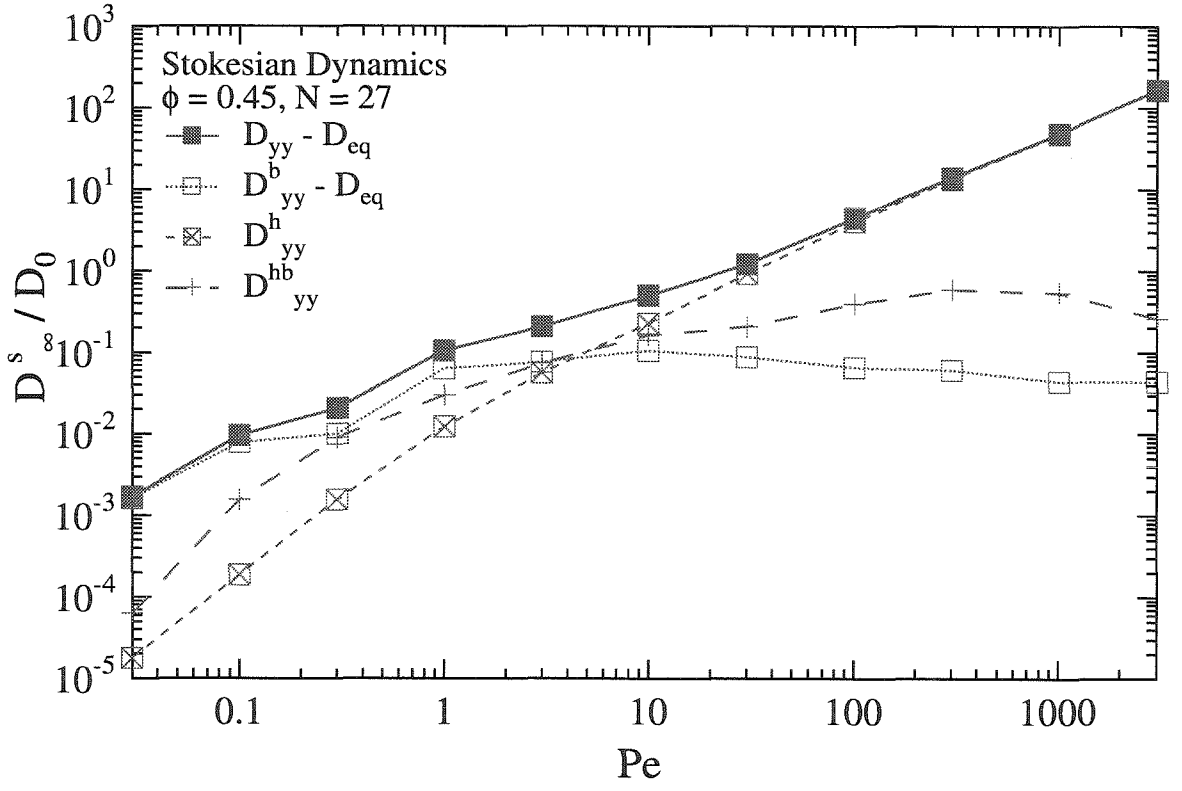

Figure 5.8: The different contributions to the yy-component of the long-time self-diffusion tensor as a function of Pe for the Stokesian Dynamics system. The equilibrium value of the self-diffusivity is subtracted from the Brownian and total diffusivities to focus on the effects of the shear flow.

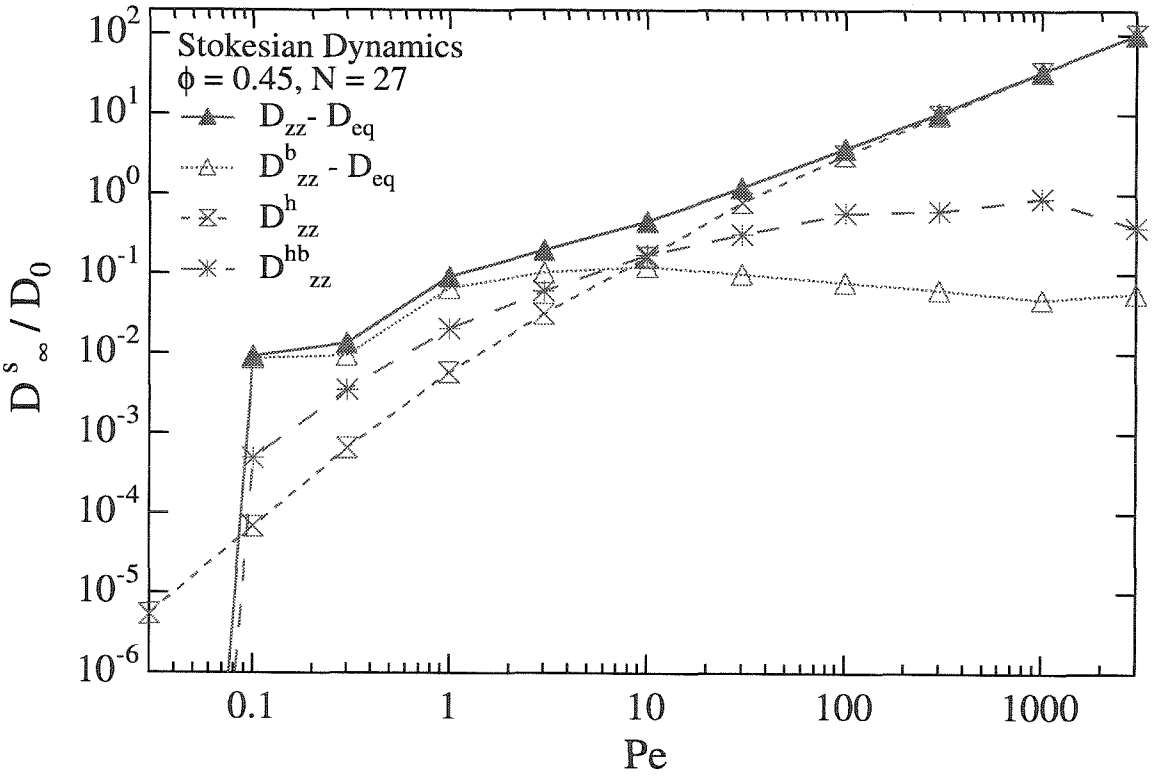

Figure 5.9: The different contributions to the zz-component of the long-time self-diffusion tensor as a function of Pe for the Stokesian Dynamics system. The equilibrium value of the self-diffusivity is subtracted from the Brownian and total diffusivities to focus on the effects of the shear flow.

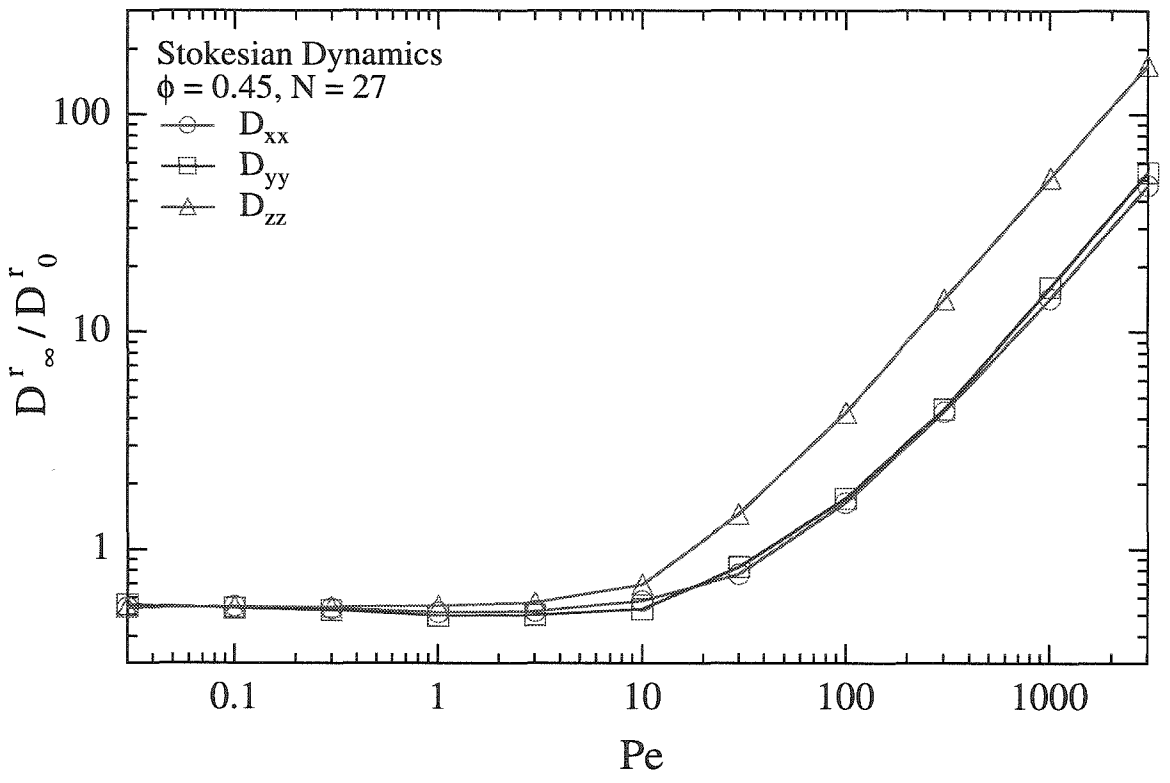

Figure 5.10: Diagonal components of the rotational long-time self-diffusion tensor as a function of Pe for the Stokesian Dynamics system.

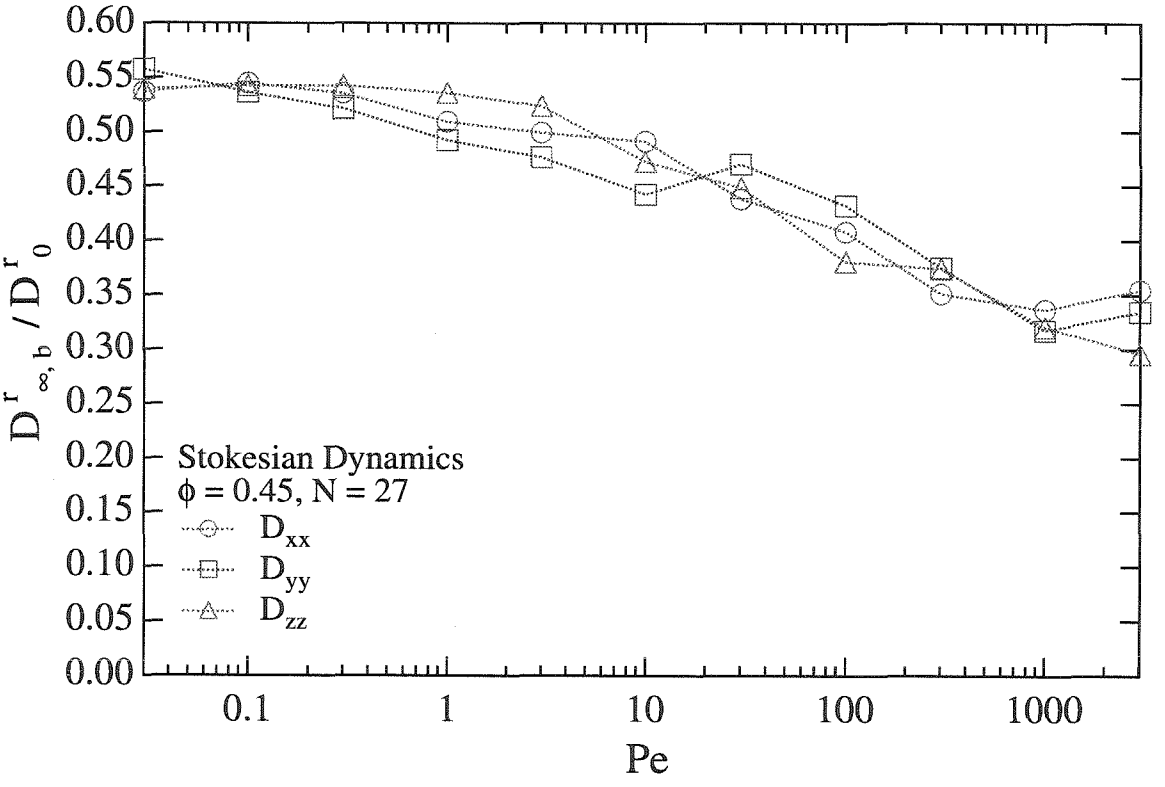

Figure 5.11: Brownian contribution to the diagonal components of the rotational long-time self-diffusion tensor as a function of Pe for the Stokesian Dynamics system.

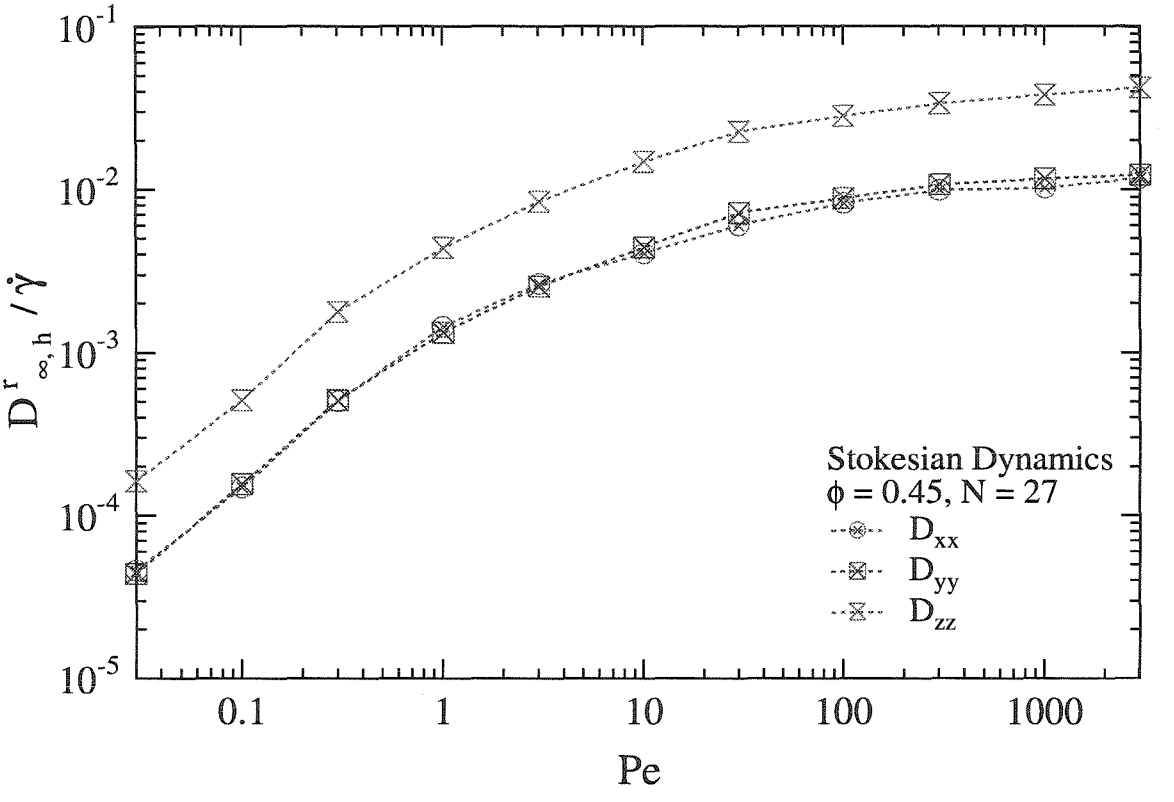

Figure 5.12: Hydrodynamic contribution to the diagonal components of the rotational long-time self-diffusion tensor, nondimensionalized by the appropriate hydrodynamic scaling, $\dot{\gamma}$, as a function of Pe for the Stokesian Dynamics system.

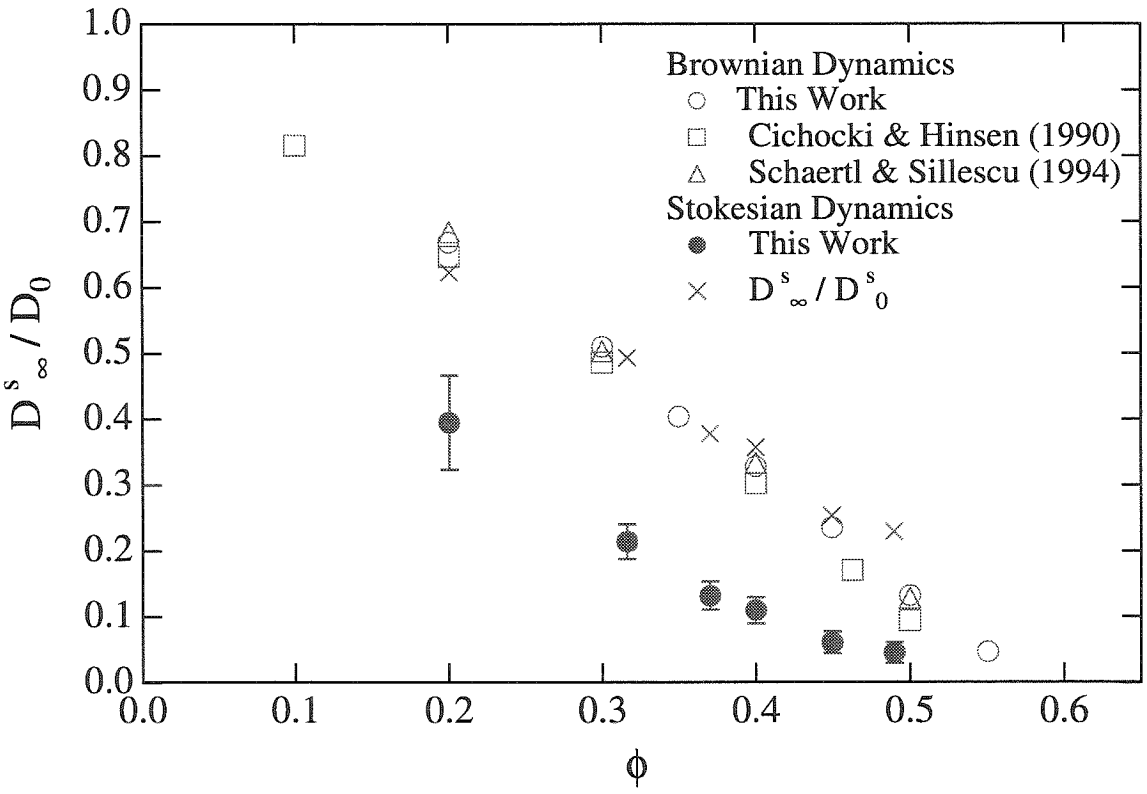

Figure 5.13: Equilibrium values of the long-time self-diffusivity as a function of ϕ. Data include those from both the Brownian Dynamics and Stokesian Dynamics systems along with previous Brownian Dynamics results. Also plotted are the Stokesian Dynamics data after division by the equilibrium short-time self-diffusivities as suggested by Brady (1994).

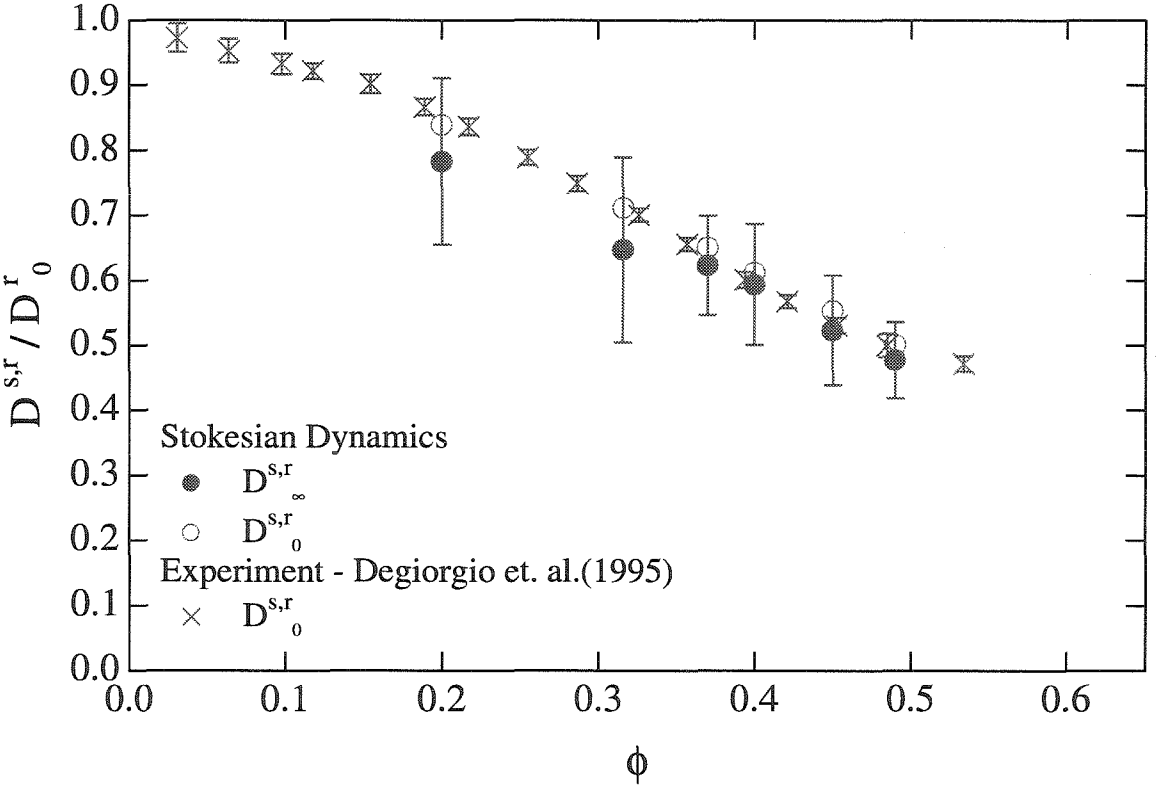

Figure 5.14: Equilibrium values of the rotational long-time self-diffusivity as a function of ϕ for the Stokesian Dyanamics system. Values of the rotational short-time diffusivity are included for comparison.

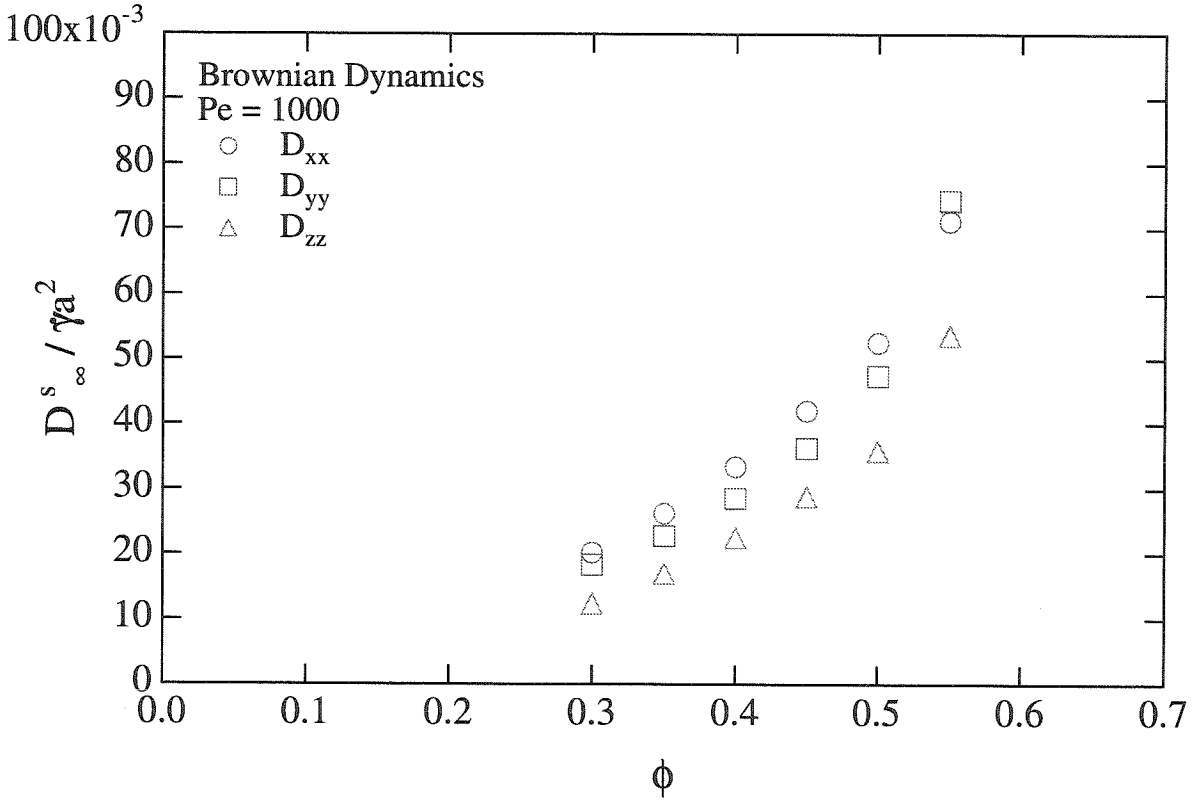

Figure 5.15: High shear values of the long-time self-diffusion tensor, nondimensionalized by $\dot{\gamma}a^2$, for the Brownian Dynamics system. The high shear points here correspond to $Pe = 1000$.

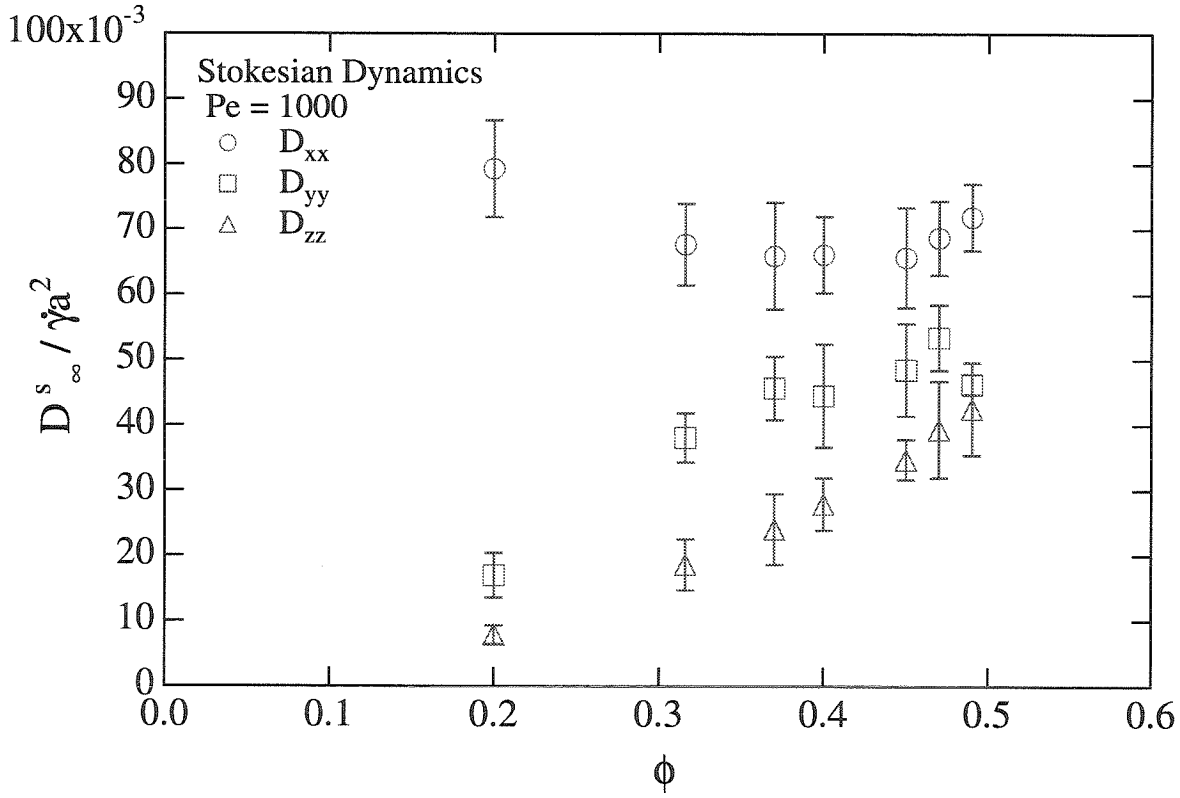

Figure 5.16: High shear values of the long-time self-diffusion tensor, nondimensionalized by $\dot{\gamma}a^2$, for the Stokesian Dynamics system. The high shear points here correspond to $Pe = 1000$.

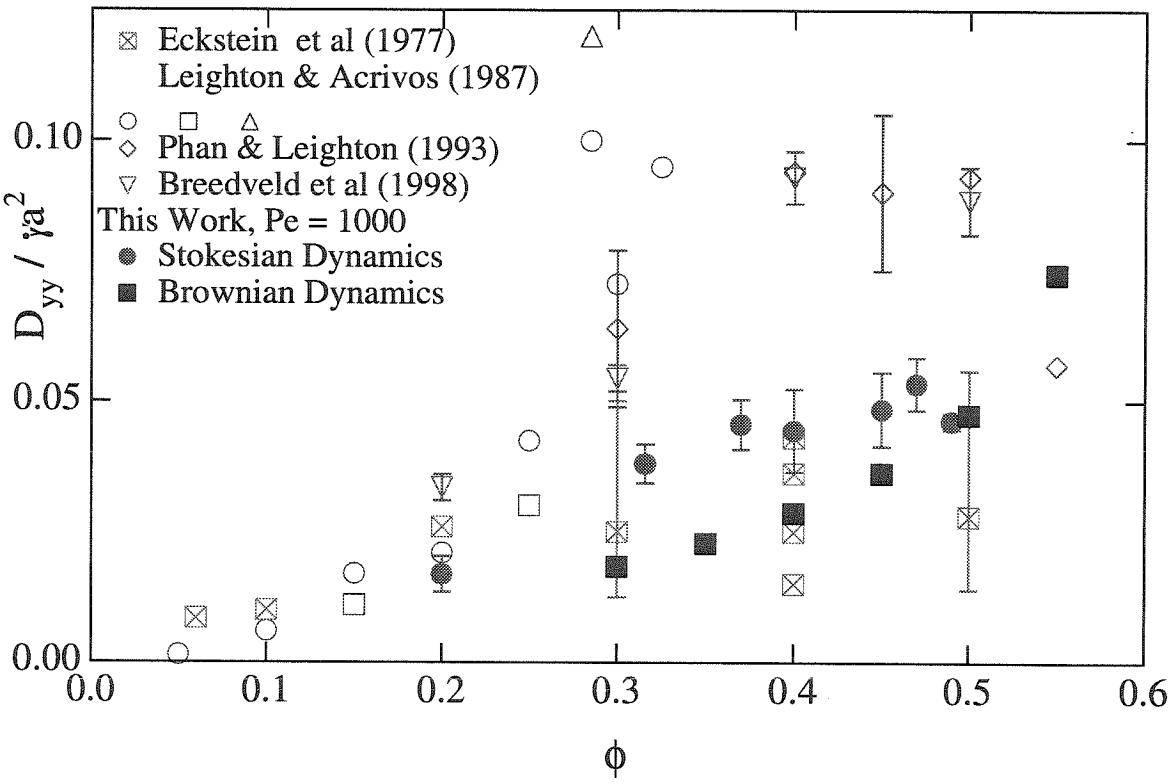

Figure 5.17: Comparison of the high shear yy-components of the long-time self-diffusion tensor from the Stokesian Dynamics and Brownian Dynamics systems with previous experimental results.

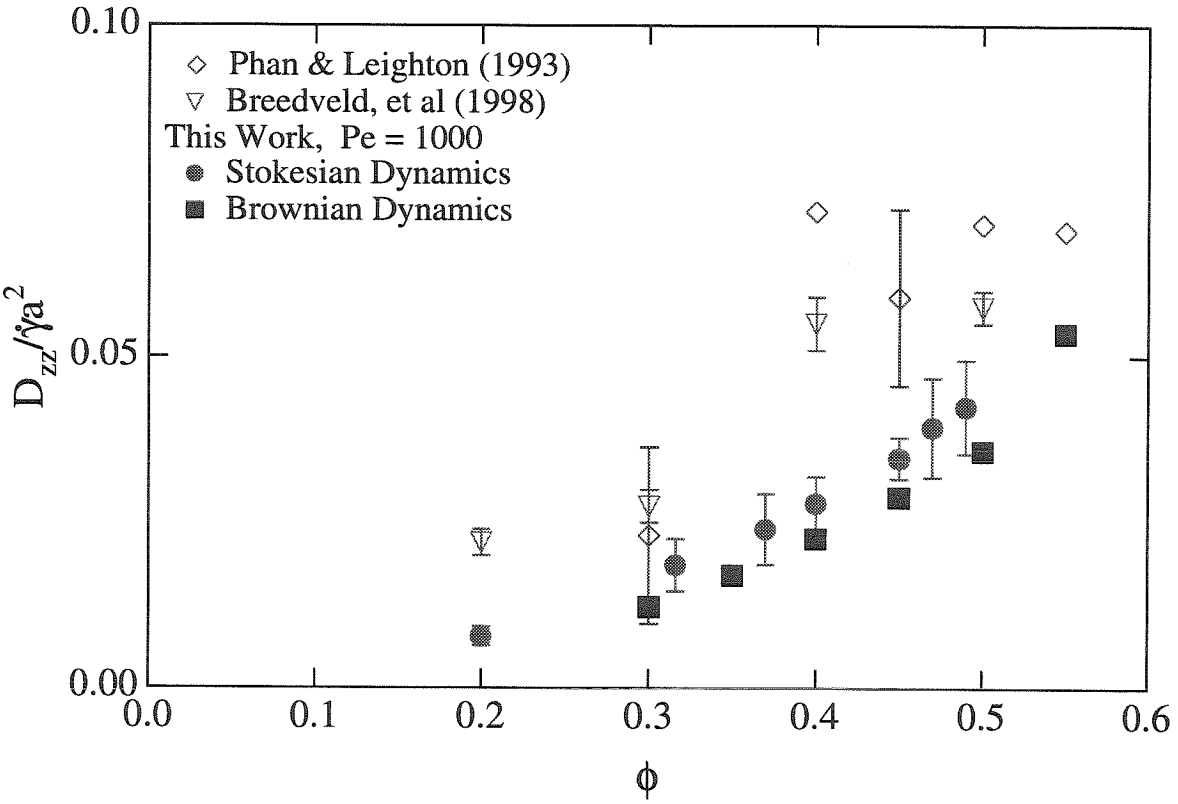

Figure 5.18: Comparison of the high shear zz-components of the long-time self-diffusion tensor from the Stokesian Dynamics and Brownian Dynamics systems with previous experimental results.

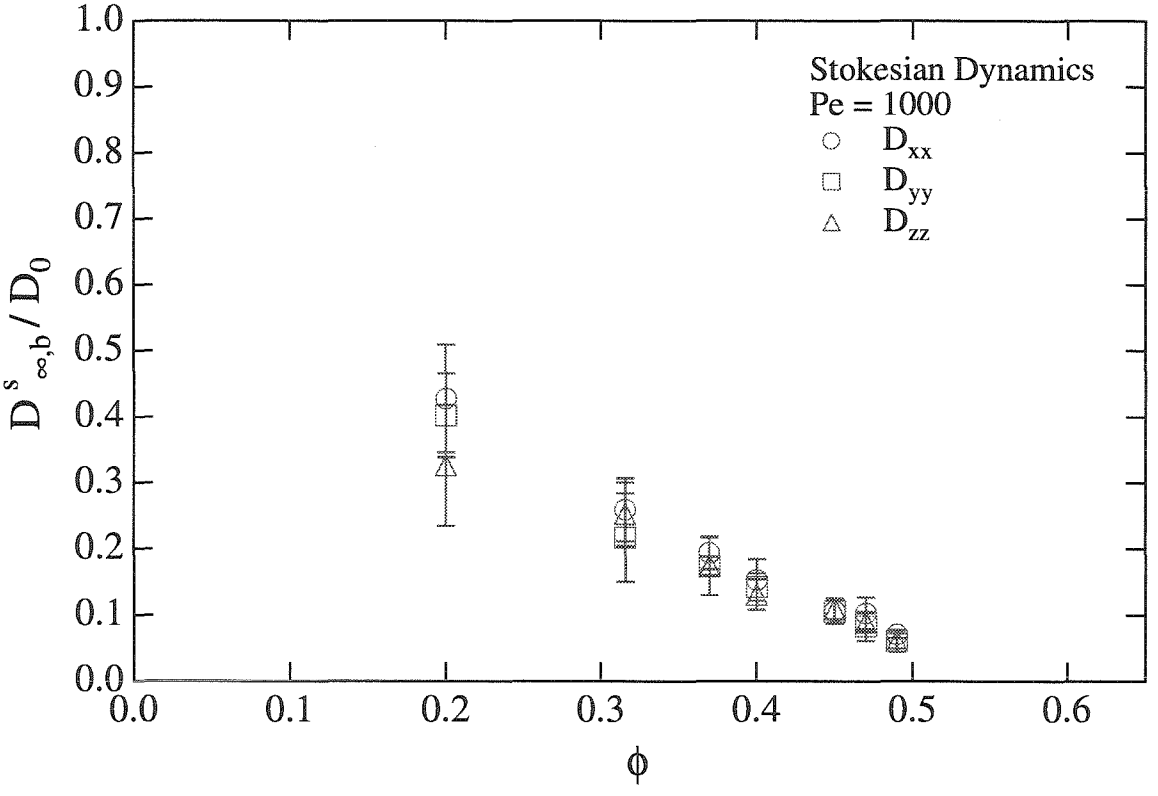

Figure 5.19: Brownian contribution to the high shear values of the long-time self-diffusion tensor for the Stokesian Dynamics system. The high shear points here correspond to $Pe = 1000$.

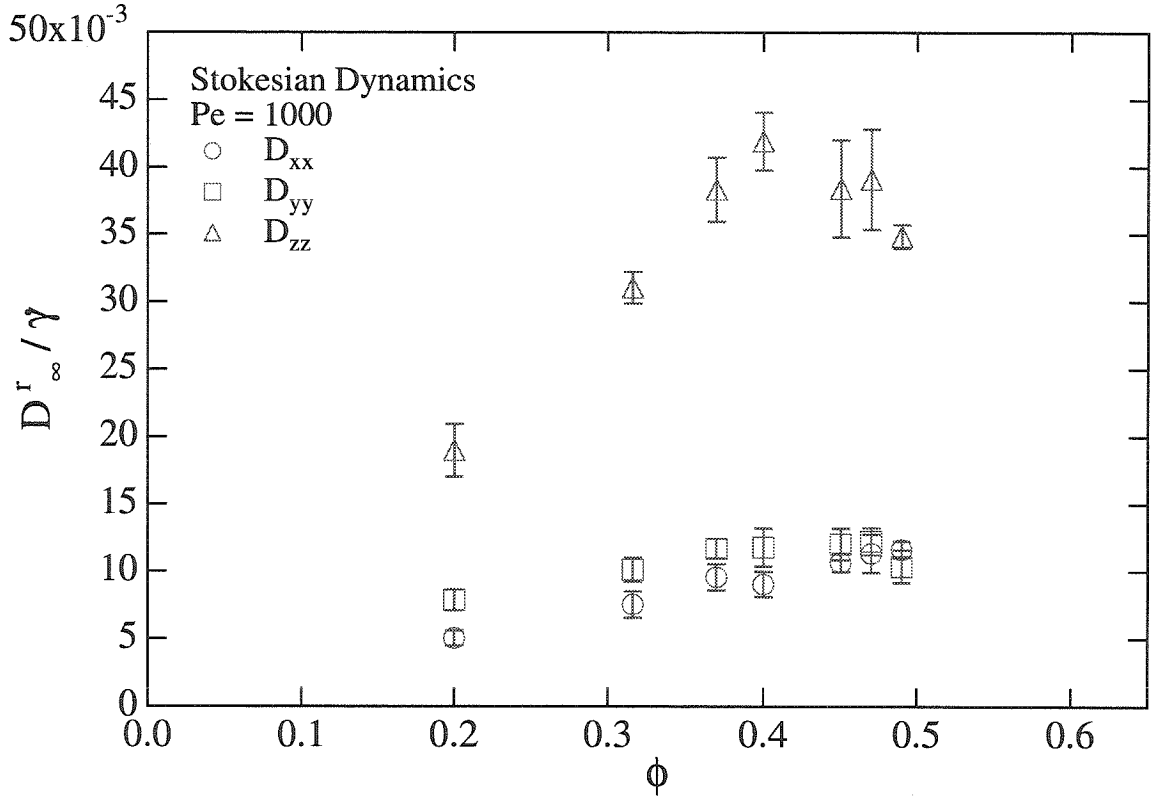

Figure 5.20: High shear values of the rotational long-time self-diffusion tensor, nondimensionalized by $\dot{\gamma}$, for the Stokesian Dynamics system. The high shear points here correspond to $Pe = 1000$.

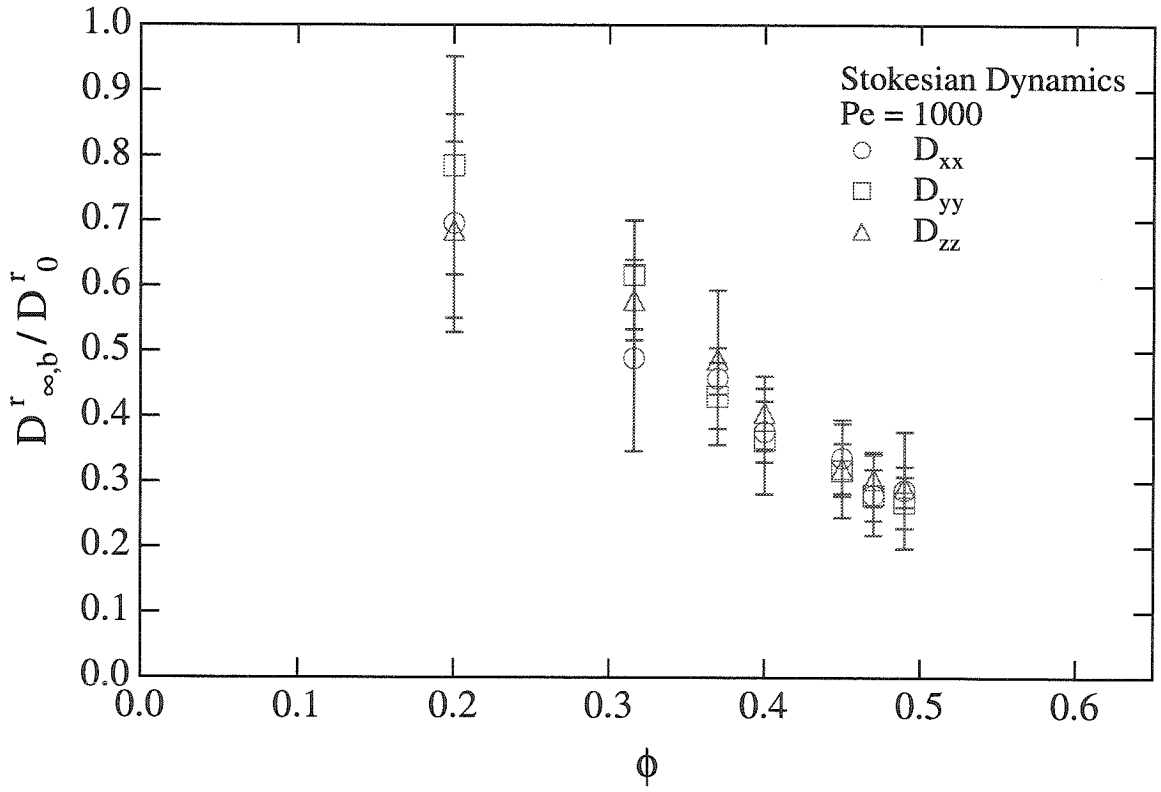

Figure 5.21: Brownian contribution to the high shear values of the rotational long-time self-diffusion tensor for the Stokesian Dynamics system. The high shear points here correspond to $Pe = 1000$.

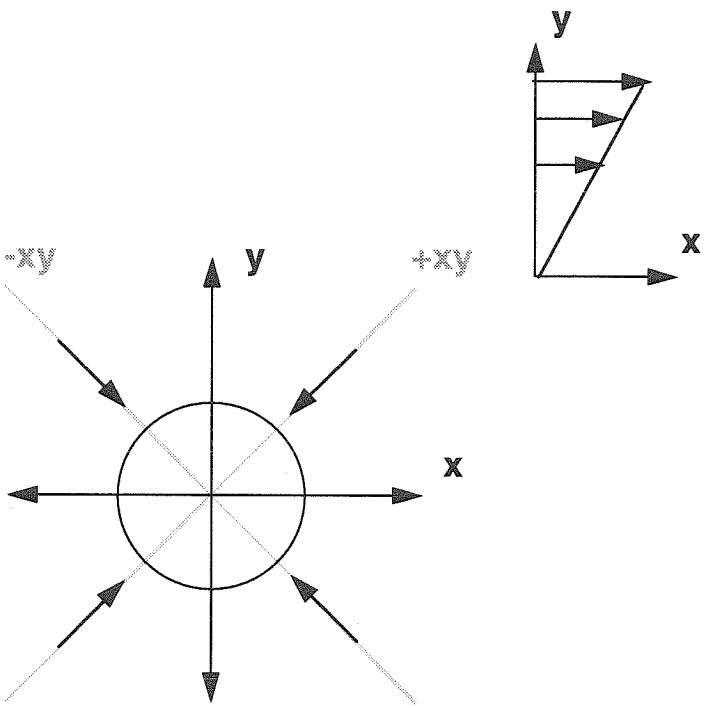

Figure 5.22: The xy-plane in simple shear flow with one particle at the origin. Arrows show impact on the motion of of the center particle due to collisions with other particles.

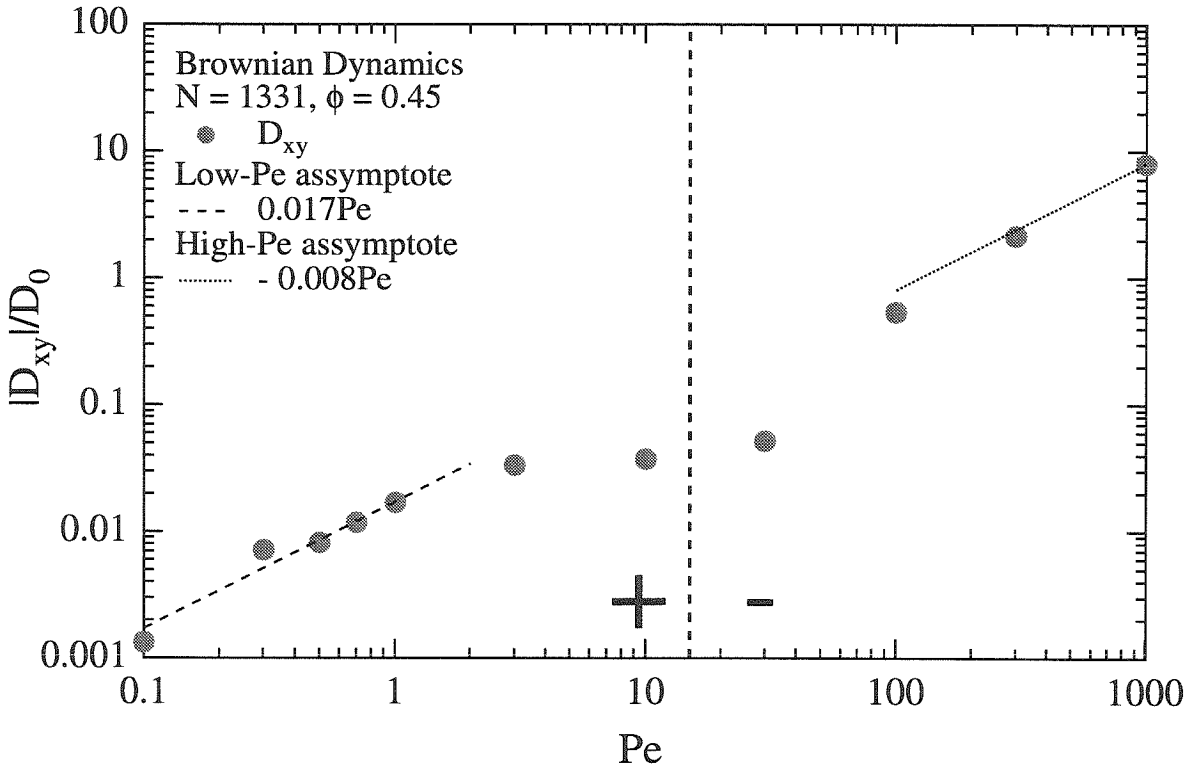

Figure 5.23: The xy-values of the long-time self-diffusion tensor as a function of Pe for the Brownian Dynamics system.

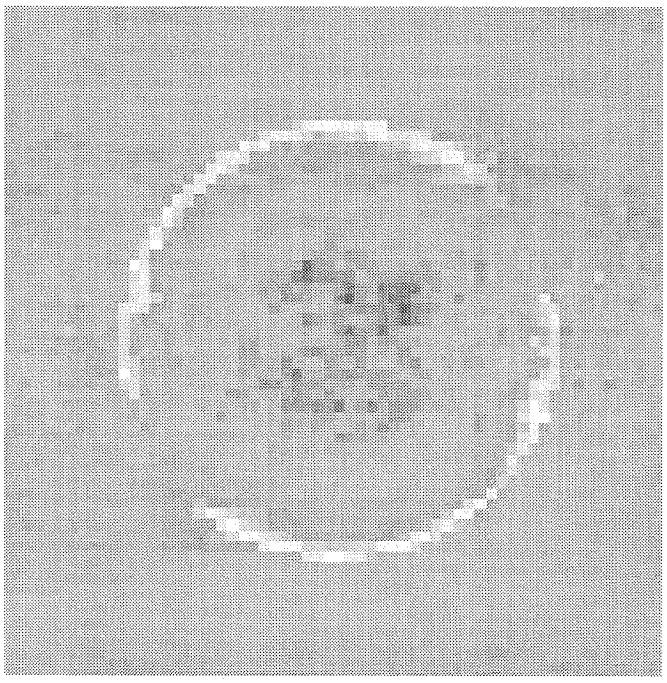

Figure 5.24: Projection of the pair-distribution function into the the xy-plane obtained from Stokesian Dynamics simulation, $\phi = 0.45$, $Pe = 1000$. High probability is represented by light shades, low probabilty by dark shades. Note the thin arcs of high probability near contact in each compressional zone characteristic of the boundary layer.

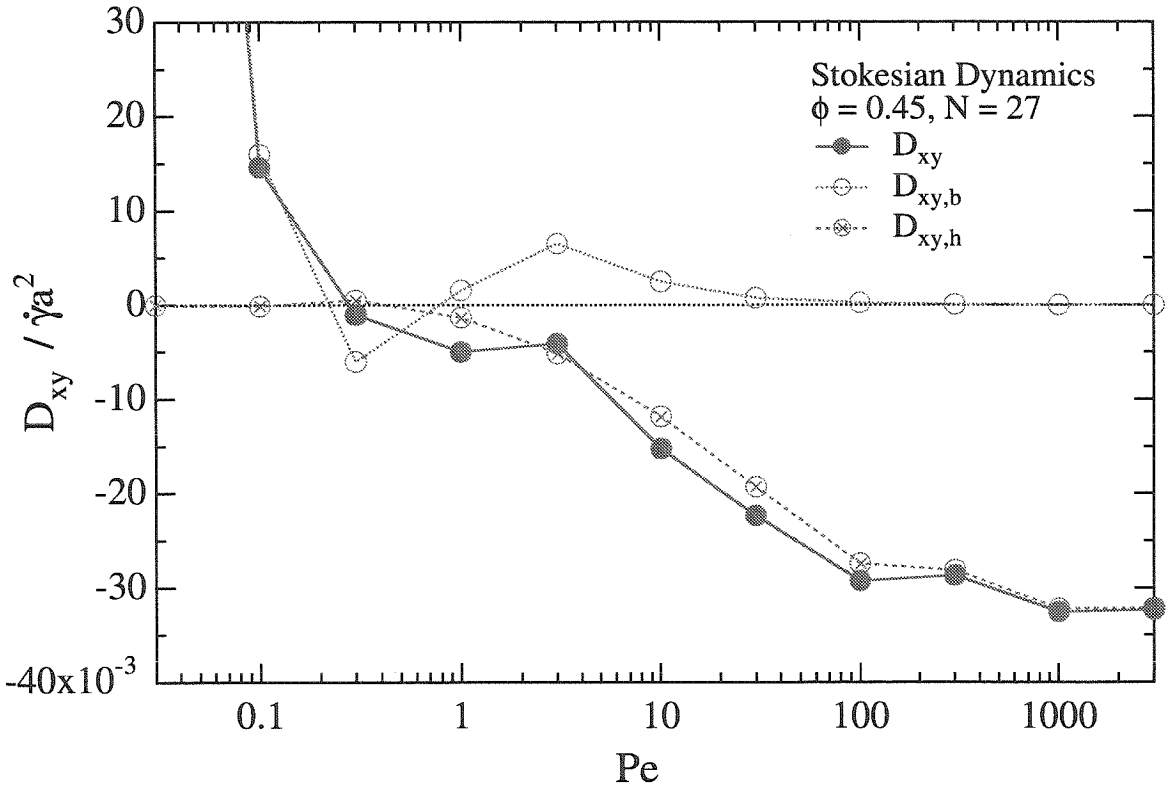

Figure 5.25: The xy-values of the long-time self-diffusion tensor and their different contributions as a function of Pe for the Stokesian Dynamics system.

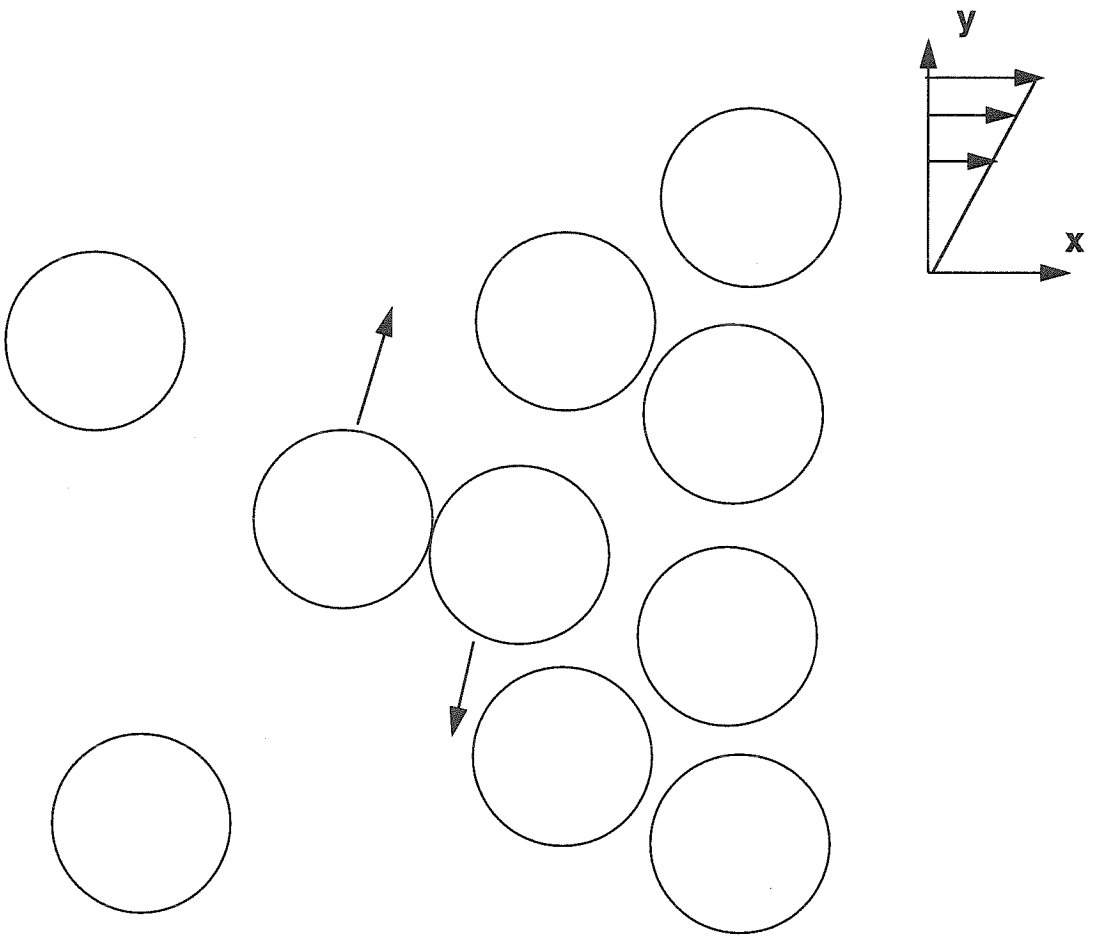

Figure 5.26: Configuration of particles with a concentration gradient in the positive x-direction showing a possible mechanism for a flux in the positive y-direction.

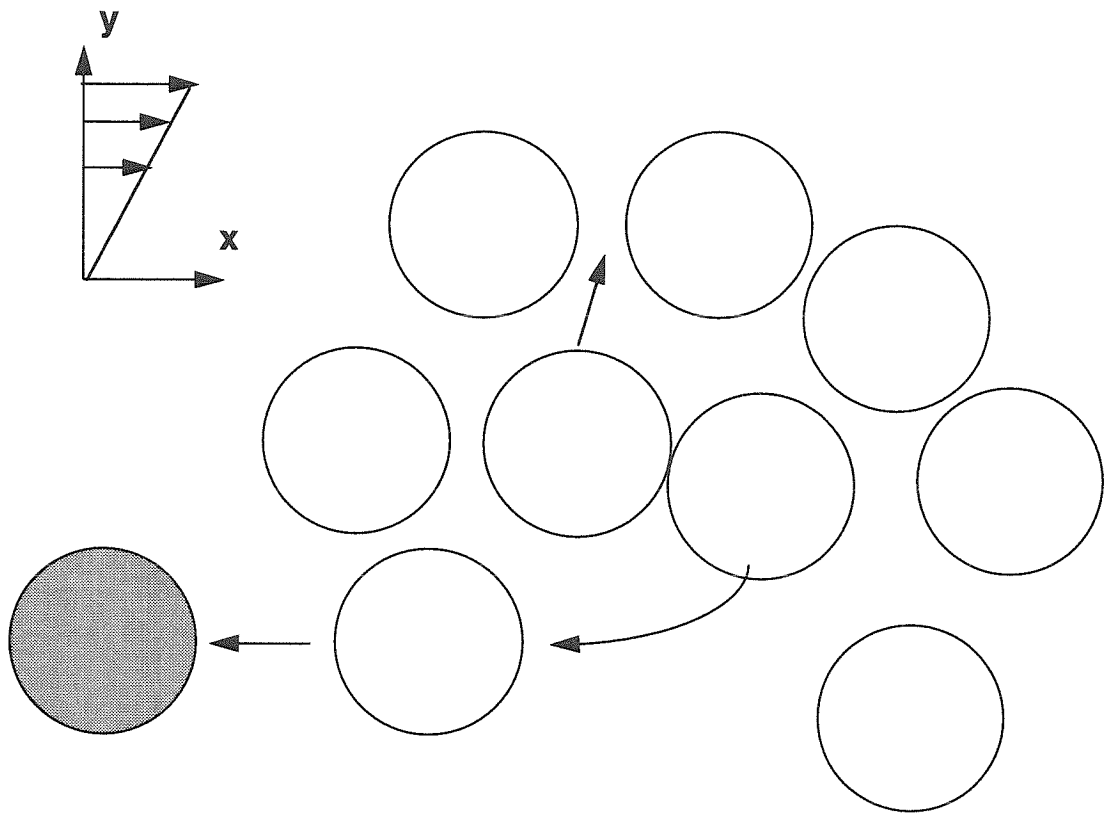

Figure 5.27: Configuration of particles with a concentration gradient in the positive y-direction showing a possible mechanism for a flux in the positive x-direction. Note that the darker particle shows where the particle would have been if it had precisely followed its affine x-displacements. Although the particle is convected to the left by the flow, there is a lag which is indicative of a postive x-flux.

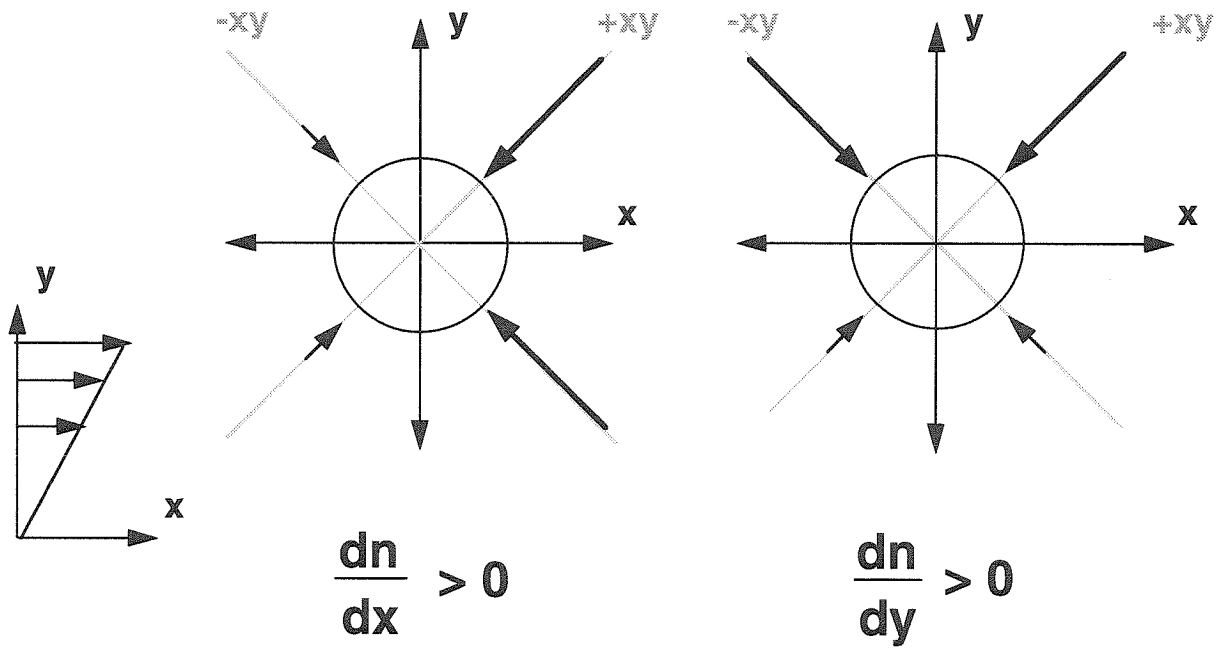

Figure 5.28: The xy-plane in simple shear flow with one particle at the origin. Arrows showing impact on the motion of the center particle due to collisions with other particles are altered by the presence of a concentration gradient. Larger arrows are drawn on the side with higher concentration due to an increase in the number of collisions in this region.

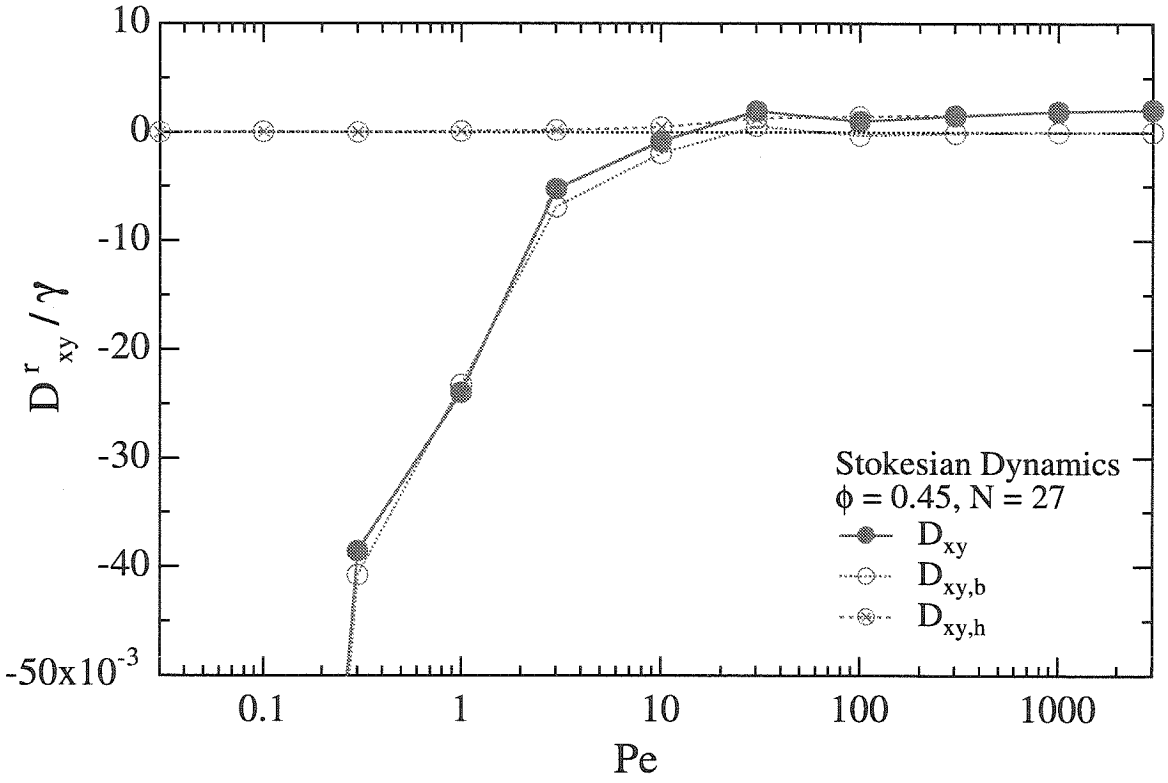

Figure 5.29: The xy-values of the rotational long-time self-diffusion tensor and their different contributions as a function of Pe for the Stokesian Dynamics system.

Brownian Dynamics, $\phi = 0.45$				
Pe	D_{xx}	D_{yy}	D_{zz}	D_{xy}
0.1	0.22990	0.23111	0.23365	0.0013276
0.3	0.24644	0.24613	0.24357	0.0070871
0.5	0.26816	0.26340	0.26211	0.0081458
0.7	0.28969	0.28946	0.27820	0.0116890
1	0.33018	0.33017	0.30990	0.0167672
3	0.49862	0.50966	0.44557	0.0330602
10	0.93003	0.94378	0.76159	0.0371206
30	1.89718	1.82687	1.44107	-0.0510344
100	4.84273	4.47138	3.50798	-0.531988
300	12.9640	11.5822	9.14422	-2.12405
1000	41.3292	36.0604	28.5020	-7.98406

Table 5.1: Values of the long-time self-diffusivity nondimensionalized by the Stokes-Einstein diffusivity, D_0, as a function of Pe for the Brownian Dynamics system. Data obtained from 91 simulations of $N = 1331$ at $\phi = 0.45$.

Brownian Dynamics, $Pe = 0$		
ϕ	N	D^s_∞
0.20	1331	0.66871
0.30	1331	0.50960
0.35	1331	0.40384
0.40	1331	0.32828
0.45	1331	0.23037
0.50	1331	0.13195
0.55	1331	0.04730

Table 5.2: Values of the long-time self-diffusivity nondimensionalized by the Stokes-Einstein diffusivity, D_0, as a function of ϕ for the Brownian Dynamics system. Data obtained from 91 simulations of $N = 1331$ at $Pe = 0$.

Brownian Dynamics, $Pe = 1000$				
ϕ	D_{xx}	D_{yy}	D_{zz}	D_{xy}
0.30	0.02014	0.01834	0.01227	-0.010836
0.35	0.02620	0.02274	0.01701	-0.011454
0.40	0.03339	0.02856	0.02251	-0.010656
0.45	0.04202	0.03623	0.02881	-0.008132
0.50	0.05254	0.04743	0.03582	-0.004267
0.55	0.07118	0.07435	0.05356	-0.000864

Table 5.3: Values of the long-time self-diffusivity, nondimensionalized by $\dot{\gamma}a^2$, as a function of ϕ for the Brownian Dynamics system. Data obtained from 91 simulations of $N = 1331$ at $Pe = 1000$.

Stokesian Dynamics, $\phi = 0.45$				
Pe	D_{xx}	D_{yy}	D_{zz}	D_{xy}
0.03	0.0708 ± 0.0142	0.0632 ± 0.0268	0.0600 ± 0.0071	0.009271 ± 0.012981
0.1	0.0805 ± 0.0174	0.0710 ± 0.0225	0.0708 ± 0.0130	0.001458 ± 0.011230
0.3	0.1105 ± 0.0140	0.0820 ± 0.0167	0.0750 ± 0.0295	-0.000319 ± 0.014583
1	0.1925 ± 0.0274	0.1672 ± 0.0291	0.1525 ± 0.0086	-0.004491 ± 0.009286
3	0.3783 ± 0.0429	0.2670 ± 0.0674	0.2575 ± 0.0263	-0.012375 ± 0.024016
10	0.9134 ± 0.1175	0.5535 ± 0.0708	0.5169 ± 0.0831	-0.152322 ± 0.045060
30	2.2422 ± 0.2694	1.2767 ± 0.1422	1.2602 ± 0.2905	-0.669959 ± 0.11388
100	7.0614 ± 0.7832	4.5410 ± 0.8919	3.7744 ± 0.5016	-2.924991 ± 0.39717
300	20.354 ± 2.801	14.079 ± 2.036	10.410 ± 1.019	-8.608622 ± 1.31423
1000	65.669 ± 7.698	48.470 ± 7.135	34.706 ± 3.091	-32.53325 ± 4.70285
3000	214.44 ± 24.66	164.60 ± 14.36	101.08 ± 13.57	-96.90744 ± 9.03423

Table 5.4: Values of the long-time self-diffusivity nondimensionalized by the Stokes-Einstein diffusivity, D_0, as a function of Pe for the Stokesian Dynamics system. Data obtained from 182 simulations of $N = 27$ at $\phi = 0.45$.

Stokesian Dynamics, $\phi = 0.45$				
Pe	$D_{xx,b}$	$D_{yy,b}$	$D_{zz,b}$	$D_{xy,b}$
0.03	0.0708 ± 0.0142	0.0631 ± 0.0270	0.0600 ± 0.0070	0.00926 ± 0.01259
0.1	0.0794 ± 0.0167	0.0693 ± 0.0220	0.0702 ± 0.0133	0.00160 ± 0.01110
0.3	0.1025 ± 0.0113	0.0715 ± 0.0164	0.0709 ± 0.0285	-0.00180 ± 0.01397
1	0.1361 ± 0.0228	0.1249 ± 0.0265	0.1274 ± 0.0065	0.00153 ± 0.00699
3	0.1861 ± 0.0260	0.1376 ± 0.0345	0.1656 ± 0.0137	0.01957 ± 0.02230
10	0.2243 ± 0.0303	0.1656 ± 0.0227	0.1852 ± 0.0380	0.02467 ± 0.02862
30	0.1974 ± 0.0335	0.1484 ± 0.0253	0.1597 ± 0.0246	0.02257 ± 0.01565
100	0.1608 ± 0.0269	0.1263 ± 0.0225	0.1404 ± 0.0192	0.02233 ± 0.00956
300	0.1253 ± 0.0333	0.1215 ± 0.0118	0.1241 ± 0.0174	0.01196 ± 0.00941
1000	0.1066 ± 0.0193	0.1054 ± 0.0167	0.1097 ± 0.0158	0.01068 ± 0.00880
3000	0.0984 ± 0.0288	0.1054 ± 0.0186	0.1190 ± 0.0135	0.00867 ± 0.00709

Table 5.5: Values of the Brownian contribution to the long-time self-diffusivity nondimensionalized by the Stokes-Einstein diffusivity, D_0, as a function of Pe for the Stokesian Dynamics system. Data obtained from 182 simulations of $N = 27$ at $\phi = 0.45$.

Stokesian Dynamics, $\phi = 0.45$		
Pe	$D_{xx,h}$	$D_{yy,h}$
0.03	$0.00001926 \pm 0.00000203$	$0.00001760 \pm 0.00000253$
0.1	0.0001944 ± 0.0000128	0.0001857 ± 0.0000226
0.3	0.00193 ± 0.00018	0.00155 ± 0.00021
1	0.01614 ± 0.00309	0.01222 ± 0.00138
3	0.08562 ± 0.0128	0.05560 ± 0.0120
10	0.42380 ± 0.0485	0.22663 ± 0.0225
30	1.56963 ± 0.2416	0.92126 ± 0.1239
100	6.29475 ± 0.6811	4.02388 ± 0.7280
300	19.4258 ± 2.4973	13.3708 ± 1.9147
1000	64.3753 ± 7.3686	47.8289 ± 7.2248
3000	213.004 ± 27.250	164.234 ± 13.797

Table 5.6: Values of the hydrodynamic contribution to the long-time self-diffusivity nondimensionalized by the Stokes-Einstein diffusivity, D_0, as a function of Pe for the Stokesian Dynamics system. Data obtained from 182 simulations of $N = 27$ at $\phi = 0.45$.

Stokesian Dynamics, $\phi = 0.45$		
Pe	$D_{zz,h}$	$D_{xy,h}$
0.03	$0.00000544 \pm 0.00000040$	$-0.000000260 \pm 0.000000333$
0.1	0.0000681 ± 0.0000072	$-0.00001266 \pm 0.00000702$
0.3	0.00065 ± 0.00008	0.000152 ± 0.000078
1	0.00567 ± 0.00081	-0.001284 ± 0.000450
3	0.03136 ± 0.0064	-0.015449 ± 0.05045
10	0.16029 ± 0.0105	-0.118214 ± 0.01863
30	0.79173 ± 0.4158	-0.577886 ± 0.05480
100	3.06428 ± 0.5035	-2.741777 ± 0.37372
300	9.67562 ± 0.9119	-8.429976 ± 1.26264
1000	33.7080 ± 3.2696	-32.23402 ± 4.53759
3000	100.580 ± 13.579	-96.46280 ± 9.00549

Table 5.7: Values of the hydrodynamic contribution to the long-time self-diffusivity nondimensionalized by the Stokes-Einstein diffusivity, D_0, as a function of Pe for the Stokesian Dynamics system. Data obtained from 182 simulations of $N = 27$ at $\phi = 0.45$.

Stokesian Dynamics, $\phi = 0.45$				
Pe	D^r_{xx}	D^r_{yy}	D^r_{zz}	D^r_{xy}
0.03	0.5367 ± 0.0727	0.5574 ± 0.0477	0.5392 ± 0.0973	-0.01719 ± 0.05674
0.1	0.5449 ± 0.0550	0.5360 ± 0.0909	0.5431 ± 0.0814	-0.04391 ± 0.05502
0.3	0.5345 ± 0.0819	0.5233 ± 0.0559	0.5446 ± 0.0559	-0.01541 ± 0.02867
1	0.5193 ± 0.1104	0.4980 ± 0.0863	0.5352 ± 0.0752	-0.03477 ± 0.05296
3	0.5181 ± 0.1106	0.4988 ± 0.0707	0.5692 ± 0.1027	-0.02084 ± 0.05119
10	0.5775 ± 0.0616	0.5312 ± 0.0757	0.6878 ± 0.0726	-0.01130 ± 0.04395
30	0.7683 ± 0.0834	0.8295 ± 0.1040	1.4453 ± 0.1251	0.07680 ± 0.09152
100	1.6305 ± 0.0552	1.7128 ± 0.0878	4.2627 ± 0.3705	0.13209 ± 0.11020
300	4.2781 ± 0.2825	4.4144 ± 0.5931	14.108 ± 0.9088	0.59823 ± 0.44364
1000	14.221 ± 0.9395	16.056 ± 1.5627	51.212 ± 4.8166	2.48665 ± 0.54856
3000	47.072 ± 3.8545	50.041 ± 5.7648	168.69 ± 15.185	8.18160 ± 1.44213

Table 5.8: Values of the rotational long-time self-diffusivity nondimensionalized by the Stokes-Einstein diffusivity, D^r_0, as a function of Pe for the Stokesian Dynamics system. Data obtained from 182 simulations of $N = 27$ at $\phi = 0.45$.

Stokesian Dynamics, $\phi = 0.45$				
Pe	$D^r_{xx,b}$	$D^r_{yy,b}$	$D^r_{zz,b}$	$D^r_{xy,b}$
0.03	0.5366 ± 0.0726	0.5572 ± 0.0477	0.5392 ± 0.0971	-0.01718 ± 0.05666
0.1	0.5448 ± 0.0549	0.5364 ± 0.0909	0.5425 ± 0.0811	-0.04417 ± 0.05521
0.3	0.5354 ± 0.0827	0.5216 ± 0.0562	0.5425 ± 0.0559	-0.01629 ± 0.02940
1	0.5154 ± 0.1070	0.4962 ± 0.0847	0.5238 ± 0.0726	-0.03409 ± 0.05090
3	0.4994 ± 0.1063	0.4770 ± 0.0663	0.5241 ± 0.0892	-0.02757 ± 0.05004
10	0.4914 ± 0.0556	0.4425 ± 0.0613	0.4727 ± 0.0911	-0.02591 ± 0.03798
30	0.4382 ± 0.0854	0.4702 ± 0.0574	0.4486 ± 0.0531	0.02058 ± 0.05174
100	0.4081 ± 0.0576	0.4321 ± 0.0656	0.3807 ± 0.0668	-0.04341 ± 0.05043
300	0.3513 ± 0.0417	0.3754 ± 0.0488	0.3741 ± 0.0518	-0.04363 ± 0.04975
1000	0.3365 ± 0.0584	0.3175 ± 0.0719	0.3203 ± 0.0381	-0.03806 ± 0.05672
3000	0.3547 ± 0.0340	0.3348 ± 0.0699	0.2961 ± 0.0254	-0.03749 ± 0.01396

Table 5.9: Values of the Brownian contribution to the rotational long-time self-diffusivity nondimensionalized by the Stokes-Einstein diffusivity, D^r_0, as a function of Pe for the Stokesian Dynamics system. Data obtained from 182 simulations of $N = 27$ at $\phi = 0.45$.

Stokesian Dynamics, $\phi = 0.45$		
Pe	$D^r_{xx,h}$	$D^r_{yy,h}$
0.03	$0.00000184 \pm 0.000000148$	$0.00000175 \pm 0.000000139$
0.1	0.0000198 ± 0.0000022	$0.00002078 \pm 0.00000337$
0.3	0.0002008 ± 0.0000162	0.0002035 ± 0.0000237
1	0.00186 ± 0.00025	0.00176 ± 0.00017
3	0.01057 ± 0.00144	0.01014 ± 0.00145
10	0.05413 ± 0.00032	0.05904 ± 0.00053
30	0.23967 ± 0.01154	0.28560 ± 0.01952
100	1.09378 ± 0.0772	1.17571 ± 0.1360
300	3.94997 ± 0.1966	4.26774 ± 0.4484
1000	13.5859 ± 0.9325	15.5347 ± 1.6502
3000	46.7306 ± 4.0167	48.9376 ± 5.5407

Table 5.10: Values of the hydrodynamic contribution to the rotational long-time self-diffusivity nondimensionalized by the Stokes-Einstein diffusivity, D^r_0, as a function of Pe for the Stokesian Dynamics system. Data obtained from 182 simulations of $N = 27$ at $\phi = 0.45$.

Stokesian Dynamics, $\phi = 0.45$		
Pe	$D^r_{zz,h}$	$D^r_{xy,h}$
0.03	$0.00000646 \pm 0.000000244$	$0.0000000349 \pm 0.0000000965$
0.1	$0.00006783 \pm 0.00000527$	$0.000001915 \pm 0.000001034$
0.3	0.0007071 ± 0.0000914	$-0.000006099 \pm 0.000009119$
1	0.00582 ± 0.00077	0.000075 ± 0.000131
3	0.03371 ± 0.00197	0.000810 ± 0.000967
10	0.19690 ± 0.01339	0.006110 ± 0.028486
30	0.90084 ± 0.03541	0.051181 ± 0.009789
100	3.75231 ± 0.29881	0.193350 ± 0.062583
300	13.4367 ± 0.9035	0.622698 ± 0.241088
1000	50.6239 ± 4.5473	2.542069 ± 0.476957
3000	168.326 ± 14.495	8.353264 ± 1.423328

Table 5.11: Values of the hydrodynamic contribution to the rotational long-time self-diffusivity nondimensionalized by the Stokes-Einstein diffusivity, D^r_0, as a function of Pe for the Stokesian Dynamics system. Data obtained from 182 simulations of $N = 27$ at $\phi = 0.45$.

Stokesian Dynamics, $Pe = 0$		
ϕ	N	D^s_∞
0.20	27	0.39490 ± 0.07068
0.316	27	0.21430 ± 0.02654
0.37	27	0.13263 ± 0.02184
0.40	27	0.10972 ± 0.01999
0.45	27	0.06151 ± 0.01675
0.49	27	0.04579 ± 0.01530

Table 5.12: Values of the long-time self-diffusivity nondimensionalized by the Stokes-Einstein diffusivity, D_0, as a function of ϕ for the Stokesian Dynamics system. Data obtained from 182 simulations of $N = 27$ at $Pe = 0$.

Stokesian Dynamics, $Pe = 0$		
ϕ	N	$D^{s,r}_\infty$
0.20	27	0.78311 ± 0.12839
0.316	27	0.64759 ± 0.14221
0.37	27	0.62275 ± 0.07644
0.40	27	0.59390 ± 0.09329
0.45	27	0.52372 ± 0.08488
0.49	27	0.47733 ± 0.05833

Table 5.13: Values of the rotational long-time self-diffusivity nondimensionalized by the Stokes-Einstein diffusivity, D^r_0, as a function of ϕ for the Stokesian Dynamics system. Data obtained from 182 simulations of $N = 27$ at $Pe = 0$.

Stokesian Dynamics, $Pe = 1000$				
ϕ	D_{xx}	D_{yy}	D_{zz}	D_{xy}
0.20	0.0793 ± 0.0074	0.0169 ± 0.0035	0.0078 ± 0.0014	-0.01441 ± 0.00271
0.316	0.0677 ± 0.0063	0.0381 ± 0.0038	0.0186 ± 0.0040	-0.02628 ± 0.00532
0.37	0.0659 ± 0.0082	0.0456 ± 0.0048	0.0240 ± 0.0054	-0.03054 ± 0.00276
0.40	0.0661 ± 0.0059	0.0445 ± 0.0079	0.0279 ± 0.0040	-0.03199 ± 0.00389
0.45	0.0657 ± 0.0077	0.0485 ± 0.0071	0.0347 ± 0.0031	-0.03253 ± 0.00470
0.47	0.0687 ± 0.0056	0.0535 ± 0.0050	0.0393 ± 0.0075	-0.03243 ± 0.00430
0.49	0.0719 ± 0.0051	0.0463 ± 0.0016	0.0425 ± 0.0071	-0.02470 ± 0.00233

Table 5.14: Values of the long-time self-diffusivity, nondimensionalized by $\dot{\gamma}a^2$, as a function of ϕ for the Stokesian Dynamics system. Data obtained from 182 simulations of $N = 27$ at $Pe = 1000$.

Stokesian Dynamics, $Pe = 1000$				
ϕ	$D_{xx,b}$	$D_{yy,b}$	$D_{zz,b}$	$D_{xy,b}$
0.20	0.4282 ± 0.0819	0.4024 ± 0.0635	0.3262 ± 0.0917	0.00283 ± 0.0540
0.316	0.2596 ± 0.0479	0.2174 ± 0.0671	0.2535 ± 0.0476	0.01579 ± 0.0291
0.37	0.1950 ± 0.0247	0.1738 ± 0.0434	0.1750 ± 0.0138	0.01278 ± 0.0317
0.40	0.1530 ± 0.0317	0.1422 ± 0.0206	0.1311 ± 0.0232	0.02336 ± 0.0152
0.45	0.1066 ± 0.0193	0.1054 ± 0.0167	0.1097 ± 0.0157	0.01068 ± 0.0088
0.47	0.1028 ± 0.0240	0.0831 ± 0.0219	0.0890 ± 0.0137	0.01192 ± 0.0030
0.49	0.0705 ± 0.0054	0.0611 ± 0.0113	0.0608 ± 0.0164	0.01439 ± 0.0087

Table 5.15: Values of the Brownian contribution to the long-time self-diffusivity nondimensionalized by the Stokes-Einstein diffusivity, D_0, as a function of ϕ for the Stokesian Dynamics system. Data obtained from 182 simulations of $N = 27$ at $Pe = 1000$.

Stokesian Dynamics, $Pe = 1000$				
ϕ	$D_{xx,h}$	$D_{yy,h}$	$D_{zz,h}$	$D_{xy,h}$
0.20	0.0793 ± 0.0066	0.0163 ± 0.0034	0.0072 ± 0.0014	-0.01440 ± 0.00261
0.316	0.0669 ± 0.0062	0.0373 ± 0.0034	0.0182 ± 0.0040	-0.02587 ± 0.00521
0.37	0.0654 ± 0.0082	0.0450 ± 0.0049	0.0231 ± 0.0053	-0.03033 ± 0.00303
0.40	0.0664 ± 0.0057	0.0437 ± 0.0076	0.0272 ± 0.0038	-0.03168 ± 0.00405
0.45	0.0644 ± 0.0074	0.0478 ± 0.0072	0.0337 ± 0.0033	-0.03223 ± 0.00454
0.47	0.0677 ± 0.0060	0.0526 ± 0.0048	0.0386 ± 0.0073	-0.03217 ± 0.00459
0.49	0.0712 ± 0.0047	0.0454 ± 0.0014	0.0415 ± 0.0071	-0.02440 ± 0.00227

Table 5.16: Values of the hydrodynamic contribution to the long-time self-diffusivity, nondimensionalized by $\dot{\gamma}a^2$, as a function of ϕ for the Stokesian Dynamics system. Data obtained from 182 simulations of $N = 27$ at $Pe = 1000$.

Stokesian Dynamics, $Pe = 1000$				
ϕ	D^r_{xx}	D^r_{yy}	D^r_{zz}	D^r_{xy}
0.20	0.0051 ± 0.0006	0.0079 ± 0.0008	0.0190 ± 0.0020	0.00156 ± 0.0002
0.316	0.0075 ± 0.0010	0.0101 ± 0.0009	0.0311 ± 0.0012	0.00226 ± 0.0007
0.37	0.0096 ± 0.0010	0.0117 ± 0.0007	0.0383 ± 0.0024	0.00291 ± 0.0007
0.40	0.0090 ± 0.0009	0.0118 ± 0.0014	0.0419 ± 0.0021	0.00260 ± 0.0007
0.45	0.0107 ± 0.0007	0.0120 ± 0.0012	0.0384 ± 0.0036	0.00187 ± 0.0004
0.47	0.0113 ± 0.0014	0.0123 ± 0.0001	0.0391 ± 0.0037	0.00110 ± 0.0010
0.49	0.0117 ± 0.0006	0.0104 ± 0.0012	0.0349 ± 0.0009	0.00110 ± 0.0004

Table 5.17: Values of the long-time rotational self-diffusivity, nondimensionalized by $\dot{\gamma}$, as a function of ϕ for the Stokesian Dynamics system. Data obtained from 182 simulations of $N = 27$ at $Pe = 1000$.

Stokesian Dynamics, $Pe = 1000$				
ϕ	$D^r_{xx,b}$	$D^r_{yy,b}$	$D^r_{zz,b}$	$D^r_{xy,b}$
0.20	0.6960 ± 0.1668	0.7849 ± 0.1671	0.6852 ± 0.1350	0.05075 ± 0.1637
0.316	0.4892 ± 0.1426	0.6169 ± 0.0838	0.5786 ± 0.0620	-0.01410 ± 0.7855
0.37	0.4584 ± 0.0245	0.4309 ± 0.0741	0.4875 ± 0.1062	-0.05683 ± 0.0694
0.40	0.3765 ± 0.0470	0.3624 ± 0.0807	0.4054 ± 0.0557	0.00675 ± 0.0310
0.45	0.3365 ± 0.0584	0.3175 ± 0.0719	0.3203 ± 0.0381	-0.03806 ± 0.0567
0.47	0.2797 ± 0.0619	0.2794 ± 0.0390	0.3039 ± 0.0421	0.02466 ± 0.0337
0.49	0.2871 ± 0.0891	0.2679 ± 0.0391	0.2920 ± 0.0305	-0.04215 ± 0.0165

Table 5.18: Values of the Brownian contribution to the long-time rotational self-diffusivity nondimensionalized by the Stokes-Einstein diffusivity, D^r_0, as a function of ϕ for the Stokesian Dynamics system. Data obtained from 182 simulations of $N = 27$ at $Pe = 1000$.

Stokesian Dynamics, $Pe = 1000$				
ϕ	$D^r_{xx,h}$	$D^r_{yy,h}$	$D^r_{zz,h}$	$D^r_{xy,h}$
0.20	0.0044 ± 0.00050	0.0076 ± 0.0007	0.0185 ± 0.0020	0.00153 ± 0.0002
0.316	0.0071 ± 0.00112	0.0099 ± 0.0008	0.0301 ± 0.0011	0.00241 ± 0.0008
0.37	0.0090 ± 0.00099	0.0114 ± 0.0006	0.0378 ± 0.0026	0.00283 ± 0.0007
0.40	0.0087 ± 0.00088	0.0115 ± 0.0012	0.0415 ± 0.0019	0.00254 ± 0.0006
0.45	0.0102 ± 0.00070	0.0117 ± 0.0012	0.0380 ± 0.0034	0.00191 ± 0.0004
0.47	0.0108 ± 0.00160	0.0119 ± 0.0010	0.0384 ± 0.0034	0.00100 ± 0.0012
0.49	0.0114 ± 0.00046	0.0101 ± 0.0011	0.0349 ± 0.0008	0.00116 ± 0.0006

Table 5.19: Values of the hydrodynamic contribution to the long-time rotational self-diffusivity, nondimensionalized by the $\dot{\gamma}$, as a function of ϕ for the Stokesian Dynamics system. Data obtained from 182 simulations of $N = 27$ at $Pe = 1000$.

Chapter 6
Concluding Remarks

The behavior of concentrated colloidal suspensions is examined theoretically and with the use of dynamic simulation. The steady-state behavior is examined using both Brownian Dynamics and Stokesian Dynamics simulation techniques. Regardless of whether hydrodynamic interactions are included or not, the suspension exhibits shear thinning at low shear rates. At high shear rates, the suspension orders in the absence of hydrodynamic interactions and remains well-dispersed and shear thickens in the presence of hydrodynamic interactions.

Steady state Stokesian Dynamics simulations have been previously performed in planar extensional flow (Sami 1996) showing behavior that is similar to that of simple shear flow. It would be of interest and relatively straightforward to perform Brownian Dynamics simulations with this type of flow to see what type of order — if any — is present at high shear rates. Strongly ordered phases are quite interesting in their own right, but cause difficulties when making comparisions with the system where hydrodynamic interactions are included and the suspensions show no order. If the suspension remains well-dispersed at high shear rates in planar extensional flow, more useful comparisons with the Stokesian Dynamics system can be made.

Extension of this work may also be made to bidisperse suspensions. Bidisperse suspensions are of interest in that they pack more efficently — smaller particles can occupy the voids between larger particles — and larger volume fractions can be studied. Bidisperse suspensions may also provide insight into the behavior of polydisperse suspensions which are prevalent in industrial applications. The particle size is included in numerous dimensionless variables and scale factors throughout the previous chapters. How does one account for the presence of two particle sizes in the system for each of these quantities? Two new axes in parameter space are added with the introduction of a second particle size: the ratio of the two sizes and the ratio of the volume fractions occupied by particles of each size. Thus, even a simple method to incorporate a second size produces a wide range of flow regimes to study.

The Brownian Dynamics algorithm used in this work is extremely simple. Although some approximation is necessary in hard-sphere Brownian Dynamics algorithms due to the singular nature of the hard-sphere potential coupled with the

dampening nature of low-Reynolds-number flow, it is forseeable that more detailed algorithms may arise to more accurately describe particle-particle collisions. These algorithms may be of use in studying the behavior of suspensions near close packing, where particle-particle collisions are much more common, and to determine whether or not there is a glass transition present in these systems.

The high computational cost of Stokesian Dynamics simulations limits the study in the previous chapters to small systems. Larger systems are necessary in order to obtain quality data at low shear rates or high densities. Improved simulation algorithms and faster computer chips are becoming available which may enable large-scale Stokesian Dynamics simulations to be performed.

Finally, the nonzero off-diagonal component to the self-diffusion tensor was discussed in the previous chapter. The mechanism for this mode of diffusion is due to a buildup of particles in the compressional zone and a depletion of particles in the extensional zone. Such conditions are usually present in any well-dispersed medium undergoing a simple shear flow. It would be quite interesting to see if there is an off-diagonal component to the self-diffusion tensor in molecular liquids, emulsions, polymer solutions, fiber suspensions, liquid crystals, etc. It would be interesting to try and measure the off-diagonal component experimentally.